PERFORMANCE OF A NEAR SHORE OSCILLATING WAVE SURGE CONVERTER WITH VARIABLE FLAP CONFIGURATIONS

by

Landon Spencer Sugar

December, 2021

Director of Thesis: Dr. Faete "JT" Filho

Major Department: Department of Engineering

Most oscillating wave surge converters (OWSCs) are designed to enter survival mode during energetic wave conditions where they forego the opportunity to extract energy in an attempt to preserve structural integrity. While this is a good tradeoff, it is important that OWSC technology progresses to a point where energy is constantly extracted when waves are present. The OWSC studied here is a variation of a device that was conceptually designed and patented by researchers at the National Renewable Energy Laboratory (NREL) and consists of multiple adjustable vanes that, when opened, allow some of the wave force to pass through the device. Currently, NREL's investigations have been limited to a single OWSC consisting of 4 and 5 adjustable vanes. Therefore, there exists a need to further investigate the performance of this nearshore variable geometry OWSC in various arrangements and configurations. This research analyzes the hydrodynamic response of a 2-vane OWSC, a 4-vane OWSC, and an array of OWSCs in a frequency-domain code, a 2-vane OWSC's power generation capabilities in a wide range of sea states in a time-domain wave energy converter simulation tool, and a fluid flow analysis of the 2-vane OWSC in standard and energetic sea states using computational fluid dynamics (CFD). It was hypothesized that opening the vane angles would significantly and consistently reduce the OWSC's hydrodynamic response to various wave frequencies, its power production capabilities,

its oscillatory motions, and the potential for wave slamming. The frequency- and time-domain results indicated that most configurations had consistent and predictable responses, while other configurations were more sensitive to the vane angle changes. The CFD results indicated that opening the vanes led to a reduction in wave slamming. However, the fluid flow became highly unpredictable as the vane angles changed, resulting in incident wave damping, inconsistent OWSC oscillations, and hydraulic jump formation.

PERFORMANCE OF A NEAR SHORE OSCILLATING WAVE SURGE CONVERTER WITH VARIABLE FLAP CONFIGURATIONS

A Thesis

Presented to the Faculty of the Department of Engineering

East Carolina University

In Partial Fulfillment of the Requirements for the Degree

Master of Science in Mechanical Engineering

by

Landon Spencer Sugar

December, 2021

PERFORMANCE OF A NEAR SHORE OSCILLATING WAVE SURGE CONVERTER WITH VARIABLE FLAP CONFIGURATIONS

By

Landon Sugar

APPROVED BY:

Director of Thesis _____

Dr. Faete "JT" Filho

Committee Member _____

Dr. Tarek Abdel-Salam

Committee Member _____

Dr. Michael Muglia

Chair of the Department _____

Dr. Barbara Muller-Borer

Dean of the Graduate School _____

Paul J. Gemperline, PhD

Dedication

All praise, glory, and recognition for this work go to our Lord and savior, Jesus Christ. This research was made possible only by the active work, power, and guidance of The Holy Spirit, and the incessant comfort that comes from God, my Father. I thank God for sending his one and only son to die for me, so that I can be in right relationship with Him. I thank God for giving me his inspired word that is fully alive and active—not just a history book. Scriptures such as Matthew 8, Judges 6-8, 1st Samuel 17, and Exodus 3-4 have been foundations on which I stand throughout the last two years. Throughout this process, The Lord has shown me that with Him, all things are possible.

I thank God for the people that surrounded and encouraged me during this journey, especially my wife Rachel, my spiritual father Kenn, and my brothers Mick, Rob, Brock and Matthew. I love you all.

I thank God for giving me such a supportive family who love me so well. Thank you for always being there for me, and for your unending patience. I love you all very much.

Acknowledgements

I would like to thank all of the faculty support I have received during this time as well. Thank you to Dr. Tarek-Abdel Salam, Dr. Faete Filho, Dr. Mike Muglia, Keith Thomson, Dr. Teresa Ryan, and Hunter Pigg. Furthermore, I would like to thank each individual at the Field Research Facility and Coastal Studies Institute for their hard work and dedication to extracting wave information. None of this work would have been possible without all of your help. Thank you.

Table of Contents

List of Tables

List of Figures

List of Acronyms

Abbreviation	Definition	Unit (if applicable)
A	Added mass term	kgm^2
a	Wave amplitude	m
A_∞	Added moment of inertia at infinite frequency	kgm^2
A_{cd}	Computational domain cross sectional area	m^2
A_d	Characteristic surface area	m^2
$\mathbf{A_r}$	time-invariant state matrix	
$\mathbf{A}(\boldsymbol{\omega})$	Added mass matrix	kgm^2
B	Radiation damping term	kgm^2/s
BEM	Boundary element method	
BEMIO	BEM Input/ Output	
BGM	Bounded Gradient Maximization	
B_{nl}	Non-linear damping	Nms/rad
B_{opt}	Optimum damping coefficient	Nms/rad
B_{PTO}	Linear damping coefficient	Nms/rad
$\mathbf{B_r}$	time-invariant input matrix	
$\mathbf{B}(\boldsymbol{\omega})$	Radiation damping matrix	
C	Courant number	
c	Phase speed	m/s
CAD	Computer-aided design	
CD	Computational domain	
C_d	Drag coefficient	
CFD	Computational Fluid Dynamics	
$c_{g,shallow}$	Group velocity of shallow waves	m/s
CICSAM	Comprehensive Interface Capturing Scheme for Arbitrary Meshes	
$\mathbf{C_r}$	time-invariant output matrix	
CSF	Continuum Surface Force	N
CSI	Coastal Studies Institute	
c_{sound}	Speed of sound	m/s
C_{ws}	Normalizing factor	
D	Mean water depth	m
d	Water depth	m
d_h	Hydraulic diameter	m
d_{mk}	Distance between the center of the m^{th} element to the center of the adjacent element	m
DOF	Degrees of freedom	
d_{tube}	Tube diameter	m
$D(\theta_{dir})$	Directional distribution	Degrees
E	Energy	kWh
$E_{irregular}$	Energy in irregular wave	J/m^2
E_k	Kinetic energy	J/m^2
E_p	Potential energy	J/m^2

E_{total}	Total linear wave energy	J/m^2
$\vec{F}$	External body forces	N
f	Wave frequency in Hertz	Hz
F_B	Buoyancy Force	N
F_e	Wave excitation force	N
FEA	Finite element analysis	
$\vec{F}_{hys}$	Hydrostatic force	N
f_p	Peak wave frequency	rad/s
F_{PTO}	Power take-off forces	N
Fr	Froude Number	
FRA	Fixed reference axis	
FRF	Field Research Facility	
FSWL	Free surface water level	
F_v	Viscous forces	N
FVM	Finite volume method	
F_{vol}	Volume force	N
F_x	Momentum balance equation	N
G	Center of gravity	m
g	Gravity	m/s^2
h	Distance from bottom of channel to free surface water level	m
H	Wave height	m
HDF5	Hierarchal Data Format 5	
H_s	Significant wave height	m
I	OWSC moment of inertia	kgm^2
IRF	Impulse Response Function	
I_{tensor}	Unit tensor	
I_{turb}	Turbulence Intensity	kg/m^3
I_{xx}, I_{yy}, and I_{zz}	Moments of inertia taken at the output coordinate system	kgm^2
JONSWAP	Joint North Sea Wave Observation Project	
JPD	Joint probability distribution	
k	spring constant	N/m
K	wave steepness / wave number	
k_{Ansys}	Scalar in Ansys	
K_e	Excitation IRF	
k_{eff}	Thermal conductivity	W/mK
K_r	Radiation IRF	
L	Distance from the bottom of OWSC to its center	m
l	OWSC shape	m
L_{max}	Length of longest panel	m
L_{xx}, L_{yy}, and L_{zz}	Moments of inertia taken with the center of mass and aligned with output coordinate system	kgm^2
m	Mass of structure	kg
M_5	Hydrodynamic moment	Nm

MAEP	Mean annual energy production	kWh
M_{air}	Mach number in air	
MCR	Multiple conditions run	
M_{d5}	5^{th} diffracting moment	Nm
$\overrightarrow{M}_{hys}$	Hydrostatic moment	Nm
M_{I5}	5^{th} Froude-Krylov moment	Nm
m_k	Spectral moment	Nm
M_{mach}	Mach number	
$M_{r5,5}$	Radiation moment	Nm
M_{water}	Mach number in water	
n	Unit normal vector	
N_{bands}	Number of wave frequency bands	
NC	North Carolina	
N_{LID}	Total number of interior lid elements	
N_p	Total number of diffracting panels	
NREL	National Renewable Energy Laboratory	
n_s	Number of edges on the element	
$\hat{n}_w$	Unit vector normal to wall	
ODE	Ordinary differential equation	
OWSC	Oscillating wave surge converter	
p	Water surface pressure	Pa
P	Wave power	kW
p_d	Dynamic pressure	Pa
PDE	Partial differential equation	
$P_{irregular}$	Power per meter wave crest in irregular wave	W/m
PM	Pierson-Moskowitz	
P_{PTO}	Instantaneous power absorbed into PTO	kW
$P_{regular}$	Power per meter wave crest in regular wave	W/m
p_s	Hydrostatic pressure	Pa
PTO	Power take-off	
PTO-Sim	Power take-off simulator	
QR	Quick response	
QTF	Quadratic transfer function	
$\vec{r}$	Hull position vector	
RANS	Reynolds-Averaged Navier-Stokes	
Re	Reynold's number	
R_f	Ramp function	
r_{fm}	Radius of m^{th} element	m
RNG	Re-Normalization group	
R_x	Roll rotation	Radians
R_y	Pitch rotation	Radians
R_z	Yaw rotation	Radians
$\Re$	Real part of equation	
$S_1^{k_{Ansys}}$	Source term of phase 1	
S_0	Wetter surface of body in calm water	

S_k	Adjacent panels	
S_m	Source mass	m
SNL	Sandia National Laboratories	
SS	State space	
SST	Shear stress transport	
STL	Stereolithographic	
SW	SolidWorks	
$S(f,\theta)$	Variance density spectrum	Hz
$S(\omega)$	Frequency dependent wave spectrum	rad/s
T	Temperature	Degrees Celsius
t	time	s
T_e	Wave energy period	s
T_e	Wave exciting torque	Nm
T_h	Hydrodynamic torque	Nm
T_r	Radiation torque	Nm
t_r	Ramp time	s
T_v	Viscous torque	Nm
$\hat{t}_w$	Unit vector tangential to wall	
U	Free stream velocity	m/s
u	x-direction water velocity	m/s
$\overrightarrow{u_1}$,	Phase-1 velocity	m/s
U_f	Volume flux	
$U_{incident}$	Uniform incident wave velocity	m/s
$\overrightarrow{u_m}$	Mixture velocity	m/s
Ur	Ursell Number	
U_{wet}	Wetted perimeter of computational domain	m
$\vec{v}$	Velocity vector	m/s
V	Fluid velocity	m/s
v	OWSC velocity	m/s
$\forall$	Volume of element	m^3
VOF	Volume of Fluid	
WAMIT	WaveAnalysisMIT	
WEC	Wave energy converter	
WEC-Sim	Wave Energy Converter Simulator	
x	Surge direction	
$\dot{x}$	Velocity vector of floating body	m/s
$\ddot{x}$	Acceleration of the structure	m/s^2
$\vec{X}_k$	Coordinates of panel geometric center of the k^{th} panel	
y	Sway direction	
z	vertical position coordinate / heave direction	
z_m	Z-coordinate of the center of the m^{th} element in the FRA	
α	peak-shape parameter exponent	
α_1	Volume fraction of phase 1	
α_q	Volume fraction coefficient	

α_{qf}	Face value of q^{th} volume fraction	
β_{lim}	Slope limiter	
γ	Non-dimensional peak-shape parameter	
$\Gamma_1^{k_{Ansys}}$	Diffusion coefficient phase 1	
$\Gamma_m^{k_{Ansys}}$	Diffusion coefficient of mixture	
ΔS_m	Area of m^{th} panel	m^2
$\Delta\omega$	Change in wave frequency	rad/s
ϵ	Phase difference	Radians
ζ	Wave profile	
η	Free surface water level	m
η_{irreg}	Irregular incident waves	
θ	Position of the OWSC	Radians
θ_{dir}	Wave direction	Radians
θ_v	OWSC's angular velocity	rad/s
θ_w	Contact angle at wall boundary	Radians
κ	Curvature	
λ	Wavelength	rad/s
μ	Molecular viscosity	Pa*s
μ_{dyn}	Dynamic viscosity	Pa*s
μ_{ocean}	Dynamic viscosity for seawater	Pa*s
$\vec{\xi}_m$	Coordinates of panel geometric center over the m^{th} panel	
ρ_1	Physical density phase 1	kg/m^3
ρ	Density of seawater	kg/m^3
$\overrightarrow{\rho g}$	Gravitational body forces	N
ρ_m	Mixture density	kg/m^3
σ	Surface tension coefficient	
τ	Time lag	s
$\bar{\bar{\tau}}$	Stress tensor	psi
υ	Phase seed	
ϕ	Velocity Potential	
$\varphi(\vec{X})$	Space dependent potential term	
φ_1	First order incident wave potential	
φ_d	Diffraction wave potential	
$\phi_1^{k_{Ansys}}$	Transport variable phase 1	
φ_{r5}	Radiation wave potential	
ω	Wave frequency	rad/s
ω_a	angular frequency	rad/s
ω_{dis}	Turbulent Dissipation Rate	
ω_e	Effective wave frequency	rad/s

1 Introduction

1.1 Oscillating Wave Surge Converter Background

An oscillating wave surge converter (OWSC) is a type of wave energy converter (WEC) that consists of a buoyant flap that is typically hinged at the sea floor in depths of 10 to 15 meters [1]. After the OWSC is struck by a wave, it pitches around the axis parallel to the wave crest and is then restored to its original position primarily by the force of buoyancy. This rotary motion can be converted in multiple ways, two which being electrically, by exciting a generator, or mechanically, by pressurizing seawater. The energy extraction capabilities of an OWSC are primarily dependent on the wave force it experiences, with other parameters affecting the extraction such as the OWSC height, width, mooring configuration, power take-off (PTO) design, and water depth. Traditionally, the main body of the OWSC has been a fixed, rectangular surface [2] or composed of several fixed cylindrical tubes [1]. However, researchers at The National Renewable Energy Laboratory (NREL) have recently introduced an OWSC design that introduces multiple adjustable vanes within the entire paddle structure. The ability to have varying vane angle configurations is a concept similar to the pitching blades of a wind turbine [3]. These adjustable vanes act as a control knob that limits the loads experienced by the device. Figure 1-1 compares the three OWSC designs discussed above.

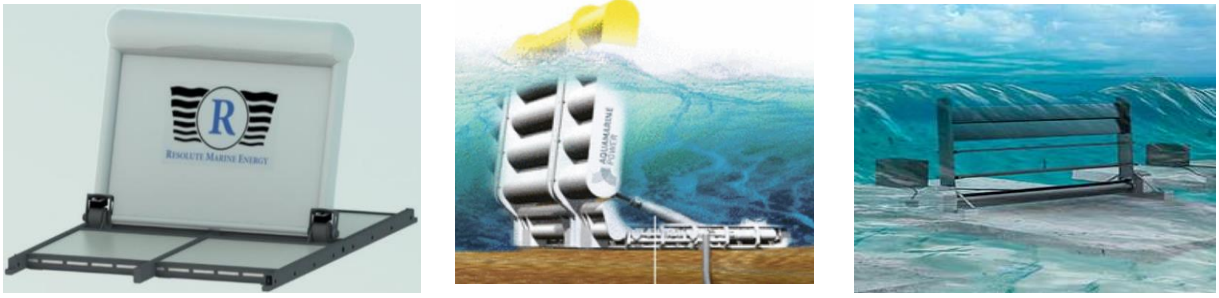

(a) **(b)** **(c)**

Figure 1-1. OWSC with (a) Rectangular Surface [2] (b) Cylindrical Tubes [1] (c) Adjustable Vanes [3]

1.2 Challenges and Needs

The technology to harvest ocean energy may be in its infancy stages relative to other renewable technologies. Because the ocean is a harsh, corrosive, environment, marine hydrokinetic energy (MHK) is particularly challenging endeavor with one of its main challenges being energy extraction in a wide array of sea conditions [3], [4], [5], [6], [7]. Currently, most OWSCs are designed to enter survival mode during extreme conditions where they forego the opportunity to extract energy in attempts to preserve structural integrity. While this has been a good tradeoff, WEC technology should be advancing to a point where energy is constantly extracted when waves are present. Until recently, most OWSC's studied have a fixed, rectangular face. However, the OWSC being studied here, conceptually designed and patented by Nathan Tom, et al. at NREL [3], [8], consists of a flap face with adjustable vanes, similar to the workings of household blinds or pitching wind turbine blades. This adjustability allows the vanes to be fully closed, partially open by some degree, and fully open to accommodate varying sea conditions. Currently, NREL's investigations have been limited to an OWSC consisting of 4 or 5 vanes [3], [8]. Therefore, this work addresses the need to further investigate the performance of this variable geometry OWSC with several modifications and implementations to investigate its performance in a wide range of sea conditions.

1.3 Specific Aims

The purpose of this research was to advance ocean renewable technologies so ocean energy can become utilized as another renewable energy technology. Specifically, this work continues to investigate a nearshore OWSC similar to Nathan Tom et al.'s variable geometry OWSC [9]. This work explored a singular OWSC with 2 adjustable vanes, a 2x2 array and 3x3 array with 2 adjustable vanes, and singular OWSC with 4 adjustable vanes. The purpose of using fewer vanes was to investigate the OWSC's sensitivity to fewer vanes and to reduce the number of moving parts in the OWSC, thus simplifying the design. Furthermore, this work includes the new addition of more vane-angle configurations, including 90° (fully closed), 60°, 45°, 30°, and 0° (fully open). From the fully closed configuration, the vanes were rotated clockwise to 60°, 45°, and 30° until fully open at 0°. This innovative, nearshore OWSC with various vane angle configurations was studied in shallow water with various wave conditions from the reference site, detailed in Section

1.6. Regarding the single 2-vane device, the specific parameters that were investigated are mentioned below, and described in detail subsequently:

- Hydrodynamic coefficients
- Power production
- Fluid flow analysis

The investigation of the 4-vane OWSC provided insight into the effects of adding more adjustable vanes within the same space. The array investigation provided insight as to how the presence and proximity of multiple OWSC's affected each other. Regarding the 4-vane configuration, the 2x2 array, and the 3x3 array, only the hydrodynamic coefficients were investigated. The 2-vane OWSC is depicted in Figure 1-2, the 4-vane OWSC is depicted in Figure 1-3, and the 2x2 and 3x3 array arrangements can be seen in Figure 1-4 and Figure 1-5 respectively. To save space, only the closed configuration for the arrays are shown.

The specific aims for using a time-domain tool in this work were to obtain the power production capabilities based on the wave data from the reference site and mean annual energy production matrices that are a function of wave height and wave period. This gave an indication as to which sea states harvested the most power over time, and how much power each configuration would harvest each year.

Since time-domain tools cannot output non-linear events such as wave slamming, described in Section 1.7, or flow field parameters such as velocity profile and dynamic pressure contours, CFD was used. These parameters provided insight as to how the fluid flow was affected by different vane angle configurations and sea states. The single OWSC arrangement in each of its five different vane angle configurations was studied in CFD to investigate the velocity profile around the OWSC, dynamic pressure contours, and determining whether or not wave slamming occurred. This was conducted for two wave conditions: one that occurs the most frequently at the reference site, and the other being a more energetic wave condition that also has a large presence at the reference site. Both of these wave conditions are explained further in Section 1.6.

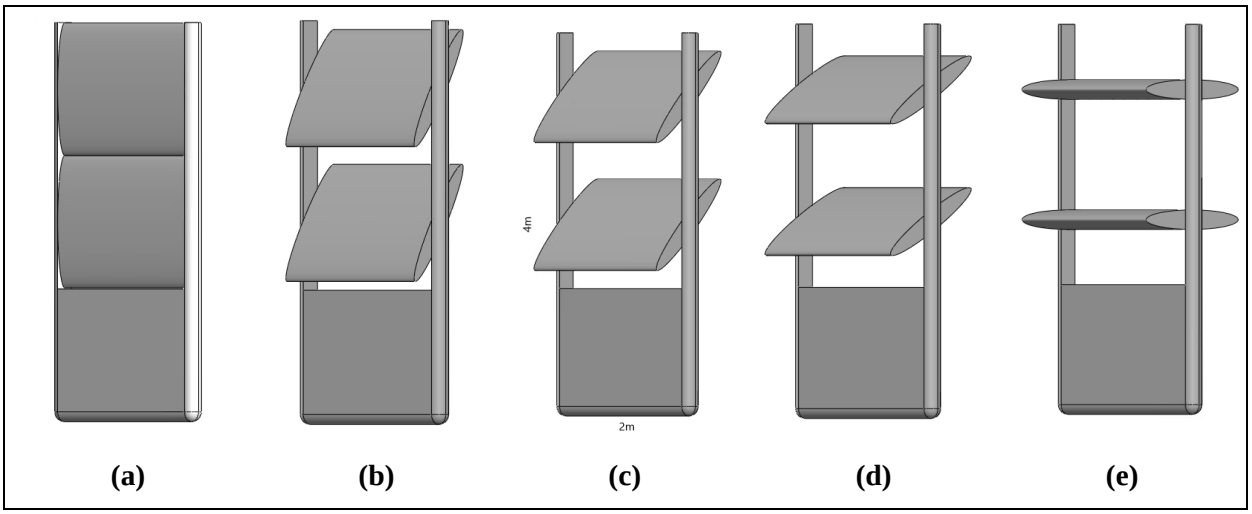

Figure 1-2. Geometry of Singular 2-Vane OWSC Structure with Various Vane Angle Configurations: (a) 90° (b) 60° (c) 45° (d) 30° (e) 0°

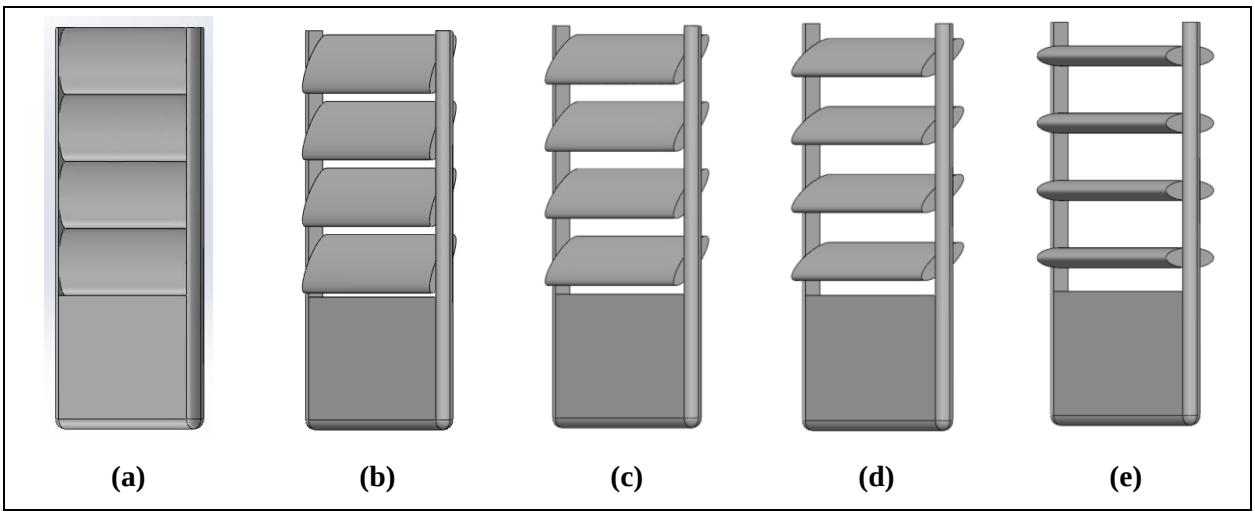

Figure 1-3. Geometry of Singular 4-Vane OWSC Structure with Various Vane Angle Configurations: (a) 90° (b) 60° (c) 45° (d) 30° (e) 0°

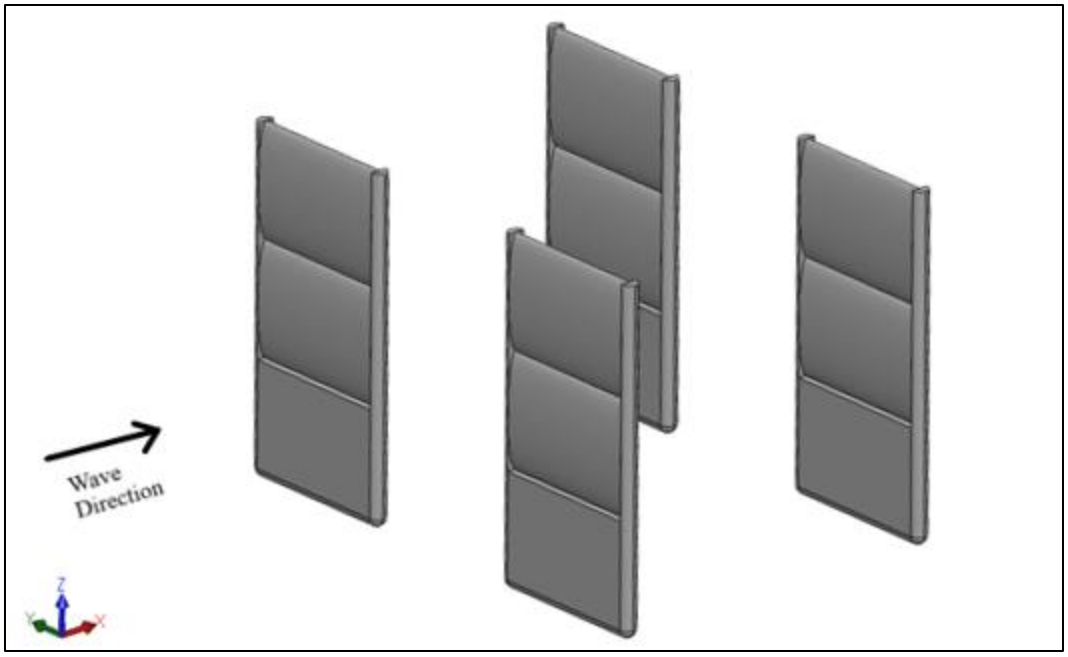

Figure 1-4. 2x2 Array Configuration of Closed 2-Vane OWSC

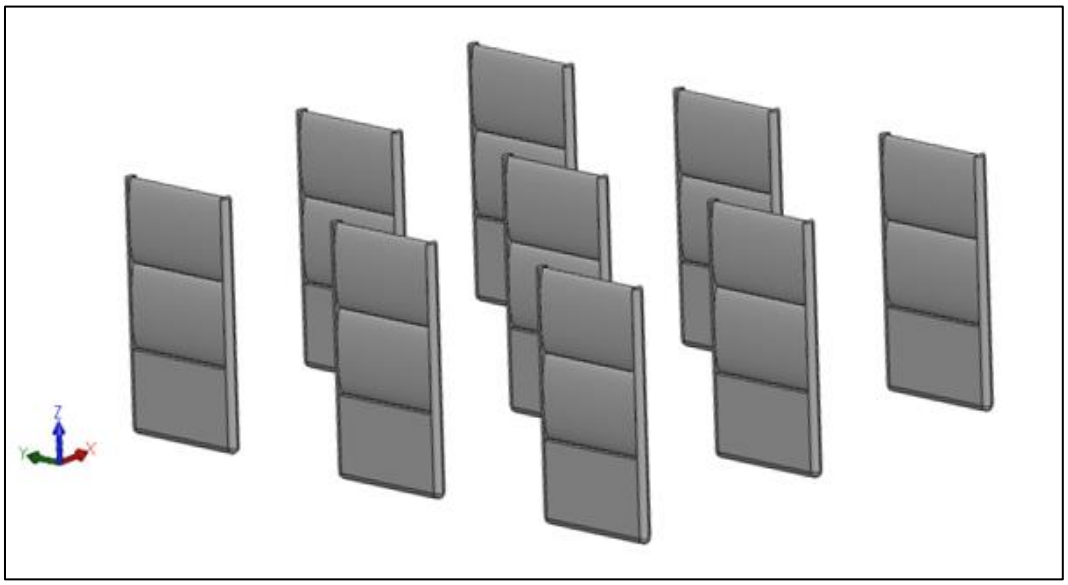

Figure 1-5. 3x3 Array Configuration of Closed 2-Vane OWSC

1.4 Significance

NREL has suggested further studies are needed on WECs in extreme conditions since these devices should be progressing towards operability in various sea conditions [9]. This research holds

significant value since it is a highly detailed extension of Nathan Tom et al.'s variable geometry OWSC that was originally intended to operate in a wide range of sea states. Specifically, the significant value lies in the detailed investigation of its performance with a fewer number of adjustable vanes, the addition of vane angle configurations, and the effects from array arrangements. This is the first time that research has been conducted on the specific OWSC being studied here, thus adding to the originality of this research [9]. Currently, the wave energy community is leveraging methodologies from offshore oil and gas structures as well as naval vessel applications. Although these methods have benefitted the wave energy community, wave energy technology should continue to progress towards commercial viability [10]. The specific aims mentioned previously will contribute to the advancement of ocean renewable energy, thus making it more economically competitive with other electricity generating technologies by reducing the levelized cost of energy [11].

1.5 Hypothesis

Waves have forward-backward, left-right, and up-down components that are also known as surge, sway, and heave respectively. Consequently, there may exist multi-directional forces that act on the OWSC being studied such as vertical forces due to the heave motion, or x- and y- directional forces due to the surge and sway motions respectively. It was expected for surge wave forces to have the greatest impact on power extraction capabilities. The OWSC being studied here has the capability of varying the vane angle, which was predicted to mitigate the experienced wave force by allowing some of the wave energy to pass through the device, thus preserving its structural integrity. It was hypothesized that opening the vanes would significantly reduce the fluid-structure interaction resulting from the surge motion of waves, leading to lower magnitude hydrodynamic coefficients, average power production per wave state, and wave slamming events that acted on the OWSC. Since there were several analyses studied in this work, the expected outcomes of each arrangements and configurations are discussed in greater detail below.

1.5.1 Hydrodynamic Coefficients - Expected Outcomes

Regarding the single 2-vane and 4-vane OWSC, it was expected that hydrodynamic coefficients would consistently and predictably decrease in magnitude as the vanes were opened, allowing for

better controllability regarding wave force on the OWSC. Since the overall dimensions of the OWSC did not change between the 2-vane and 4-vane OWSC, it was expected that that 4-vane OWSC would experience larger hydrodynamic coefficient magnitudes since 4 adjustable vanes occupied more space than 2 adjustable vanes. Regarding the 2x2 and 3x3 array, it was expected that the OWSCs next to each other would not experience any effect from the surrounding OWSCs. However, it was expected for the hydrodynamic coefficients of the OWSCs located in front of and behind one another to reduce in magnitude and show signs of numerical instability.

1.5.2 Power Production - Expected Outcomes

In this section, only the single 2-vane OWSC was investigated in each vane angle configuration for a wide range of sea states based on data from the reference site. It was expected that there would exist a consistent decrease in power production potential as the vanes are opened. Since the power contribution matrix was most important, it was expected for the sea state that yields the highest potential energy production would not be the sea state that actually contributes the most power for that specific location.

1.5.3 Fluid Flow Analysis - Expected Outcomes

In this section, the 2-vane OWSC was investigated in all of its vane angle configurations in two sea states: one that was the most common at the reference site, and one that was more energetic than the former. When the vanes were not fully closed, it was expected that the upper and lower tips of each vane would contribute to the highest fluid velocity and turbulence. When the vanes were fully closed, more turbulence was expected at the tip of the upper vane than the lower vane. It was expected that the highest dynamic pressure contour would exist on the seaward face of the OWSC as it interacted with the incident wave, and on the landward face of the OWSC when it pitched seaward. Wave slamming, described in Section 1.7, was not expected to occur for the calmer sea state. However, wave slamming was expected for the closed configuration during the more energetic sea state. Furthermore, if wave slamming existed among either of the wave conditions, it was expected for this phenomenon to diminish as the vane angles approached 0°, or fully open.

1.6 Reference Site

Before launching a WEC for testing, there should be knowledge of the wave energy resource and wave characteristics at the reference site of interest. This is helpful in determining the site's suitability for renewable energy devices. Typically, a nearby research facility, in this case the Field Research Facility (FRF) in Duck, North Carolina (NC), has deployed and/or maintained data-collecting buoys situated along the coast. Led by the United States Army Corps of Engineers, FRF focuses on monitoring waves, tides, currents, local meteorology, and the consequent beach response. Another nearby research facility in NC is the Coastal Studies Institute (CSI), a research and educational facility led by East Carolina University. CSI and FRF are approximately 26 miles apart, so their nearshore characteristics are quite similar—a wide continental shelf, a sandy sea floor, and a gently sloping bathymetry [12]. The reference site used for this research was nearshore, hindcast data obtained at 36.1858 N, 75.7486 W at a 4.8 m water depth. The wave environment had an annual average power flux of approximately 3.28 kW/m [12]. Researchers at CSI produced a statistical model that was used to characterize the wave energy resource at the Jennette's Pier and FRF testing sites. This model uses historical data to produce a joint probability distribution (JPD) of sea states and a 31-year hindcast dataset, so energetic sea states could be identified [12]. A JPD is a 2-D or 3-D histogram that is characterized by two variables and plots the probability of that event occurring. Here, the two variables are significant wave height, H_s, and energy period, T_e. The JPD of sea states shows the frequency of occurrence of a specific sea state bin. For example, in Figure 1-6 the most common sea state occurrence, $0.5 < H_s < 1.0$ and $5 < T_e < 6$, accounts for 14.53% of the annual total. Similarly, Figure 1-7 shows the percentage of contribution to the total wave energy per year which is 28,815 kWh/m, or 3.29 kW/m if omnidirectional wave are considered [12]. Here, the sea state that contributes to the most energy is in the range of $1 < H_s < 1.5$ and $5 < T_e < 6$. It should be noted that the sea state with the highest frequency of occurrence does not always correlate to the sea state that contributes the highest amount of wave energy [13]. The mean, 5^{th} and 95^{th} percentiles of wave steepness are shown in the JPD figures. Because the depth at this region of study is 4.8 meters, the reference site suitable for testing nearshore OWSCs. More information on the reference site described here can be found in [12].

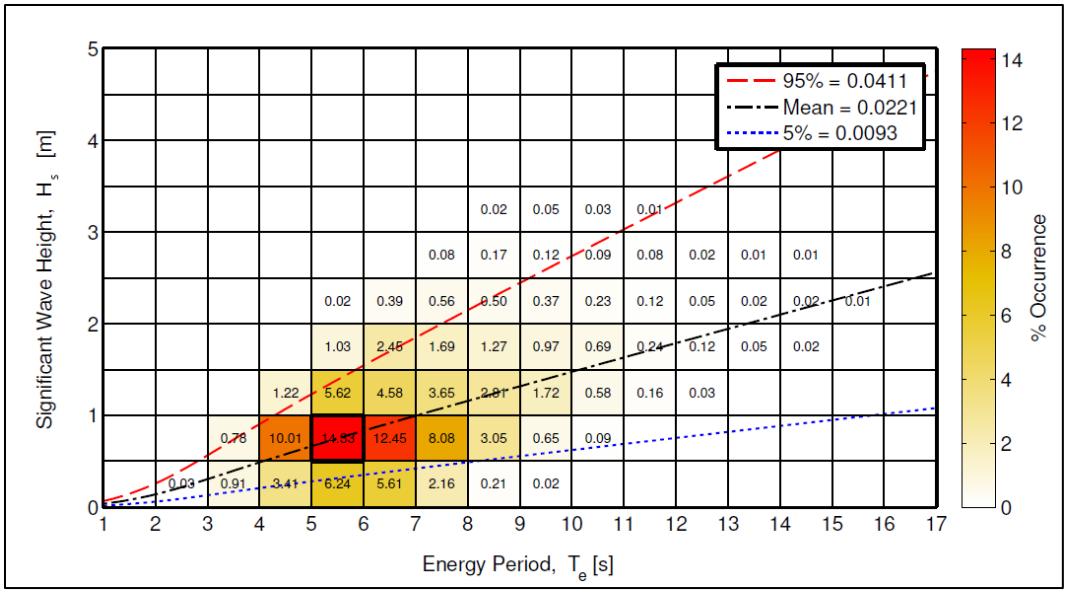

Figure 1-6. Joint Probability Distribution at the Reference Site in Duck, NC [12]

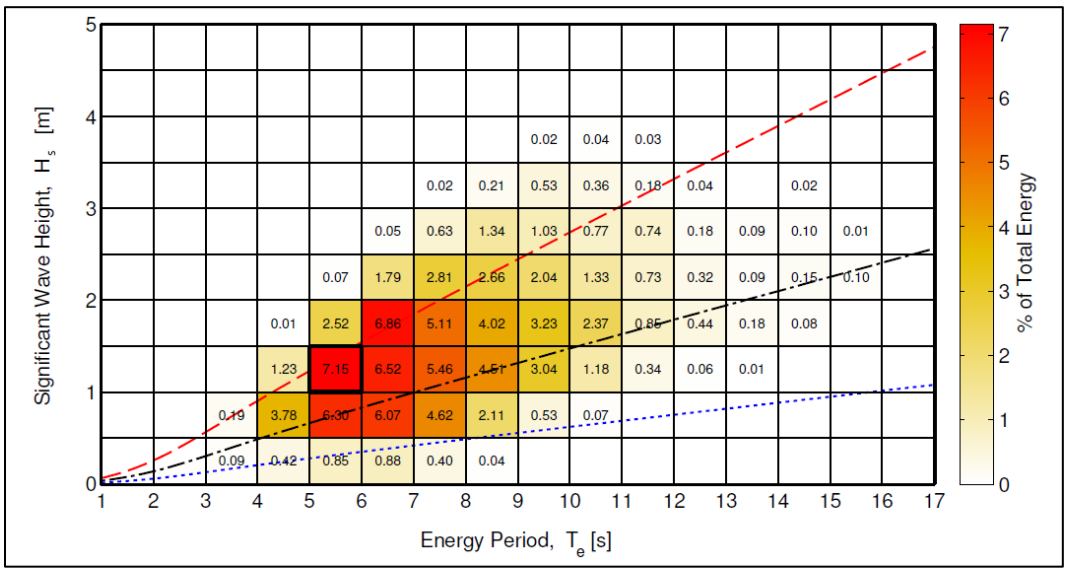

Figure 1-7. Percentage of Total Energy Contribution at the Reference Site in Duck, NC [12]

1.7 Wave Slamming

Wave slamming is a highly non-linear force that acts on maritime structures. For OWSCs, wave slamming occurs primarily in energetic sea states. This is when the OWSC pitches seaward and reaches a vertical position in the wave trough, and the water line in front of the OWSC drops resulting in a high magnitude slamming force that can structurally affect the device. Slamming occurs when the OWSC impacts the water free surface rather than an incident wave impacting

the device, and can usually be identified as a stream of water jetting off the front face of the OWSC [14]. An example of the OWSC wave slamming event can be seen in Figure 1-8 and described in [1], [14]. It is important to understand whether or not a specific wave condition will result in wave slamming of an OWSC so it can be properly damped to avoid structural overload. Wave slamming can also be identified as a sharp spike in pressure on the OWSC face. Experimental or numerical models may be used to observe the slamming phenomenon. Moreover, CFD is a widely used tool for investigating this, and will be used in this work. This will be discussed further in Section 2.11.

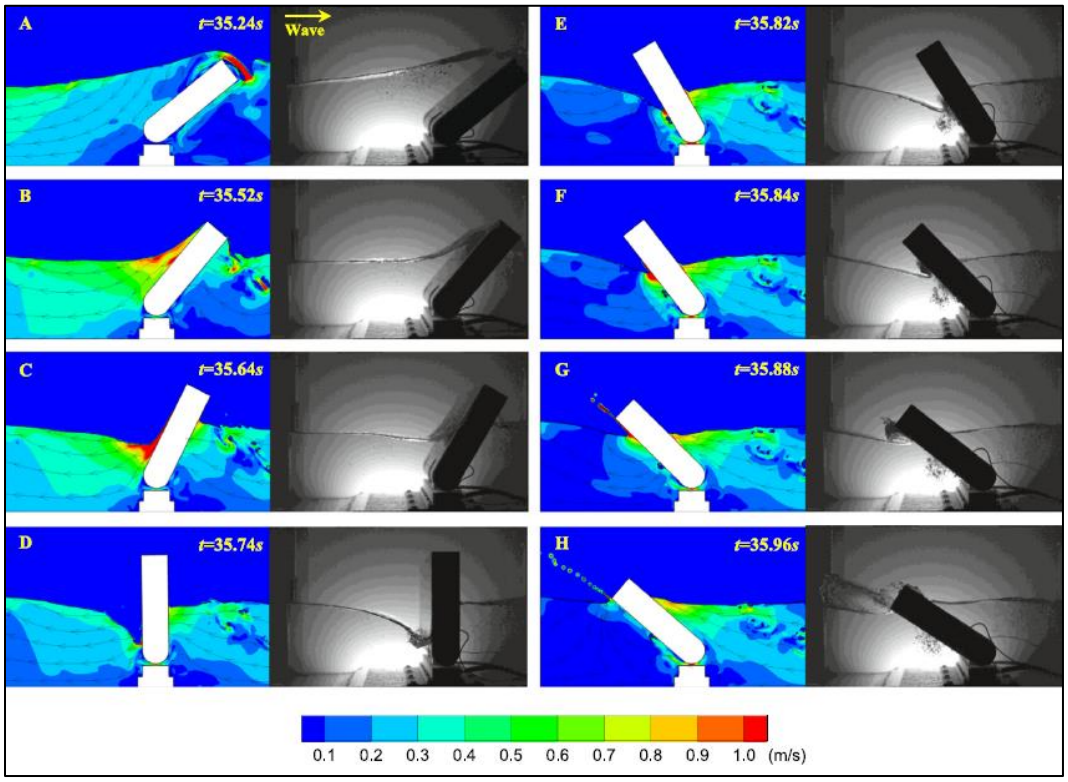

Figure 1-8. Example of Wave Slamming Event [1]

2 Background Research

2.1 Renewable Energy

It is evident that today's societal, cultural, and evolutionary needs have resulted in an increased demand for electricity. However, the burning of fossil fuels for energy has been shown to have severe, irreversible effects on the Earth's inhabitants and atmosphere [15]. One solution that has greatly matured over the last decade is the use of renewable energy systems. Renewable energy resources are naturally occurring sources that provide a sustainable supply of energy such as solar or wind power [15]. Within the last few decades, renewable energies have begun to replace other energy systems that emit harmful exhausts such as coal burning. In fact, some wind and solar power applications are now less expensive than some fossil fuel options [16]. While solar and wind energy technologies are proven to be capable, there still exists a relatively untapped, renewable energy source that can provide a significant amount of energy—the ocean. This includes tidal energy, ocean thermal energy, and wave energy to name a few. There have been many attempts to harness the energy in ocean waves, with ideas and patents dating back to 1799 from Monsieur Girard [17]. WECs extract wave energy to generate electricity or mechanical energy. One example is a WEC harvesting mechanical energy to pressurize seawater for desalination [18], [19]. Primarily due to the infancy of WECs and the harsh conditions of the ocean, a common challenge in this area of study is maximizing power capture from incidental waves [20]. Engineering technology from existent non-renewable sources, like oil rigs and naval vessels, help provide informed solutions for wave energy extraction. Further research in ocean energy is needed in the areas of levelized cost of energy, maximum energy extraction, control system implementation, mooring and PTO optimization, and physical model development to name a few [21], [22]. Since ocean energy technologies are still in the early stages of development, there exists a high capital investment. However, as research continues to advance in the aforementioned areas, the cost of ocean energy is likely to drop to competitive levels [23].

2.2 Wave Power Resource

Long and consistent gusts of wind across the ocean's surface will generate waves. This energy grows in density as it evolves from solar energy to wind energy, and then from wind energy to

wave energy. Wave energy is more concentrated than wind energy and solar energy. Therefore, ocean energy has a higher energy density than other renewable resources [24]. This wave power can be captured and transformed into usable energy to provide approximately 80% of the electricity that North America consumes annually [25]. Historically, wave power varies from 10 kW/m in geographical locations such as the Gulf of Mexico, to over 120 kW/m in areas such as Chile [25]. Globally, greatest wave power density is between 40º and 60º latitude, and -40º and -60º latitude [25]. Within the United States, the power potential of marine energy resources is 2,300 TWh/ year as seen in Figure 2-1 [26].

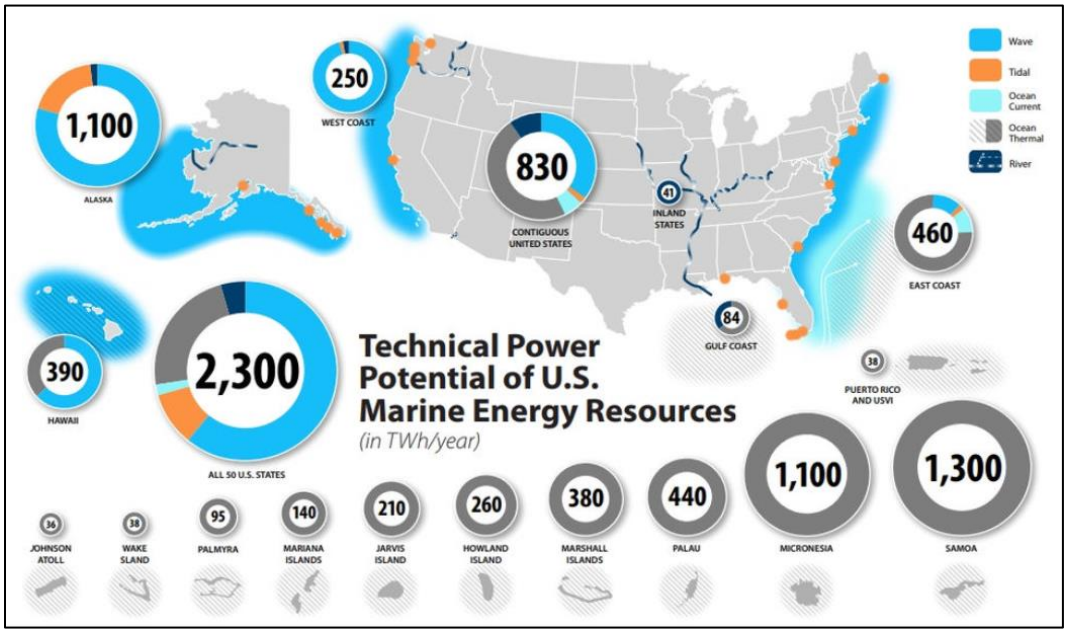

Figure 2-1. Annual Mean Global Wave Energy Density [26]

2.3 Wave Classification

Surface waves, also known as wind-driven waves, are created by a steady wind across the surface of a body of water. On a small scale, one can visualize this by blowing air over a cup of water and observing the ripples. Whether or not ocean waves are small ripples or large swells depends on the wind's consistency of speed, direction, and fetch [27]. These two factors determine the amplitude of, and thus the energy within, the waves [28]. A wave is considered fully developed at the moment just before it white caps, when much of the energy is lost [29].

The power output potential of a WEC is different in deep, intermediate-deep, and shallow water

since water depth affects wave characteristics such as wavelength, wave height, and period. In deep water, where water depth, d, is greater than half of the average wavelength, λ, wave particles travel in orbital motions since they experience no effects from the sea floor. However, in reality there exists an effect called Stokes drift, where a particle in dynamic water experiences a velocity in the direction of wave propagation, which results in the particle's path not being fully closed. If this particle was followed in real-time, its path would have a helical shape. Generally, the Stokes drift velocity is the difference between the mean Lagrangian velocity of the water particle, and the mean Eulerian, or horizontal, flow velocity of the fluid [30]. More information on the Stokes drift wave particle motion in deep water can be found in [31]. For a deep-water wave, the wave power, P, typically measured in kilowatts per meter wave width, is proportional to the wave energy period, measured in seconds, and to the squared significant wave height, measured in meters [32], [33]. H_s is defined as the square root of the zeroth-order moment of the wave spectrum, or the area, multiplied by four [34]. In intermediate-deep water, where the water depth is between half of the average wavelength, and 1/20 of the wavelength, the wave particles begin to rotate in an elliptical motion since they experience friction forces from the sea floor. Frictional drag from the bottom causes a wave to lose energy. In shallow water, where water depth is less than 1/20 the average wavelength, the particle motion becomes even more elliptical due to effects from shoaling. The energy in the wave then becomes more concentrated towards the crest of the wave, resulting in increased horizontal particle acceleration. That is, the top of the wave begins to move faster than the bottom, and the front surface of the wave becomes steeper than the back surface, resulting in wave capping [35], [36]. Just before white capping, the wave is considered fully developed. More information on the particle motion for shallow water waves, excluding the effects of Stokes drift can be found in [37]. The equations for the wave energy flux and wave power are described further in Section 2.6.

2.4 Fixed Oscillating Wave Surge Converter

The OWSC utilizes the surge motion of waves, or the forward-backward motion in the x-direction. Nearshore waves contain a large amount of concentrated energy due to shoaling effects which is particularly useful for OWSCs [38]. The design of an OWSC consists of a paddle that is hinged from its bottom in shallow depths of 10-20 meters, where it is free to rotate about the axis parallel

to the incoming wave crest, shown in Figure 2-2 [38]. After the OWSC is struck with the wave and pitches around this axis, it is restored to its original position by the force of buoyancy. This rotary motion is commonly converted in one of two ways: electrically, by exciting a generator, or mechanically, by pressurizing hydraulic fluid. The high-pressure seawater can be pumped on shore for hydroelectricity or direct seawater desalination. The benefit of OSWCs is their manufacturability, maintainability, scalability, and power absorption metrics [9], [39]. The energy extraction capabilities for an OWSC are primarily dependent on the wave force it experiences, with various other parameters affecting this metric, such as the OWSC height, width, mooring configuration, PTO, and water depth [9]. The energy extraction characteristics are determined by the movement of ocean waves, having primary interests in the horizontal particle velocity field, the wave period and the wave height [40],[41],[42]. These characteristics will vary depending on the wave spectrum being used in the analysis. There have been several commercial implementations of the OWSC such as the Oyster developed by Aquamarine Power [43], WaveRoller by AW-Energy [44], and the Oscillating Wave Surge Converter by Resolute Marine Energy [45]. Current research shows that OWSCs are among the highest performing wave energy converters in terms of power capture capability**Error! Reference source not found.** [39], [46].

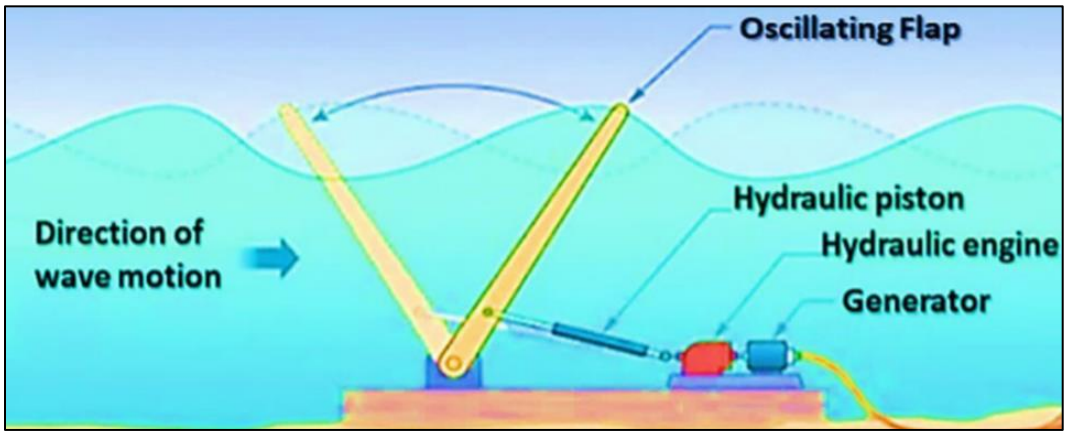

Figure 2-2. Operating Principle of a Bottom-Fixed Oscillating Wave Surge Converter [38]

2.5 Linear Wave Theory

Generally, waves can be classified as linear or nonlinear, regular or irregular, and unidirectional or omnidirectional [47]. Regular and irregular waves are discussed in Section 2.10.5 and Section 2.10.6 respectively. Free surface waves result from forces that act on an otherwise still body of

water to deform the fluid [47]. Such forces may include the wind blowing, gravitational effects, or a passing vessel. Quantifying free surface waves requires the use of equations derived based on potential flow theory—which assumes flow is incompressible and irrotational [48]. In this study, water is assumed incompressible so the density will remain constant throughout calculations, and since is difficult to compress physically. At 0°C and zero-pressure limit, the compressibility is 5.1e-10 Pa^{-1} [48]. As pressure increases, the compressibility of water decreases. The assumption of incompressibility allows for the fluid velocity, *V*, to satisfy the equation of continuity to yield

$$\frac{\partial V}{\partial \mathrm{x}} + \frac{\partial V}{\partial \mathrm{y}} + \frac{\partial V}{\partial \mathrm{z}} = 0$$

Furthermore, the water is assumed irrotational because the wave being studied will not interact with any other water motions. This assumes the water particles will be fixed so only normal forces will be considered. This assumption is important so the velocity can be expressed in terms of velocity potential, ϕ. The velocity potential is a scalar function whose gradient at any point in a fluid is the velocity vector [49]. The velocity potential is given by

$$u = \frac{\partial \phi}{\partial \mathrm{x}} \ , \qquad v = \frac{\partial \phi}{\partial \mathrm{y}} \ , \qquad w = \frac{\partial \phi}{\partial \mathrm{z}}$$

Although the exact solution is highly complex, the velocity potential can be substituted into the continuity equation

$$\frac{\partial^2 \phi}{\partial \mathrm{x}^2} + \frac{\partial^2 \phi}{\partial \mathrm{y}^2} + \frac{\partial^2 \phi}{\partial \mathrm{z}^2} = 0$$

to obtain the Laplace differential equation from mass balance:

$$\frac{\partial^2 u}{\partial \mathrm{x}^2} + \frac{\partial^2 v}{\partial \mathrm{y}^2} + \frac{\partial^2 w}{\partial \mathrm{z}^2} = 0$$

To solve the Laplace equation, the velocity potential and kinematic boundary condition are needed. The kinematic boundary condition represents the motion of the free surface, and states that a fluid particle at the surface should remain at the water surface at all times. The equation below is a mathematical representation of the kinematic boundary condition of a fluid particle at the free surface water level, η, or the interface between the water and air

$$\begin{cases} \frac{\partial \phi}{\partial \mathrm{z}} = \frac{\partial \eta}{\partial \mathrm{t}} & \text{at } z = 0 \\ \frac{\partial \phi}{\partial \mathrm{z}} = 0 & \text{at } z = -d \end{cases}$$

Where -*d* indicates a water depth below the surface water level. An analytical solution of this Laplace equation for an oscillating regular wave that develops in the positive x-direction is defined as:

$$\eta(x,t) = a\sin(\omega t - Kx)$$

Where *a* is wave amplitude, ω is wave frequency, *t* is time, and $K = 2\pi/\lambda$ is the wave steepness. The velocity potential of this equation is

$$\phi = \hat{\phi}\cos(\omega t - Kx)$$

where

$$\hat{\phi} = \frac{\omega a}{k}\frac{\cosh\left[K(d+z)\right]}{\sinh(Kd)}$$

Along with the kinematic boundary condition, a second condition exists on the free surface that requires water surface pressure, *p*, to be equal to the atmospheric pressure—the dynamic boundary condition. This condition is derived from Bernoulli's Equation, and it deals with the force on the water surface [50]. The momentum balance equation, based on Newton's second law, is given as

$$\frac{\partial(\rho u)}{\partial \mathrm{t}} + \frac{\partial u(\rho u)}{\partial \mathrm{x}} + \frac{\partial v(\rho u)}{\partial \mathrm{y}} + \frac{\partial w(\rho u)}{\partial \mathrm{z}} = F_x$$

Ignoring non-linear terms and simplifying yields the linearized Bernoulli equation for unsteady flow

$$\frac{\partial \phi}{\partial \mathrm{t}} + \frac{p}{\rho} + \mathrm{g}z = 0$$

In terms of velocity potential, the linearized Bernoulli equation for unsteady flow can be rewritten as

$$\frac{\partial \phi}{\partial \mathrm{t}} + \mathrm{g}\eta = 0$$

Linear wave theory [51] is the simplest solution to this equation, as it is a first order approximation for the velocity field. Linear wave theory assumes linear boundary conditions in deep water. That is, the water depth, *d*, and wavelength, λ, being much larger than the wave height. Therefore, when the vertical position, *z*, is zero, the kinematic and dynamic boundary conditions respectively can be reduced to

$$\frac{\partial \phi}{\partial \mathrm{z}} - \frac{\partial \eta}{\partial \mathrm{t}} = 0$$

$$-\frac{\partial \phi}{\partial \mathrm{t}}+\mathrm{g}\eta \;=\; 0$$

2.6 Wave Energy

The total linear wave energy per unit area, E_{total}, is a relationship that includes both kinetic, E_k, and potential, E_p, energy and is defined as

$$E_{total} = E_k + E_p$$

Water particles that have a velocity also have kinetic energy. Water particles whose elevation has changed due to wave crest and troughs have potential energy. This kinetic and potential energy can be defined by

$$E_k = \frac{1}{2}mv^2 = \frac{1}{2}\frac{\rho}{\lambda}\int_0^{\lambda}\int_{-d}^{a(t)} (u^2 + w^2)\, dz\, dx = \frac{1}{4}\rho g a^2$$

$$E_p = mgd = \frac{1}{2}\frac{\rho g a}{\lambda}\int_0^{\lambda} \cos^2(kx - \omega t) dx = \frac{1}{4}\rho g a^2$$

H_s is the significant wave height, and it is defined as four times the square root of the zeroth-order area of the wave spectrum being studied. Traditionally, the significant wave height was defined as the mean wave height from trough to crest of the highest third of the waves, or $H_{1/3}$ [52]. In this paper, H_s will be used. The total energy in a regular wave can be simplified to

$$E_{total} = \frac{1}{2}\rho g H_s^2 \;\; \left[\frac{\mathrm{J}}{m^2}\right]$$

Where ρ is the density of seawater and g is gravity. Aforementioned, as a wave begins to form, its velocity and power are influenced by the water depth, which can be classified as deep, intermediate-deep, or shallow water. The power, or wave energy flux, per meter wave crest in regular waves, $P_{regular}$, can be represented by the following equations for shallow waves

$$P_{regular} = E_{regular} \cdot c_{g,shallow}$$

The shallow water wave celerity, $c_{g,shallow}$, is determined by water depth, not wave period. It is defined by

$$c_{g,shallow} = \sqrt{gh}$$

When an irregular wave is correlated with a spectrum, the wave energy, $E_{irregular}$, and power per

meter wave crest, $P_{irregular}$, are defined as

$$E_{irregular} = \frac{\rho g H_{m0}^2}{16}$$

$$P_{irregular} = E_{irregular} \cdot c_{g,shallow}$$

2.7 Equations of Motion for an OWSC

There are two major forces that act on the OWSC—viscous and non-viscous forces. Viscous terms include drag and friction and can be calculated using CFD. Non-viscous terms include the radiation force, F_r, and the wave excitation force, F_e, which are calculated using hydrodynamic coefficients. Newton's second law can be used to describe the mass balance

$$\Sigma F = m\ddot{x} = F_e + F_r + F_v + F_{PTO}$$

Where F is equal to the total forces acting on the structure, both viscous and non-viscous, m is the mass of the structure, and $\ddot{x}$ is the acceleration term of the structure. Viscous forces, F_v, and power take-off forces, F_{PTO} are also represented in this equation. Since an OWSC oscillates back and forth, the forces on the OWSC must be equal and opposite to the displacement, thus

$$-kx = m\ddot{x}$$

where k is the spring constant, and

$$k = m\omega_a^2$$

Where ω_a is the angular frequency of the oscillations. If this motion is damped, another term, which is related to velocity, is added

$$-kx - lv = m\ddot{x}$$

Where l is the OWSC shape, and v is the velocity. This equation above represents a damped oscillator that has no forces acting on it. If a force does act upon it, the result is

$$F(t) = m\ddot{x} + lv + kx$$

The motion of the OWSC as it pitches about the y-axis is represented by θ. The term k, which is the spring constant in the equations above, is now the hydrostatic restoring force, F_B, which is the force that restores the OWSC to its upright position after being struck by a wave. As the OWSC oscillates in the water, a non-linear damping term is introduced from the drag associated with the water. According to [28], since the OWSC is free to pitch about the y-axis in a circular direction,

the force term may be changed to torque, and the mass term may be changed to moment of inertia. Therefore, the original equation of motion can be rewritten in terms of hydrodynamic torque, T_h, as

$$T_h = T_e - I\ddot{x} + T_r + T_v$$

Where I is the OWSC moment of inertia and $\ddot{x}$ is the angular acceleration. It should be noted here that T_h ,or hydrodynamic torque, can be found using any boundary element method (BEM) software. The hydrodynamic torque corresponds to the overall torque that the OWSC experiences by the surrounding water. It is composed of the wave exciting torque, T_e, the inertia of the surrounding fluid, angular acceleration of the OWSC, radiation torque, T_r, and viscous torque, T_v. The following equation represents the wave excitation torque of a pitching OWSC for a singular wave frequency in the time domain:

$$T_e = (I + A)\theta_a + B\theta_v + F_B\theta + B_{nl}\theta_v^2$$

Where A, is the added mass, B and B_{nl} are the radiation damping coefficient and the non-linear damping coefficient respectively, and θ_v and θ are body velocity and position respectively. The non-linear damping term fluctuates between positive and negative, depending on the OWSCs forward or backward motion, and is proportional to the OWSC's velocity squared. The wave exciting torque is calculated by summing the Froude/Krylov moments and the diffraction moments. The diffraction moment is a combination of wave reflection and diffraction while the Froude-Krylov term results from the undisturbed wave's pressure on a fixed body [53].

The radiation torque is the physical response of an OWSC as it is impacted by the wave. It is characterized by the OWSC's hydrodynamic coefficients—added mass and radiation damping. These terms play a large role in determining the body's response to waves in shallow water, and whether or not the device is numerically stable [54]. The added mass coefficient, related to the body's acceleration, is the inertia that is added to the OWSC due to its exposure to dynamic water. Physically speaking, added mass is the mass added to a system due to the fact that an accelerating or decelerating body must move some volume of surrounding fluid as it moves, since both the OWSC and sea water cannot occupy the same physical area of space [55]. Radiation damping, related to the body's velocity, is the outward generation of waves, caused by the velocity of the

OWSC after it is struck by an ocean wave. That is, as the OWSC is struck by a wave on one face, the resulting pitching motion will create waves on the opposite face of the OWSC [53]. The radiation torque for an OWSC is defined as

$$T_r = -A_\infty \theta_a - \int_{-\infty}^{\infty} K_R(t-\tau)\,\theta_v(\tau)\,\mathrm{d}\tau$$

Where A_∞ is the added moment of inertia at infinite frequency, and τ is time lag. For WECs, a three-dimensional diffraction theory software, as described in Section 2.8.1, must be used to obtain the radiation torque and wave excitation torque. Assuming linear wave theory, the viscous torque is defined as

$$T_v = \left(-\frac{1}{2}\rho C_d A_d |V_i - V|(V_i - V)\right) L$$

Where L is the distance from the bottom of the OWSC to the center of the OWSC in the zed direction, C_d is the drag coefficient, A_d is the characteristic surface area, V_i is calculated by $L\theta_v$, and V is fluid velocity. The equation of motion for an OWSC calculated using three-dimensional hydrodynamic diffraction theory, described in Section 2.9. Figure 2-3 is a tree diagram of the required elements for calculating the equations of motion for an OWSC.

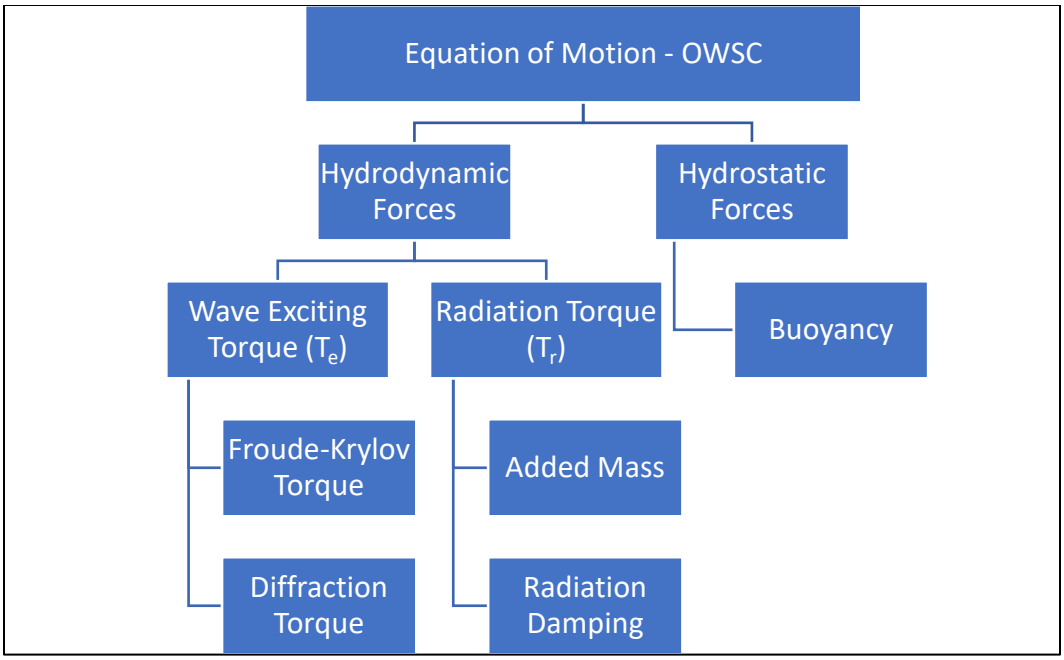

Figure 2-3. Tree Diagram of Elements for Calculating an OWSC's Equation of Motion

2.8 Numerically Modeling Wave Energy Converters

2.8.1 Frequency Domain vs. Time Domain Analysis

Either a frequency- or time-domain may be used in a numerical model when studying wave energy converters. Choosing between the two depends on the device being studied, and the desired outputs. Typically, device that has not been numerically studied is first analyzed in the frequency domain to develop a fundamental understanding of how it will respond in dynamic and static water. This is important since the device will have a different response for each wave frequency that it is subjected to. One advantage of modeling in the frequency domain is the decreased simulation time, as compared to a time domain analysis. Frequency domain modeling can be completed with different software packages like Aqwa Diffraction, WaveAnalysisMIT (WAMIT), developed by researchers at the Massachusetts Institute of Technology, or NEMOH, developed by Ecole Centrale de Nantes [56]. A disadvantage of a frequency domain model is that it is not capable of modeling nonlinear effects or control strategies. A time domain analysis is capable of modeling control strategies and reporting parameters such as device position, velocity and acceleration, PTO forces, and power generation potential. For OWSCs, a convolution integral of the impulse response function may be used to characterize the hydrodynamic coefficients in the time domain. Time domain modeling can be completed with different software packages like Aqwa Response or WEC-Sim [57]. A major consideration in choosing between time and frequency domain modeling is the tradeoff between model accuracy and simulation run time [28]. When modeling a WEC in the frequency domain, the user must define specific wave conditions and the device's mass properties, such as mass, inertia, and center of gravity, and wave spectrum. The frequency domain outputs are used to calculate the device's equations of motion, as discussed in Section 2.7. When modeling a WEC in the time domain, the user must input the same mass properties, a PTO configuration, and the hydrodynamic coefficient results from the frequency domain analysis. Figure 2-4 and Figure 2-5 show a block diagram of the requirements for conducting a frequency domain analysis and time domain analysis respectively.

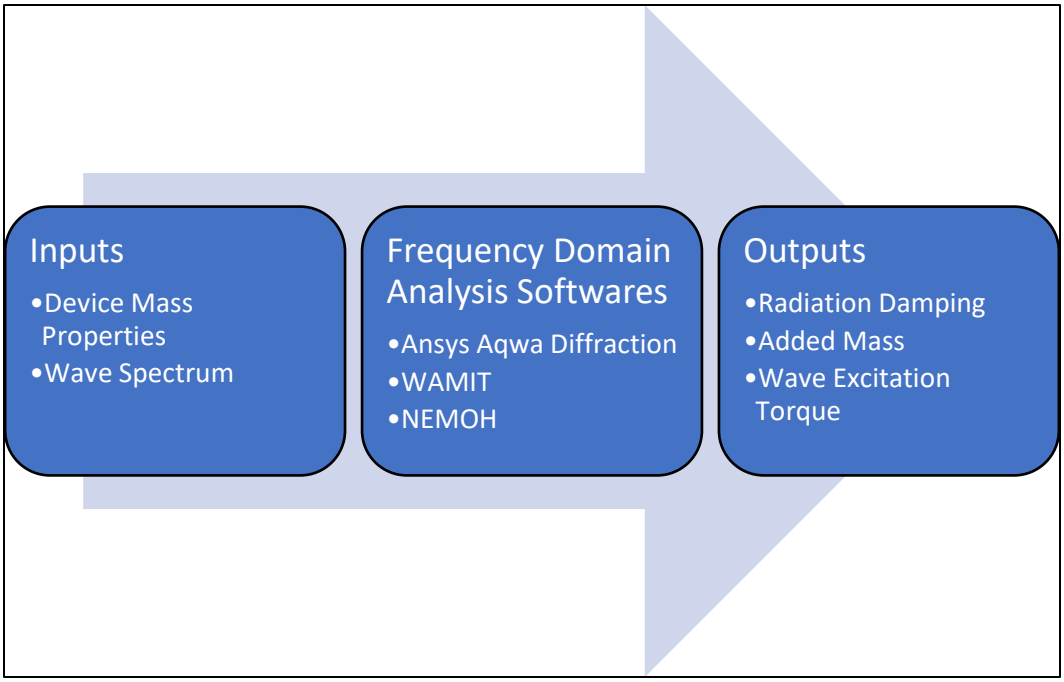

Figure 2-4. Flow Chart of Frequency Domain Analysis

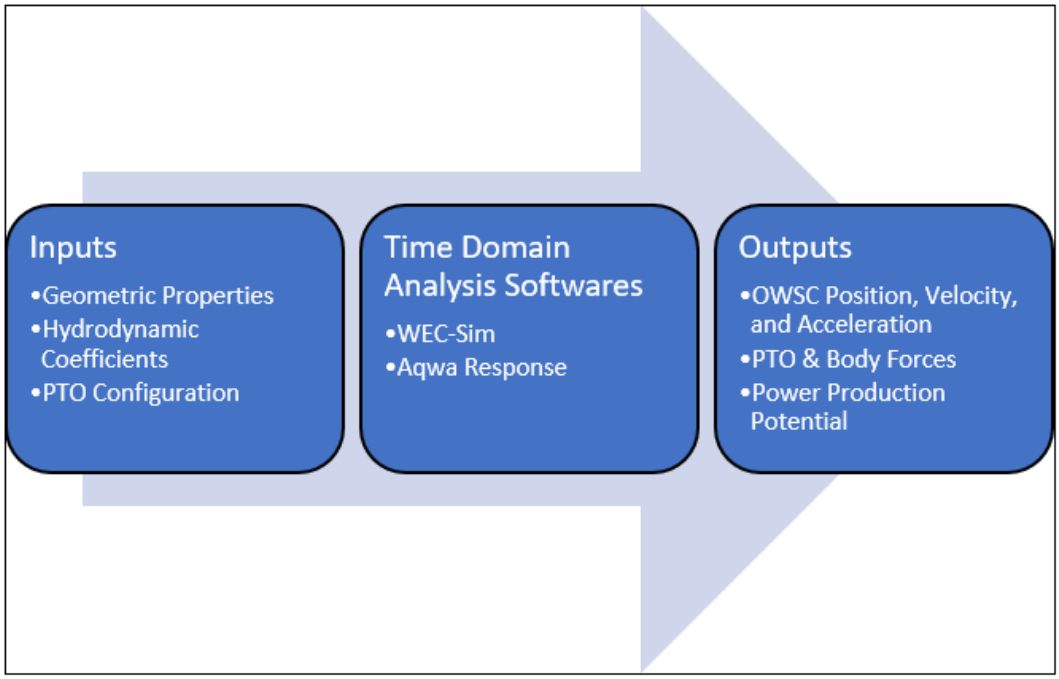

Figure 2-5. Flow Chart of Time Domain Analysis

2.8.2 Computational Fluid Dynamics

CFD can be easily understood when it is broken down into each of its acronym constituents—computational, fluid, and dynamics. "Computational" means that a computer is necessary to run the analysis, otherwise known as a numerical analysis. "Fluid" means that specific fluids, whether a gas or liquid, is being analyzed in the numerical analysis. In the case that a gas, such as air, is being examined, the term aerodynamics would be used. In the case a liquid, such as water, is being analyzed, the term hydrodynamics would be used. Finally, the term "dynamics" means the fluid is in motion. This motion is either the result of an object passing through the fluid, or thermal effects that drive the flow. The Volume of Fluid (VOF) method is a free-surface modeling technique that can describe the interaction of a WEC that is exposed to multiple phases. The open channel wave boundary condition can be used to analyze the fluid flow around the OWSC when it is exposed to waves [14], [58]. For a WEC in normal operating conditions, the fluid-structure interactions can be modeled using common numerical analyses described in [44], [59]. High-fidelity VOF analyses can be used to explore non-linear effects such as wave slamming, which have been proven to cause structural damage to devices [10]. Furthermore, VOF analyses can provide insight as to how the fluid flows as it interacts with the oscillating device. Figure 2-6 is a flow chart for analyzing a WEC in CFD.

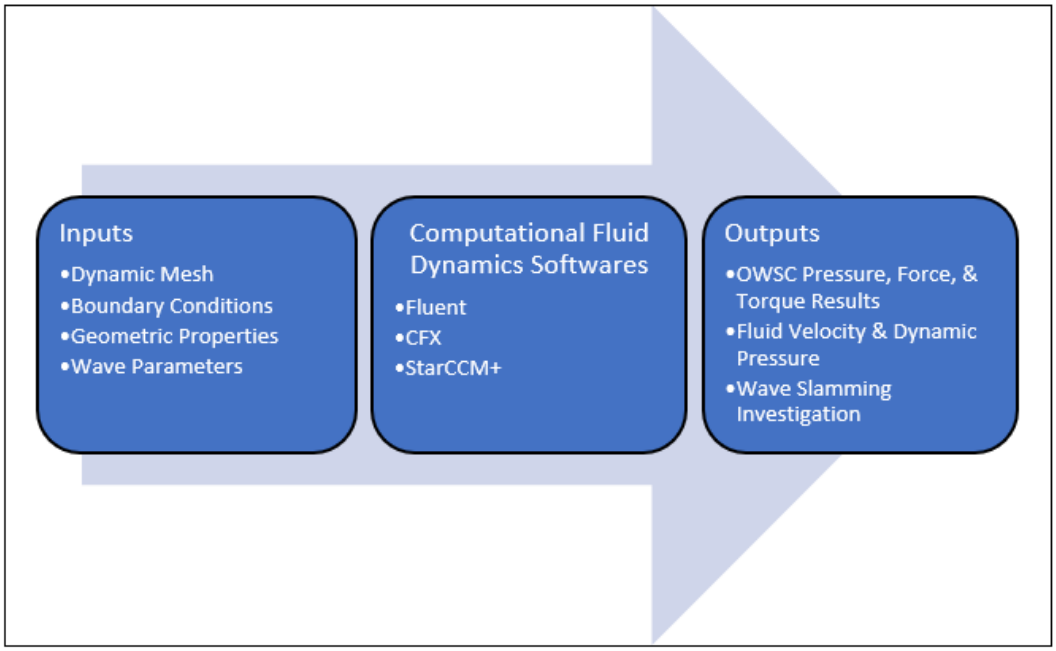

Figure 2-6. Flow Chart of Modeling in CFD

2.9 Hydrodynamic Diffraction

2.9.1 Boundary Element Method

BEM solves the first order hydrodynamics around the boundaries of the device being studied, not its internal structure. Therefore, only a boundary mesh is needed, making BEM a quick and efficient simulation tool. Aqwa is a frequency-domain, BEM code that was developed to model and predict how a device or structure will respond to different wave frequencies using three-dimensional diffraction theory. Hydrodynamic loads are typically caused by the kinematics of wave water particles, the motion of structures, and the interactions between the waves and structures. The areas of highest interest are drag load, wave exciting load, and inertia load. BEM programs are developed based on the potential flow and radiation/diffraction theory and, therefore, operate under the assumptions that velocity potential is irrotational, inviscid, and incompressible [60].

2.9.2 BEM Coordinate System

It is common practice to define the coordinate system of hydrodynamic problems with the origin in the mean surface of the fluid. In Aqwa, this is the fixed reference axis (FRA), global axes, or OXYZ, where the origin is at the mean surface, and the z-axis points vertically upwards. More information on the coordinate system can be found in [61].

2.9.3 Hydrostatic Forces and Moments

When a body is submerged in water, the volume of displaced water can be found by integrating over the amount that is submerged

$$\nabla = \int_{S_0} z n_3 \, dS$$

Where S_0 is the wetted surface of the body in calm water, n is the unit normal vector of the body surface point outwards, and z is the vertical coordinate of the wetter surface point referenced to the FRA. The buoyancy of a submerged body can be represented by the upward force, F_B, due to the displaced water

$$F_B = \nabla \rho g$$

More generally, hydrostatic force and moment are the fluid loads that act on the body in calm water. The hydrostatic force, $\vec{F}_{hys}$, can be found by integrating the hydrostatic pressure over the wetted surface up to the free surface water level. The hydrostatic moments, $\vec{M}_{hys}$, are taken about the center of gravity of the body

$$\vec{F}_{hys} = -\int_{S_0} p_s \vec{n} dS$$

$$\vec{M}_{hys} = -\int_{S_0} p_s (\vec{r} \times \vec{n}) dS$$

Where p_s is the hydrostatic pressure, and $\vec{r}$ is the position of a vector of a point on the hull surface with respect to the COG in the FRA [61].

2.9.4 Radiation and Diffraction Wave Forces

Aqwa, as well as other BEM solvers, operates under the following assumptions obtained from linear wave theory [61]:

- The body/bodies have zero or very small forward speed
- The fluid is inviscid and incompressible
- The fluid flow is irrotational
- The incident regular wave train is of small amplitude compared to its length
- The motions are of small amplitude since they are to the first order

2.9.5 General Formula in Zero-Forward Speed Case

The fluid flow field surrounding a floating body by a velocity potential is defined by

$$\varphi(\vec{X}, t) = a\varphi(\vec{X})e^{-i\omega t}$$

The space dependent potential term, $\varphi(\vec{X})$, due to incident, diffracted, and radiated waves is governed by

$$\varphi(\vec{X})e^{-i\omega t} = \left[(\varphi_1 + \varphi_d) + \sum \varphi_{r5}\theta\right] e^{-i\omega t}$$

Where φ_1 is the first order incident wave potential, φ_d is the diffraction wave potential, φ_{r5} is the radiation wave potential resulting from the 5th motion, and θ is the rotational movement of the OWSC's center of gravity about the y-axis. Once the wave velocity potentials are known, the first order hydrodynamic pressure distribution can be found with the linearized Bernoulli equation

$$p^{(1)} = -\rho \frac{\partial \varphi(\vec{X}, t)}{\partial t} = i\omega\rho\varphi(\vec{X})e^{-i\omega t}$$

Once the pressure distributions are known, different fluid forces can be calculated by integrating the pressure over the wetted surface of the body. To obtain a general form of the forces and moments, unit normal vectors of the hull surface are used for notation, and the first order components can be expressed as

$$F_j e^{-i\omega t} = -\int_{S_0} p_s \vec{n}_j dS = [-i\omega\rho \int_{S_0} \varphi(\vec{X}) n_j dS]\, e^{-i\omega t}$$

The total first order hydrodynamic force can then be written as

$$F_j = \left[\left(F_{Ij} + F_{dj}\right) + \sum_{k=1}^{6} F_{rjk} x_k \right]$$

Where j = 1, 6, depending on the motion of interest. Here, the rotation about the y-axis, or the 5th motion, is of interest. Therefore, the subscript j can be replaced with the index 5. Therefore, the first order hydrodynamic moment for an OWSC that pitches about the y-axis, M_5, is given as

$$M_5 = \left[(M_{I5} + M_{d5}) + \sum M_{r5,5}\theta_5 \right]$$

Where M_{I5} is the 5th Froude-Krylov moment due to the incident wave, and M_{d5} is the 5th diffracting moment due to the incident wave. The diffraction term is a combination of wave reflection and diffraction [53]. The Froude-Krylov term results from the undisturbed wave's pressure on a fixed body. When these two quantities are summed, the resulting term is known as the wave excitation torque. Therefore, wave excitation torque is the torque that is induced on the OWSC due to the incident wave, while the OWSC is fixed in place. The 5th Froude-Krylov moment and diffracting moment due to incident wave are given respectively as

$$M_{I5} = -i\omega\rho \int_{S_0} \varphi_I(\vec{X}) n_j dS$$

$$M_{d5} = -i\omega\rho \int_{S_0} \varphi_d(\vec{X}) n_j dS$$

$M_{r5,5}$ is the radiation moment due to the radiation wave induced by the 5th rigid body motion, or pitch. It is the physical response of a OWSC as it is impacted by the wave. The radiation moment is a complex number can be broken down into its respective real and imaginary parts. Respectively, this is the radiation damping and added mass terms, governed by

$$A_{5,5} = \frac{\rho}{\omega} \int_{S_0} Im[\varphi_{r5}(\vec{X})] n_5 dS$$

$$B_{5,5} = -\rho \int_{S_0} Re[\varphi_{r5}(\vec{X})] n_5 dS$$

Where S_0 is the wetted body surface, n unit normal vector of the OWSC surface that points outward. The subscript, 5, represents the moment acting on the OWSC as it pitches about the y-axis. Here, $n_5 = \vec{r} \times \vec{n}$, where $\vec{r} = \vec{X} - \overrightarrow{X_g}$ is the position vector of a point on the OWSC's surface with respect to the center of mass. The added mass coefficient, related to the body's acceleration, is the inertia that is added to the OWSC because of its exposure to oscillating motions in dynamic water. Physically speaking, added mass is the weight added to a system due to the fact that an accelerating or decelerating body must move some volume of surrounding fluid with it as it moves, since both the OWSC and sea water cannot occupy the same physical area of space [55]. Radiation damping, related to the body's velocity, is the outward generation of waves, caused by the velocity of the OWSC after it is struck by an ocean wave. That is, as the OWSC is struck by a wave on one face, the resulting pitching motion will create waves on the opposite face of the OWSC [53]. Therefore, the higher the radiation damping term, the more energy absorbed by the OWSC [61].

2.9.5.1 Source Distribution Method

The fluid structure interaction is described by the following equations:

- Laplace equation which is applicable everywhere in the fluid domain:

$$\Delta\varphi = \frac{\partial^2\varphi}{\partial X^2} + \frac{\partial^2\varphi}{\partial Y^2} + \frac{\partial^2\varphi}{\partial Z^2} = 0$$

- Linear free surface equation for zero forward speed case when z= 0:

$$-\omega^2\varphi + g\frac{\partial\varphi}{\partial z} = 0$$

- Body surface conditions on the wetted body surface where φ_1 is the velocity potential of the first linear wave:

$$\frac{\partial\varphi}{\partial n} = \begin{cases} -i\omega n_j & \text{for radiation potential} \\ -\dfrac{\partial\varphi}{\partial n} & \text{for diffraction potential} \end{cases}$$

- Seabed surface conditions at a depth, *d*

$$\frac{\partial\varphi}{\partial z} = 0 \text{ on } z = -d$$

A radiation condition is added so as $\sqrt{(x^2 + y^2)} \rightarrow \infty$, the wave disturbances will diminish. Using Green's theorem, the diffraction and radiation wave velocity potential can be given as:

$$c\varphi(\vec{X}) = \int_{S_0} \left\{ \varphi(\vec{\xi}) \frac{\partial G(\vec{X}, \vec{\xi}, \omega)}{\partial n(\vec{\xi})} - G(\vec{X}, \vec{\xi}, \omega) \frac{\partial\varphi(\vec{\xi})}{\partial n(\vec{\xi})} \right\} dS$$

Where,

$$c = \begin{cases} 0 & \vec{X} \in \Omega \cup S_0 \\ 2\pi & \vec{X} \in S_0 \\ 4\pi & \vec{X} \in \Omega \end{cases}$$

The fluid potential is then expressed in the following manner after introducing further source distributions over the mean wetted surface

$$\varphi(\vec{X}) = \frac{1}{4\pi} \int_{S_0} \sigma(\vec{\xi}) G(\vec{X}, \vec{\xi}, \omega) dS \quad \text{where } \vec{X} \in \Omega \cup S_0$$

The mean wetted surface can be found by the hull surface boundary condition

$$\frac{\partial\varphi(\vec{X})}{\partial n(\vec{X})} = -\frac{1}{2}\sigma(\vec{X}) + \frac{1}{4\pi}\int_{S_0}\sigma(\vec{\xi})\frac{G(\vec{X},\vec{\xi},\omega)}{\partial n(\vec{X})}\,dS \quad \text{where } \vec{X} \in S_0$$

The Hess-Smith constant panel method is used in Aqwa to close the equations above. The surface is divided into quadrilateral or triangular panels, or elements. Aqwa assumes the potential and source strength for each element is constant and uses the corresponding mean values of that element's surface. Thus, the discrete integral form of the two above equations are as follows:

$$\varphi(\vec{X}) = \frac{1}{4\pi}\sum_{N_p}^{m=1}\sigma_m G(\vec{X},\vec{\xi}_m,\omega)\Delta S_m \quad \text{where } \vec{X} \in \Omega \cup S_0$$

$$\frac{\partial\varphi(\vec{X}_k)}{\partial n(\vec{X}_k)} = -\frac{1}{2}\sigma_k + \frac{1}{4\pi}\sum_{N_p}^{m=1}\sigma_m\frac{\partial G(\vec{X}_k,\vec{\xi}_m,\omega)}{\partial n(\vec{X}_k)}\,\Delta S_m \quad \text{where } \vec{X}_k \in S_0, k = 1, N_p$$

Where N_p is the total number of panels over the mean wetted hull surface, ΔS_m is the area of the m[th] panel, $\vec{\xi}_m$ is the coordinates of panel geometric center over the m[th] panel, and $\vec{X}_k$ is the coordinates of panel geometric center of the k[th] panel. Aqwa uses a Green's function database to calculate the Green's function and its first order derivatives quickly and efficiently [61]. The low frequency limit in rad/s of this database is

$$\omega_{min} = -0.001\sqrt{\frac{g}{d}}$$

2.9.6 Removal of Irregular Frequencies

Irregular frequencies may occur during the hydrodynamic analysis of a floating structure which can lead to large errors over a wide range of frequencies. These errors may cause outliers in the hydrodynamic coefficients, especially when surface piercing structures or highly interactive structures are being modeled [62]. In these cases, resonant wave frequencies due to standing waves between the structures may also occur. In Aqwa, the internal lid method is used for the

source distribution approach. Here, the fluid field exists interior to the mean wetted body surface which satisfies the same free-surface boundary condition experienced by the floating body. In Aqwa, the interior mean free surface is represented by a series of interior lid panels [61].

2.9.7 Mesh Quality Check

The mesh quality can severely affect the accuracy of the hydrodynamic results. In Aqwa, the following requirements must be satisfied [61]:

- The hull surface must be represented by a sufficient number of quadrilateral and/or triangular elements.
- The element normal must point toward the surrounding fluid field.
- The hull surface, especially the mean wetted hull surface part, must be fully covered by panels without gaps or overlap between panels.
- The mean wetted hull surface is required when the source distribution approach is used. All elements above the mean surface water level are treated as non-diffracting elements. Each element has to satisfy the following requirements
    - The elements should be nearly the same as the elements adjacent to it. N_{LID} is the total number of interior lid elements over the interior imaginary mean surface level, and $S_k$is any adjacent panel area:

$$\frac{1}{3} \leq \frac{\Delta S_m}{\Delta S_k} \leq 3 \text{ , where } m = 1, N_p + N_{LID}$$

    - The panel aspect ratio should not be too small. Here, L_{max} is the length of the longest size of the m^{th} element:

$$C\frac{\Delta S_m}{L_{max}^2} \geq \frac{1}{3} \text{ , where } m = 1, N_p + N_{LID}$$

$$C = \begin{cases} 1.0 & \text{for quadrilateral elements} \\ 2.3 & \text{for triangular elements} \end{cases}$$

- The center of each element should not be too close to the centers of adjacent elements.

$$d_{mk} \geq r_{fm}\text{, where } m = 1, N_p + N_{LID}$$

Where d_{mk} is the distance between the center of the m^{th} element to the center of the adjacent element. If d_{mk} is less than 0.1 times the radius of the m^{th} element, r_{fm}, there will be a fatal error.

- The element shape must be regular. To ensure this, a shape factor for the element is presented:

$$f_{Sm} = \frac{n_s}{2\Delta S_m}\sqrt{B}\text{, where } m = 1, N_p + N_{LID}$$

Where n_s is the number of edges on the element and

$$B = \min\left\{\left[\left(\vec{X}_i - \vec{X}_m\right) \times \left(\vec{X}_{i+1} - \vec{X}_m\right)\right] \cdot \left[\left(\vec{X}_{i+1} - \vec{X}_m\right) \times \left(\vec{X}_{i+2} - \vec{X}_m\right)\right]\right\}$$

Where $\vec{X}_i$, $\vec{X}_{i+1}$, and $\vec{X}_{i+2}$ are the nodal coordinates of any 3 nodes of the m^{th} element in order, and $\vec{X}_m$ is the coordinates of this element's center. Therefore, it is required that

$$f_{Sm} \geq \begin{cases} 0.2 & \text{otherwise an error is issued} \\ 0.02 & \text{otherwise a fatal eror is issued} \end{cases}$$

- The element size should be small relative to the wavelength

$$L_{max} \leq \frac{1}{7}\lambda\text{, where } m = 1, N_p + N_{LID}$$

- The centers of the diffracting elements should be above the seabed to avoid singularities

$$z_m + d \geq \frac{1}{2}r_{fm}\text{, where } m = 1, N_p + N_{LID}$$

Where z_m is the z-coordinate of the center of the m^{th} element in the FRA.

2.10 Power Production

WEC-Sim is an open-source WEC simulation software developed by NREL, and Sandia National Laboratories (SNL). It is a MATLAB/Simulink-based, time-domain numerical model that is used to solve the system dynamics of WECs that consist of multiple bodies, PTO systems, and mooring configuration [63]. It is used to calculate a WEC's dynamic response to ocean waves and power production capabilities. Since WEC-Sim is an open-source tool, the MATLAB code may be modified to fit the objectives of the user. The solver runs by solving for the equations of motion in 6 degrees of freedom (DOF) that a structure will encounter in water. It uses a radiation and diffraction method to integrate the linear hydrodynamic coefficients obtained from BEM solvers such as WAMIT, NEMOH, or Aqwa. With these hydrodynamic coefficients, the system dynamics are solved for in the time-domain so power production calculations can be made. Simulink is integrated into MATLAB by utilizing the WEC-Sim component library and the optional PTO simulator (PTO-Sim) component library. The WEC-Sim component library utilizes SimMechanics and consists of elements that represent each item in the WEC device. They include

- Fixed or rigid body elements
    - Represent each body of the WEC device
- Fixed or floating constraints
    - Represents the allowable motion of the device
- Global reference frame
    - Represents the fixed sea floor
- Moorings
    - Represented as slack, fixed, or taught
- Rotational or translational PTOs
    - Represents the specified power conversion mechanism

The elements required to run a WEC-Sim analysis include the geometry files, the BEM output files containing the hydrodynamic coefficient results, the wecSimInputFile.m file to define the simulation parameters, and a Simulink model file. Figure 2-7 shows a schematic representation of the WEC-Sim working principle [64],[65]. User defined functions can be created to output the

desired results, which, in most cases, are in the form of a power matrix. A power matrix generally takes the form of a heat map since it shows the amount of power that a WEC can produce as a function of wave height and wave period. They are useful in determining how much power a WEC will contribute for a specific sea state. Although CFD is also capable of doing this, the computational time for WEC-Sim is significantly less, so multiple wave conditions can be examined in a fraction of the time.

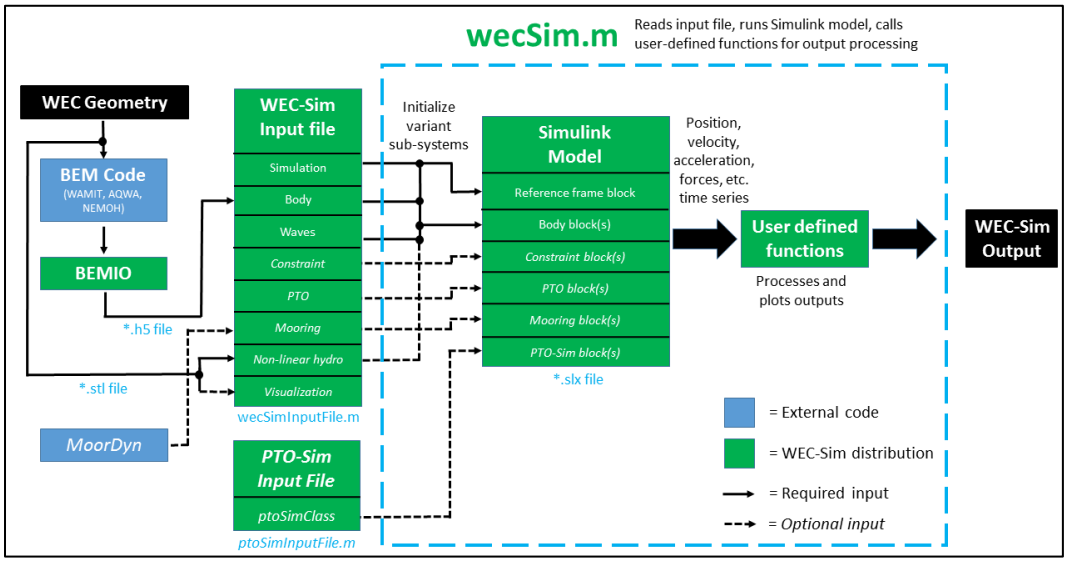

Figure 2-7. WEC-Sim Workflow Diagram [65]

2.10.1 Coordinate System and Units

The WEC-Sim coordinate system is the same coordinate system employed in Aqwa. The approaching waves travel with a zero-degree wave heading angle in the positive x-direction, while the positive z-direction indicates the vertical upward motion, and the y-direction is defined by the right-hand rule. WEC-Sim defines all of these motions in a 6x6 matrix where the surge (x), sway (y), heave (z), roll (R_x), pitch (R_y), and yaw (R_z) motions correspond to the first through sixth positions respectively. For an OWSC where the pitch motion is of interest, the 5th position will be analyzed. That is, the 5th row of the 5th column. The standard units in WEC-Sim are in the metric system as meters-kilograms-seconds, the angular measurements are in radians, and the wave heading angles are in degrees.

2.10.2 Boundary Element Method Input/ Output

WEC-Sim models wave forces by using hydrodynamic coefficients obtained from BEM solvers such as Aqwa, WAMIT, and NEMOH. BEM Input/ Output (BEMIO) is used to pre- process the hydrodynamic data obtained from the BEM solver so it can be used in WEC-Sim. It reads the raw BEM result files and calculates the radiation and excitation impulse response functions (IRFs) and saves the data in a Hierarchal Data Format 5 (HDF5). BEMIO also plots the normalized hydrodynamic data for user verification. The hydrodynamic data are normalized as follows:

- Hydrostatic restoring stiffness: $\frac{C_{i,j}}{\rho g}$
- Added Mass: $\frac{A_{i,j}}{\rho}$
- Radiation Damping: $\frac{B_{i,j}}{\rho \omega}$
- Wave Excitation Force: $\frac{F_{exc,i}}{\rho g}$

For an OWSC, the i^{th} and j^{th} terms would be replaced with the 5th index of each hydrodynamic coefficient matrix.

2.10.3 Time-Domain Formulation

The equation of motion for a floating body about its center of gravity is represented in the time domain as:

$$m\ddot{x} = F_{exc}(t) + F_{rad}(t) + F_{PTO}(t) + F_v(t) + F_{me}(t) + F_B(t) + F_m(t)$$

Although these terms have already been defined previously, they will be rewritten below for ease of understanding. The mass of the device is represented by m, $\ddot{x}$ is the translational and rotational acceleration vector of the body, $F_{exc}(t)$ is the wave excitation force and torque of a 6-element vector, $F_{rad}(t)$ is the radiated wave force and torque vector, $F_{PTO}(t)$ is the PTO force and torque vector, $F_v(t)$ is the viscous damping force and torque vector, $F_{me}(t)$ is the Morison Element force and torque vector, $F_B(t)$ is the hydrostatic restoring force and torque vector due to buoyancy, and $F_m(t)$ is the mooring force and torque vector.

2.10.4 Numerical Methods

WEC-Sim can model regular and irregular waves, including various wave spectrums such as Pierson-Moskowitz (PM) and the Joint North Sea Wave Observation Project (JONSWAP). However, $F_{exc}(t)$ and $F_{rad}(t)$ are calculated differently for regular waves and irregular wave simulations. It is common practice to model simple WEC designs in a sinusoidal steady-state response with regular waves, described in Section 2.10.4.2. However, for irregular waves the convolution integral method is recommended to represent the fluid memory retardation force on the WEC [56]. To reduce simulation time, the state space presentation method can be specified to approximate the convolution integral as a system of linear ordinary differential equations (ODEs).

2.10.4.1 Ramp Function

To avoid transient flows at the beginning of the simulation, a ramp function, R_f is used. This ramp function, described below, is used to eventually calculate the $F_{exc}(t)$ term.

$$R_f(t) = \begin{cases} \frac{1}{2}\left(1 + \cos\left(\pi + \frac{\pi t}{t_r}\right)\right) & \frac{t}{t_r} < 1 \\ 1 & \frac{t}{t_r} \geq 1 \end{cases}$$

Where t_r is the ramp time.

2.10.4.2 Sinusoidal Steady-State Response

The sinusoidal steady-state response is only valid for the simulation of regular waves, where the period, wave height, and wavelength are all consistent. Regular waves are described further in Section 2.10.5. The $F_{rad}(t)$ term for sinusoidal wave can be described as

$$F_{rad}(t) = -\boldsymbol{A}(\boldsymbol{\omega})\ddot{X} - \boldsymbol{B}(\boldsymbol{\omega})\dot{X}$$

Where $\boldsymbol{A}(\boldsymbol{\omega})$ and $\boldsymbol{B}(\boldsymbol{\omega})$ are the added mass matrix and radiation damping matrix as a function of wave frequency and $\dot{x}$ is the velocity vector of the floating body. The term for regular waves is described as

$$F_{exc}(t) = \Re\left[R_f(t)\frac{H}{2}\,F_{exc}(\omega, \theta_{dir})e^{i\omega t}\right]$$

Where $\Re$ is the real part of the of the equation, F_{exc} is the frequency dependent complex wave-excitation amplitude vector, and θ_{dir} is the wave direction.

2.10.4.3 *Convolution Integral Formulation*

When simulating irregular waves, the OWSC's dynamics are greatly impacted by fluid memory. The convolution integral captures and stores the fluid memory effect using the Cummins equation. For irregular waves, $F_{rad}(t)$ is calculated using

$$F_{rad}(t) = -\boldsymbol{A}_{\infty}\ddot{x} - \int_0^t K_r(t-\tau)\dot{x}(\tau)d\tau$$

Where K_r is the radiation IRF, defined as

$$K_r(t) = \frac{2}{\pi}\int_0^{\infty} \boldsymbol{B}(\boldsymbol{\omega})\cos(\omega t)\, d\omega$$

For irregular waves, the free surface elevation is formed from a linear superposition of a number of regular wave components. Each of these components are taken from the specific wave spectrum, $S(\omega)$, which describes the wave energy, using wave height and peak wave period, over an array of wave frequencies. For irregular waves,

$$F_{exc}(t) = \Re\left[R_f(t)\sum_{j=1}^{N_{bands}} F_{exc}(\omega_j, \theta_{dir})e^{i(\omega_j t + \upsilon_j)}\sqrt{2S(\omega_j)d\omega_j}\right]$$

Where υ is the randomized phase seed and N_{bands} is the number of wave frequency bands used to discretize the wave spectrum. Each time a case a run, new phases are generated. However, WEC-Sim allows irregular wave fields to be repeated using wave seeds. That is, the phase for irregular wave cases are always randomly generated for each case. However, to reproduce the same time-series every time an irregular wave simulation is run, the wave seed can be specified as 1, 2, 3,…,etc. The excitation IRF for irregular waves, $K_e(t)$, is defined as

$$K_e(t) = \frac{1}{2\pi}\int_{0-\infty}^{\infty} F_{exc}(\omega, \theta_{dir})e^{i\omega t}d\omega$$

2.10.4.4 State Space

It is highly desirable to represent $K_r(t)$ in state space (SS) form since it has been shown to drastically decrease computational time and allow control system implementation that typically rely on linear state space models [66], [67]. A linear state space model is constructed from a set of ODEs, where as K_r is computed from a set of PDEs. Therefore K_r is approximated from state space matrices, or

$$K_r(t) = \boldsymbol{C_r} e^{\boldsymbol{A_r} t} \boldsymbol{B_r}$$

Where $\boldsymbol{A_r}$, $\boldsymbol{B_r}$, and $\boldsymbol{C_r}$ are the time-invariant state, input, and output matrices respectively.

2.10.5 Regular Waves

Since this research focuses on a nearshore OWSC, only shallow-water regular and irregular waves will be discussed. A regular, or monochromatic, wave is defined as a propagating sinusoidal wave with a constant amplitude, frequency, and wave number. This oscillating sinusoidal wave can be defined with the following equation

$$\eta(x, y, t) = \frac{H}{2} \cos(\omega t - K(x \cos \theta_{dir} + y \sin \theta_{dir}) + \phi)$$

The phase speed, *c*, of a regular wave is its forward speed with constant phase. This, therefore, means that the time derivative of the phase is zero, resulting in the following equation for phase speed

$$c = \frac{\omega}{K}$$

2.10.6 Irregular Waves

The uncertain wave dynamic of irregular, or polychromatic, waves can be modeled by using an infinite sum of sinusoidal wave components that propagate with numerous wavelengths. Furthermore, these waves do not have consistent amplitudes, frequencies, wave numbers, or angles of incidence like regular waves. This largely unpredictable and incessantly changing phenomenon is the most realistic representation of real ocean conditions. The irregular wave shape can be

decomposed with a Fourier transfer function as the sum of a large number of regular sinusoidal waves, described in [68]. Irregular incident waves, $\eta_{irreg}(x, y, t)$, can be represented by the following equation

$$\eta_{irreg}(x, y, t) = \sum_{i=1}^{N} \frac{H_{irreg}}{2} \cos\left(\omega_{irreg} t - K_{irreg}\left(x \cos\theta_{dir,irreg} + y \sin\theta_{dir,irreg}\right) + \phi_{irreg}\right)$$

Where the subscript, *irreg*, indicates that the variables are randomized for irregular waves [34]. To generate the wave energy density spectrum of the irregular waves, the variance density spectrum is needed. The one-dimensional variance density spectrum only considers the frequencies present in the irregular wave. As the interval of all the frequencies, Δω, approaches zero, a continuous distribution of the variance over the entire frequency interval, also called the variance density spectrum, $S(f,\theta)$, is attained. Here, f is the wave frequency in Hertz. Since real waves propagate in a certain direction, a two-dimensional variance density spectrum is considered in the positive xy-plane. The variance density spectrum can be multiplied by the density of sea water and the gravitational constant to obtain the wave energy density spectrum, described in [34]. The general form of the wave spectra the WEC-Sim uses is

$$S(f, \theta_{dir}) = S(f, \theta_{dir}) = S(f) D(\theta_{dir})$$

Where $D(\theta_{dir})$ is the directional distribution that is defined by

$$\int_0^{\infty} \int_{-\pi}^{\pi} S(f)\, D(\theta_{dir}) d\theta_{dir} df = \int_0^{\infty} S(f) df$$

The total energy in the two-dimensional spectrum must be the same as the total energy in the one-dimensional spectrum

$$S(f) = A_{ws} f^{-5} \exp[-B_{ws} f^{-4}]$$

Where A_{ws} and B_{ws} depend on the wave spectrum being used. The spectral moments, m_k, where k = 1, 2, 3,…, are defined as

$$m_k = \int_0^{\infty} f^k S(f) df$$

2.10.6.1 Pierson-Moskowitz (PM) Spectrum

The PM spectrum is expressed in terms of significant wave height and average wave period for fully developed sea states, where the growth of waves are not affected by fetch. Pierson and Moskowitz supposed that if the wind maintained speed for a long time over a large area, the waves would be in equilibrium with the wind—hence a fully developed sea [69]. The spectral density of the surface elevation for the PM spectrum is given by

$$S_{PM}(f) = \frac{H_s^2}{4}\left(1.057 f_p\right)^4 f^{-5} \exp\left[-\frac{5}{4}\left(\frac{f_p}{f}\right)^4\right]$$

Where f_p is he peak wave frequency. This leads to coefficients being in the following form:

$$A_{ws} = \frac{H_s^2}{4}\left(1.057 f_p\right)^4 \approx \frac{5}{16} H_s^2 f_p^4 \approx \frac{B_{ws}}{4} H_s^2$$

$$B_{ws} = \left(1.057 f_p\right)^4 \approx \frac{5}{4} f_p^4$$

2.10.6.2 JONSWAP Spectrum

The JONSWAP spectrum is a modified PM spectrum that is used to describe a wave system where there is an imbalance of energy flow, or non-fully developed seas, due to high wind speeds [70]. JONSWAP is used for developing seas in a fetch-limited situation. The only difference in the JONSWAP spectrum and the PM spectrum is the addition of an enhancement factor to increase the peak spectral value. That is, if the peak spectral value is set to unity, then JONSWAP equals PM [71]. The spectral density of the surface elevation for the JONSWAP spectrum is

$$S_{JS}(f) = C_{ws}(\gamma) S_{PM} \gamma^{\alpha}$$

Where γ is the non-dimensional peak-shape parameter, and C_{ws} is the normalizing factor given by

$$C_{ws}(\gamma) = \frac{\int_0^{\infty} S_{PM}(f) df}{\int_0^{\infty} S_{PM}(f) \gamma^{\alpha} df} = 1 - 0.287 \ln(\gamma)$$

And α is the peak-shape parameter exponent given by

$$\alpha = \exp\left[-\left(\frac{\frac{f}{f_p}-1}{\sqrt{2}\sigma}\right)^2\right], \qquad \sigma = \begin{cases} 0.07 & f \le f_p \\ 0.09 & f \ge f_p \end{cases}$$

This peak-shape parameter itself is given by the following relationship with significant wave height and wave period

$$\gamma = \begin{cases} 5 & \text{for } \frac{T_e}{\sqrt{H_s}} \le 3.6 \\ \exp\left(5.75 - 1.15\frac{T_e}{\sqrt{H_s}}\right) & \text{for } 3.6 \le \frac{T_e}{\sqrt{H_s}} \le 5 \\ 1 & \text{for } \frac{T_e}{\sqrt{H_s}} > 5 \end{cases}$$

This leads to coefficients taking the following form:

$$A_{ws} = \frac{B_{ws}}{4} H_s^2 C_{ws}(\gamma)\gamma^{\alpha}$$

$$B_{ws} = \frac{5}{4} f_p^4$$

2.10.7 Power Take-Off

There are three types of PTO mechanisms that can be modeled in WEC-Sim: linear, hydraulic, and mechanical. For this work, a linear PTO was used and defined as a linear spring and mass damper. It is common practice to model the PTO as a purely resistive model when analyzing power capture, where the spring stiffness term is omitted [72], [73], [74], [75]. The PTO system here was controlled by applying resistive forces against the motion of the OWSC. The instantaneous power absorbed by the PTO, P_{PTO}, is given by [72]

$$P_{PTO}(t) = -B_{PTO} v(t)$$

Where B_{PTO} is the linear damping coefficient. To maximize P_{PTO}, the damping coefficient can be optimized at each wave period. The optimum damping coefficient, B_{opt}, can be determined to maximize the instantaneous power absorbed for single degree-of-freedom devices is given by [76]

$$B_{opt} = \sqrt{B_{5,5}^2 + \left(\frac{F_B}{\omega} - \omega\left(I + A_{5,5}\right)\right)^2}$$

Where F_B is the hydrostatic restoring force, or buoyancy force, and I is the inertia of the OWSC. The hydrodynamic coefficients used to calculate B_{opt} should be taken at the OWSC's hinge instead of the COG [76].

2.10.8 Nonlinear Buoyancy and Froude-Krylov Wave Excitation

The instantaneous water surface elevation and body position introduce various nonlinear hydrodynamic forces. Instead of using BEM results, the nonlinear buoyancy and Froude-Krylov forces are calculated by integrating the hydrostatic and hydrodynamic pressures over each element on the wetted OWSC surface for each time step. Since elements that are above the mean surface level, non-wetted elements, have unrealistically large values, the Wheeler stretching method was applied to correct the wave elevation so that the instantaneous wave elevation is equal to the water depth. While this method can be used for weak nonlinear hydrodynamics, it is not intended for strongly nonlinear events such as wave slamming or wave breaking. The corrected wave instantaneous wave elevation is defined in WEC-Sim as

$$z^* = \frac{D(D+z)}{(D+\eta)} - D$$

Where D is the mean water depth [76].

2.11 Flow Field Analysis

Fluent is a computational fluid dynamics software that is capable of simulating fluid flow, heat and mass transfer, chemical reactions, and other related phenomena using numerical analysis and data structure solvers [77].

2.11.1 Fluid Flow in CFD

Fluent solves the mass conservation equations for incompressible and compressible flows that take the form of

$$\frac{\partial \rho}{\partial t} + \nabla(\rho \vec{v}) = S_m$$

Where $\vec{v}$ is the velocity vector, and the source S_m is the mass added to the continuous phase from the dispersed second phase and any user-defined sources. That is, the continuous phase is the air, and the secondary phase is the flowing fluid, typically water. The equation for conservation of momentum in a non-accelerating reference frame is given by

$$\frac{\partial}{\partial t}(\rho \vec{v}) + \nabla(\rho \vec{v}\vec{v}) = -\nabla p + \nabla \times (\bar{\bar{\tau}}) + \rho \vec{g} + \vec{F}$$

Where $\bar{\bar{\tau}}$ is the stress tensor, $\overrightarrow{\rho g}$ is the gravitational body force(s), and $\vec{F}$ is the external body force(s). The stress tensor is given by

$$\bar{\bar{\tau}} = \mu \left[(\nabla \vec{v} + \nabla \vec{v}^T) - \frac{2}{3} \nabla \times \vec{v} I_{tensor} \right]$$

Where μ is the molecular viscosity, I_{tensor} is the unit tensor, and the second term on the right-hand side refers to the effect of volume dilation [78].

2.11.2 Multiphase Flow

Most CFD programs offer a specific flow regime that can account for free surface modelling. This regime is the multiphase flow model, which can be categorized as: gas-liquid or liquid-liquid flows, gas-solid flows, liquid-solid flows, and three-phase flows. Within these categories, Fluent can use either the Volume of Fluid model, Mixture model, and Eulerian model [78].

Fluent solves transport equations during multiphase flows for *per phase* scalars and *mixture* scalars. For an arbitrary k_{Ansys} scalar in *phase-1*, denoted by $\phi_1^{k_{Ansys}}$, Fluent solves the transport equation inside the volume that is occupied by *phase-1* using

$$\frac{\partial \alpha_1 \rho_1 \phi_1^{k_{Ansys}}}{\partial t} = \nabla\left(\alpha_1 \rho_1 \overrightarrow{u_1} \phi_1^{k_{Ansys}} - \alpha_1 \Gamma_1^{k_{Ansys}} \nabla \phi_1^{k_{Ansys}}\right) = S_1^{k_{Ansys}} \qquad k_{Ansys} = 1, \ldots, N$$

Here, the variable *1* is used to denote single-phase or multi-phase flow. α_1, ρ_1, and $\overrightarrow{u_1}$, are volume fraction, physical density, and velocity of *phase-1*, respectively. $\Gamma_1^{k_{Ansys}}$ and $S_1^{k_{Ansys}}$ are defined by the user and are the diffusion coefficient and source term respectively. The mass flux for *phase-1*, F_1, is given as

$$F_l = \int_S \alpha_1 \rho_1 \overrightarrow{u_1} \cdot d\vec{S}$$

If the transport variable described by $\phi_1^{k_{Ansys}}$ represents the physical field that is shared between phases, then $\phi_1^{k_{Ansys}}$ is associated with a mixture of phases, $\phi^{k_{Ansys}}$, represented by

$$\frac{\partial \rho_m \phi_1^{k_{Ansys}}}{\partial t} = \nabla\left(\rho_m \overrightarrow{u_m} \phi^{k_{Ansys}} - \Gamma_m^{k_{Ansys}} \nabla \phi^{k_{Ansys}}\right) = S_m^{k_{Ansys}} \qquad k_{Ansys} = 1, \ldots, N$$

Where the mixture density, ρ_m, the mixture velocity, $\overrightarrow{u_m}$, and the mixture diffusivity for the scalar k_{Ansys} $\Gamma_m^{k_{Ansys}}$ are calculated with

$$\rho_m = \sum_1 \alpha_1 \rho_1$$

$$\rho_m \overrightarrow{u_m} = \sum_1 \alpha_1 \rho_1 \overrightarrow{u_1}$$

$$F_l = \int_S \rho_m \overrightarrow{u_m} \cdot d\vec{S}$$

$$\Gamma_m^{k_{Ansys}} = \sum_1 \alpha_1 \Gamma_1^{k_{Ansys}}$$

$$S_m^{k_{Ansys}} = \sum_1 S_1^{k_{Ansys}}$$

To calculate the mixture diffusivity, the individual diffusivities for each material associated with each individual phase mush be specified [78].

2.11.3 Flow Regime

Selecting the proper multiphase regime depends on the model that with adequately describe the flow characteristics. In the case of this work, a gas-liquid flow regime will be adopted. The following are the gas-liquid or liquid-liquid flow regimes available in Fluent [78]:

- Bubbly flow: This is the flow of discrete gaseous or fluid bubbles in a continuous fluid.
- Droplet flow: This is the flow of discrete fluid droplets in a continuous gas.
- Slug Flow: This is the flow of large bubbles in a continuous fluid.
- Stratified/ free-surface flow: This is the flow of immiscible fluids separated by a clearly defined interface

2.11.4 Euler-Lagrange and Euler-Euler Approaches

There are two approaches for completing numerical calculations of multiphase flows in Fluent: The Euler-Lagrange approach and the Euler-Euler approach. The Euler-Lagrangian approach is a discrete phase model that solves the Navier-Stoke equations by treating the fluid phase as a continuum. The dispersed phase is solved by tracking a large number of particles, bubbles, or droplets through the calculated flow field. This allows for the dispersed phase and fluid phase to exchange mass, momentum, and energy. In the mixture, this approach assumes that the dispersed phase occupies a low volume fraction. Each individual particle or droplet trajectories are computed at specific intervals during the calculation of the fluid phase. The Euler-Lagrange is an appropriate approach when modeling spray dryers, coal and liquid fuel combustion, and some particle-laden flows. However, this approach is not suitable for modeling liquid-liquid mixtures, fluidized beds, or applications where the volume fraction of the secondary phase, typically water, must be known. The Euler-Euler approach uses volume fractions where the volume of one phase cannot be occupied by another phase. The volume fractions are assumed to be continuous functions of space and time whose sum is equal to one. Conservation equations are derived for each phase to obtain a set of equations that are closed by providing constitutive relations obtained from either empirical information or kinetic theory. In Fluent, there are three Euler-Euler multiphase models available, VOF model, Mixture model, and Eulerian model. In this study, the VOF model was adopted [78].

2.11.5 Volume of Fluid Model

The VOF model tracks the surface of a fixed Eulerian mesh and is designed for two or more immiscible fluids, where the intersection between both phases is of interest. This model is used particularly for motion of large bubbles in a liquid, the motion of liquid after a dam break, and the steady or transient tracking of any liquid-gas interface. The VOF model tracks the volume fraction of each fluid in the computational domain by solving one set of momentum equations. The volume fraction is specified to describe the percentage of fluid inside an element. In a control volume, the sum of these is unity. The variables and properties in any element are given as either a single pure phase, or a mixture of the phase, depending on the volume fraction values. That is, if the q^{th} fluid's volume fraction in an element is denoted as α_q, then the following three conditions are possible:

- $\alpha_q = 0$: The cell is empty of the q^{th} fluid
- $\alpha_q = 1$: The cell is full of the q^{th} fluid
- $0 < \alpha_q < 1$: The cell contains the interface between the q^{th} fluid and one or more other fluids

Based on the local value of α_q, the appropriate properties and variables will be assigned to each control volume within the domain. When modeling transient flow, the momentum equations must be discretized for time and space over a specific time-step.

2.11.5.1 Implicit Scheme

The implicit scheme uses the volume fraction from the current time step, rather than using the volume fraction from the previous step. It uses multiple iterations for the transport equation for the volume fraction of the secondary phase and may be used for steady-state or transient solutions. The various finite-difference interpolation methods for the implicit scheme are QUICK, first- and second-order upwind, and the modified high-resolution capturing scheme. The face flux for each element is determined by

$$\frac{\alpha_q^{n+1}\rho_q^{n+1} - \alpha_q^n \rho_q^n}{\Delta t} V + \sum_f \left(\rho_q^{n+1} U_f^{n+1} \alpha_{qf}^{n+1}\right) = \left[S_{\alpha_q} + \sum_{p=1}^{n} \left(\dot{m}_{pq} - \dot{m}_{qp}\right)\right] V$$

Where U_f is the volume flux through the face, *n+1* is the index of the instantaneous time step, *n* is the index of the preceding time step, α_{qf} is the face value of the q^{th} volume fraction, calculated from the interpolation schemes, and V is the volume of the element.

2.11.5.2 Explicit Scheme

The explicit scheme calculations are based on the values of the volume fraction at the previous time step, rather than the volume fraction at the current time step. This is represented by

$$\frac{\alpha_q^{n+1}\rho_q^{n+1} - \alpha_q^n \rho_q^n}{\Delta t} V + \sum_f \left(\rho_q U_f^n \alpha_{qf}^n\right) = \left[\sum_{p=1}^{n} \left(\dot{m}_{pq} - \dot{m}_{qp}\right) + S_{\alpha_q}\right] V$$

Fluent uses various schemes to interpolate the values of the fluids near the surface. This includes the Geo-Reconstruction scheme, the Donor-Acceptor scheme, the Comprehensive Interface Capturing Scheme for Arbitrary Meshes (CICSAM), the Compressive scheme, and the Bounded Gradient Maximization (BGM) scheme.

The Geo-Reconstruction scheme is applicable for general unstructured meshes and uses a piecewise-linear approach. It is the most accurate scheme in Fluent and uses a linear slope for the interface between the two fluids at any given element, making it a simple approach for calculating volume fraction.

The Donor-Acceptor scheme is used to obtain the face fluxes whenever an element is completely filled with one of the two phases. It identifies one element as a donor of a specific amount fluid and a neighboring element as the acceptor element of that same fluid. The transferred fluid is dependent on the capacity of the accepting element and the amount of donated fluid from the donor element.

The CICSAM scheme is typically used for flows with large viscosity ratios between the phases and produces an interface almost as sharp at the Geo-Reconstruction scheme.

The Compressive scheme in made up of zonal discretization schemes and phase localization schemes that are available for explicit VOF models. This Immiscible Fluid Model should be activated to model immiscible fluids. The slope limiter, β_{lim}, values can be described by

- $\beta_{lim,\ max} = 0$; The first order upwind scheme is used.
- $\beta_{lim,\ max} = 1$; The second order reconstruction bounded by the global minimum/ maximum of the volume fraction is used.
- $\beta_{lim,\ max} = 0 < \beta_{lim} < 1$; The first and second order compressive schemes are combined.
- $\beta_{lim,\ max} = 2$; The compressive scheme is used.
- $\beta_{lim,\ max} = 1 < \beta_{lim} < 2$; The second order and compressive schemes are combined.

The BGM scheme is similar to the Geo-Reconstruction scheme in that it uses a sharp interface between the phases in the VOF model. However, this scheme will not be used in the study since it is not applicable to transient modeling.

2.11.5.3 Fluid Properties

The foundational equation for density of an element that contains two phases, seawater and air, is given by

$$\rho = \alpha_{water}\rho_{seawater} + (1 - \alpha_{seawater})\rho_{air}$$

For a VOF model with two phases, the volume-averaged density is represented by

$$\rho = \sum_{q=1}^{2} \alpha_q \rho_q$$

2.11.5.4 Momentum Equation

Fluent uses one momentum equation to calculate the velocity of each phase. This equation was given in Section 2.11.1 and is dependent on the fluid density and molecular viscosity. The accuracy of the momentum equation is higher when the velocities between each phase are small. This difference in velocity is represented by the viscosity ratio, where magnitudes larger than $1x\ 10^3$ indicate convergence. In this study, the velocities between phases are small.

2.11.5.5 *Energy Equation*

The energy equations, related to the momentum equations, take on the form of

$$\frac{\partial}{\partial t}(\rho E) + \nabla \times [\vec{v}(\rho E + p)] = \nabla\left(k_{eff}\nabla T\right) + S_h$$

Where T is temperature, and energy, E, is

$$E = \frac{\sum_{q=1}^{n} \alpha_q \rho_q E_q}{\sum_{q=1}^{n} \alpha_q \rho_q}$$

Each phase has its respective E_q, based on specific heat and shared temperature. The density and thermal conductivity, k_{eff} , are shared by each phase, and the source terms, S_h, contains contributions from heat sources. In this study, the temperature difference between seawater and air is not substantial to affect the convergence and correctness of the results.

2.11.5.6 *Turbulence*

Osborne Reynolds is known for experimentally demonstrating laminar and turbulent flow through a tube. In 1833, he studied the behavior of water in a glass pipe at varying flow rates by introducing dye to the flowing water. When the flow velocity was low, the dyed layer of water continued to flow linearly—or laminar flow. However, at higher velocities the dyed layer began to break up and disperse throughout the fluid, becoming disordered and non-linear—or turbulent flow. In Fluent, turbulence can be modeled with a variety of models. The highest velocity at which a fluid can travel without becoming turbulent is known as the critical velocity. The Reynolds number is a dimensionless number that is used to determine the critical velocity. The Reynolds number, *Re*, is defined as

$$Re = \frac{\rho V d_{tube}}{\mu}$$

Where ρ is the fluid density, d_{tube} is the diameter of the testing tube, and μ_{dyn} is dynamic viscosity. The following Reynolds numbers describe different types of flow [79]:

- *Re* < 2,000; Laminar flow

- 2,000 < *Re* < 4,000; Transitional flow
- *Re* > 4,000; Turbulent flow

The turbulence model being studied here is comprised of the turbulent kinetic energy, *k*, and the specific dissipation rate, ω_{dis}, which is calculated from a ratio of *k* and *ε*, the rate of dissipation of turbulent kinetic energy

$$k = \frac{3}{2} I_{turb}^2 U^2$$

And

$$\varepsilon = \frac{k^{\frac{3}{2}}}{0.3d}$$

Where I_{turb} is he intensity of the turbulence, and *U* is the free stream velocity.

A turbulence model must be used in Fluent to close the Reynolds-Averaged Navier-Stokes (RANS) equations. However, there does not exist a turbulence model that is universally accepted as the best model. The model must be selected based on its relevance to the type flow physics, the established practice for a specific class of problem, the required level of accuracy, and the available computational power. The possible turbulence models are selected based on their ability to simulate wave interaction with an OWSC. The capabilities and limitations of the most commonly used turbulence models for VOF simulations are briefly described below [78]:

- Standard k-ε: This model, developed by [80], is the simplest and most commonly used model in CFD. It can be applied to a wide range of turbulent applications and provide a sensible level of accuracy. It is a semi-empirical model based on model transport equations from the turbulence kinetic energy and its dissipation rate. This model is well-suited for free surface flow applications which flow is far away from wall boundaries.
- Re-Normalization Group (RNG) k-ε: Compared to the Standard k-ε model, the RNG model improves increases the reliability and accuracy of results by simulating swirling flows more accurately using the Navier-Stokes equations. It was developed by [81] and has an additional term in its ε equation that improves the accuracy for rapidly strained flows.

- Realizable k-ε: This model, developed by [82], has improved predictions of the spreading rate of planar and round jets. It is most likely to provide superior performance for flows involving rotation, boundary layers under strong adverse pressure gradients, separation, and recirculation. It has a new formulation for the turbulent viscosity and a new transport equation for the dissipation rate that was derived from an exact equation for the transport of mean-square vorticity fluctuation.
- Standard k-ω: This model was developed by [83] and incorporates modifications for low-Reynolds-number effects, compressibility, and shear flow spreading. It is designed to predict far wakes, mixing layers, and plane, round, and radial jets, and is suitable for wall-bounded flows and free shear flows. This model is used when the behavior of flow near a wall boundary.
- Shear Stress Transport (SST) k-ω: This model was developed by [84] to essentially blend the robust and accurate formulation of the k-ω model in the near-wall region with the free-stream independence of the k-ε model in the far field. The SST k-ω model includes more advanced features such as a damped cross-diffusion derivative term in the ω equation, a modified turbulent viscosity to aid in the transport of shear stress, and different modeling constants. This model is more reliable and accurate for a wider range of flows such as adverse pressure gradient flows, airfoils, and shock waves. It also supports turbulence damping in interfacial cells, which is critical for capturing interfacial instabilities.
- Transition SST: This model combines the SST k-ω transport equations with the intermittency and transition onset transport equations, which may be user-controlled, in terms of momentum-thickness Reynolds number. This model was developed by [85].

2.11.5.7 Time Dependence

When solving a time dependent VOF model, the resolution of the turbulent structures in time is essential for a successful simulation run. The following equation is solved using an explicit time-marching scheme

$$\frac{1}{\rho_q}\left[\frac{\partial}{\partial t}\left(\alpha_q \rho_q\right) + \nabla\left(\alpha_q \rho_q \vec{v}_q\right) = S_{\alpha q} + \sum_{p=1}^{n}\left(\dot{m}_{pq} - \dot{m}_{qp}\right)\right]$$

For the integration of the volume fraction equation, the Fluent solver will automatically refine the time step. However, this time step can be influenced by modifying the Courant number, *C*—a condition that is required in PDEs to ensure convergence. The Courant number is defined as

$$C = \frac{v\Delta t}{\Delta y} < 1$$

Where *v* is the velocity of the flow, Δt is the change in time, and Δy is the change in length along the direction of flow. In an explicit Eulerian model, the Courant number cannot be greater than one since information can only travel through one grid element per time step. If it is greater than one, the solver will not have time to analyze the physical responses and will abort. Typically, low Courant numbers, around 0.3 or 0.4, are used to ensure convergence [78].

2.11.5.8 Surface Tension

Surface tension is force only at the surface of a fluid that results from attractive forces between the molecules of a fluid. The VOF model in Fluent has the capabilities of modeling surface tension and its effects at the interface of the two phases—in this case, the intersection of the seawater and air. Here, a constant surface tension was used since this study considered the force of gravity. Since surface tension is a function of temperature, the value for surface tension at 30° Celsius is 0.0728 N/m^2 [86]. In Fluent, the surface tension is modeled as a continuum surface force (CSF) and then adds this force to the momentum equation, which can be expressed as a volume force, F_{vol}, using the divergence theorem. If two phases are present in a cell, the volume force is represented by

$$F_{vol} = \sigma_{ij} \frac{\rho \kappa_i \nabla \alpha_i}{\frac{1}{2}(\rho_i + \rho_j)}$$

Where σ is the surface tension coefficient, and κ is curvature defined in terms of the divergence of the unit normal [78].

2.11.5.9 Wall Adhesion

A wall adhesion angle, otherwise known as a contact angle, may also be specified in Fluent. This is the angle at which the fluid contacts the wall. It is a dynamic boundary condition that adjusts

based on the surface contours of the wall. The surface normal at the cells adjacent to the OWSC is defined by

$$\hat{n} = \hat{n}_w \cos(\theta_w) + \hat{t}_w \sin(\theta_w)$$

Where $\hat{n}_w$ is the normal unit vector to the wall, $\hat{t}_w$ is the tangential unit vector to the wall, θ_w is the contact angle at the wall boundary, and $\hat{n}$ is the unit normal,

$$\hat{n} = \frac{n}{|n|}$$

Where *n* is the surface normal,

$$n = \nabla \alpha_q$$

Once the local curvature of the surface is determined, the body force term will be adjusted in the surface tension equation [78].

2.11.5.10 *Open Channel Flow*

The open channel boundary condition can be used to model scenarios such as dams, rivers, and surface-piercing structures in unbounded streams. In these models, the quantities of interest include the behavior of the free surface and wave propagation. The open channel flow is governed by the Froude Number, *Fr*,

$$Fr = \frac{V_0}{\sqrt{gh}}$$

Where *h* is the distance from the bottom of the channel to the free surface water level, or the water depth. Here, wave speed governs much of the characteristics of the Froude number, and is defined as

$$V = V_0 \pm \sqrt{gh}$$

Open channel flow can be categorized in three classifications:

- Fr < 1; Subcritical flow – disturbances in flow can travel upstream and downstream. Therefore, downstream flow can affect upstream flow.

- Fr = 1; Critical flow – waves that propagate upstream remain stationary.
- Fr > 1; Supercritical flow – disturbances in flow cannot travel upstream. Therefore, downstream flow does not affect upstream flow [78].

2.11.5.11 Open Channel Wave Boundary Conditions

This boundary condition allows the user to simulate ocean waves and their interaction with the sea floor, or other structures—whether fully submerged or surface piercing. This upstream boundary condition is applied to the inlet of the VOF model, typically in the form of inlet velocity. Shallow, shallow/intermediate, and short gravity waves can be simulated with various wave theories such as Airy, Stokes, Solidary or Cnoidal to name a few. Since shallow/intermediate were simulated here, the following conditions should be met:

- The maximum ratio of wave height to water depth must not exceed 0.78
- The maximum ratio of wave height to wavelength for linear waves must not exceed $0.0625 \tanh\left(2\pi \frac{H}{\lambda}\right)$
- The maximum ratio of wave height to wavelength for non-linear waves must not exceed $0.142 \tanh\left(2\pi \frac{H}{\lambda}\right)$

The wave steepness, a ratio of wave height to wavelength, is used to determine which wave theory is most suitable for the model. Waves with a lower steepness are typically modeled with small amplitude wave theory, or Airy wave theory, whereas a larger wave steepness is typically modeled with a higher-order wave theory such as 2nd, 3rd, 4th, or 5th order Stokes wave theory. To determine which wave theory fits best, the Ursell Number, *Ur*, may be calculated with

$$Ur = \frac{H\lambda^2}{h^3}$$

Fluent describes the wave profiles, ζ, for any incident wave as

$$\zeta = a\cos\left(k_x x + k_y y - \omega_e t + \epsilon\right)$$

Where ϵ is the phase difference, ω_e is the effective wave frequency, and x and y represent the parallel and perpendicular directions of flow respectively, assuming that the wave travels in the positive x direction such that

$$K_x = K\cos\theta_{dir}$$
$$K_y = K\sin\theta_{dir}$$

The effective wave frequency is defined as

$$\omega_e = \omega + kU_{incident}$$

Where $U_{incident}$ is the uniform incident wave velocity and ω is the wave frequency defined as

$$\omega = \sqrt{gk\tanh(kh)}$$

The velocity components for shallow waves are defined as

$$\begin{pmatrix} u \\ v \end{pmatrix} = \frac{gkA}{\omega}\frac{\cosh[k(z+h)]}{\cosh(kh)}\begin{pmatrix} \cos\theta \\ \sin\theta \end{pmatrix}\cos\left(k_x x + k_y y - \omega_e t + \epsilon\right)$$

Where z is the height in the z-direction from the free surface towards the atmosphere, and u and v are the velocity components in the x- and y- direction [78].

2.11.6 Flow Characteristics

2.11.6.1 Compressibility

A fluid can be either a gas or a liquid, compressible or incompressible. A fluid is considered compressible if its density changes when the fluid is subjected to high pressures. A fluid is considered incompressible if it can maintain a constant density as it is subjected to high pressures. Most liquids are incompressible while gases, depending on its density and the density of its surroundings, can be either compressible or incompressible. A fluid's compressibility can be measured by finding the Mach number, M_{mach}, shown below.

$$M_{mach} = \frac{V}{c_{sound}}(1.4 \times 10^{-4})$$

Where c_{sound} is the speed of sound. A fluid is considered incompressible when the following condition is satisfied [78]

$$\frac{1}{2}M_{mach}^2 \ll 1(1.4 \times 10^{-5})$$

The speed of sound in sea water a temperature of 30°C is about $1{,}500\,\frac{\mathrm{m}}{\mathrm{s}}$, [87]. Since the velocity of a shallow water wave depends on the depth of the water, the group celerity of a wave in 3.1 m deep water is $5.51\,\frac{\mathrm{m}}{\mathrm{s}}$. Therefore, the Mach number for ocean water, M_{water}, is

$$M_{water} = \frac{5.51}{1{,}500}(1.4 \times 10^{-4}) = 5.14\ \times 10^{-7}$$

The greatest wind speed at the reference site used in this work is about $10\,\frac{\mathrm{m}}{\mathrm{s}}$. At 30°C, the speed of sound is approximately $350\,\frac{\mathrm{m}}{\mathrm{s}}$. Therefore, the Mach number for air, M_{air}, is

$$M_{air} = \frac{10}{350}(1.4 \times 10^{-4}) = 4 \times 10^{-6}$$

In this case, $\frac{1}{2}M_{mach}^2$ for both air and sea water are far less than 1.4×10^{-5}, and were modeled as incompressible fluids.

2.11.6.2 *Reynolds Number Calculation*

Another important aspect of CFD modeling is whether or not the flow is laminar or turbulent by using the Reynolds number, defined in Section 2.11.5.6. At a temperature of 30°C, the dynamic viscosity of seawater, μ_{ocean}, is $0.789 \times 10^{-3}\,\frac{Ns}{m^2}$, the density of sea water is $1{,}025\,\frac{kg}{m^3}$, the shallow wave group velocity is $5.51\,\frac{m}{s}$,and the hydraulic diameter, d_h, which is equivalent to the characteristic length of the computational domain, will be found using

$$d_h = \frac{4A_{cd}}{U_{wet}}$$

Where A_{cd} is the cross-sectional area of the 5.8 m × 60 m computational domain, and U_{wet} is the wetted perimeter of the computational domain, where the water depth is 3.1 m, or 126.2 m [87]. Therefore, the hydraulic diameter is 11 m. The Reynolds number can then be calculated as

$$Re = \frac{\rho v d_h}{\mu_{ocean}} = \frac{1025 \times 5.51 \times 11}{0.789 \times 10^{-3}} = 7.87 \times 10^7$$

Therefore, the flow is determined to be turbulent.

2.11.6.3 Dynamic Pressure

Dynamic pressure, p_d, is the kinetic energy of a flowing fluid per unit volume, and is expressed as

$$p_d = \frac{1}{2}\rho v^2$$

Dynamic pressure can be calculated as the difference in total pressure and static pressure. It is widely used in CFD to analyze the pressures that act on structures as the fluids flow around it.

3 Methodology

This section describes the simulation parameters that were chosen to model the OWSC in its various configurations and arrangements. Section 3.1 describes the process of obtaining the OWSC's hydrodynamic coefficients using a BEM program, Aqwa. This includes the single 2-vane OWSC, the single 4-vane OWSC, and the 2x2 and 3x3 array in each vane angle configuration. Section 3.2 describes the process of obtaining the MAEP matrices for each vane angle configuration of the single 2-vane arrangement. The MAEP matrices were calculated using WEC-Sim. Finally, Section 3.3 describes the CFD process of investigating the fluid flow field and whether or not wave slamming occurs. This was conducted in Fluent. The exact steps taken to model the device in SolidWorks can be found in Appendix A. The exact steps taken to simulate the device in Aqwa, WEC-Sim, and Fluent can be found in Appendix B, C, and D respectively.

3.1 Hydrodynamic Coefficients

The objective of using Aqwa was to obtain the device's hydrodynamic coefficients, such as radiation damping, added mass, and wave excitation torque, to describe how the structure would react in water. That is, for the OWSC with 2 adjustable vanes and the OWSC with 4 adjustable vanes. Hydrodynamic coefficients were calculated from velocity potentials, and they were needed to solve for some of the force/moment terms in the general equations of motion for the OWSC. Further descriptions of these hydrodynamic terms and their meaning can be seen in Section 2.7. A mesh sensitivity study was performed to ensure the results were not sensitive by mesh density. The results are presented in Section 4.1. A study was conducted to validate the hydrodynamic results ensure that all boundary conditions, parameters, and conditions are set up properly in Aqwa. The results for the hydrodynamic validation study are presented in Section 4.1.2. Furthermore, the setup used here was replicated to analyze the 2-vane configuration and 4-vane configuration, as well as the OWSC sensitivity due to a 2x2 array and 3x3 array of OWSCs. In this research, Aqwa version 18.1 with a student license under the authority of East Carolina University was used. Before initiating the simulation, a CAD geometry was available with its physical properties such as mass and moment of inertia for each body. The process for creating that geometry can be found in Appendix A.

3.1.1 Device Parameters

Most BEM programs require the device being studied to be oriented with the z-axis as the vertical axis, the x-axis as the direction of wave propagation, and the y-axis defined by the right-hand rule. The origin of the z-axis was at the FSWL with the positive z-direction being away from the sea floor. BEM programs only meshes surfaces, not solid bodies. Therefore, the thickness of the OWSC was 0 meters. A water depth of 3.3 m was selected, with a nominal water density of 1,025 kg/m^3. This depth was selected so there were not any nodes that coincide with the seabed. A point mass was added at the OWSC's COG since WEC-Sim simulations require hydrodynamic coefficients be calculated at the device's COG. Hydrodynamic coefficients were also calculated at the OWSC's hinge in order to calculate the optimum damping value for the PTO in WEC-Sim. A list of the simulation and OWSC parameters can be seen in Table 3-1.

Table 3-1. BEM Simulation Parameters

Water Depth [m]	3.3
Point Mass [kg]	346
Water Density [kg/m^3]	1025
OWSC Density [kg/m^3]	256.25
Location of Mass [m]	[0, 0, 1.28688]
Moments of Inertia, L_{xx}, L_{yy}, and L_{zz} [kg/m^2]	574.75, 462.47, 114.2

3.1.2 Meshing

The defeaturing tolerance and maximum element define the density of the mesh as well as the maximum allowable wave frequency that can be analyzed. The defeaturing tolerance specifies how Aqwa will treat sharp radii and other curvature. The maximum element size directly relates to the maximum panel size on the model. A smaller maximum element size resulted in an increase in elements, and thus an increase in result accuracy. Furthermore, a finer mesh resulted in a larger allowable maximum frequency, which was beneficial in analyzing the convergence of

the OWSC's impulse response function and its stability. Consequently, as the number of elements in the simulation increased, so did the simulation time. A mesh sensitivity study was performed for each vane angle configuration in this work and can be seen in Section 4.1. It should be noted that the defeaturing tolerance did not exceed 60% of the maximum element size, as stated by the Aqwa manual. Furthermore, the total number of elements did not exceed 18,000, and the total number of diffracting elements did not exceed 12,000. It should be noted that in the 2x2 and 3x3 array analysis, the number of diffracting elements still must not exceed 12,000. The exact details of the mesh can be seen in Table 3-2.

Table 3-2. Details of Mesh

Meshing Type	Program Controlled
Defeaturing Tolerance	0.01 m
Maximum Element Size	0.08 m
Total Elements	8,511
Diffracting Elements	6,822

3.1.3 Wave Conditions

For this study, waves were considered to be unidirectional. The wave heading angle, relative to the OWSC, was 0° since waves that are perpendicular to the OWSC were of most interest. It was important to analyze a large number of intermittent wave frequencies so there would be more points to study on the hydrodynamic curves. Furthermore, a large number of intermittent wave frequencies would help WEC-Sim generate more accurate results since the IRFs would have more time to converge. Aqwa is capable of analyzing up to 100 intermittent wave frequencies. Therefore, here, 80 intermittent wave frequencies were used to capture a sufficient amount of data points.

3.2 Power Production

The objective of this section was to extend the work of [7] by analyzing the energy production capabilities of a variable-geometry OWSC that had 2 adjustable vanes and an increased number of angle configurations. Mean annual energy production (MAEP) matrices were developed in WEC-Sim to show the amount of power that each OWSC configuration contributed over time as a function of wave height and wave period. Overall MEAP values were obtained by summing the

values of each sea state bin. Figure 1-6 and Figure 1-7 respectively show the percentage of wave occurrence and the percentage of wave energy contribution at the reference site in Duck, North Carolina [12]. WEC-Sim has a built-in multiple conditions run (MCR) function, where batches of simulations can be run consecutively and stored as individual files. This function allows the user to run simulations over a wide array of sea states. A workflow diagram of the WEC-Sim code can be seen in Figure 2-7. In this work, WEC-Sim was used to generate the MAEP matrices of each vane angle configuration in the single OWSC arrangement [56].

3.2.1 Pre-Processing Hydrodynamic Data

BEM Input/Output (BEMIO) is a pre- and post- processing tool in WEC-Sim that takes hydrodynamic data from BEM codes and interprets the data so multibody dynamics simulations of WECs can be completed. BEMIO was used to generate plots of the nondimensionalized hydrodynamic coefficients. The radiation damping term was nondimensionalized by the product of density and wave frequency, the added mass term was nondimensionalized by density of seawater, and the wave excitation was nondimensionalized by the product of density and gravity. BEMIO calculated the necessary impulse response functions to ensure the device was numerically stable. It was important to analyze these results and ensure the radiation damping and wave excitation terms tended towards zero as the wave frequency approached infinity. Furthermore, it was important for the added mass term to approach a constant horizontal asymptote as wave frequency approached infinity. Meeting these conditions was a good indication that the impulse response functions were wholly stable, as they, too, tended towards zero as wave frequency approached infinity [88].

3.2.2 WEC-Sim Simulink File

A Simulink model was created to be read by WEC-Sim that prescribed a global reference frame, various bodies, constraints, and joints. The global reference frame was a fixed frame that acted as the sea floor to which all other parts of the WEC referenced. Two rigid bodies were used to model the OWSC base and the OWSC flap itself. It should be noted that in this case, a base was modeled in SolidWorks and used in WEC-Sim solely for visual purposes. The base was modeled as a non-diffracting body, so it was not considered in any calculations and therefore did not

affect any of the results. The OWSC base was connected to the global reference frame via a fixed constraint, and the OWSC base was connected to the OWSC flap via a rotational joint. This joint was constrained to pitch only about the y-axis. Within this joint, the rotational joint was limited to rotate ± 30° by using end stops. This was chosen because it has been recommended for OWSCs to not exceed 30° rotation in operable sea states [89], [90].

3.2.3 WEC-Sim Input File

A fixed time-step simulation solver was used in this work since extreme conditions are not being analyzed. Furthermore, it was found that for this work specifically, there was no difference in OWSC performance between a fixed and variable time-step. It was recommended for 100 time-steps per wave period to be used to provide an accurate hydrodynamic force calculation [65]. Since the smallest wave period analyzed here was 2.5 seconds, a time-step size of 0.01 seconds was selected to ensure higher accuracy [65]. A ramp time of 100 seconds was used to avoid singularities, while an end time of 400 seconds was used to ensure the waves were fully developed. Irregular waves were modeled using the Pierson-Moskowitz spectrum so more realistic wave conditions could be observed. A phase seed of 1 was used to replicate the time-series each time a simulation with irregular waves was run. That is, by using a phase seed of 1, the random wave phase generated by WEC-Sim was seeded and produced the same wave phase for each simulation. The mass and moment of inertia were specified for the OWSC flap, while the base was defined as a nonhydrodynamic body. Details on the specific device parameters can be seen in Appendix C. The simulation data settings are specified in Table 3-3. The OWSC was analyzed as a purely mechanical system, where spring stiffness of the PTO was set to zero, since the OWSC itself already provided a spring force due to its buoyancy [91]. Furthermore, optimizing PTO stiffness has proven to be highly complex [9], [56], [72], [92], [93], [94]. For this work, the optimum PTO damping value, B_{opt} was calculated for each wave period and for each vane angle configuration, as described in Section 2.10.7. The values for B_{opt} are shown in Figure 3-1.

Table 3-3. Simulation Data Settings

Solver Type	*ode4*
Ramp Time	100 seconds
End Time	400 seconds
Fixed Time Step Size	0.01 seconds
Wave Type	PM
Phase Seed	1

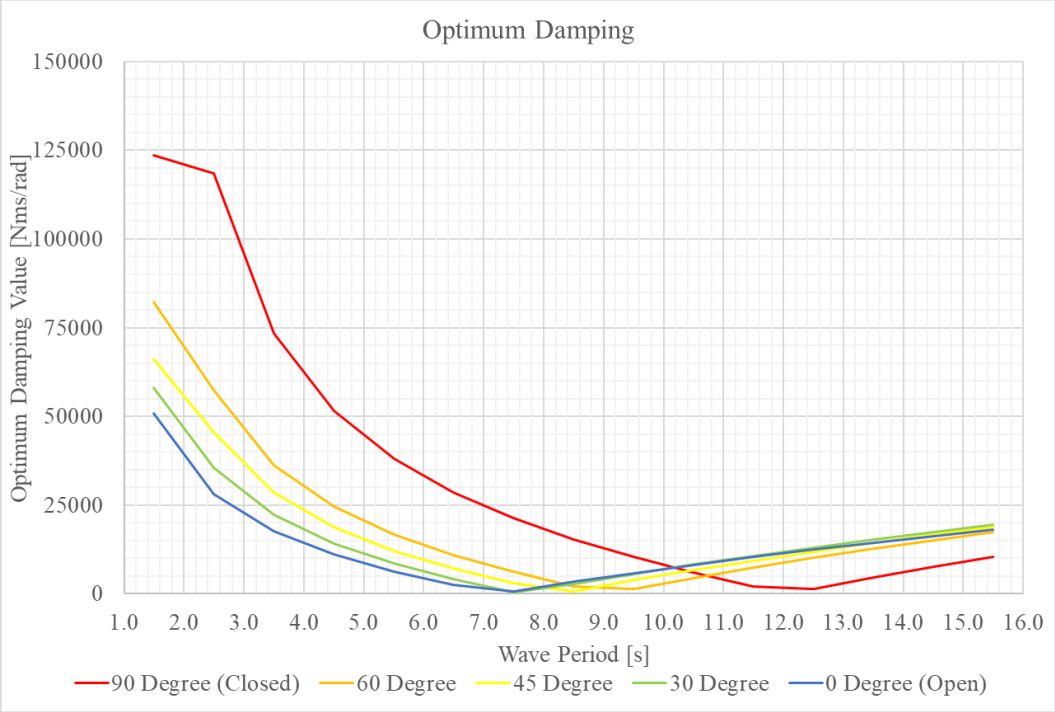

Figure 3-1. Optimum Damping Values for Each Vane Angle Configuration at Various Sea States

A table was populated with the wave height, wave period, and optimum PTO damping values, and it was read by WEC-Sim after the MCR option was initiated. The wave data was selected by referencing Figure 1-6 while the optimum PTO damping values were selected based on calculated results in Figure 3-1.

3.2.4 User-Defined Functions for Post Processing

User-defined functions were created to extract specific information on body forces and PTO forces. This way, information such as simulation time, mechanical torque, and mechanical power, could be stored and plotted for each vane angle configuration at each sea state. The body and PTO forces that were experienced during the 100 second ramp time were not considered when calculating the average force, torque, and power results.

3.2.5 Free-Decay Test

A free-decay test was performed within WEC-Sim for two main reasons; First to ensure a large enough hydrostatic restoring force was acting on the OWSC, and second to ensure that the radiation forces were being calculated correctly and not causing any numerical instability. The OWSC had an initial angular displacement of 15°, or 0.262 radians. The free decay test was performed on the open configuration, and the results for two different scenarios are shown below. First in Figure 3-2, when the flap is critically damped, and second in Figure 3-3, when there is no damping constraint on the OWSC, and it is free to oscillate. The results indicated that the hydrostatic restoring forces are strong enough to restore the OWSC to equilibrium, or 0°, and that the radiative forces are being calculated correctly and not causing any instability issues.

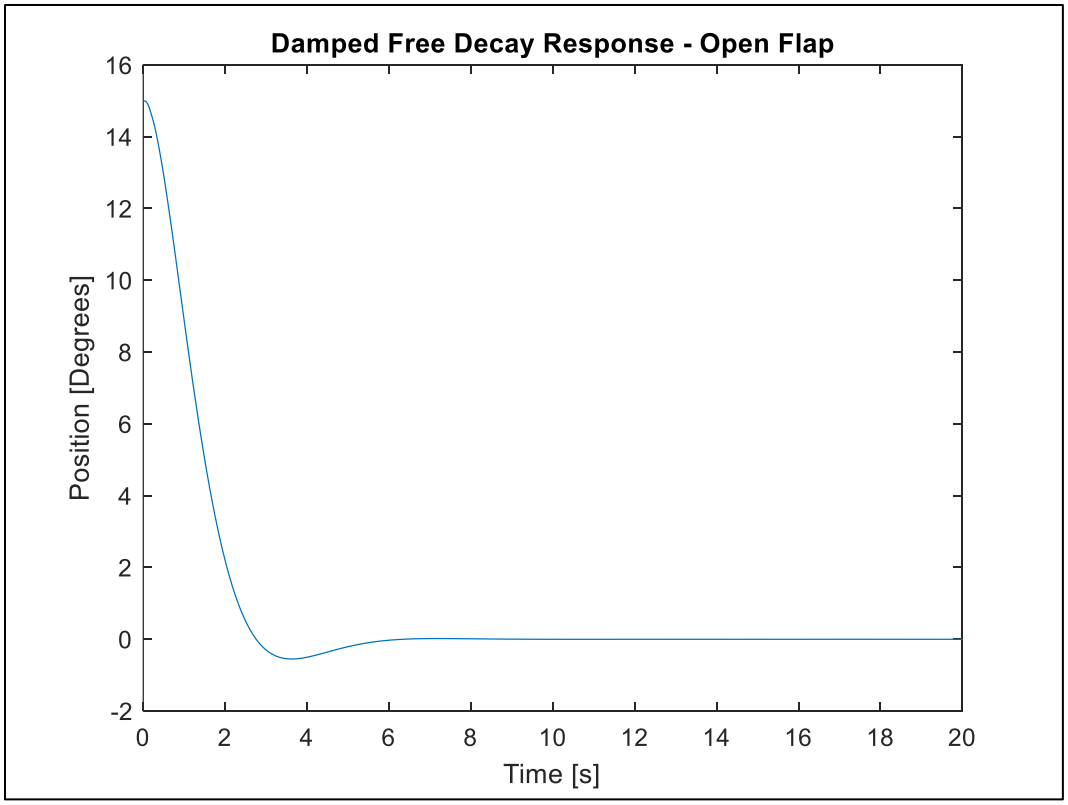

Figure 3-2. Damped Free Decay Response for Open Configuration

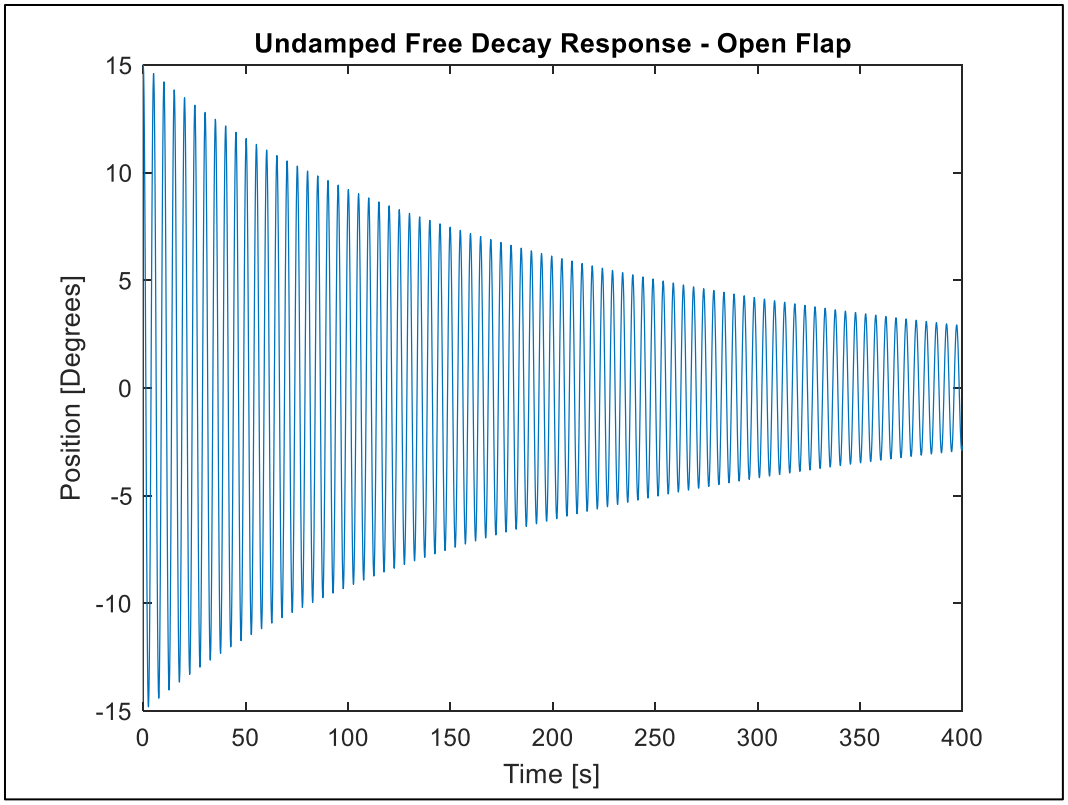

Figure 3-3. Undamped Free Decay Response for Open Configuration

3.3 Fluid Flow Analysis

This section explains the process of conducting a detailed flow field analysis in the CFD program, Fluent. The fluid flow analysis included investigating the wave slamming phenomenon, velocity profile, and dynamic pressure contours that acted around the nearshore OWSC. Two wave conditions were simulated:

- Wave Condition 1: H_s = 0.75 m and T_e = 5.5 s
- Wave Condition 2: H_s = 1.75 m and T_e = 6.5 s

These wave conditions were selected based on the JPD plot from the reference site, described in Section 1.6. Wave condition 1 had the highest sea state occurrence while wave condition 2 was more energetic and also had a high occurrence percentage. A mesh sensitivity study was conducted to ensure the results were not sensitive to the mesh density. The results are presented in Section 4.3.1.

3.3.1 CFD Meshing

Meshing is the process by which a continuous geometric model is broken down into thousands, or millions, of small shapes to properly analyze the model. Three different bodies were used to partition the mesh, allowing for better control of mesh distribution. The outer domain surface was modeled with quadrilateral elements since it was not a dynamic zone and quadrilateral elements aided in convergence. The inner domain surface was modeled with triangular elements since it was a deforming zone. Finally, the mesh around the boarder of the OWSC was refined with a triangular mesh since this area was particularly interesting. It was important that the mesh skewness did not exceed 0.7 and the orthogonal quality was larger than 0.6 to ensure the simulation did not fail due to negative cell volume. Proximity and curvature sizing parameters were used into order to capture the small gaps and sharp radii of the OWSC. To determine the which mesh density to use, a mesh sensitivity study was conducted and is explained in the subsequent section.

3.3.2 Simulation Parameters

A pressure-based solver was used with transient time so results could be investigated at different time steps. The VOF multiphase flow model was used to model open channel flow so the interaction between the OWSC and the two phases, air and sea water, could be investigated. Both fluids were considered incompressible based on determining the Mach number as shown in Section 2.11.6.1. The primary phase, air, had a density of 1.225 kg/m^3 and a dynamic viscosity of 1.7894e-5 kg/ms. These values were default in the Fluent database. At 30°C, sea water has a density and dynamic viscosity of 1,025 kg/m^3 and 0.0014 kg/ms respectively [95]. Implicit body force was analyzed to improve solution convergence by accounting for the partial equilibrium of the pressure gradient and body forces in the momentum equations [96]. The surface tension force that naturally acts between the two fluids was defined 0.0728 N/m [97].

The flow was considered turbulent based on the calculation of the Reynolds number in Section 2.11.6.2. The Realizable k-ε turbulence model with scalable wall functions was used to close the RANS equations since has been used to model WECs in the past, and it greatly aided with convergence [98]. It should be noted that the torque on the OWSC due to wave loads is not

sensitive to the turbulence model according to [58]. Shallow/Intermediate waves were defined at the inlet since the OWSC was considered nearshore. The third-order Stokes wave theory was selected based on the wave theory criterion in Figure 3-4.

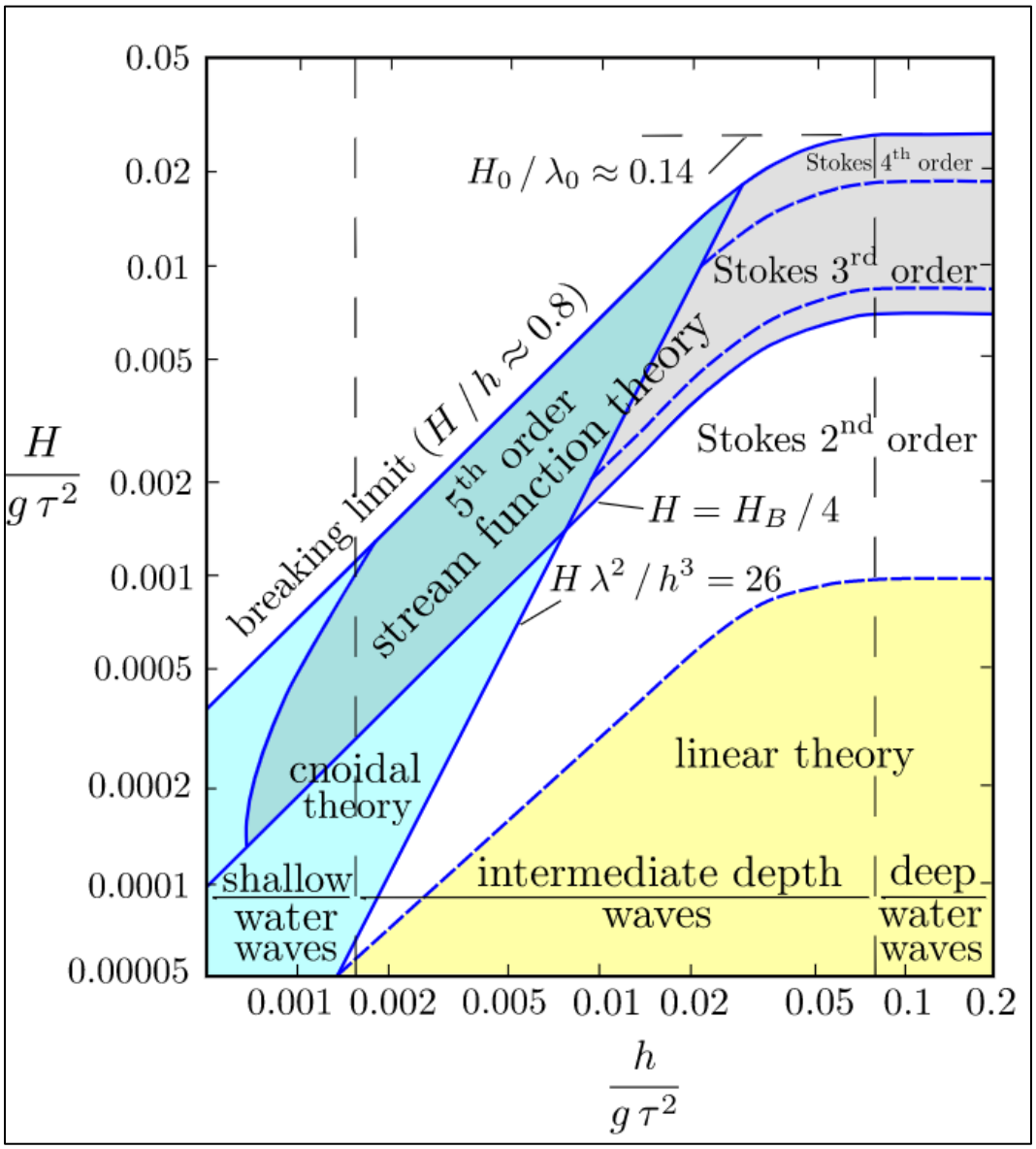

Figure 3-4. Process for Selecting Appropriate Wave Theory (Image Obtained from [99])

The operating pressure at the pressure outlets were modeled using a value of 101325 Pa, and a numerical beach was implemented so the waves would dampen after they pass the OWSC instead of refracting.

A dynamic mesh was applied to track the transient response of a rigid body due to input forces. In this case, the input forces were ocean waves, and the rigid body was the OWSC. Smoothing and remeshing mesh methods were applied to the deforming, inner domain to allow the triangular elements to stretch, compress, divide, and combine as a result of the OWSC's oscillations. These mesh methods also improved convergence and provided the most stability throughout the simulation. The OWSC was modeled as a rigid, 1-DOF body which allowed it to rotate, but not deform. Furthermore, this allowed external forces and moments on the OWSC to be calculated. Its mass, center of rotation coordinates, and inertia values were obtained from SolidWorks. The optimum damping term, calculated in Section 3.2.3, was used to mimic the PTO, and the OWSC was constrained to rotate ±30°. Implicit update with 0.001 residual criteria was used to enhance convergence and numerical stability.

The PISO scheme was selected since this was a transient simulation [96]. A PRESTO pressure discretization was selected since the geometry contained curved domains and since there was a large flow of water [96]. Fluent contains a feature that enhances VOF convergence and numerical stability by optimizing the remaining discretization techniques and under-relaxation factors. The settings that were chosen were verified to be highly appropriate for the oscillating device. The simulation was initialized in calm water using a hybrid initialization based on the inlet boundary condition.

For adequate data capture, the total simulation time was 25 seconds. To ensure each iteration converged to 0.001, the following calculation parameters, shown in Table 3-4, were selected

Table 3-4. Calculation Parameters for CFD Simulation

Calculation Parameter	Quantity
Time Steps	2500
Time Step Size	0.01
Iterations per Time Step	75

The total aggregate pressure, x- and y-forces, and moments that acted on the OWSC due to waves were exported to investigate the multi-directional forces that act on the OWSC.

Furthermore, these output files were used in a comparison study with WEC-Sim to ensure all boundary conditions were set up properly, shown in Section 4.3.2. Solution export quantities such as fluid velocity, fluid dynamic pressure, and volume of fraction were specified so investigations and animations could be made in post processing programs. This provided insight as to how the vane angle changes and wave conditions affected the fluid-structure interaction. CFD-Post was used for post processing the Fluent results.

4 Results

4.1 Hydrodynamic Diffraction Results

For the 2-vane and 4-vane scenario, depicted in Figure 1-2 and Figure 1-3, the hydrodynamic coefficients were calculated at the OWSC's hinge. All simulation parameters were kept consistent between configurations and scenarios. The only thing that changed was either the number of vanes being studied, the vane angle configuration, or the arrangement of arrays. Section 4.1.1 explains the results for the mesh sensitivity analysis conducted in the BEM code, while Section 4.1.2 explains the results for the hydrodynamic validation study with [3].

4.1.1 Mesh Sensitivity Analysis

It is important that the hydrodynamic results are not sensitive to the mesh size. In order to ensure this consistency, a mesh sensitivity analysis was conducted only on the OWSC itself since the base is fixed in place and does not have a radiation damping or added mass term. Aqwa calculates the pressures and forces on each meshed element using the Hess-Smith constant panel method where the mean wetted surface of the OWSC is divided into quadrilateral or triangular panels. Generally, a finer mesh will lead to greater accuracy with the tradeoff being computational time [60], [53], [100]. In Aqwa, the mesh size is explicitly related to the maximum allowable wave frequency. That is, the finer the mesh, the higher the maximum allowable wave frequency. Therefore, to maintain consistency among cases, the maximum allowable wave frequency was set to 8 rad/s, with approximately 0.1 rad/s intervals. The mesh density is calculated by initiating a maximum element size and defeaturing tolerance. The maximum element size is the maximum segment length from one node to another. The defeaturing tolerance, which must be at least 60% smaller than the maximum element size, defines how Aqwa handles curvature and sharp radii. The defeaturing tolerance was set to 0.01 meters and kept constant. Once all of the simulation parameters were set up, six cases were initiated where the only difference among them was the density of the mesh. Aforementioned, the Aqwa solver is limited to 18,000 elements—12,000 of which may be diffracting [60]. Therefore, the range of mesh sizes used in the sensitivity analysis ranged from coarse to fine, approximately 3,000 diffracting elements to 11,150 diffracting elements respectively. A total of 80 wave frequencies per simulation were chosen as it is necessary

to have a wide array of wave frequency values. The exact details of each mesh case are reported in Table 4-1.

Table 4-1. Exact Details for Mesh Sensitivity Analysis

Mesh	Total Elements	Diffracting Elements	Defeaturing Tolerance (m)	Maximum Element Size (m)
1	3,984	3,155	0.01	0.15
2	6,055	4,818	0.01	0.11
3	8,511	6,822	0.01	0.08
4	11,402	9,115	0.01	0.075
5	12,727	10,155	0.01	0.07
6	13,972	11,152	0.01	0.067

Once each simulation was conducted, all the hydrodynamic coefficients were plotted in Microsoft Excel to observe whether or not convergence occurred. Results from Figure 4-1, Figure 4-2, and Figure 4-3 show that there was a very small difference in hydrodynamic coefficients among the range of mesh sizes. Since the results are independent of mesh size, the medium sized mesh, Mesh 3, was used. This was also chosen while considering the computational expense.

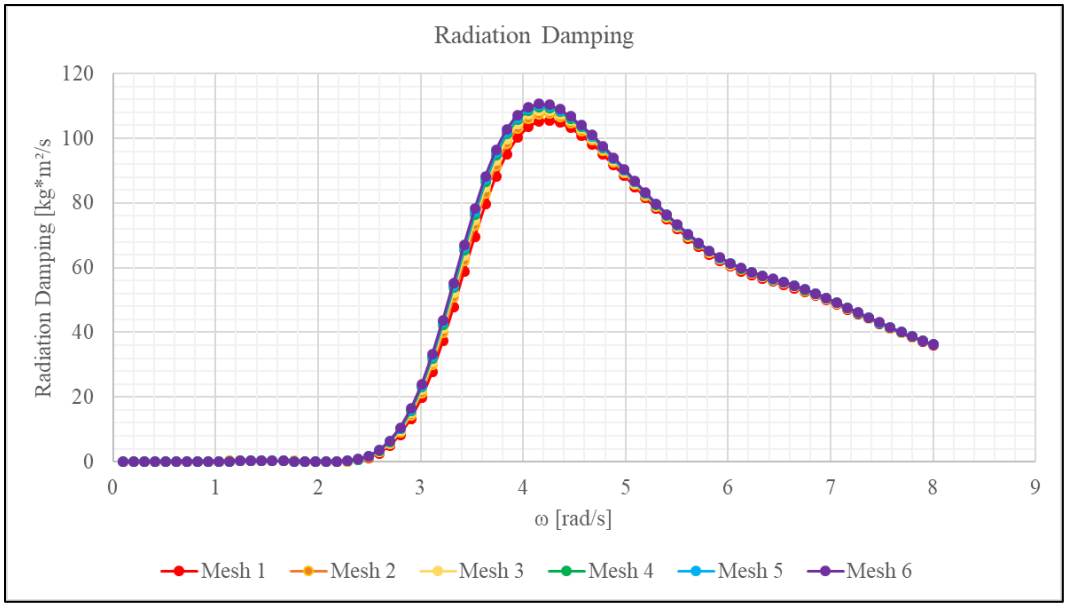

Figure 4-1. Radiation Damping Term in Mesh Sensitivity Analysis

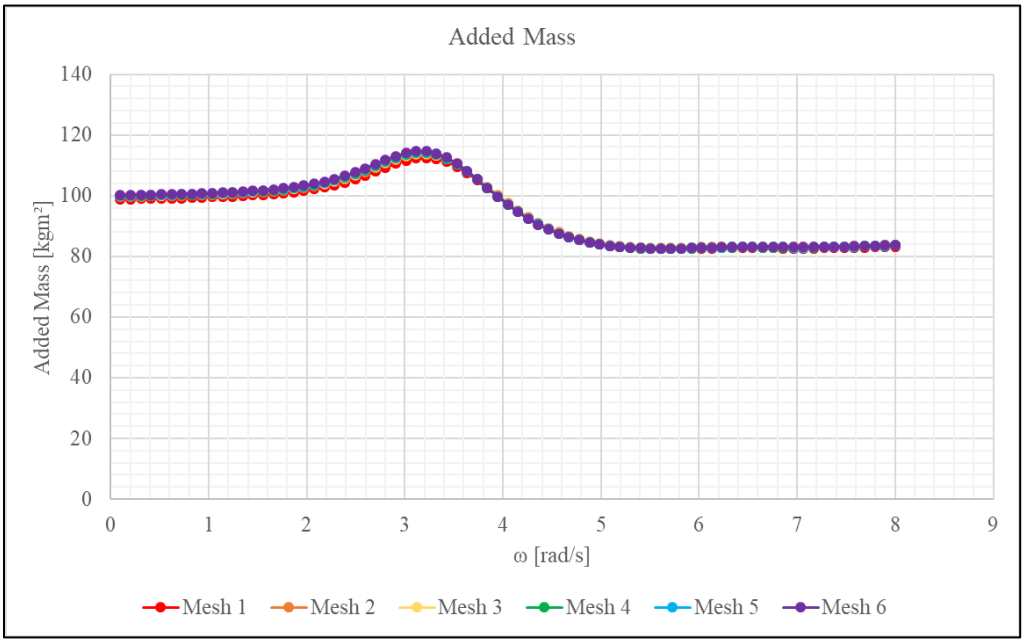

Figure 4-2. Added Mass Term in Mesh Sensitivity Analysis

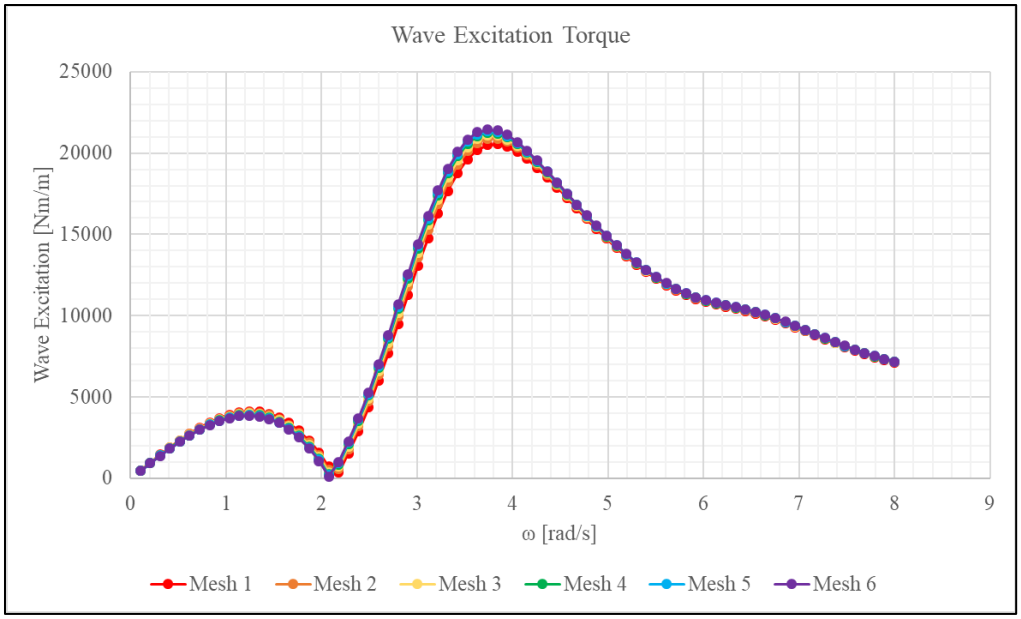

Figure 4-3. Wave Excitation Torque Term in Mesh Sensitivity Analysis

4.1.2 Hydrodynamic Validation

A hydrodynamic validation study was necessary to ensure that all boundary conditions, parameters, and conditions were set up properly in the BEM program. The hydrodynamic coefficients of the OWSC in its fully open configuration, including radiation damping, added mass, and wave excitation torque, were analyzed. The validation was accomplished by replicating the geometry found in the work of Tom et. al [3], where the authors used WAMIT as their BEM software. The authors of [3] provided the original CAD design as well as their output results from WAMIT, and so the OWSC geometry was exactly the same in Aqwa. Table 4-2 show the parameters that the authors used in [3], as compared to the values used in Aqwa, and Figure 4-4 shows the geometry of the OWSC. The reason the water depth was different for the Aqwa simulation is because the Aqwa solver would experience a fatal error in simulation if there an object too close to the sea floor. Furthermore, Aqwa requires that some portion of the object being studied pierces the surface of the water. To satisfy this, the OWSC pierced the water surface by 0.03 meters. The difference in maximum wave frequency is because the mesh size and maximum wave frequency are linked in Aqwa. Therefore, the mesh size that was selected in Aqwa only allowed for a maximum wave frequency of 5.545 rad/s.

Table 4-2. Hydrodynamic Validation Setup

Parameter	**WAMIT** [3]	Aqwa
OWSC Density, [kg/m^3]	"Half of seawater"	512.5
Water Depth, [m]	10	10.1
Surface Piercing Amount [m]	0	0.03
Maximum Wave Frequency [rad/s]	7.5	5.545

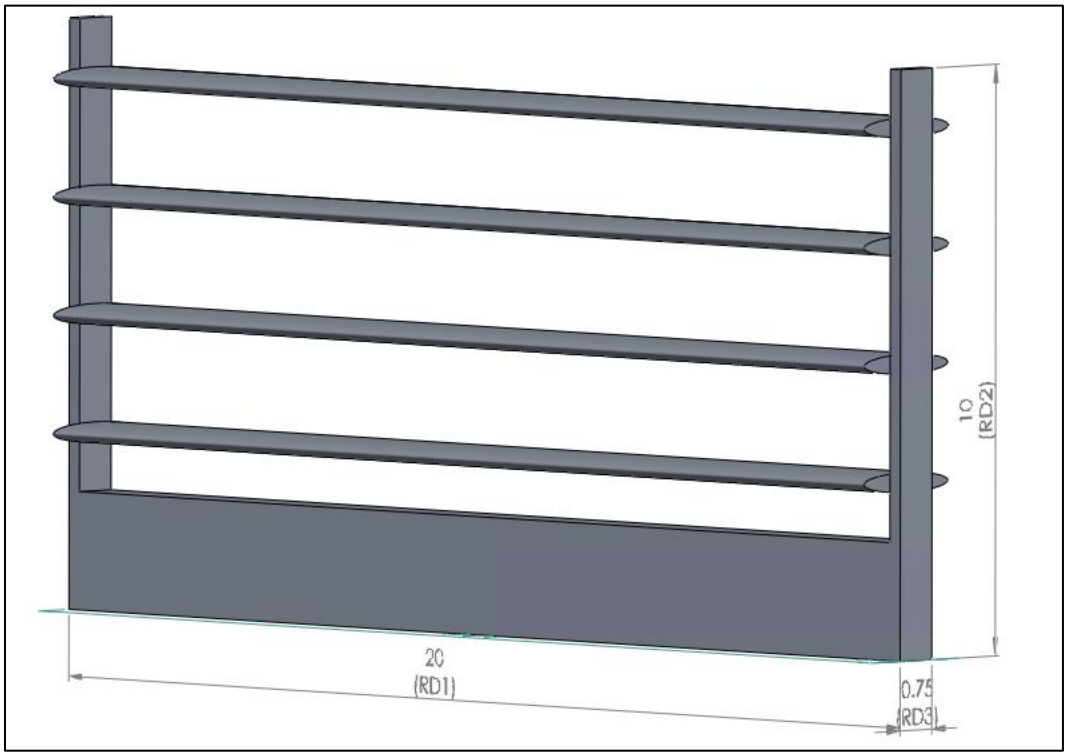

Figure 4-4. OWSC Geometry used for Hydrodynamic Validation Study (Image used with Permission from the Author [3])

Since WAMIT and Aqwa are two independent BEM programs, the results from WAMIT could not be analyzed explicitly. In order to plot the results from the two programs, the BEM output files were analyzed in BEMIO. This code parsed the hydrodynamic coefficients from Aqwa and WAMIT and plotted the nondimensionalized hydrodynamic coefficients against each other. The results for the hydrodynamic validation study can be seen in Figure 4-5, Figure 4-6, and Figure

4-7. The results from Aqwa were slightly different than those obtained from [3]. The slight differences could be a result of the different values for water depth or surface piercing amount. Overall, the results agree well, and the simulation parameters used in the hydrodynamic validation study were used.

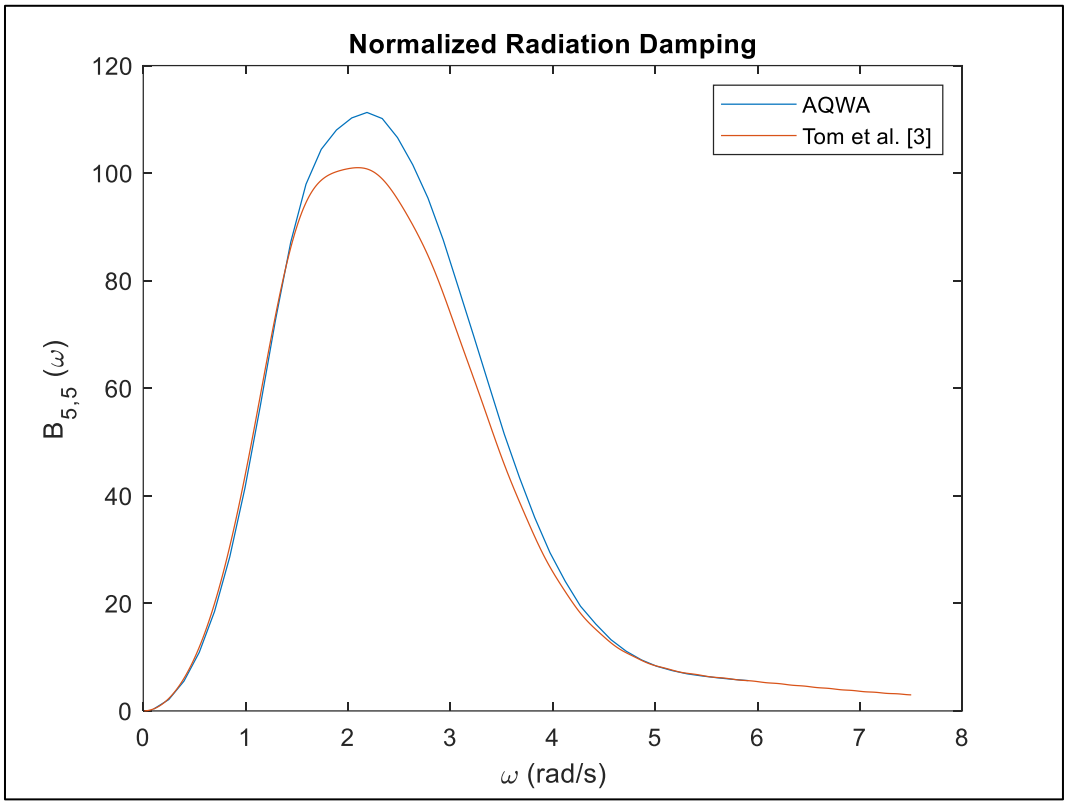

Figure 4-5. Comparison of Normalized Radiation Damping Results

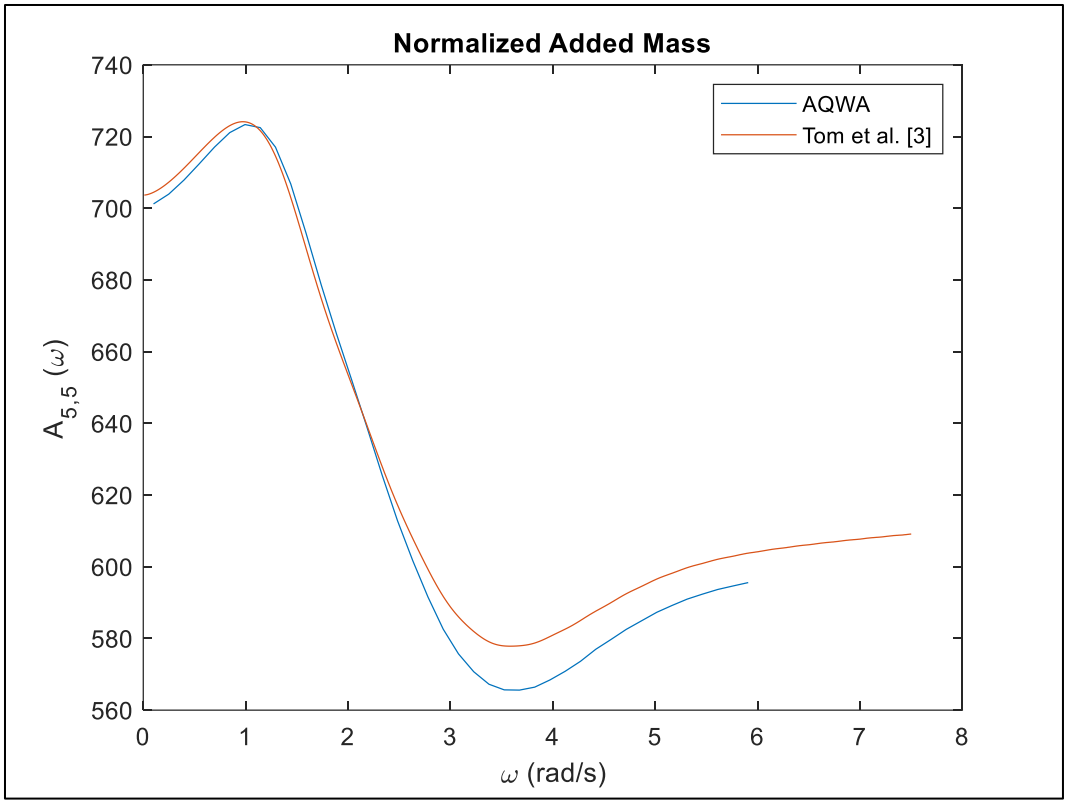

Figure 4-6. Comparison of Normalized Added Mass Results

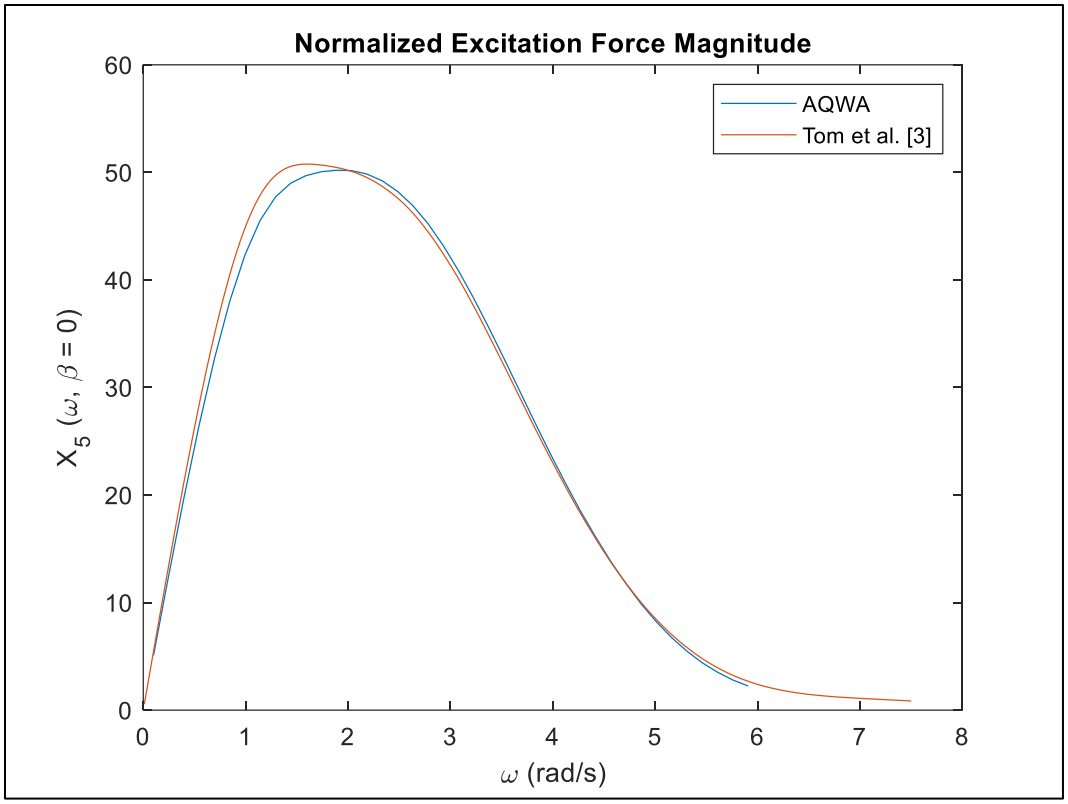

Figure 4-7. Comparison of Normalized Wave Excitation Results

4.1.3 Radiation Damping

For the 2- and 4- vane scenarios respectively, the average frequencies at which the maximum radiation damping values occurred are shown in Table 4-3 and Table 4-4. It appeared the 2-vane scenario experienced lower magnitudes of radiation damping than the 4-vane scenario for each respective configuration, which could result in its motion being less damped than the 4-vane scenario. The results from **Figure *4-8.* Pitch Radiation Damping Term for the 2- and 4- Vane Scenarios Calculated at the Hinge**Figure 4-8 indicated that the radiation damping term was sensitive to the number of vanes. The maximum radiation damping terms for the 2-vane scenario all occurred at relatively similar wave frequencies—3.9 rad/s ± 0.2 rad/s. The 4-vane scenario had maximum radiation damping magnitudes that occurred at a frequency range between 3.4 rad/s and 4.8 rad/s. For both scenarios in the closed configuration, wave frequencies below 1 rad/s and above 3.9 rad/s had magnitudes around zero and that tended towards zero respectively, indicating numerical stability. For the remaining configurations, wave frequencies below 2 rad/s and above 4 rad/s had damping values around zero and that tended towards zero respectively,

also indicating stability. These effects could be due to sub-resonant and over-resonant wave frequencies. Regarding the 4-vane scenario, the 60° and 45° configuration had similar magnitude, but were offset by about 0.37 rad/s. This could mean that the 15° change from 60° to 45° slightly influenced the natural frequency of the OWSC. However, this 15° change did not appear to influence the 4-vane configuration as much as it influenced on the 2-vane configuration. The largest difference in magnitude between the 2-vane and 4-vane scenario occurred when the vanes were positioned at 45°, where the difference in magnitude was 29,503 kgm^2/s. When the vanes were fully open, the largest difference in frequency at which maximum radiation damping occurred between the 2-vane and 4-vane scenario was 2.8 rad/s, or a wave period of approximately 2.24 seconds.

Table 4-3. Maximum Radiation Damping for 2-Vane OWSC

Configuration	Maximum Radiation Damping (kgm^2/s)	Respective Wave Frequency (rad/s)
90°	86,539	3.8
60°	87,045	3.7
45°	18,350	3.9
30°	8,432	4.0
0°	181	3.0

Table 4-4. Maximum Radiation Damping for 4-Vane OWSC

Configuration	Maximum Radiation Damping (kgm^2/s)	Respective Wave Frequency (rad/s)
90°	96,634	3.6
60°	47,987	3.7
45°	47,854	3.3
30°	18,558	3.2
0°	4,498	4.8

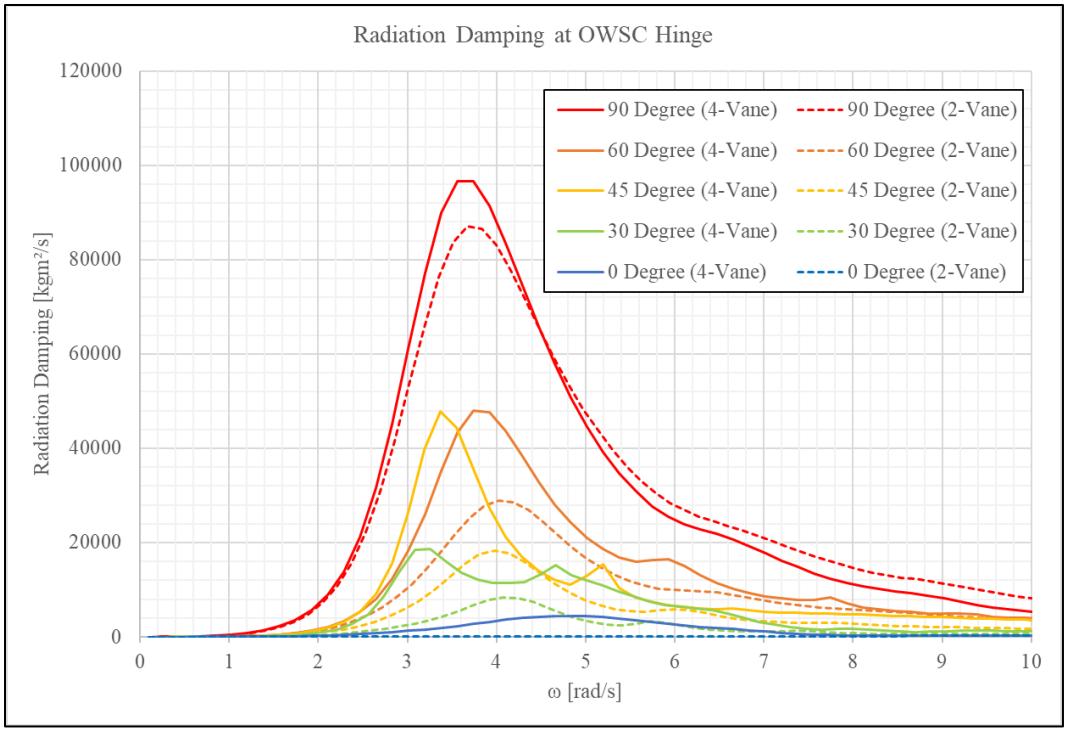

Figure 4-8. Pitch Radiation Damping Term for the 2- and 4- Vane Scenarios Calculated at the Hinge

4.1.4 Added Mass

Similar to the radiation damping results, the closed configuration experienced the largest added mass term, followed by the 60°, 45°, 30°, and open configuration. Regarding the greatest magnitude of added mass values, both scenarios experienced a wave frequency difference of 0.3 rad/s between the fully closed configuration and the other configurations. This indicated that the vane angle configuration had an effect on which wave frequency results in a larger added mass term. Considering the fully closed 2- and 4-vane scenarios respectively, the largest fluid inertia force that was added to the OWSC as it accelerated was 36,689 kg·m^2 and 38,476 kg·m^2. These values were close compared to the other maximum inertia forces for different angle configurations. For example, the 30° 4-vane scenario experienced a similar maximum added mass term to the 45° 2-vane scenario. As the wave frequency approached infinity, both scenarios tended towards the same horizontal asymptote for their respective configurations, indicating numerical stability. The 4-vane scenario experienced greater peak magnitudes that were sharper in curvature, while the 2-vane configuration experienced a smoother transition between its

maximum and minimum values for added mass. This indicates that the magnitude of added mass for the 4-vane scenario may be more sensitive to the wave frequency than the 2-vane scenario. Results for the pitch added mass terms for all configurations of the 2- and 4- vane scenarios can be seen in Figure 4-9.

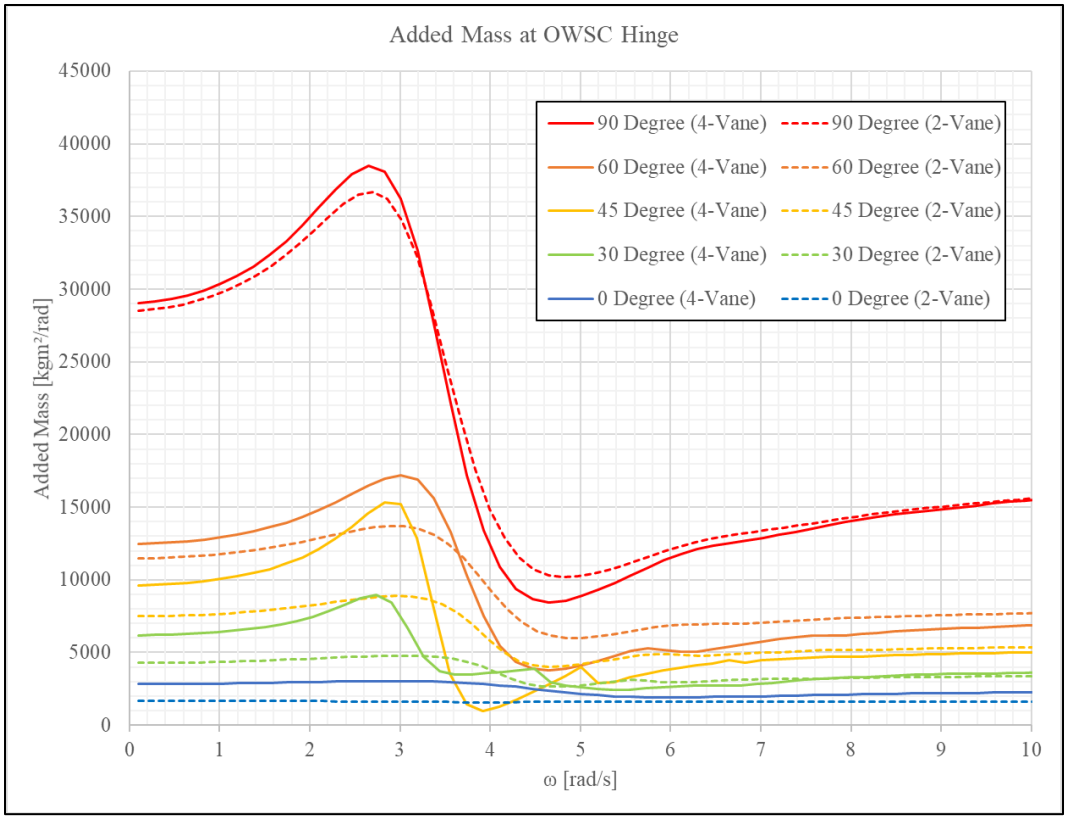

Figure 4-9. Pitch Added Mass Term for the 2- and 4- Vane Scenarios Calculated at the Hinge

4.1.5 Wave Excitation

Compared to the closed configuration, the values for wave excitation toque varied considerably among each scenario and vane angle orientation. At first glance, both scenarios seemed to experience similar results for the closed configuration with the exception to the 4-vane scenario having a greater magnitude. This could be due to the 4-vane scenario having a slightly larger surface area than the 2-vane scenario, resulting in the greater torque. It also appeared that mode shapes began to develop as the vanes progressed towards fully open. That is, each configuration appeared to have multiple wave frequencies at which there is a spike in the wave excitation torque.

Regarding the 2-vane scenario, the closed configuration appeared to have one predominant mode shape at 3.2 rad/s, the 60° configuration appeared to have two mode shapes, and the 45° and 30° configuration appeared to have three mode shapes. The open configuration appeared to only have one predominant mode shape that culminated at a frequency of 2.02 rad/s. Regarding the 4-vane scenario, the closed configuration appeared to have one predominant mode shape at 3.2 rad/s, the 60°, 45° and 30° configuration appeared to have three mode shapes, and the open configuration appeared to have only one predominant mode shape that culminated at a frequency of 4.15 rad/s. The results from the 4-vane 60° and 45° configuration may indicate that the 15° change in vane angle did not have a large effect on the maximum wave excitation torque magnitude. It did, however, appear to affect the wave frequency at which this maximum magnitude occurred. In this case, the difference in wave frequency was 0.37 rad/s. Comparing the results of both scenarios, it appeared that the 2-vane scenario was less sensitive to the change in wave frequency than the 4-vane. It should be noted that the wave excitation terms all approached zero as the wave frequency approached infinity, which indicates numerical stability as mentioned previously. Results for the pitch wave excitation terms for all configurations of the 2- and 4- vane scenarios can be seen in Figure 4-10.

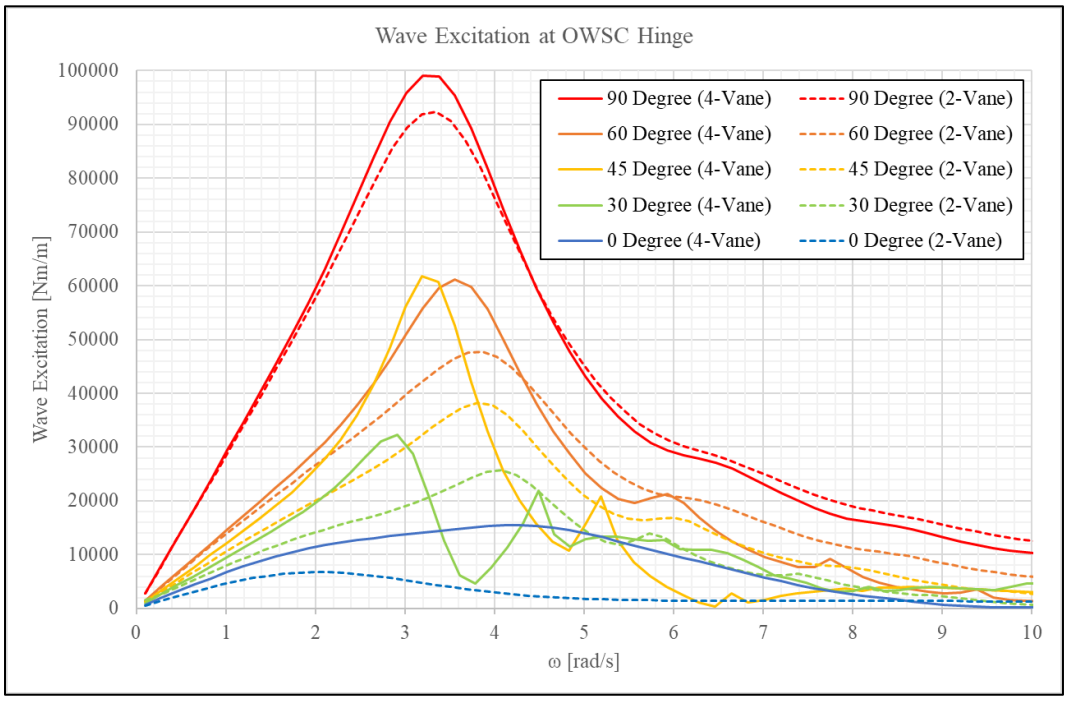

Figure 4-10. Pitch Wave Excitation Torque Term for the 2- and 4- Vane Scenarios Calculated at the Hinge

4.1.6 2x2 Array

Figure 4-11, Figure 4-12, and Figure 4-13 show the radiation damping, added mass, and wave excitation torque results respectively for the closed configuration. The radiation damping and added mass results appear to indicate that the inclusion and proximity of other OWSCs do not affect these specific hydrodynamic coefficients. However, Figure 4-13 shows that the back-left and back-right OWSCs, experienced a lower magnitude for wave excitation due to the position of the leading flaps. In all configurations, except for when the fully open configuration, the leading OWSCs appeared to experience a higher wave excitation torque than the OWSCs following them. Figure 4-14, Figure 4-15, and Figure 4-16show the results for the 60° configuration. Figure 4-17, Figure 4-18, and Figure 4-19 show the results for the 45° configuration, and Figure 4-20, Figure 4-21, and Figure 4-22 show the results for the 30° configuration. In each of these, the rear OWSCs appeared to experience a higher peak radiation damping and added mass value. As the vane angles approached 0°, the peaks grew in magnitude. Figure 4-23, Figure 4-24, and Figure 4-25 show the results for the fully open configuration, where all hydrodynamic coefficients appeared to be the same, regardless of proximity. As wave frequency increased, the radiation damping terms tended away from zero and the added mass terms did not approach a constant horizontal asymptote, which could indicate divergence. The wave excitation torque values were consistent, but the leading OWSCs seemed to show signs of instability as they approached a frequency of 9 rad/s.

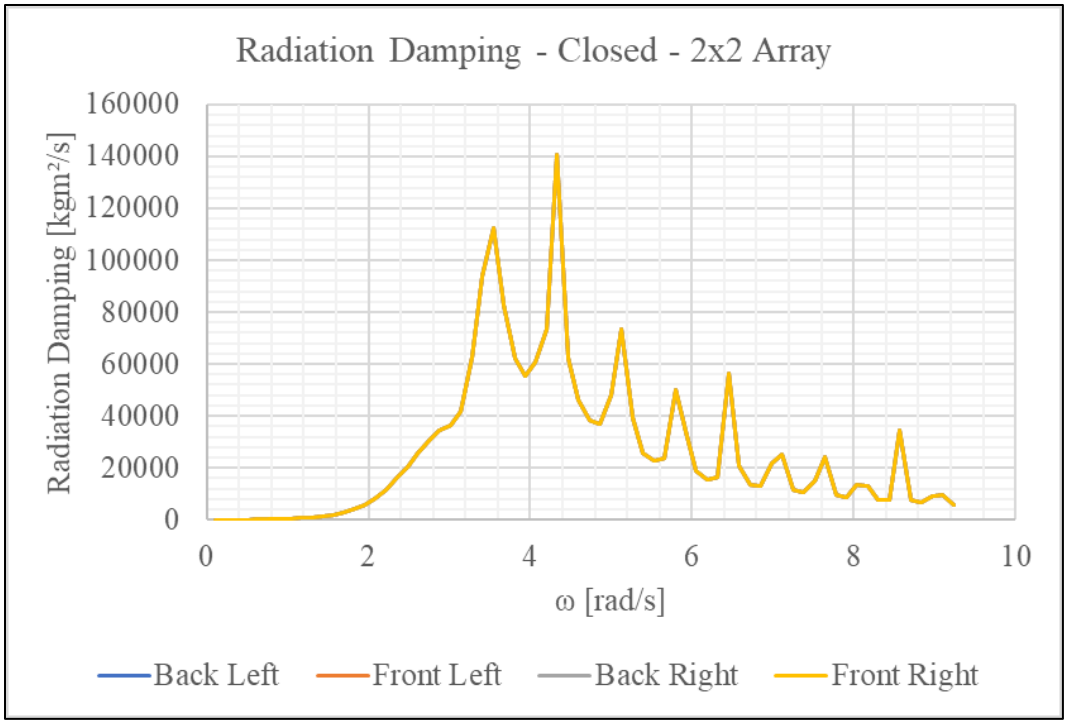

Figure 4-11. 2x2 Array - Radiation Damping Calculated at the Hinge for the Closed Configuration

Figure 4-12. 2x2 Array - Added Mass Calculated at the Hinge for the Closed Configuration

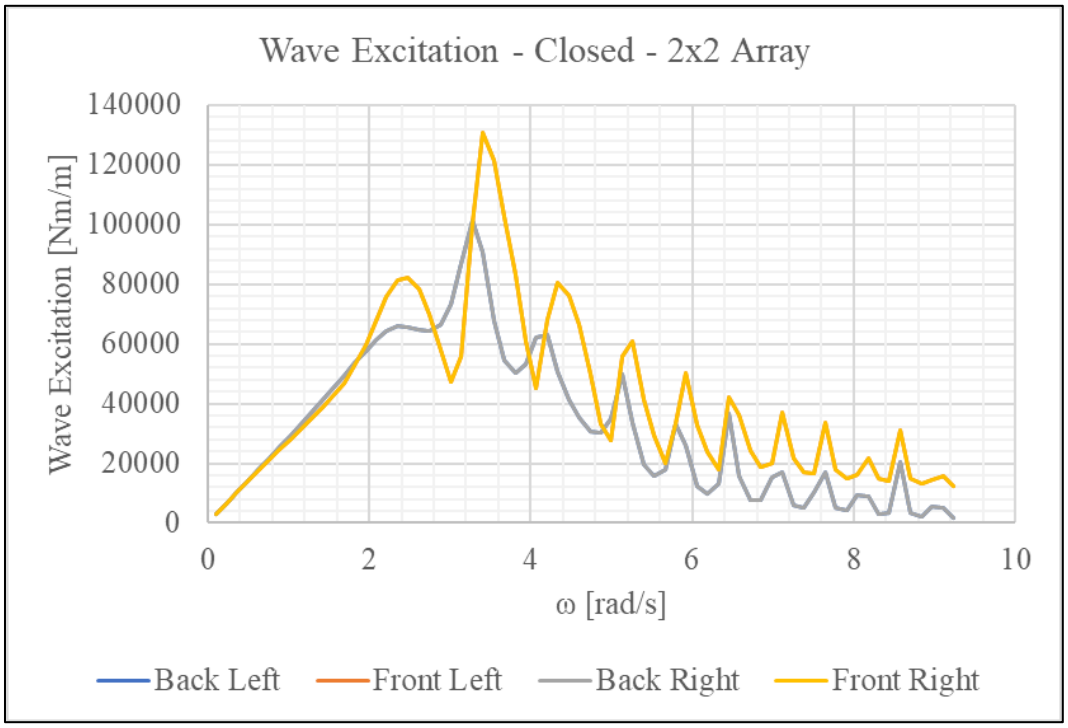

Figure 4-13. 2x2 Array - Wave Excitation Calculated at the Hinge for the Closed Configuration

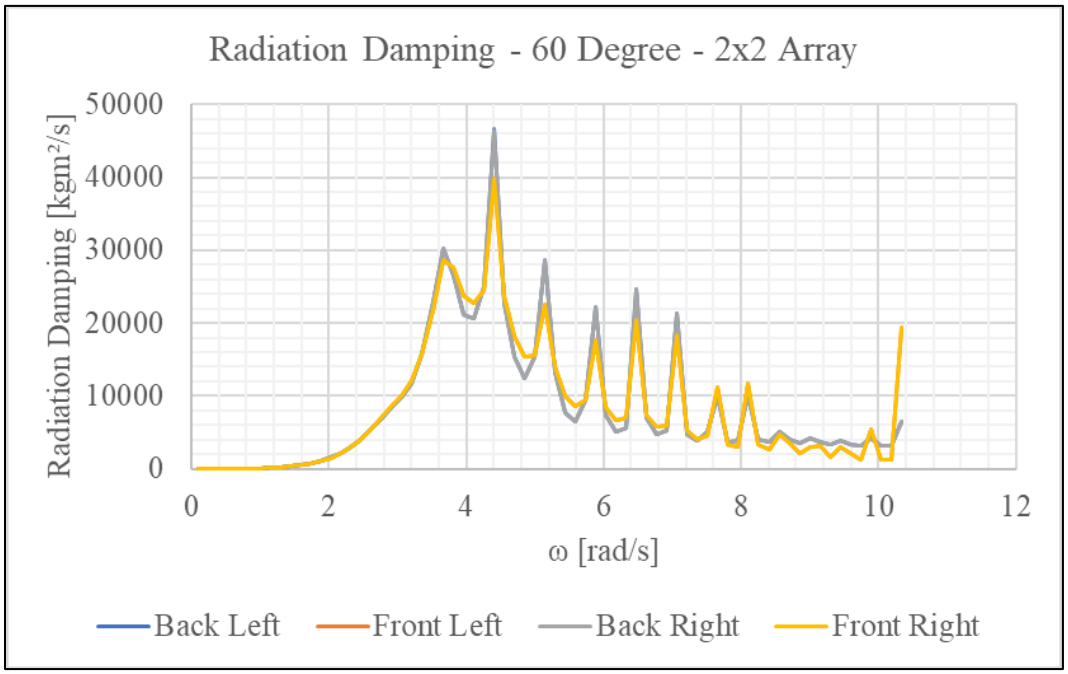

Figure 4-14. 2x2 Array - Radiation Damping Calculated at the Hinge for the 60 Degree Configuration

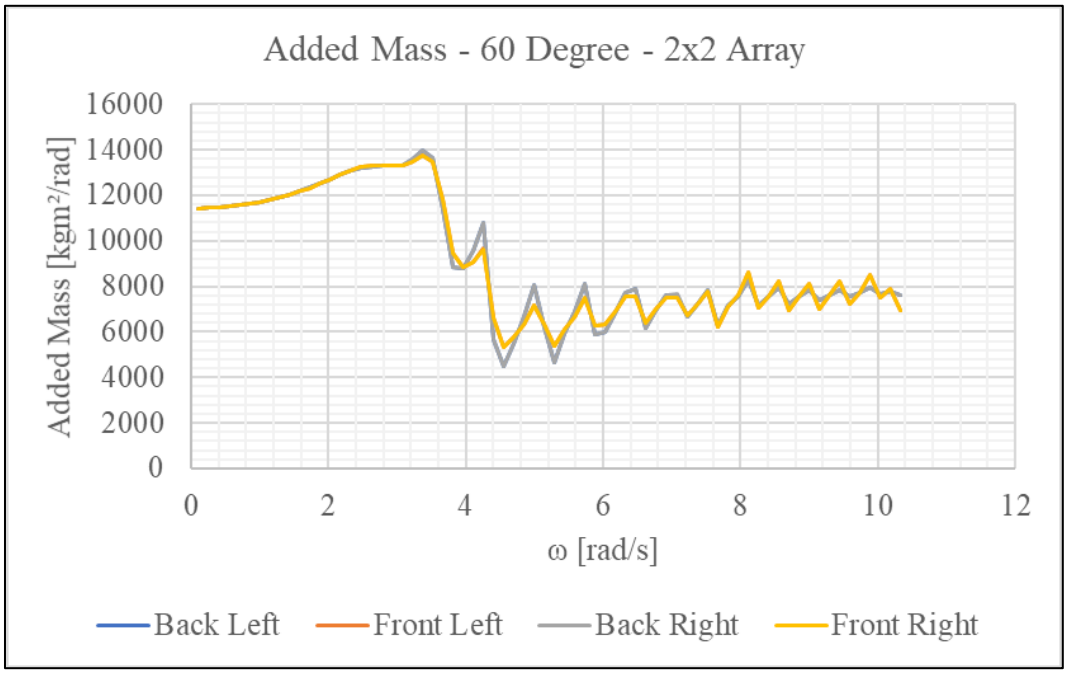

Figure 4-15. 2x2 Array - Added Mass Calculated at the Hinge for the 60 Degree Configuration

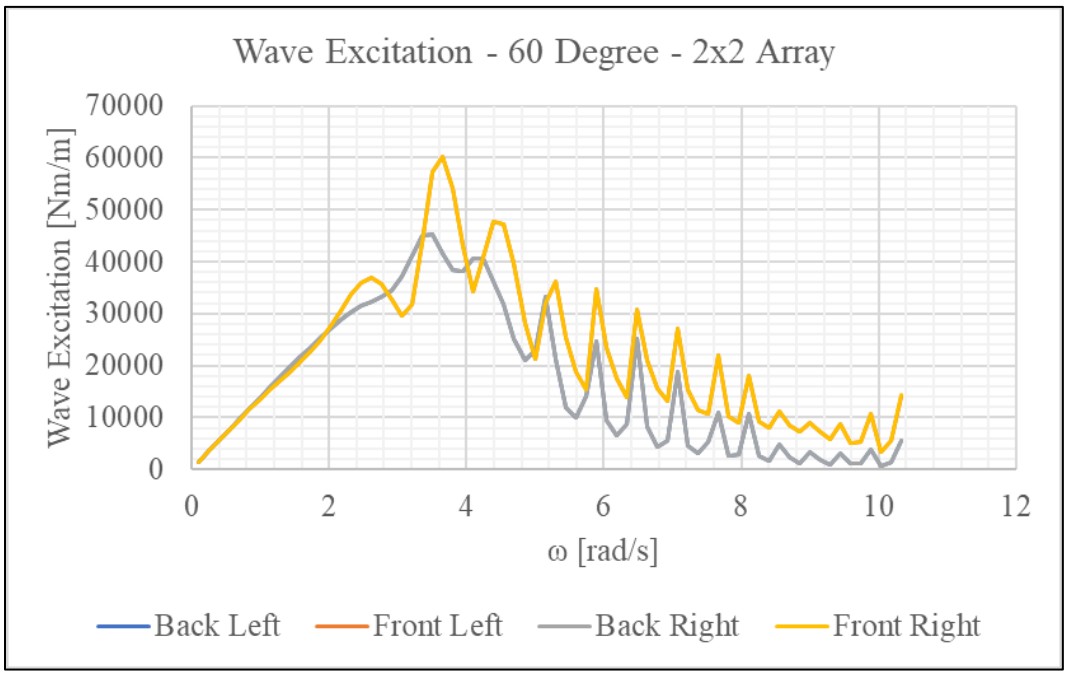

Figure 4-16. 2x2 Array - Wave Excitation Calculated at the Hinge for the 60 Degree Configuration

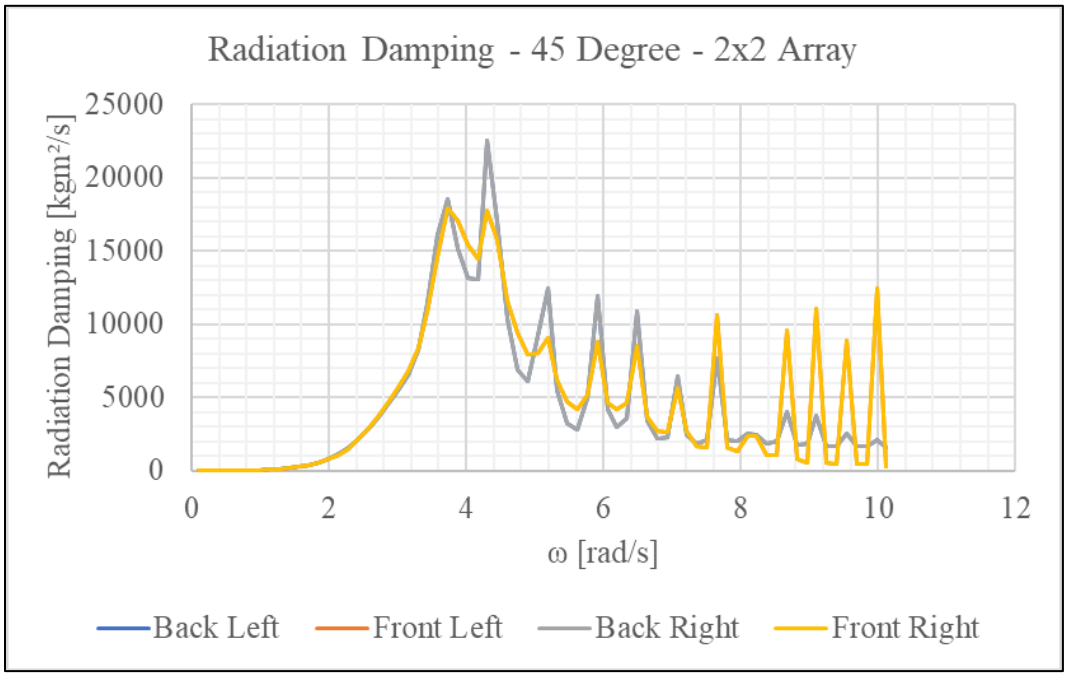

Figure 4-17. 2x2 Array - Radiation Damping Calculated at the Hinge for the 45 Degree Configuration

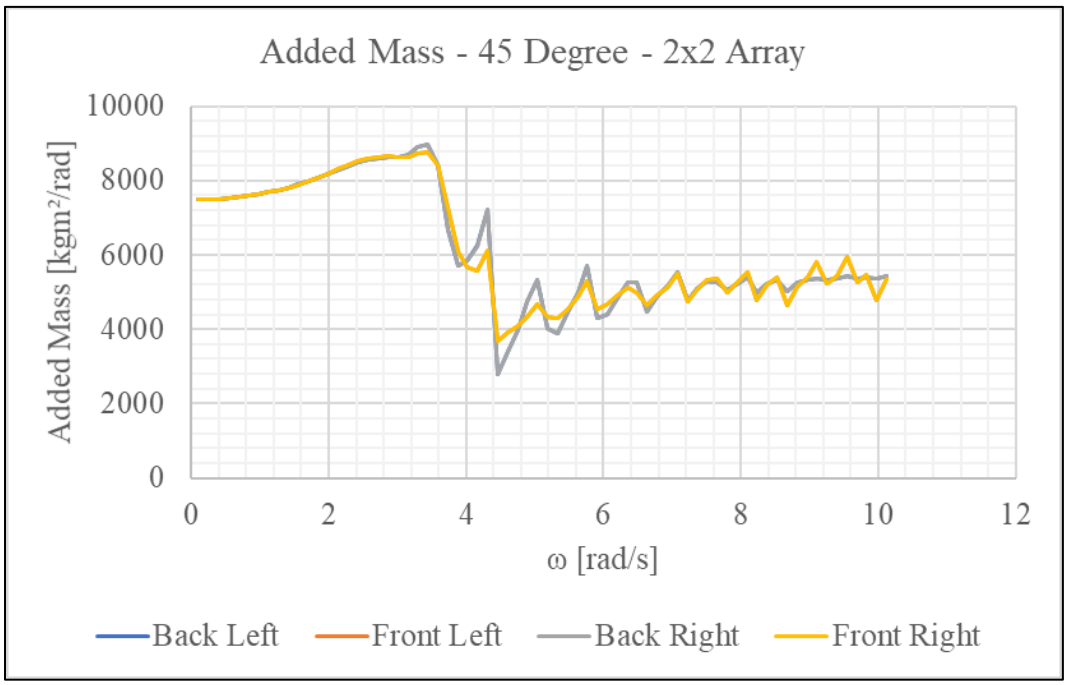

Figure 4-18. 2x2 Array - Added Mass Calculated at the Hinge for the 45 Degree Configuration

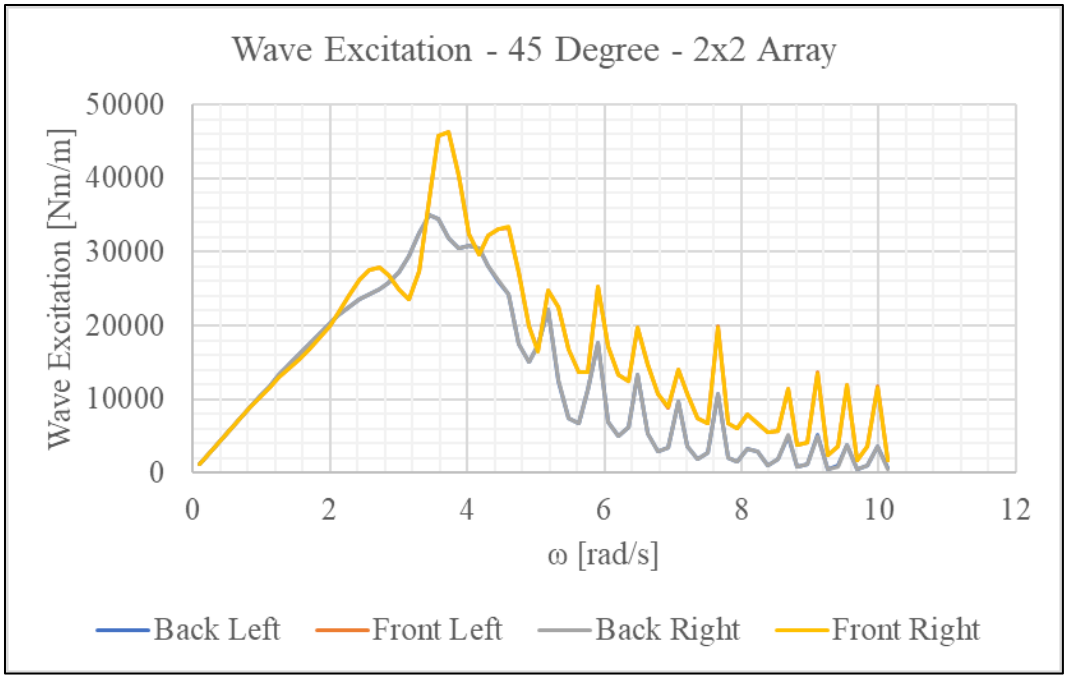

Figure 4-19. 2x2 Array - Wave Excitation Calculated at the Hinge for the 45 Degree Configuration

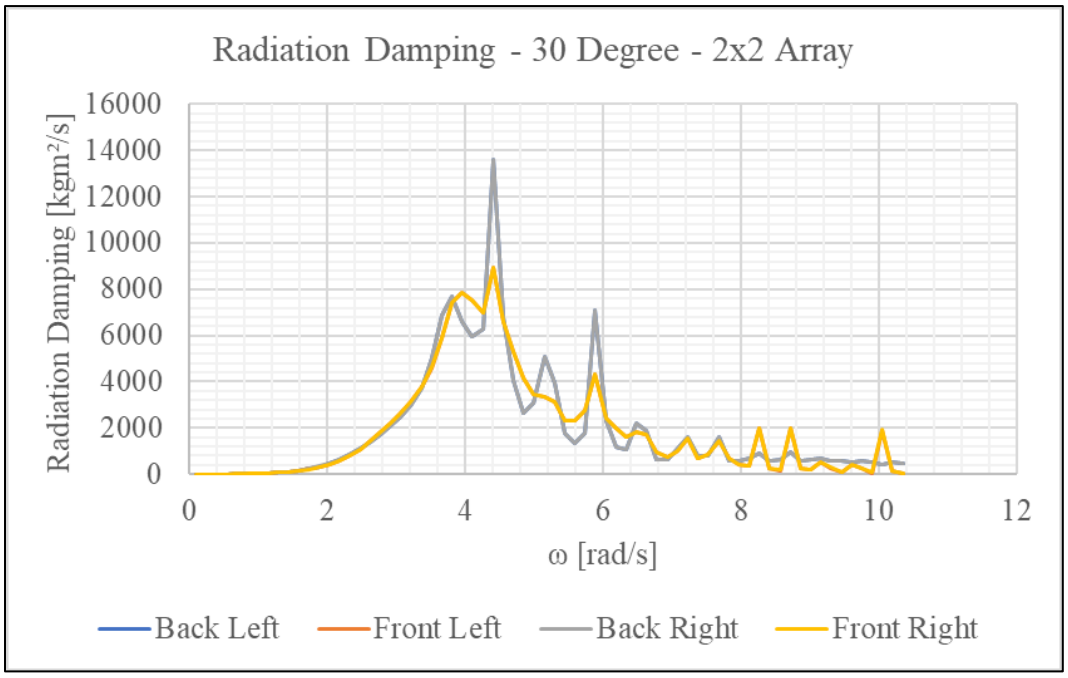

Figure 4-20. 2x2 Array - Radiation Damping Calculated at the Hinge for the 30 Degree Configuration

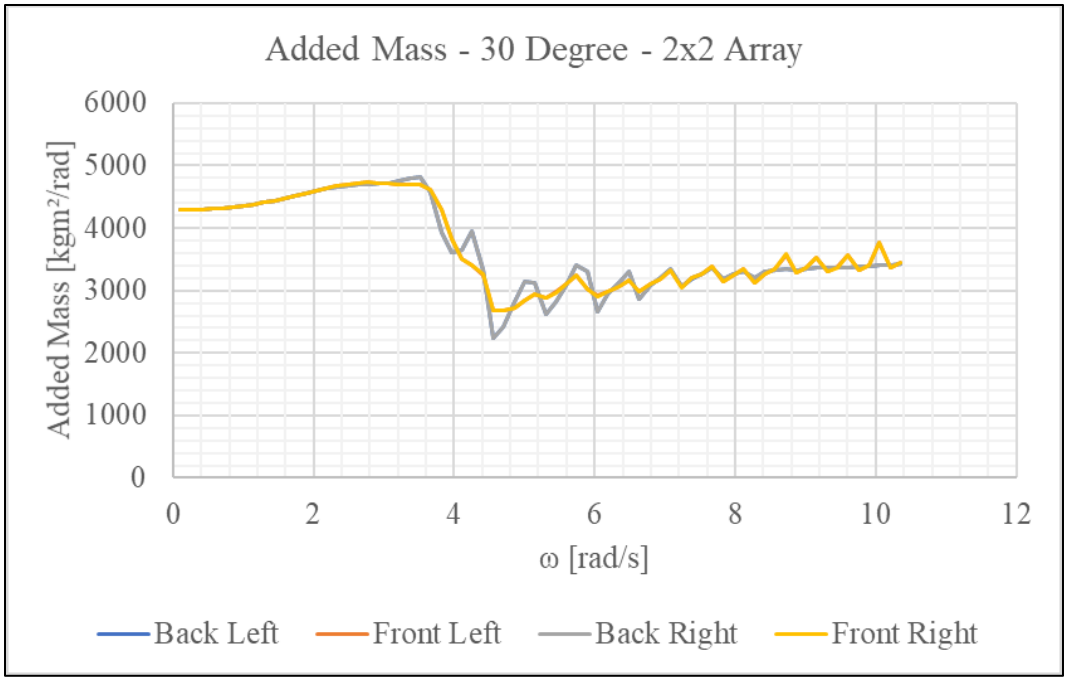

Figure 4-21. 2x2 Array - Added Mass Calculated at the Hinge for the 30 Degree Configuration

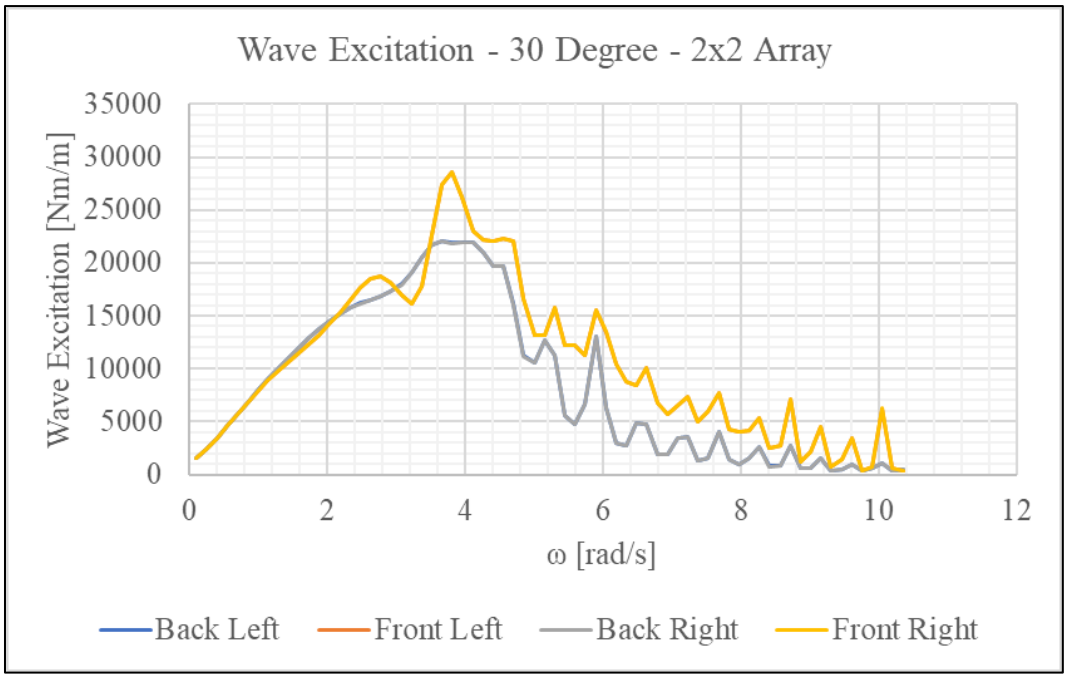

Figure 4-22. 2x2 Array - Wave Excitation Calculated at the Hinge for the 30 Degree Configuration

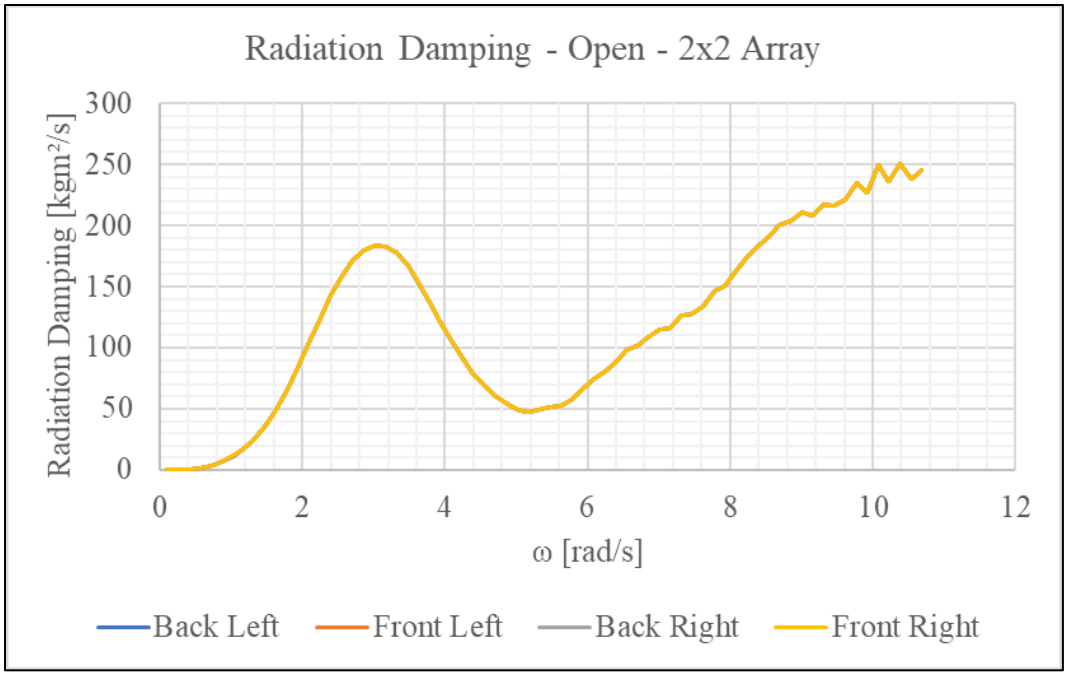

Figure 4-23. 2x2 Array - Radiation Damping Calculated at the Hinge for the Open Configuration

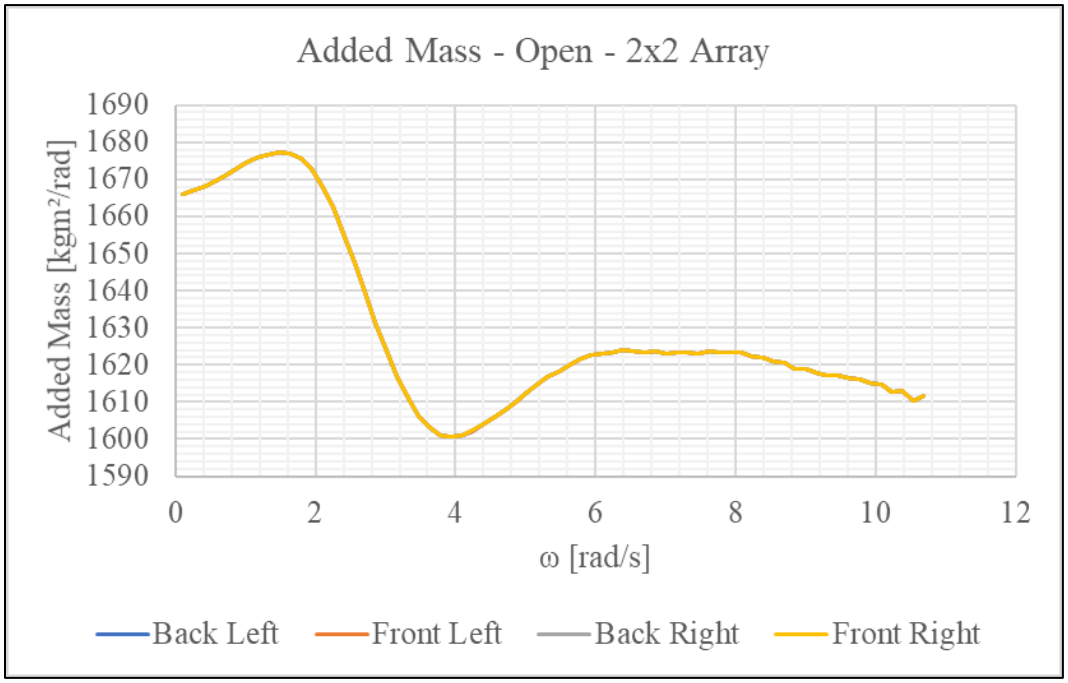

Figure 4-24. 2x2 Array - Added Mass Calculated at the Hinge for the Open Configuration

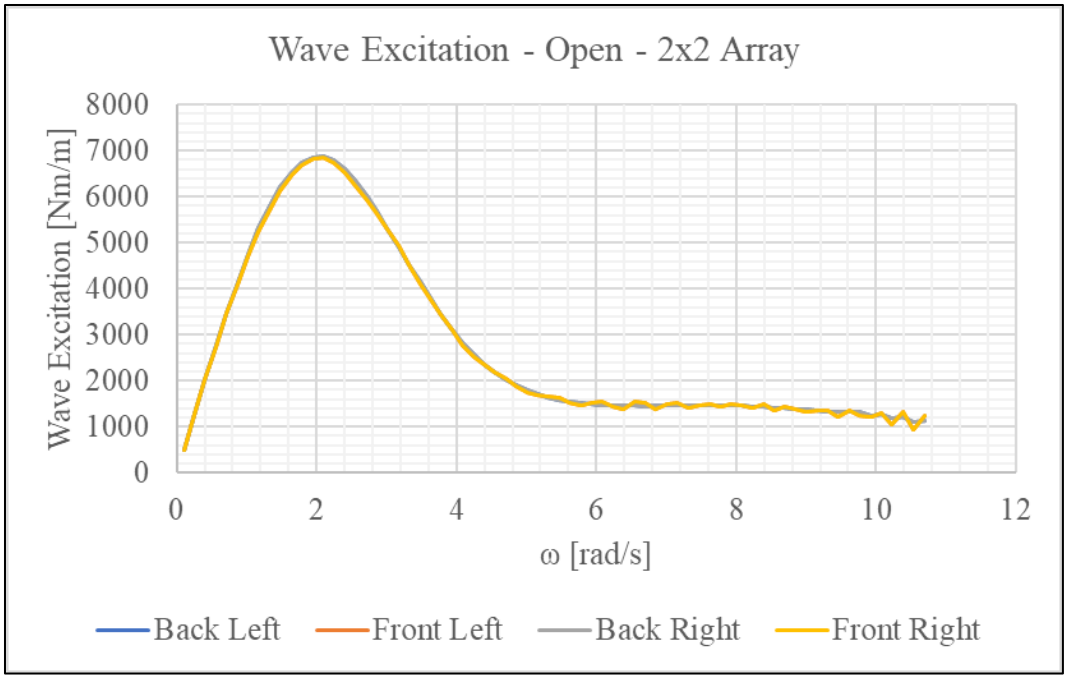

Figure 4-25. 2x2 Array - Wave Excitation Calculated at the Hinge for the Open Configuration

4.1.7 3x3 Array

Figure 4-26, Figure 4-27, and Figure 4-28 show the radiation damping, added mass, and wave excitation torque results respectively for the closed configuration. The radiation damping results appear to indicate that the middle-middle and middle-right devices experienced the greatest magnitude for radiation damping. Almost all the results appeared to have 5 distinct mode shapes at 3.5 rad/s, 4.4 rad/s, 5.2 rad/s, 5.9 rad/s, and 6.2 rad/s. The added mass results show some negative added mass values, which could be due to the shallowly-submerged structure having some elements that enclose a portion of the free-surface, as was the case in [101]. The wave excitation results each experience a maximum magnitude in the 3.4 rad/s to 3.8 rad/s range. Here, the middle-middle and front-middle OWSCs experienced the greatest wave excitation. This could be due to the OWSCs being exposed to radiated and diffracted waves on the front and rear sides of the OWSC.

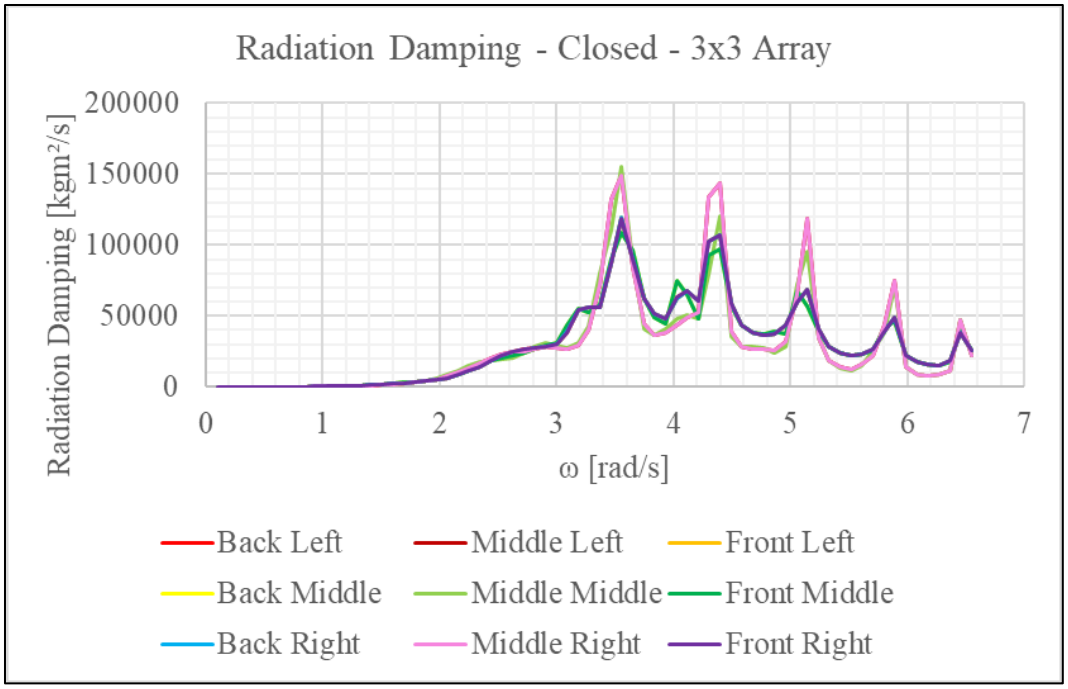

Figure 4-26. 3x3 Array - Radiation Damping Calculated at the Hinge for the Closed Configuration

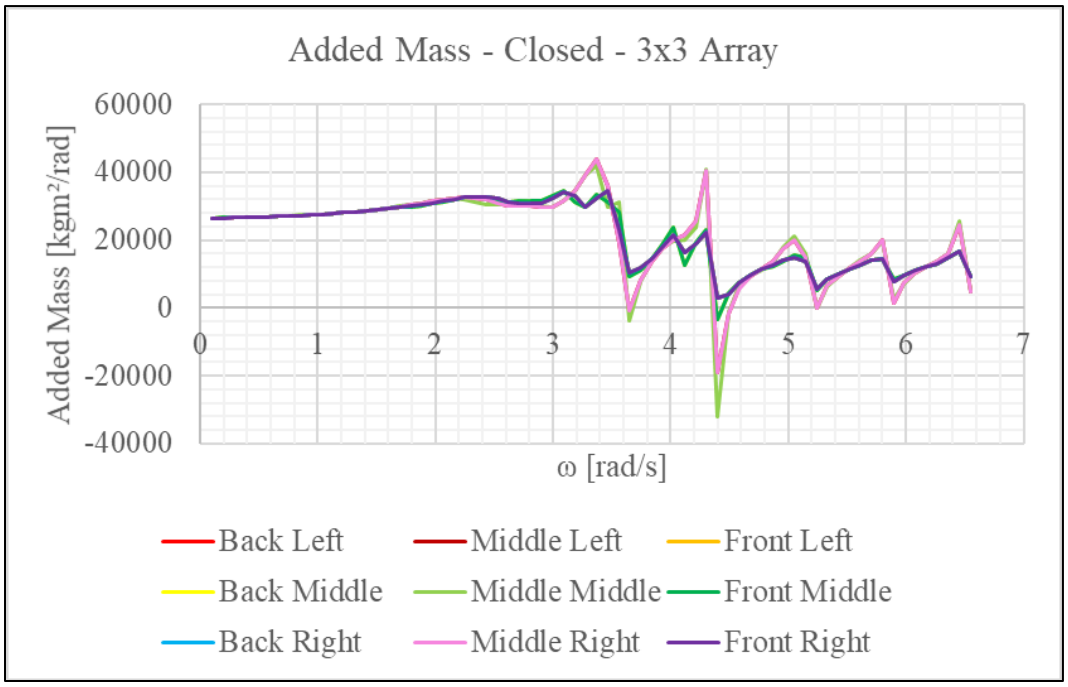

Figure 4-27. 3x3 Array – Added Mass Calculated at the Hinge for the Closed Configuration

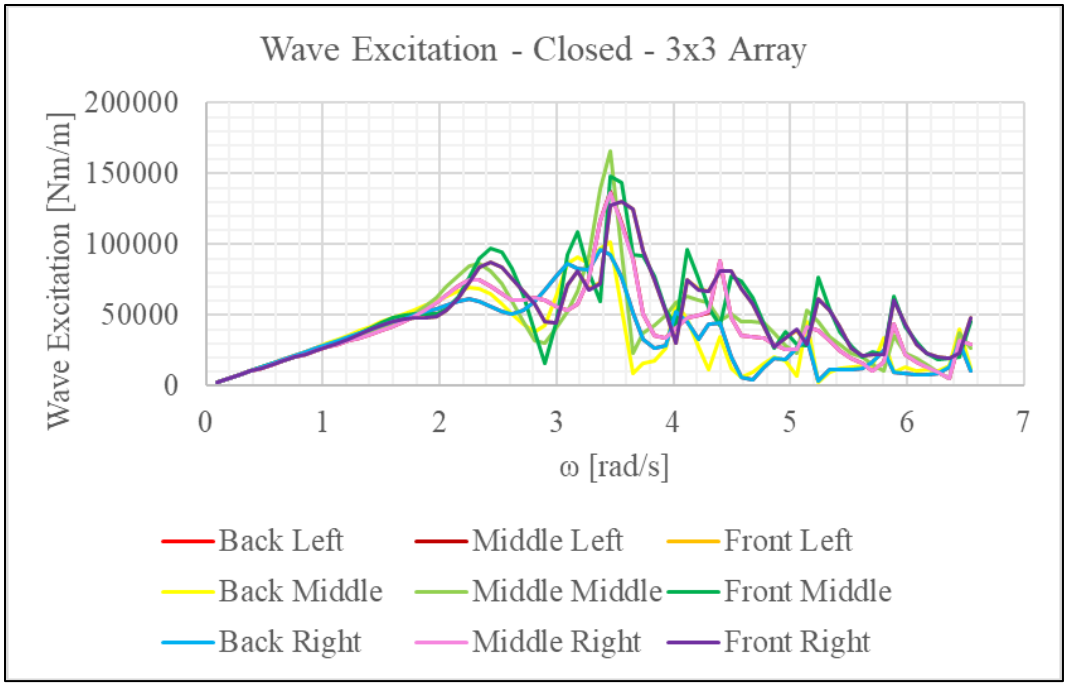

Figure 4-28. 3x3 Array – Wave Excitation Calculated at the Hinge for the Closed Configuration

The hydrodynamic coefficients results for the 60° configuration can be seen in Figure 4-29, Figure 4-30, and Figure 4-31. The results for the 45° configuration can be seen in Figure 4-32, Figure 4-33, and Figure 4-34. The result for the 30° configuration can be seen in Figure 4-35, Figure 4-36, and Figure 4-37. For the 60° configuration, there were 7 distinct peaks in the radiation damping results, and the maximum magnitudes occurred at 7.7 rad/s, followed by 4.4 rad/s and 5.2 rad/s. For the 45° configuration, there were 8 distinct peaks for radiation damping, having magnitudes at 4.3 rad/s, followed by 5.9 rad/s, and finally 3.8 rad/s. For the 30° configuration, there were 7 distinct peaks having magnitudes at 4.5 rad/s, followed by 3.8 rad/s and then 5.3 rad/s. For each of these 3 configurations, the middle-left, middle-middle, and middle-right OWSCs appeared to experience the largest magnitudes, indicating that the middle row of OWSCs could have experienced the most damping overall. None of the added mass terms were negative for the 60°, 45°, or 30° configuration, however each of the OWSCs in the middle row experienced a sharp peak at their troughs at 4.5 rad/s. For the 60°, 45°, and 30° configuration respectively, the middle-middle OWSC experienced the largest magnitude for added mass of 17,718 kgm^2/rad, 11,273 kgm^2/rad, 4,841 kgm^2/rad. A large difference is apparent in the 15° angle change from 45° to 30° configuration for added mass. This indicated that the fluid inertial

force that is added to the middle-middle OWSC could be sensitive to this 15° change. The wave excitation results for the 60°, 45°, and 30° configurations indicate that the largest magnitudes occur for the OWSCs in the front row, followed by the middle row, and finally the back row. There appeared to be multiple peaks at various frequencies, but the highest peaks occurred in the 3.6 rad/s to 3.8 rad/s range. As expected, the magnitudes at which these peaks occurred dropped as the OWSCs approached a fully open position. Furthermore, there was a larger difference in magnitude between the 45° and 30° configuration of 21,763 Nm/m, compared to the difference in magnitude between the 60° and 45° configuration of 15,359 Nm/m. It should be noted that Aqwa's solver is limited to 12,000 diffracting mesh elements. Therefore, since the 2x2 arrangement had total diffracting 4 bodies, each body was limited to a maximum of 3,000 elements per body. A source of error could be due to a coarser mesh that resulted from an increased number of OWSC's being analyzed.

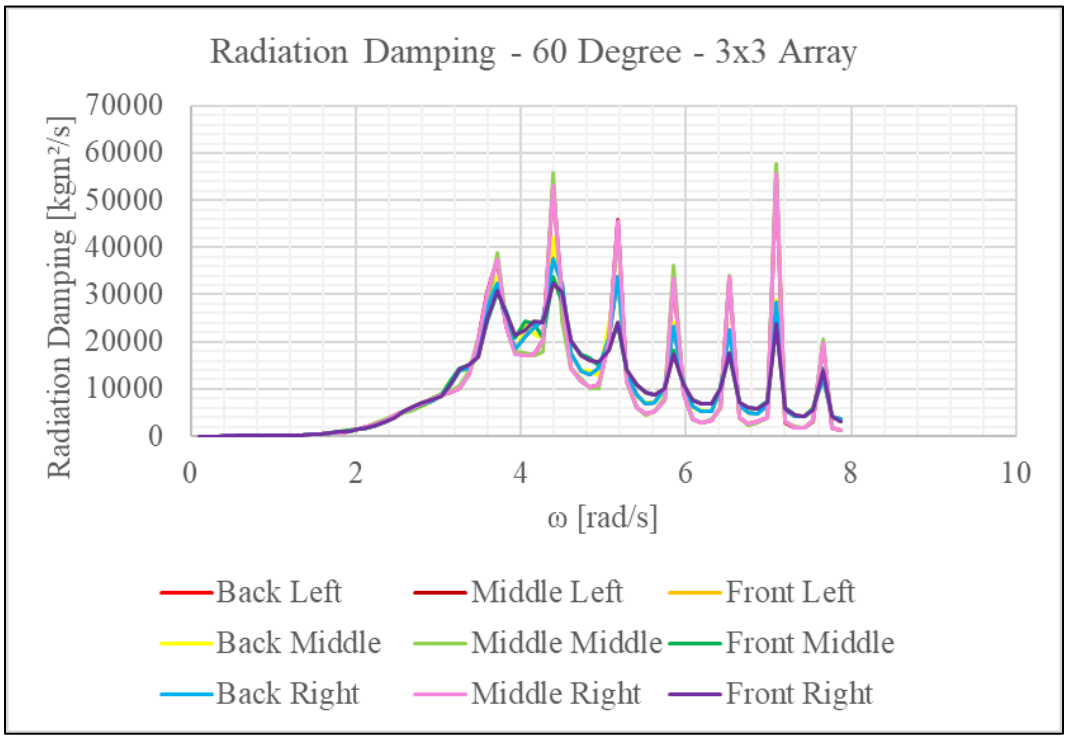

Figure 4-29. 3x3 Array - Radiation Damping Calculated at the Hinge for the 60° Configuration

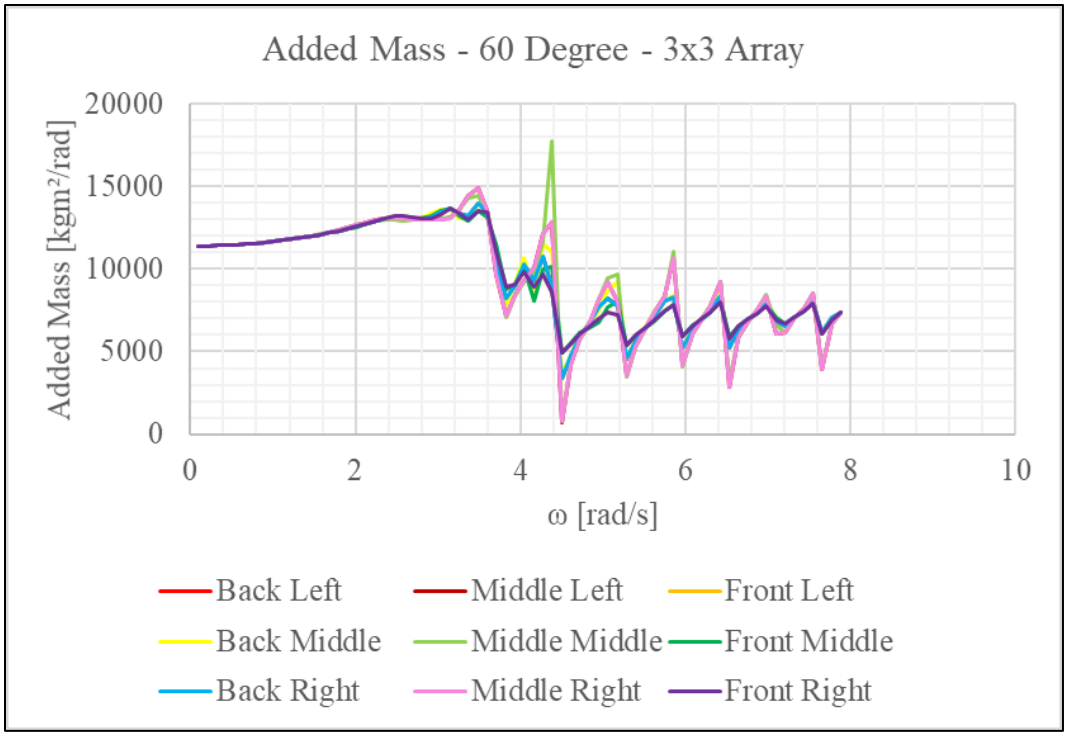

Figure 4-30. 3x3 Array – Added Mass Calculated at the Hinge for the 60° Configuration

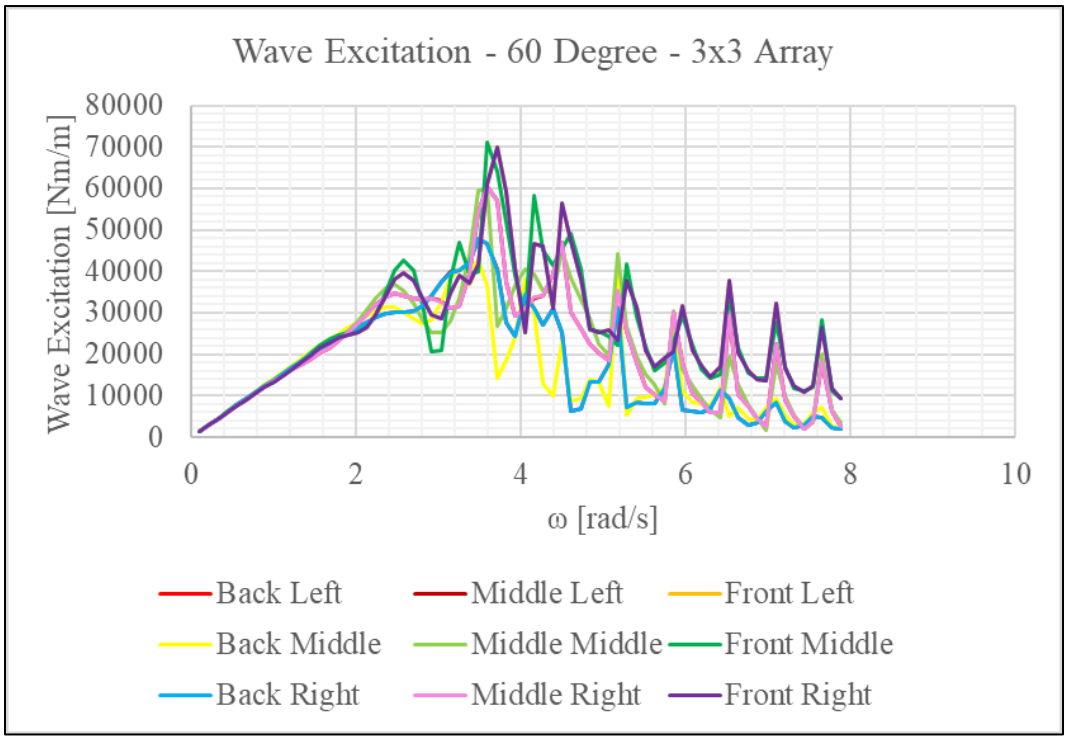

Figure 4-31. 3x3 Array – Wave Excitation Calculated at the Hinge for the 60° Configuration

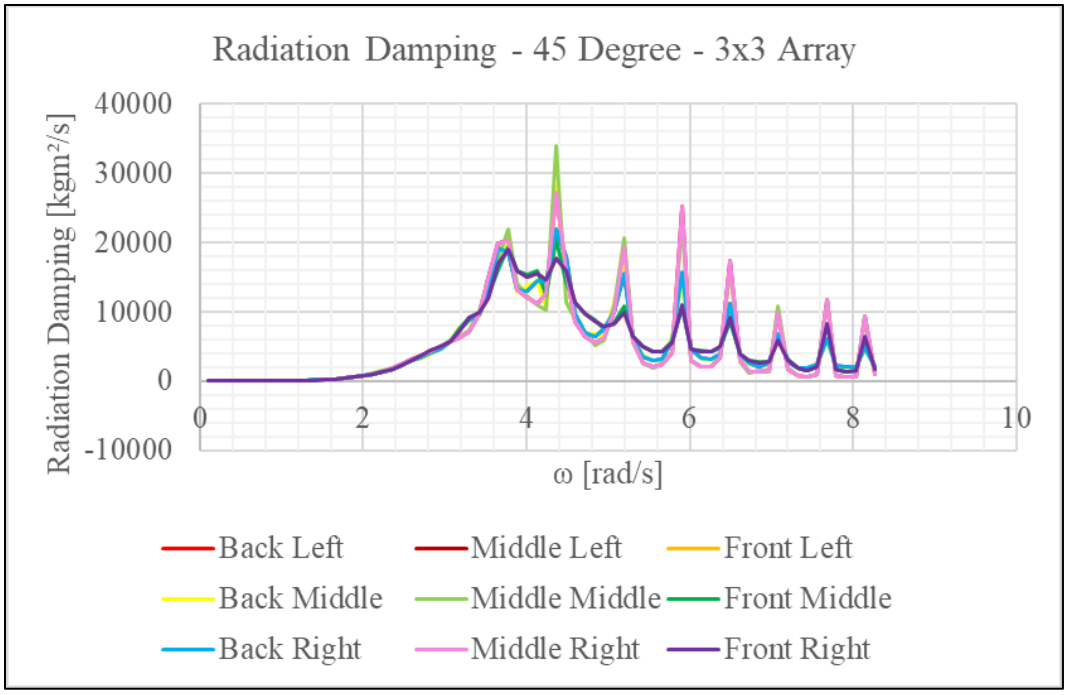

Figure 4-32. 3x3 Array - Radiation Damping Calculated at the Hinge for the 45° Configuration

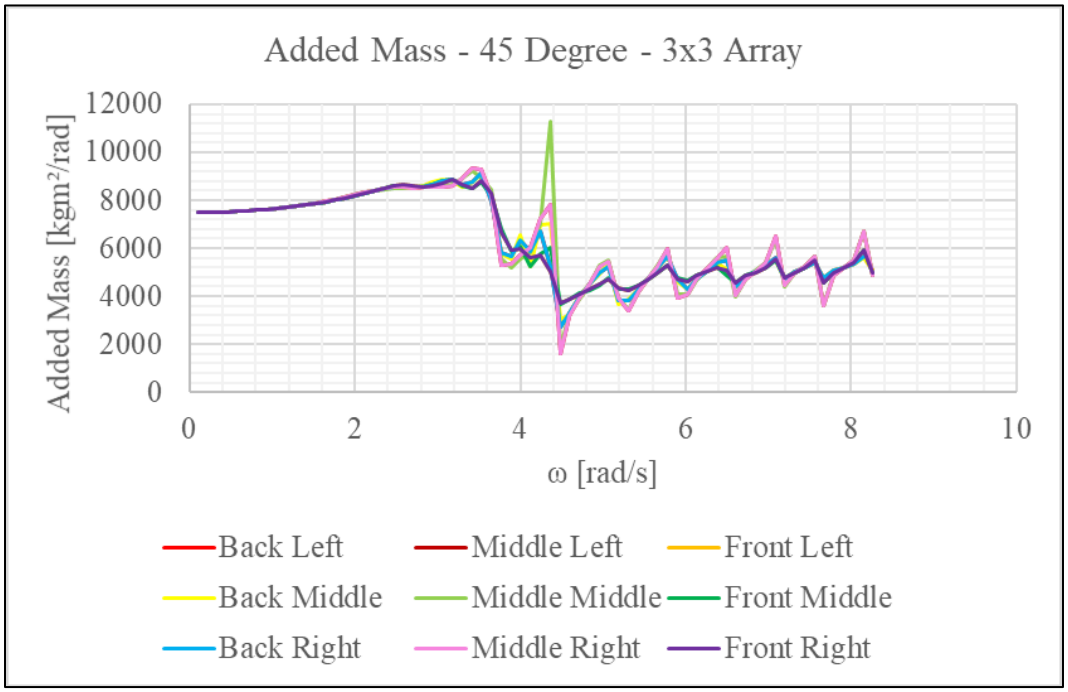

Figure 4-33. 3x3 Array – Added Mass Calculated at the Hinge for the 45° Configuration

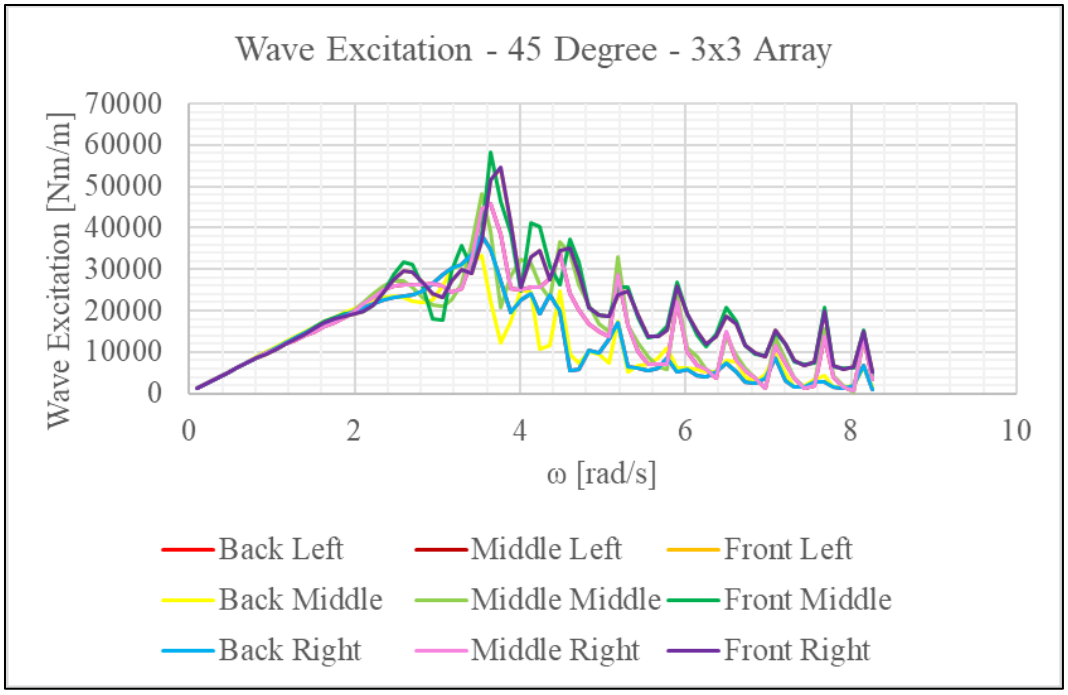

Figure 4-34. 3x3 Array – Wave Excitation Calculated at the Hinge for the 45° Configuration

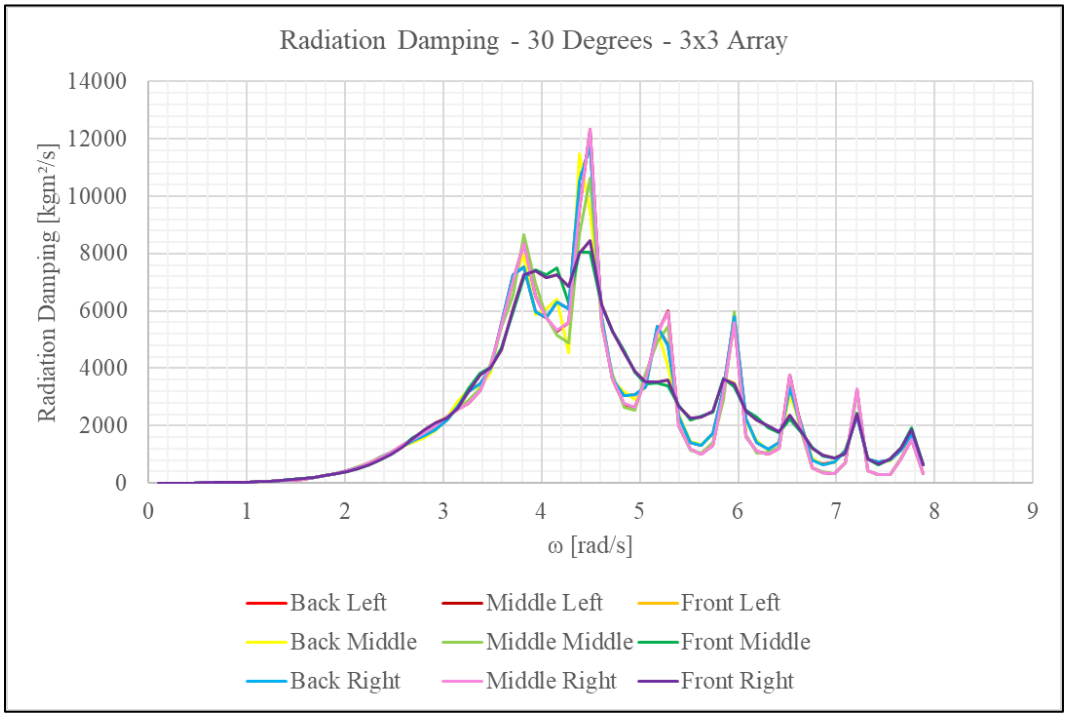

Figure 4-35. 3x3 Array - Radiation Damping Calculated at the Hinge for the 30° Configuration

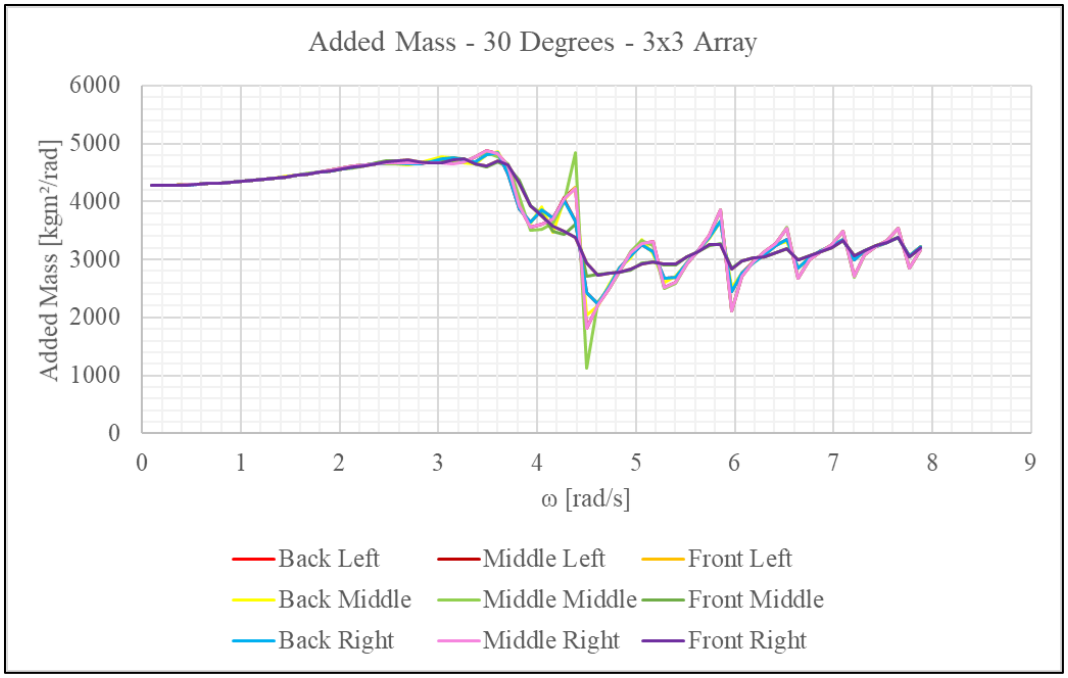

Figure 4-36. 3x3 Array – Added Mass Calculated at the Hinge for the 30° Configuration

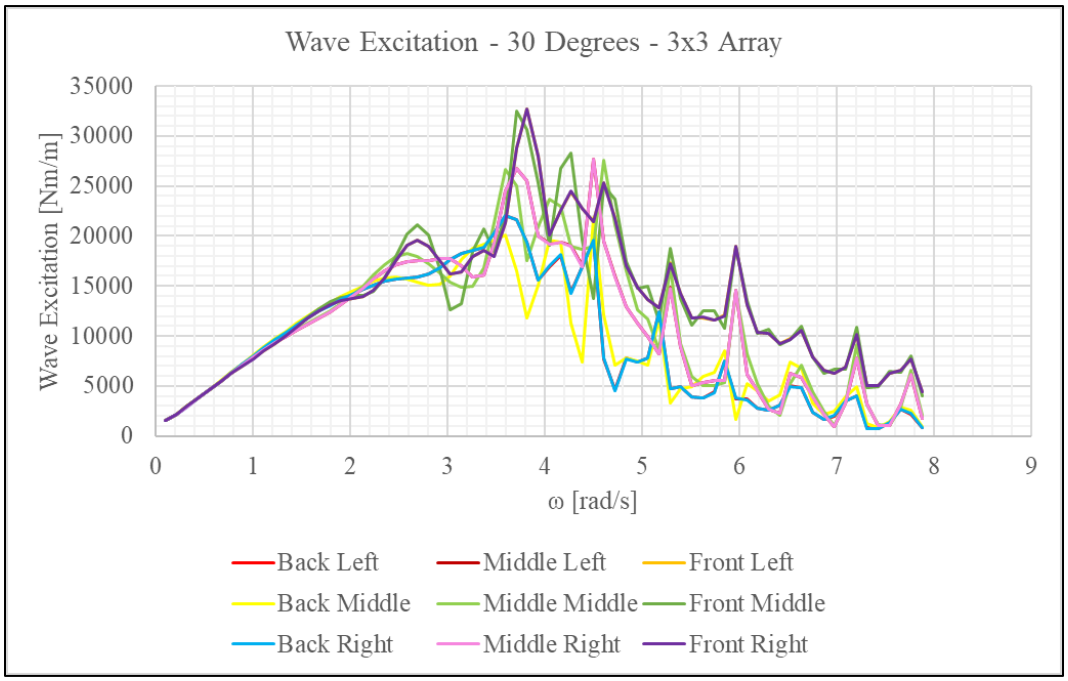

Figure 4-37. 3x3 Array – Wave Excitation Calculated at the Hinge for the 30° Configuration

Figure 4-38, Figure 4-39, and Figure 4-40 show the results for the fully open configuration, where all hydrodynamic coefficients were exactly the same for each OWSC, regardless of proximity. As wave frequency increased, the radiation damping terms tended away from zero and the added mass terms did not approach a constant horizontal asymptote. This indicates that the OWSCs may have experienced some instability at higher wave frequencies. The wave excitation torque values were consistent, but the leading OWSCs showed signs of instability as they approached a frequency of 9 rad/s.

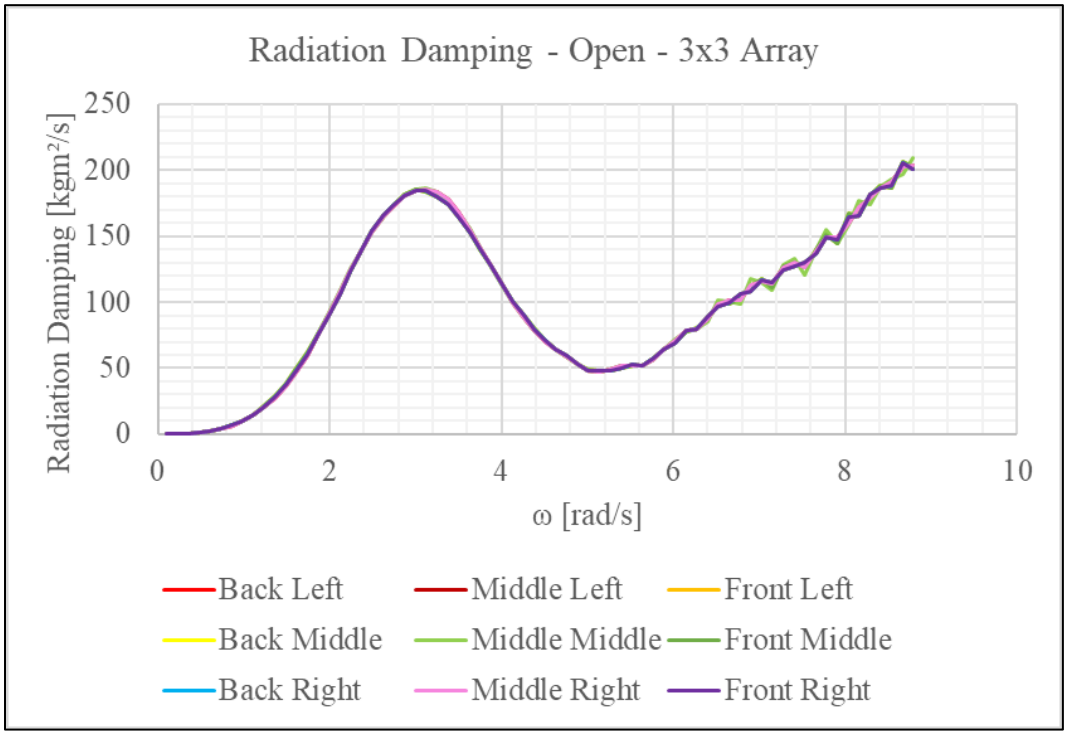

Figure 4-38. 3x3 Array - Radiation Damping Calculated at the Hinge for the Open Configuration

Figure 4-39. 3x3 Array – Added Mass Calculated at the Hinge for the Open Configuration

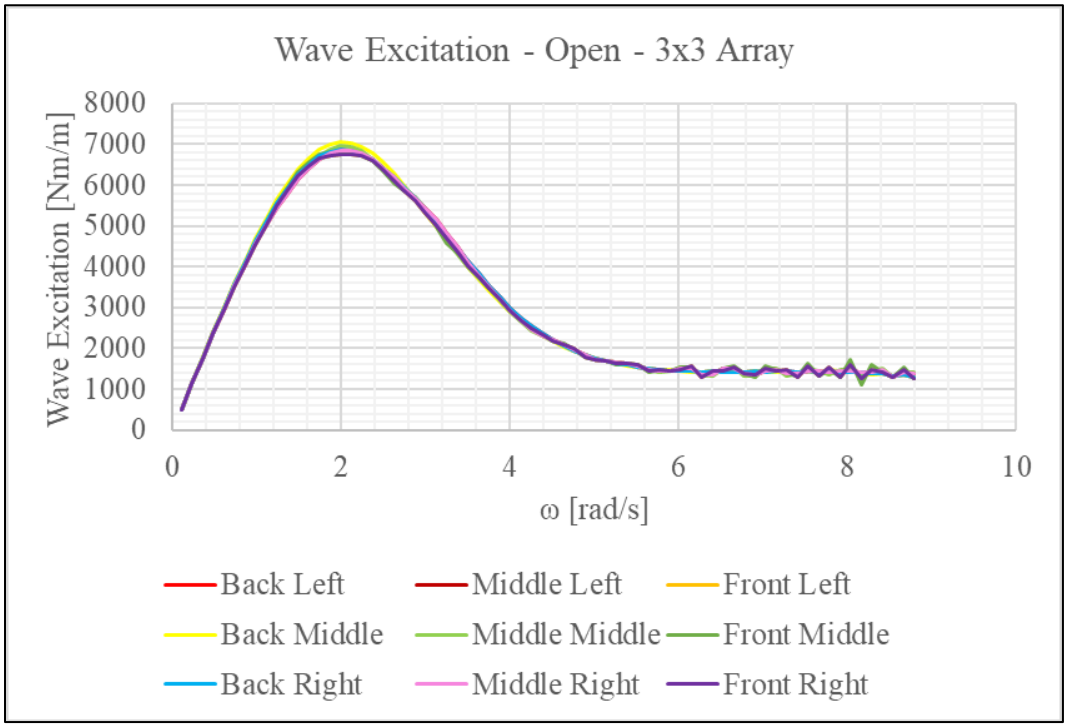

Figure 4-40. 3x3 Array – Wave Excitation Calculated at the Hinge for the Open Configuration

4.2 Power Production Results

This section presents a matrix of mechanical power for the closed configuration, and the MAEP matrices for each vane angle configuration in a wide range of sea states that frequently occur in NC. Figure 4-41 shows the mechanical power into the PTO and the MAEP matrix for the closed configuration. There was a gradual increase of mechanical power when T_e exceeded 12.5 seconds, which is believed to be due to the increasing magnitude of B_{opt}, seen in Figure 3-1. For the closed configuration, the largest amount of power absorbed was 7,755 Watts when T_e was 7.5 seconds and H_s was 2.75 meters. However, referring back to Figure 1-6 it can be seen that this sea state only had a frequency of occurrence of 0.02%. Therefore annually, only 620 W of power would result from this sea state. The largest percentage of occurrence was 14.53%, when H_s was 0.75 meters and T_e was 5.5 seconds. The MAEP matrix was obtained by multiplying the mechanical torque and the frequency of wave occurrences, Figure 1-6 [102]. The MAEP matrix showed that the maximum power produced annually was 10.24 kW, when H_s was 1.25 meters and T_e was 5.5 seconds. At this sea state, the OWSC's mechanical power into the PTO was 1,822 Watts. Summing all of the values in the MAEP matrix resulted in the overall MEAP. The overall mean annual energy production for the closed configuration was 115.06 kW. Regarding the 60° configuration, the maximum power produced annually was 6.663 kW, when H_s was 1.25 meters and T_e was 5.5 seconds. At this sea state, the OWSC's mechanical power into the PTO was 1.19 Watts. The overall MAEP was 63.89 kW. The mechanical power into the PTO and MAEP matrix for the 60° configuration can be seen in Figure 4-42. Regarding the 45° configuration, the maximum power produced annually was 6.04 kW, when H_s was 0.75 meters and T_e was 6.5 seconds. At this sea state, the OWSC's mechanical power into the PTO was 485 W, and the overall MAEP was 51.48 kW. The mechanical power into the PTO and MAEP matrix for the 45° configuration can be seen in Figure 4-43. Regarding the 30° configuration, maximum power produced annually was 5.01 kW, when H_s was 0.75 meters and T_e was 6.5 seconds. At this sea state, the OWSC's mechanical power into the PTO was 402 Watts, and the overall MAEP was 37.25 kW. The mechanical power into the PTO and MAEP matrix for the 30° configuration can be seen in Figure 4-44. Finally, regarding the open configuration, the maximum power produced annually was 2.26 kW when H_s was 0.75 meters and T_e was 6.5 seconds. At this sea state, the OWSC's mechanical power into the

PTO was 179 W, and the overall MAEP was 15.58 kW. The mechanical power into the PTO and MAEP matrix for the open configuration can be seen in Figure 4-45. Table 4-5 shows the overall MAEP for each configuration, as well as the maximum power that is contributed annually, as well as the sea state at which this maximum power occurs. As expected, there was a noticeable drop in power production as the vane angle approached 0°. However, the reduction in power was not as drastic between the 60° and 45° configuration, compared to the 90° and 60° configuration. The percent difference in MEAP values between the 60° and 45° configuration was 9.76%, while the percent difference in MEAP values between the 90° and 60° configuration was 42.4%. It was expected for there to be a linear, predictable relationship in power reduction as the vanes change angles. However, it appeared there was an inconsistent change in MAEP values as the vane angle incremented from closed to 60°. Therefore, it is recommended that future analyses are conducted on a vane angle of 75°.

Closed Configuration - Mechanical Power

H (m) \ T (s)	1.5	2.5	3.5	4.5	5.5	6.5	7.5	8.5	9.5	10.5	11.5	12.5	13.5	14.5	15.5	16.5
4.75																
4.25																
3.75																
3.25								6871	4577	2539	1016					
2.75							7755	5915	3930	2203	905	552	1357	1588		
2.25					6220	6500	5979	4793	3320	1839	744	496	1177	1288	1310	
1.75					3615	3918	4009	3576	2699	1530	605	384	861	970		
1.25				1677	1822	1874	2070	2289	1788	1245	479	295				
0.75			662	604	655	658	684	856	896	655						
0.25		66	74	67	73	73	74	83	88							

Power (W)

Closed Configuration - Mean Annual Energy Production

H (m) \ T (s)	1.5	2.5	3.5	4.5	5.5	6.5	7.5	8.5	9.5	10.5	11.5	12.5	13.5	14.5	15.5	16.5
4.75																
4.25																
3.75																
3.25								137	229	76	10					
2.75							620	1006	472	198	72	11	14	16		
2.25					124	2535	3348	2397	1228	423	89	25	24	26	13	
1.75					3724	9598	6776	4541	2618	1056	145	46	43	19		
1.25				2046	10242	8581	7554	6661	3076	722	77	9				
0.75			516	6097	9510	8197	5523	2609	582	59						
0.25		2	67	229	453	408	160	17	2							

Energy (Wh)

Figure 4-41. Closed— Mechanical Power Input into the PTO (top) and MAEP Matrix (bottom)

60° Configuration- Mechanical Power																		
H (m)	4.75																	Power (W)
	4.25																	
	3.75																	
	3.25								1524	935	1531	1651						
	2.75							2781	1244	818	1302	1407	1359	1188	970			
	2.25					3765	3440	2307	999	623	1051	1153	1083	922	735	604		
	1.75					2336	2434	1826	778	447	826	882	799	652	505			
	1.25				1007	1186	1358	1254	602	328	598	587	503					
	0.75			387	363	428	500	602	446	228	336							
	0.25		41	43	40	48	55	71	98	81								
		1.5	2.5	3.5	4.5	5.5	6.5	7.5	8.5	9.5	10.5	11.5	12.5	13.5	14.5	15.5	16.5	
		T (s)																

60° Configuration - Mean Annual Energy Production																		
H (m)	4.75																	Energy (Wh)
	4.25																	
	3.75																	
	3.25								30	47	46	17						
	2.75							222	211	98	117	113	27	12	10			
	2.25					75	1342	1292	500	231	242	138	54	18	15	6		
	1.75					2406	5962	3087	988	433	570	212	96	33	10			
	1.25				1229	6663	6220	4577	1753	564	347	94	15					
	0.75			302	3671	6212	6223	4866	1361	148	30							
	0.25		1	39	138	296	307	154	21	2								
		1.5	2.5	3.5	4.5	5.5	6.5	7.5	8.5	9.5	10.5	11.5	12.5	13.5	14.5	16	16.5	
		T (s)																

Figure 4-42. 60° Configuration — Mechanical Power Input into the PTO (top) and MAEP Matrix (bottom)

45° Configuration - Mechanical Power																		
H (m)	4.75																	Power (W)
	4.25																	
	3.75																	
	3.25								642	1638	1495	1407						
	2.75							1687	536	1382	1251	1168	1033	835	651			
	2.25					3154	2536	1308	446	1100	1008	916	786	620	476	383		
	1.75					2009	1890	1017	328	805	752	652	540	414	313			
	1.25				870	1060	1189	761	201	543	481	386	308					
	0.75			328	315	387	485	461	136	291	213							
	0.25		35	36	35	43	55	82	59	45								
		1.5	2.5	3.5	4.5	5.5	6.5	7.5	8.5	9.5	10.5	11.5	12.5	13.5	14.5	15.5	16.5	
		T (s)																

45° Configuration - Mean Annual Energy Production																		
H (m)	4.75																	Energy (Wh)
	4.25																	
	3.75																	
	3.25								13	82	45	14						
	2.75							135	91	166	113	93	21	8	7			
	2.25					63	989	732	223	407	232	110	39	12	10	4		
	1.75					2069	4631	1719	417	781	519	156	65	21	6			
	1.25				1062	5955	5447	2779	586	934	279	62	9					
	0.75			256	3184	5629	6038	3725	415	189	19							
	0.25		1	33	120	270	309	176	12	1								
		1.5	2.5	3.5	4.5	5.5	6.5	7.5	8.5	9.5	10.5	11.5	12.5	13.5	14.5	16	16.5	
		T (s)																

Figure 4-43. 45° Configuration — Mechanical Power Input into the PTO (top) and MAEP Matrix (bottom)

30° Configuration - Mechanical Power																		
H (m)	4.75																	Power (W)
	4.25																	
	3.75																	
	3.25								1344	1438	1170	1011						
	2.75							398	1163	1201	958	810	684	553	441			
	2.25					2415	1591	365	923	946	732	603	503	401	317	259		
	1.75					1602	1212	274	669	672	505	404	331	259	202			
	1.25				689	887	836	184	433	406	290	225	180					
	0.75			239	250	336	402	105	224	173	116							
	0.25		24	27	28	38	54	36	35	22								
		1.5	2.5	3.5	4.5	5.5	6.5	7.5	8.5	9.5	10.5	11.5	12.5	13.5	14.5	15.5	16.5	
		T (s)																

30° Configuration - Mean Annual Energy Production																		
H (m)	4.75																	Energy (Wh)
	4.25																	
	3.75																	
	3.25								27	72	35	10						
	2.75							32	198	144	86	65	14	6	4			
	2.25					48	620	205	462	350	168	72	25	8	6	3		
	1.75					1650	2970	463	849	652	348	97	40	13	4			
	1.25				840	4984.9	3829	671	1261	699	168	36	5					
	0.75			186	2530	4881.7	5010	847	682	112	10							
	0.25		1	24	95	238	302	79	7	0								
		1.5	2.5	3.5	4.5	5.5	6.5	7.5	8.5	9.5	10.5	11.5	12.5	13.5	14.5	15.5	16.5	
		T (s)																

Figure 4-44. 30° Configuration — Mechanical Power Input into the PTO State (top) and MAEP Matrix (bottom)

Open Configuration - Mechanical Power																		
H (m)	4.75																	Power (W)
	4.25																	
	3.75																	
	3.25								592	588	484	428						
	2.75							246	498	488	396	346	297	239	188			
	2.25					874	496	208	404	388	309	264	222	174	134	106		
	1.75					634	384	155	306	287	222	181	147	112	85			
	1.25				245	373	291	107	213	186	132	101	79					
	0.75			59	89	146	179	67	115	79	51							
	0.25		3	7	10	17	28	23	15	9								
		1.5	2.5	3.5	4.5	5.5	6.5	7.5	8.5	9.5	10.5	11.5	12.5	13.5	14.5	15.5	16.5	
		T (s)																

Open Configuration - Mean Annual Energy Production																		
H (m)	4.75																	Energy (Wh)
	4.25																	
	3.75																	
	3.25								12	29	15	4						
	2.75							20	85	59	36	28	6	2	2			
	2.25					17	194	117	202	144	71	32	11	3	3	1		
	1.75					653	942	262	389	278	153	44	18	6	2			
	1.25				298	2096.8	1332	391	620	319	76	16	2					
	0.75			46	894	2121.3	2226	544	352	52	5							
	0.25		0	6	34	105	160	49	3	0								
		1.5	2.5	3.5	4.5	5.5	6.5	7.5	8.5	9.5	10.5	11.5	12.5	13.5	14.5	16	16.5	
		T (s)																

Figure 4-45. Open Configuration — Mechanical Power Input into the PTO (top) and MAEP Matrix (bottom)

Table 4-5: Summary of Highest Contribution of Energy

Configuration	MAEP (kW)	Max Power Sea State	Max Power (kW)
Closed	115.1	H_s = 1.25 m T_e = 5.5 s	10.24
60°	63.89	H_s = 1.25 m T_e = 5.5 s	6.66
45°	51.48	H_s = 0.75 m T_e = 6.5 s	6.04
30°	37.25	H_s = 0.75 m T_e = 6.5 s	5.01
Open	15.58	H_s = 0.75 m T_e = 6.5 s	2.23

4.3 Fluid Flow Analysis Results

4.3.1 Mesh Sensitivity Study

Simulation results could be inaccurate if the mesh is too coarse [103]. Furthermore, if the mesh is too fine the simulation can be very computationally demanding. Therefore, a tradeoff between the two was made by conducting a mesh sensitivity study. The three different mesh densities used here can be seen in Table 4-6 and Figure 4-46.

Table 4-6. Mesh Sensitivity Sizes Used in Fluent

Mesh Type	Element Size	Number of Elements
Coarse	0.25 m	7,162
Medium	0.1 m	32,082
Fine	0.075 m	55,555

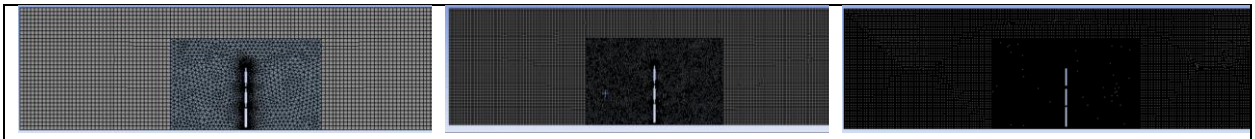

Coarse Mesh Medium Mesh Fine Mesh

Figure 4-46. Different Mesh Densities Used in Fluent Mesh Sensitivity Analysis

The mesh sensitivity analysis was conducted on the closed configuration where the total pressure, torque, and x-direction force on the OWSC were compared. Simulation settings were replicated exactly for each mesh case, with exception to mesh density. More information on the simulation setup will be discussed later. The mesh sensitivity results are shown in Figure 4-47, Figure 4-48, and Figure 4-49 for the x-direction force, total pressure, and torque on the OWSC respectively. The results indicated that some instability existed in the simulation which took the form of extreme singularities. This instability may be a result of the oscillating motion of the OWSC complicating the flow field, as was the case in [58]. The most instability occurred for the coarse mesh and the least instability occurred with the fine mesh. The medium mesh experienced a small amount of instability, but its results agreed well with the fine mesh results. Although the fine mesh led to more numerical stability, the computational demand for the fine mesh was much greater than the

medium mesh, as seen in Table 4-6. A tradeoff between simulation time and numerical stability was made, and the medium mesh was selected.

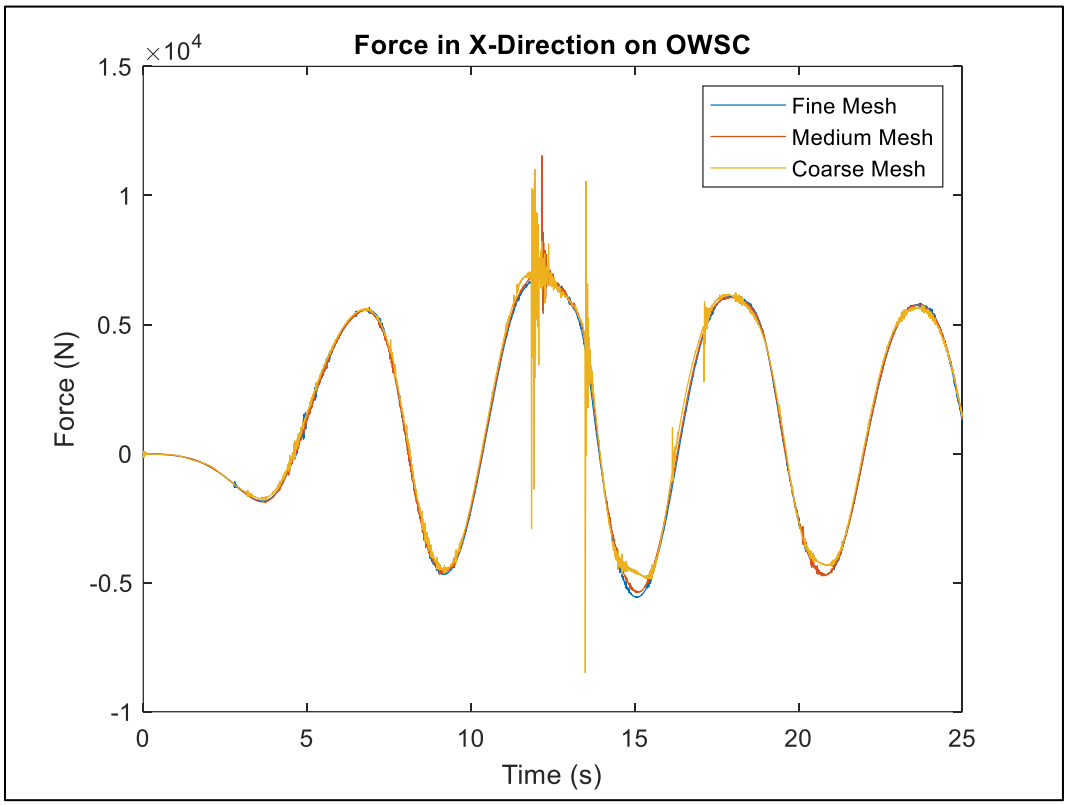

Figure 4-47. Mesh Comparison of Force in X-Direction on OWSC

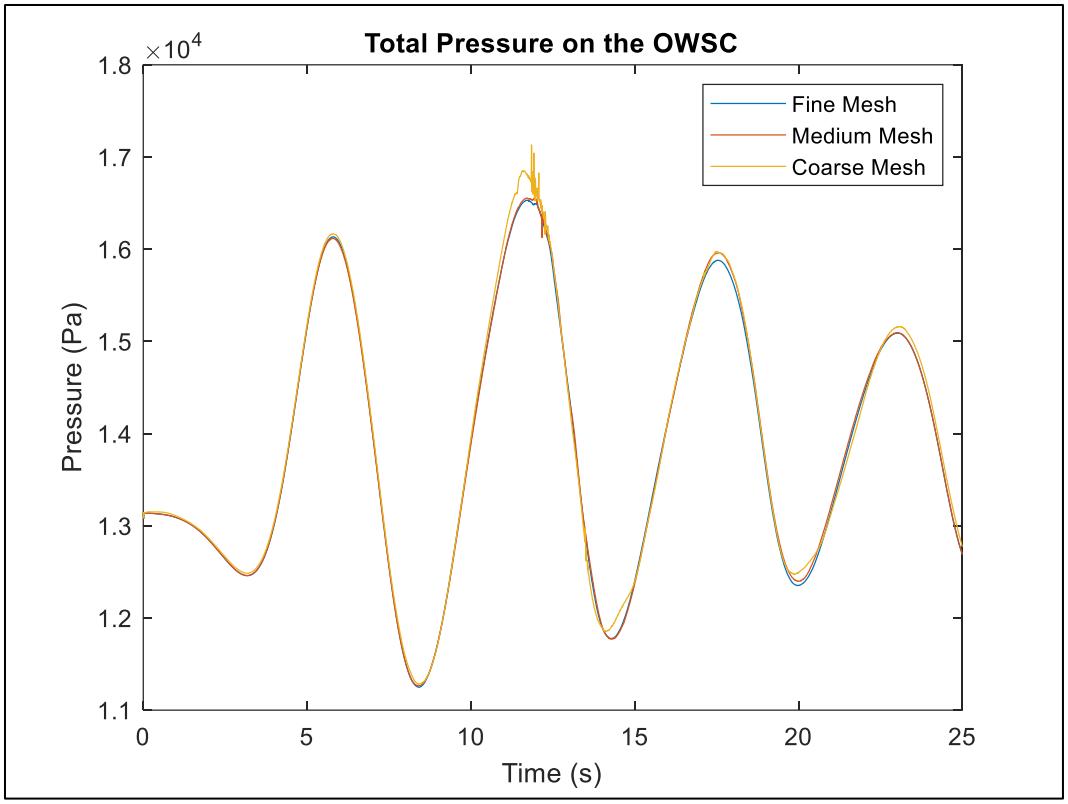

Figure 4-48. Mesh Comparison of Pressure on OWSC

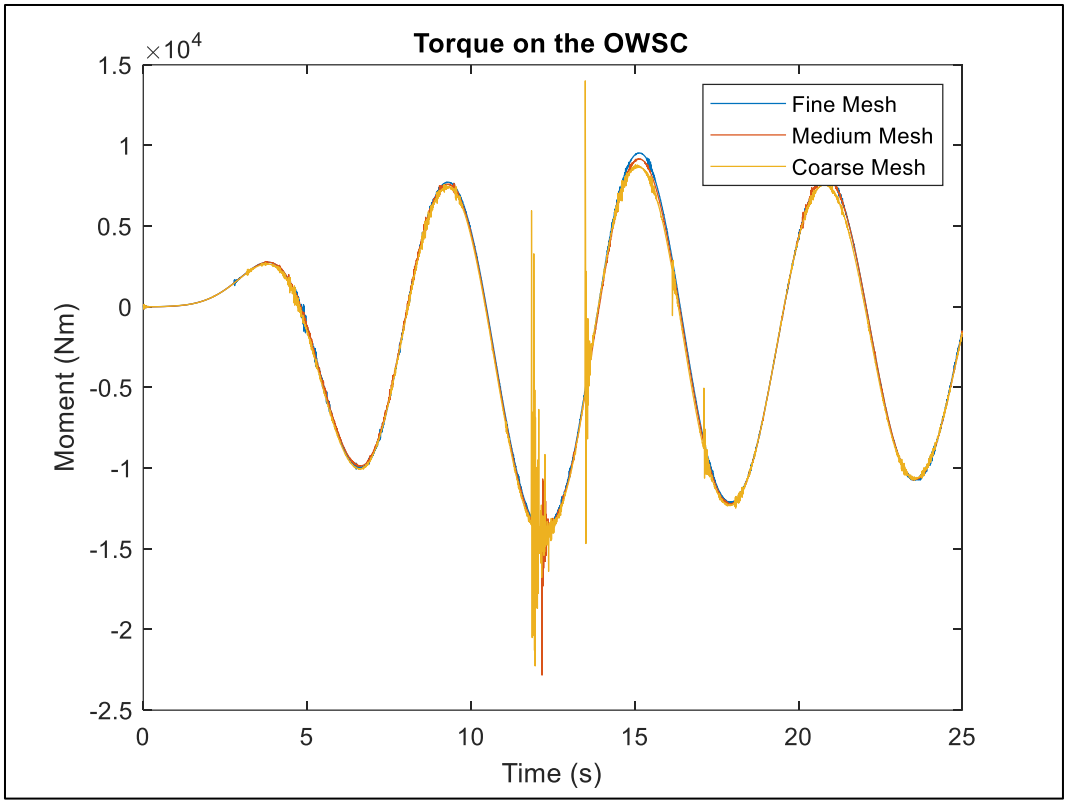

Figure 4-49. Mesh Comparison of Torque on OWSC

4.3.2 Comparing WEC-Sim and Fluent Results

Simulation parameters such as wave heigh, wave period, device properties, and PTO parameters were set up as similarly as possible when conducting the comparison study between WEC-Sim and CFD. The torque results and the x-direction force results on the closed configuration can be seen in Figure 4-50 and Figure 4-51 respectively. Overall, the results appear to agree well, considering they are on the magnitude of 10^4 for torque and 10^3 for force. The low magnitudes for the CFD results from 0 to 5 seconds are believed to be due to the wave ramp up. The slight differences in magnitude could be because Linear Wave Theory was used in WEC-Sim and Third Order Stokes Waves were used in Fluent. Finally, slight differences in results could also be due to solver differences when defining the PTO parameters. The spikes in CFD values are believed to be due to small singularities, as described in Section 4.3.1.

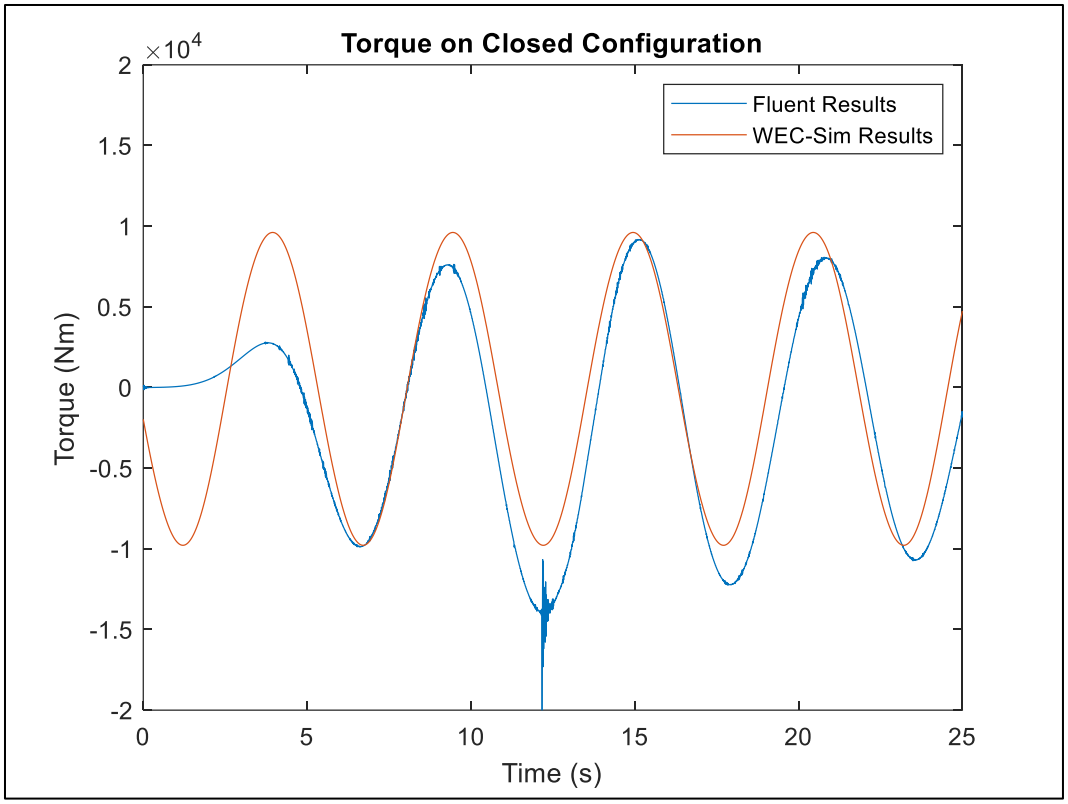

Figure 4-50. Comparison Results for OWSC Torque

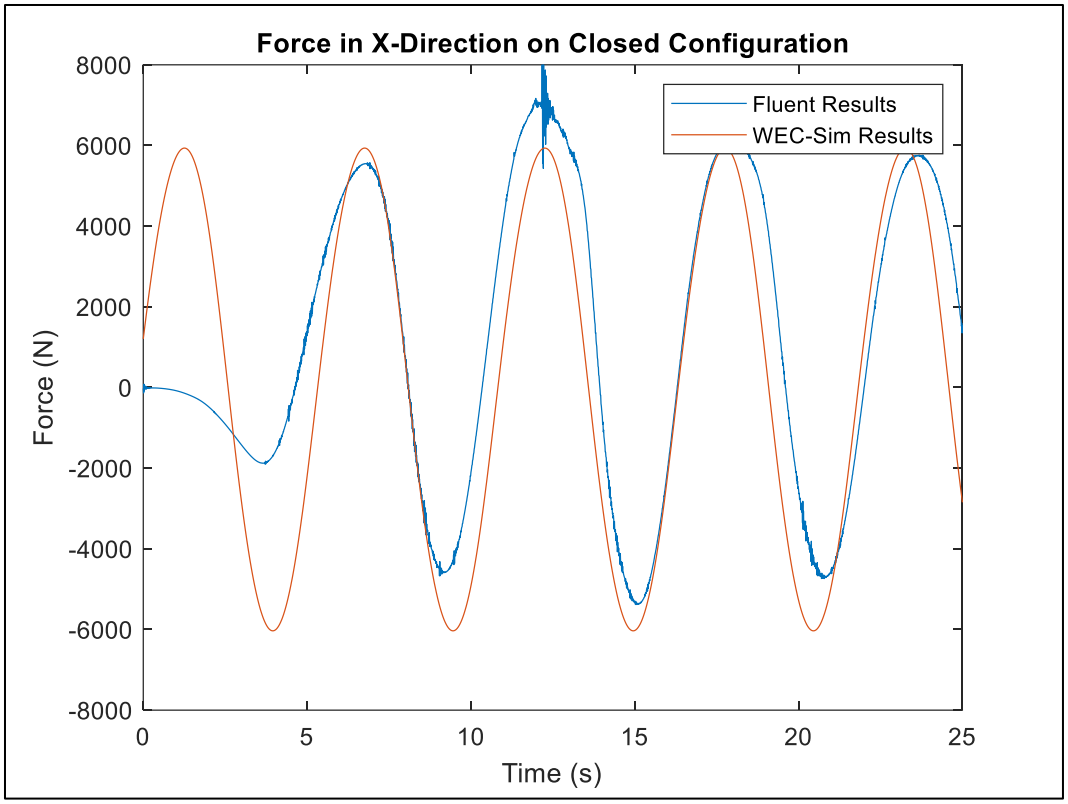

Figure 4-51. Comparison Results for OWSC X-Direction Force

4.3.3 Force, Torque, and Pressure on the OWSC

The following results are from wave condition 1, where the wave height was 0.75 meters, and the wave period was 5.5 seconds. Each vane angle configuration was simulated under the same wave conditions and setup parameters. The results for aggregate forces in the x- and y-direction, aggregate torque, and total aggregate pressure on the OWSC can be seen in Figure 4-52, Figure 4-53, Figure 4-54, and Figure 4-55 respectively.

Regarding x-direction force, Figure 4-52, the closed configuration experienced the largest maximum force, while the 60°, 45°, and 30° configurations appeared to have very similar force magnitudes. Tt was expected for a larger difference to exist between these configurations since more water is able to pass through the device as the vanes approached fully open. The open configuration appeared to experience a force that was similar in trough magnitude to the 60°, 45°, and 30° configurations, but differed in crest magnitude. The open configuration actually experienced a higher peak x-direction force than the 60°, 45°, and 30° configurations. This may

have been caused by wave-surge forces that acted on the bottom of the vanes as the OWSC rotated landward.

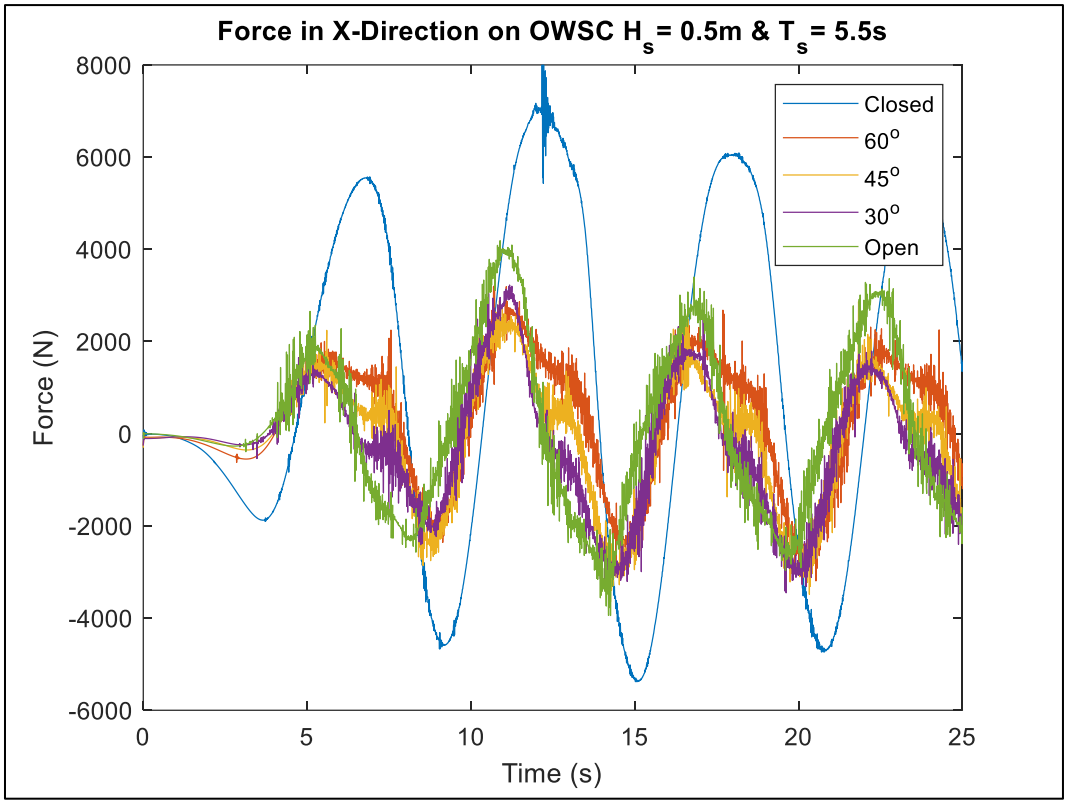

Figure 4-52. X-Direction Force for Each Configuration with Exact Wave Conditions

Regarding y-direction force, shown in Figure 4-53, the open configuration experienced the greatest maximum force magnitude as expected. Similar to the x-direction force results, the results for the 60°, 45°, and 30° configurations here appear to be relatively consistent with one another, indicating that the angle of the vanes may have had little influence on the force that the OWSC experienced as a whole. It should be noted that specific points were not examined in Fluent; Instead, the aggregate OWSC forces were obtained and reported. This could be contributing some error to the results.

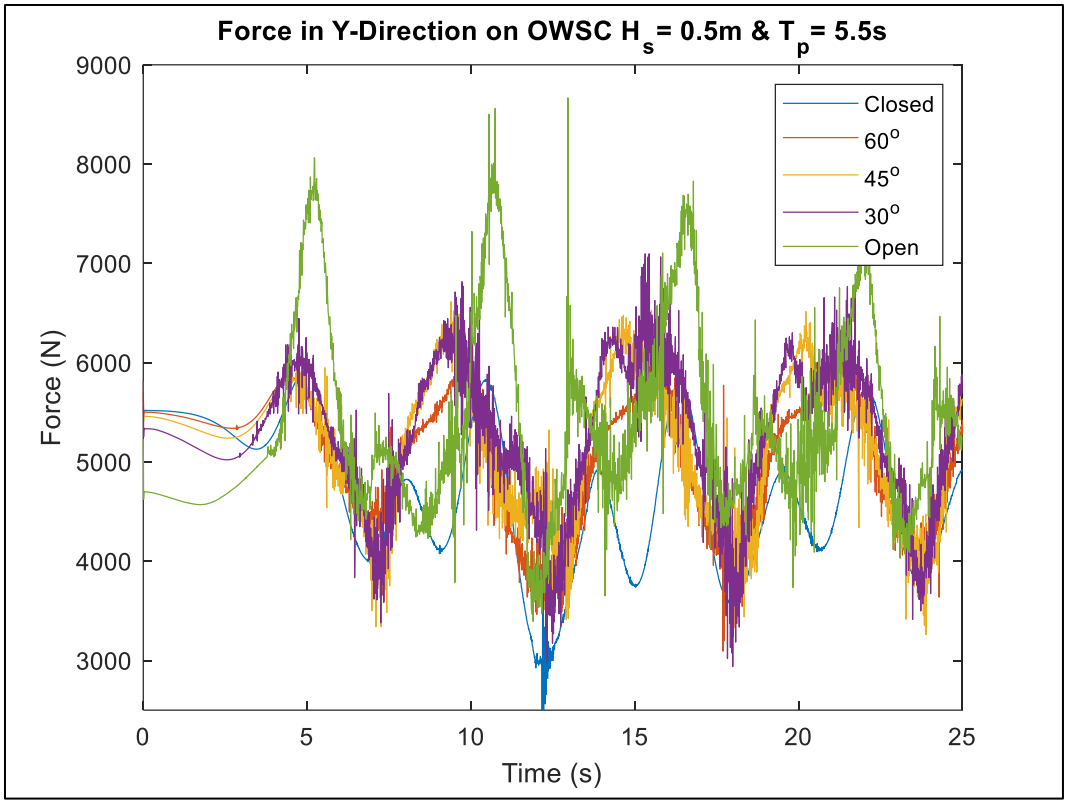

Figure 4-53. Y-Direction Force for Each Configuration with Exact Wave Conditions

The torque results, in Figure 4-54, indicated that the closed configuration experienced a significantly higher torque compared to the other configurations. Although it was expected for the closed configuration to experience the highest torque magnitude, it was not expected for maximum torque values to differ by almost 60% between the closed configuration and other configurations. Similar to the x-direction force results, the 60°, 45°, and 30° configurations each had magnitudes that did not differ as much as expected. The open configuration seemed to behave differently than all of the other configurations which may have been due to insufficient hydrostatic restoring forces.

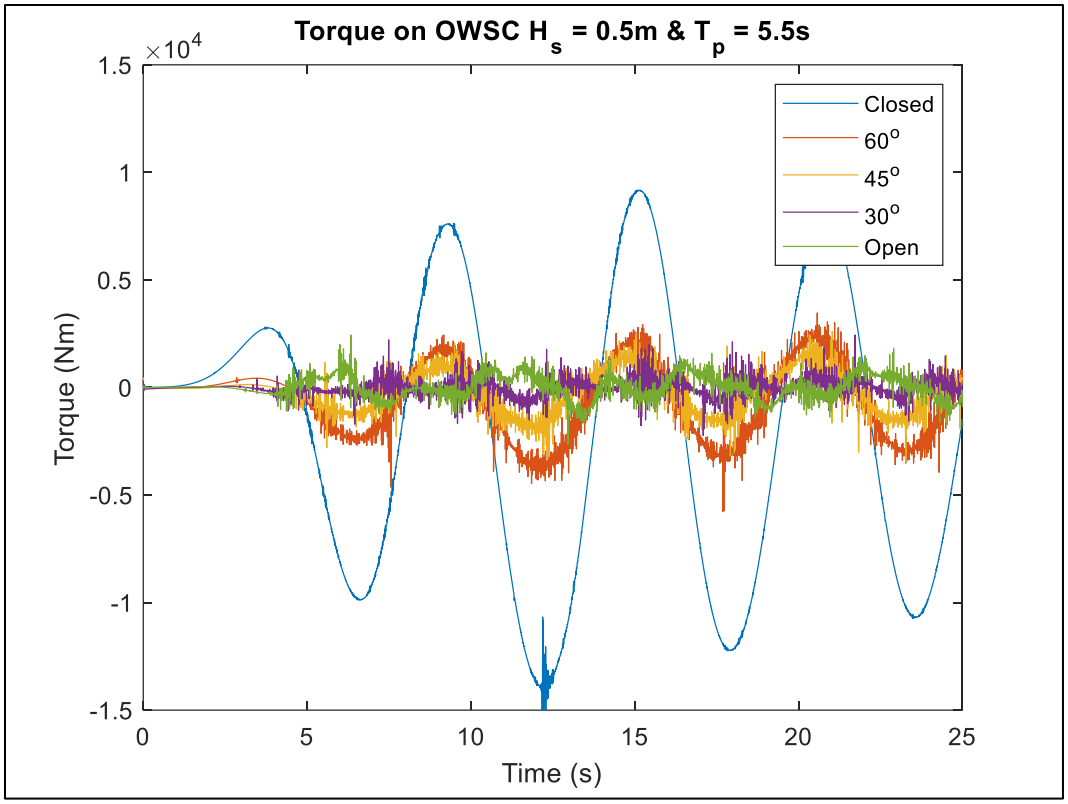

Figure 4-54. Torque for Each Configuration with Exact Wave Conditions

The results for total pressure on the OWSC can be seen in Figure 4-55. As expected, the closed configuration experienced the greatest maximum pressure. Unexpectedly, the open configuration experienced a pressure that was similar to the results of the 60°, 45°, and 30° configurations. The 60° configuration, overall, experienced the lowest magnitude of maximum pressure compared to the other configurations. Since the 45° and 30° configurations appeared to have close results, it is recommended that future studies include either the 45° configuration or the 30° configuration instead of both.

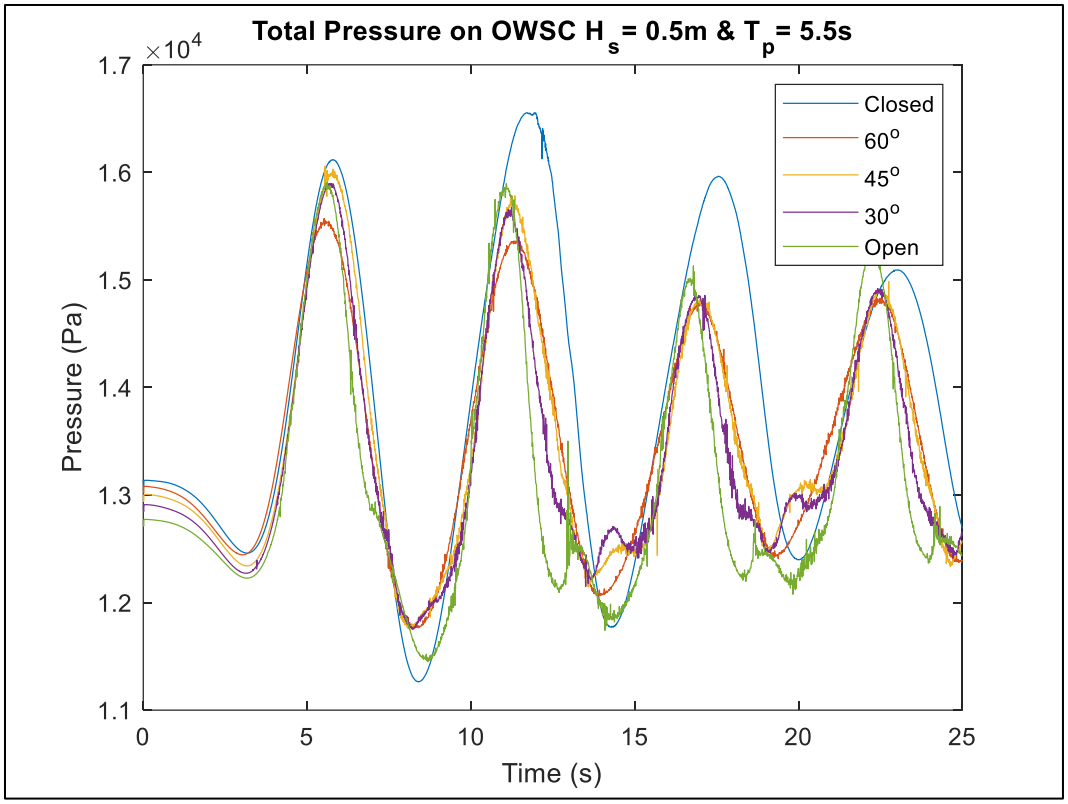

Figure 4-55. Total Pressure for Each Configuration with Exact Wave Conditions

4.3.4 Fluid Flow Results

The force, torque, and pressure results from the section above indicated that the largest magnitudes occurred at a simulation time around 12 seconds. Therefore, the investigation of velocity profile, dynamic pressure contour, and whether or not wave slamming occurs were investigated around this time frame for wave condition 1 and 2 to maintain consistency. Figure 4-56 depicts the language that is used while describing the results.

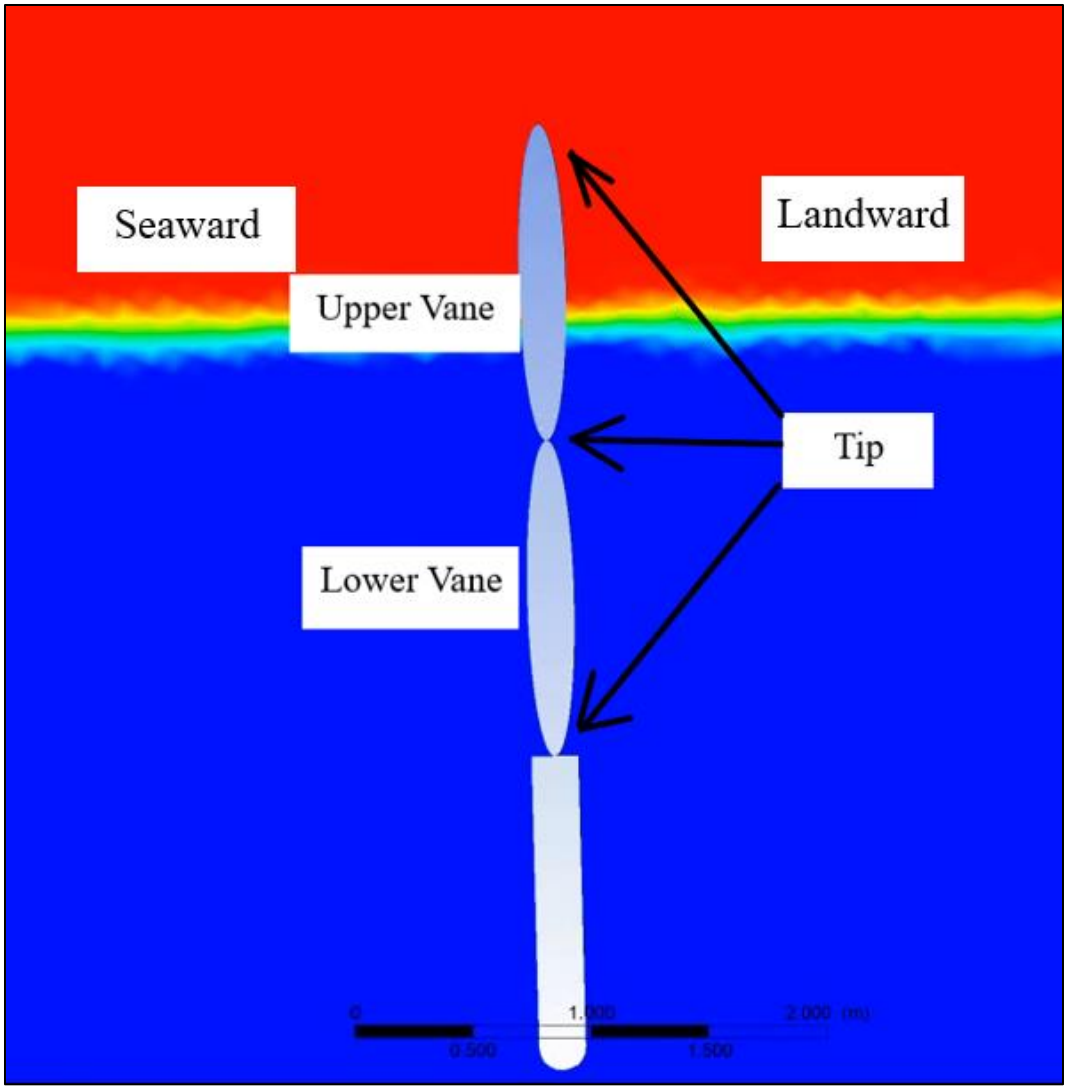

Figure 4-56. OWSC Location Language While Describing Fluent Results

4.3.5 Closed Configuration

For the closed configuration in wave condition 1, the upper tip of the upper vane tended to experience a fluid velocity of 3.12 m/s and swirling effects as it oscillated landward. The dynamic pressure due to these swirling effects was 1,420 Pa. The velocity results can be seen in Figure 4-57. This was possibly due to the sharp radii of at vane tips. The swirling motion could introduce resistance to motion, which could reduce OWSC's velocity during its seaward oscillation which could result in lower power capture. Although wave slamming did not occur at this wave condition, the drop in water level on the seaward face of the upper vane, shown in

Figure 4-58 was a preliminary sign of potential wave slamming. Therefore, wave slamming may occur during more energetic wave conditions.

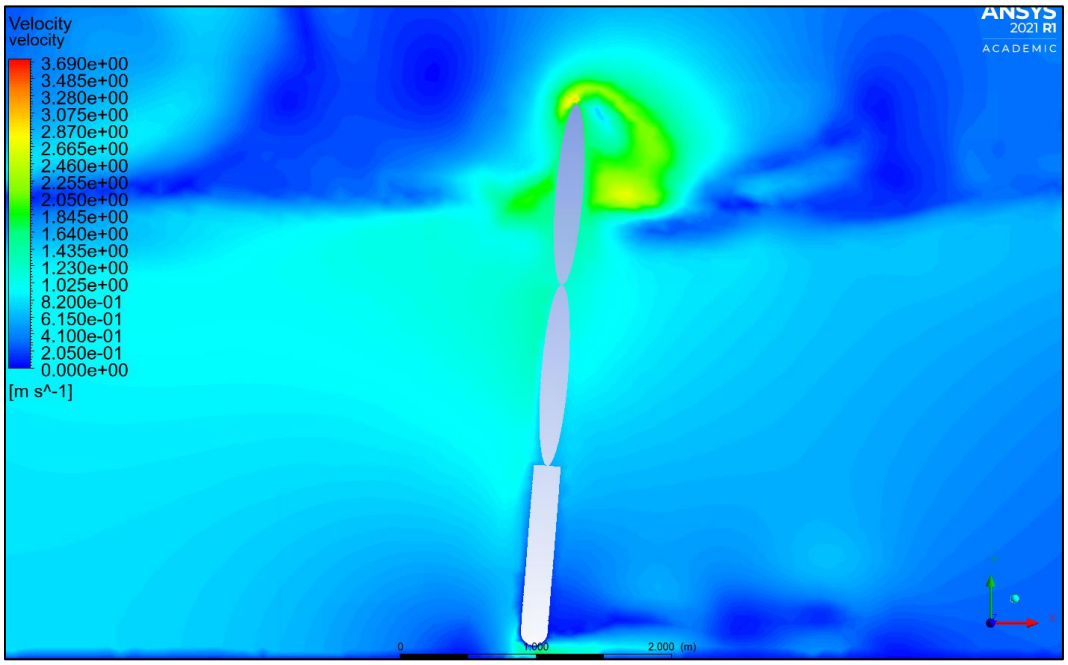

Figure 4-57. Velocity Contour on Closed Configuration—Wave Condition 1

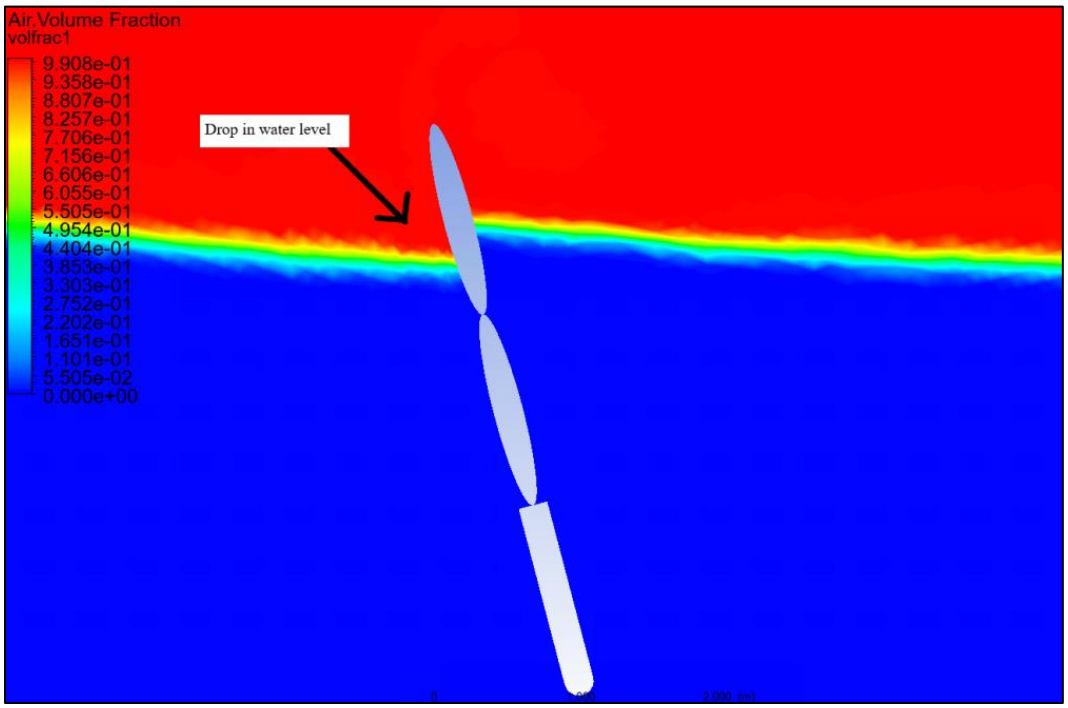

Figure 4-58. Preliminary Wave Slamming Phenomenon on Closed Configuration in Wave Condition 1

For wave condition 2, the OWSC also experienced the highest velocity at the tip of the upper vane. In this wave condition, the device impacted the end stop as it pitched landward from the first incident wave, and a swirling vortex was formed on the tip of the landward side of the upper vane, shown in Figure 4-59. Similar to wave condition 1, the subsequent seaward pitch achieved a higher velocity since there was a larger drop in water level on the seaward face of the OWSC. This effect can be seen in Frame A of . This resulted in the OWSC being thrusted seaward, with a small amount of water jet spraying off the OWSC face, indicating some wave slamming. Although the OWSC did not reach its seaward end stop, it created a radiated wave that dampened some of the speed and force from the second incident wave, similar to wave condition 1. The interaction of the incident wave with radiated wave caused severe wave overtopping and thus a reduction of experienced wave force. Although the wave force was reduced due to the radiated wave, it still impacted the end stop with a velocity of 8.23 m/s. Most of the dynamic pressure spikes occurred when the OWSC impacted the end stop. The maximum pressure spike was 9,970 Pa. In both the velocity contours and pressure field animations, a tail of rotating dynamic fluid can be seen rushing off the tip of the upper vane. At the moment the OWSC reached its end stop and the wave continued to flow over it, there was a noticeable hydraulic jump which caused the wave to become sub-critical in speed, frame A of Figure 4-60. Essentially, the hydraulic jump caused the water to double back on itself, thus creating another wave coming from the negative x-direction toward the OWSC, depicted in Figure 4-60. This backwards wave caused the radiated wave from the OWSC to be larger, potentially dampening more of the incident wave. The hydraulic jump also resulted in a small wave slamming event on the seaward side of the OWSC. Had the OWSC been able to rotate ±40° or ±50°, this phenomenon may have been avoided.

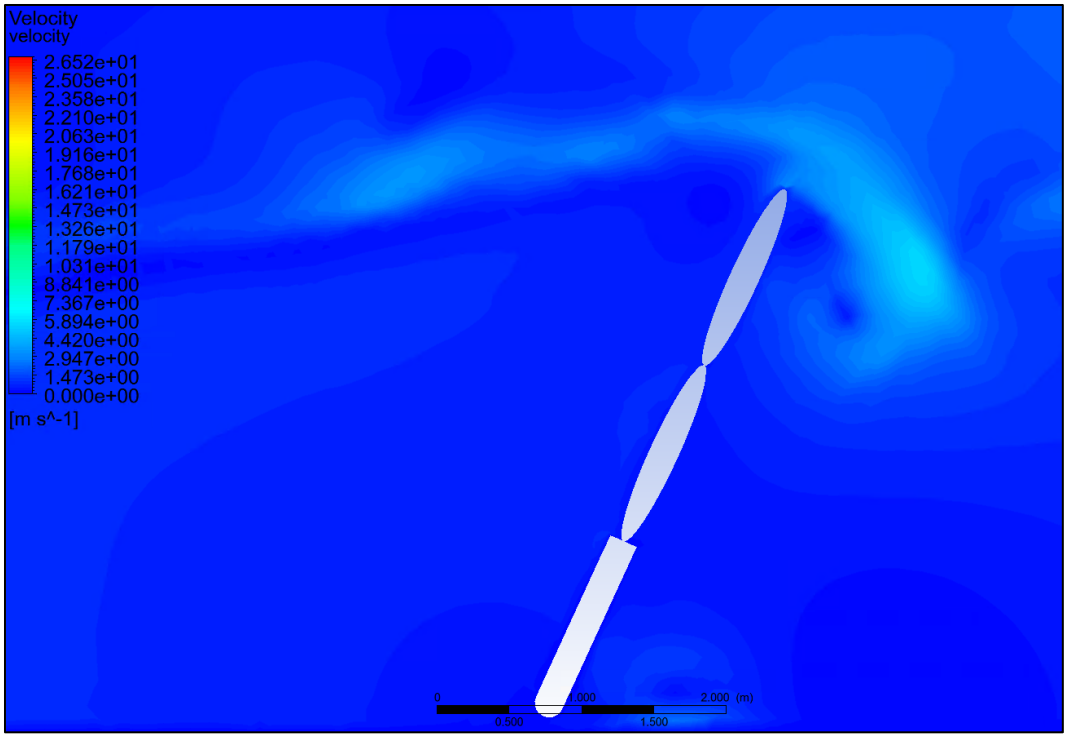

Figure 4-59. Swirling at the Tip of the Upper Vane Due to Impact with End Stop

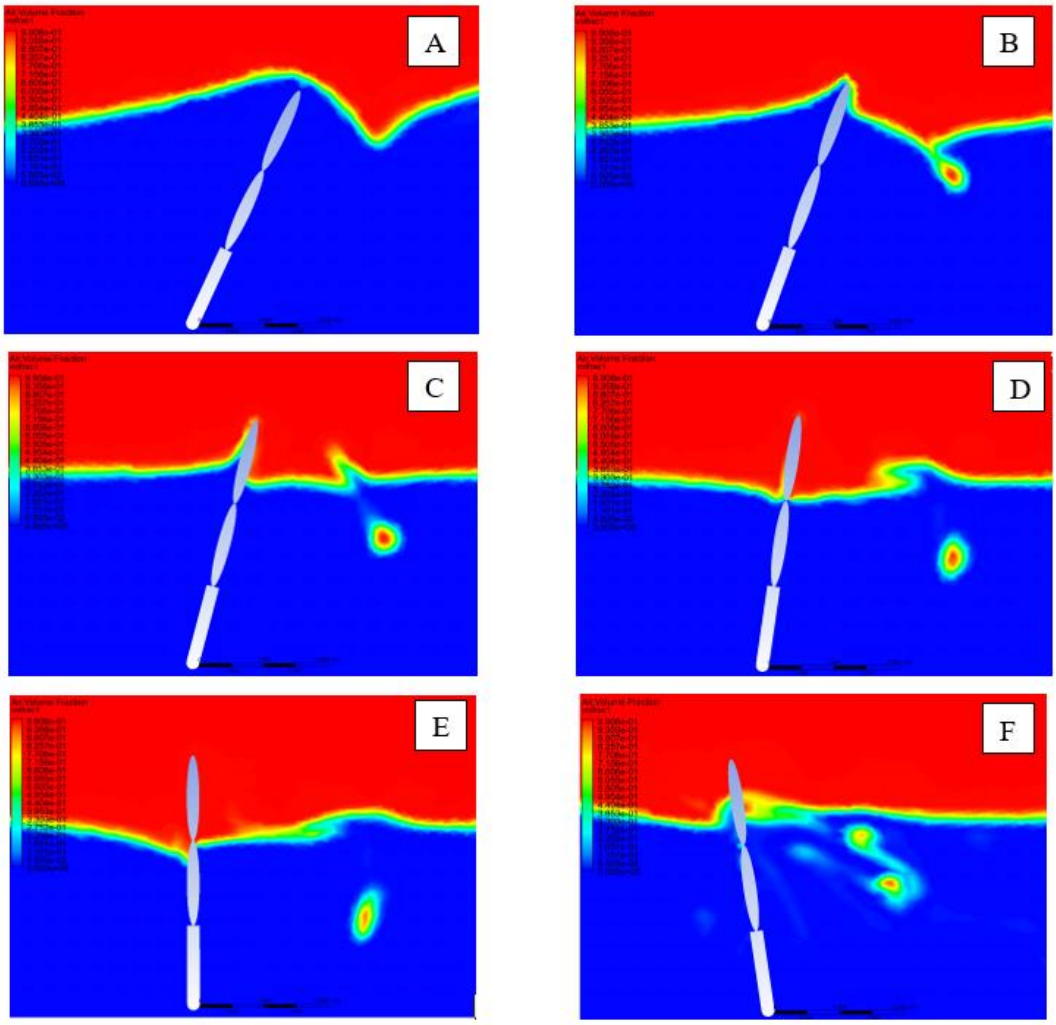

Figure 4-60. Hydraulic Jump Phenomenon for Closed Configuration in Wave Condition 2

4.3.6 60° Configuration

For the 60° configuration in wave condition 1, the velocity results were not consistent with the expected outcomes. The OWSC, in its 60° configuration, experienced the highest velocity at the upper tip of the upper vane during its landward oscillation. During the seaward pitch after the first incident wave, there was a larger fluid velocity around the perimeter of the upper vane, especially at the tip. Compared to the other configurations, the fluid velocity was lowest for the 60° configuration. A reduction of velocity directly impacts how much power an OWSC can produce. Since velocity profiles in WEC-Sim cannot be investigated, this phenomenon may not have accounted for, which could lead to inaccurate results. The volume fraction animations show that the slope of the 60° vanes contribute to some radiated wave formation. The water slid off the

vane at the same time the OWSC pitched seaward, which resulted in this radiated wave. The radiated wave did not appear to be large enough to significantly dampen the force of the incident wave. No signs of wave slamming, nor preliminary wave slamming were observed in this wave condition. As the OWSC pitched landward, most of the dynamic pressure occurred underneath the lower vane and within the gap between the upper and lower vanes. While the OWSC pitched seaward, most of the dynamic pressure was located on the top of the upper vane, having a maximum pressure of 2,092 Pa.

For the 60° configuration in wave condition 2, the OWSC experienced wave overtopping as it pitched landward which led to it quickly approaching and striking the end stops. This caused turbulent swirling at the tips of the upper and lower vanes, shown in Figure 4-61, having reached velocities of up to 6.32 m/s and 3.61 m/s respectively. Before the OWSC started pitching seaward again, there were indications of hydraulic jump since there was a significant reduction in water level on the landward side of the vane. These dip in water level be seen in frame B of Figure 4-62. The 60° configuration quickly shed the water and oscillated seaward at a velocity of 6.25 m/s. Although there was a reduction in water level at the front of the upper vane—a preliminary wave slamming characteristic—the wave slamming event did not occur since an air pocket was created underneath the upper vane which allowed the water level to be restored. Because of this, the wave slamming event was mitigated. This can be seen in frames A – F in Figure 4-62. The dynamic pressure was most active as the OWSC pitched seaward and as the OWSC impacted the end stops. The location of these pressure contours were on both tips of each vane, and underneath the lower vane. There was approximately 6,000 Pa of pressure that acted on the top surface of the upper vane as the OWSC pitched seaward.

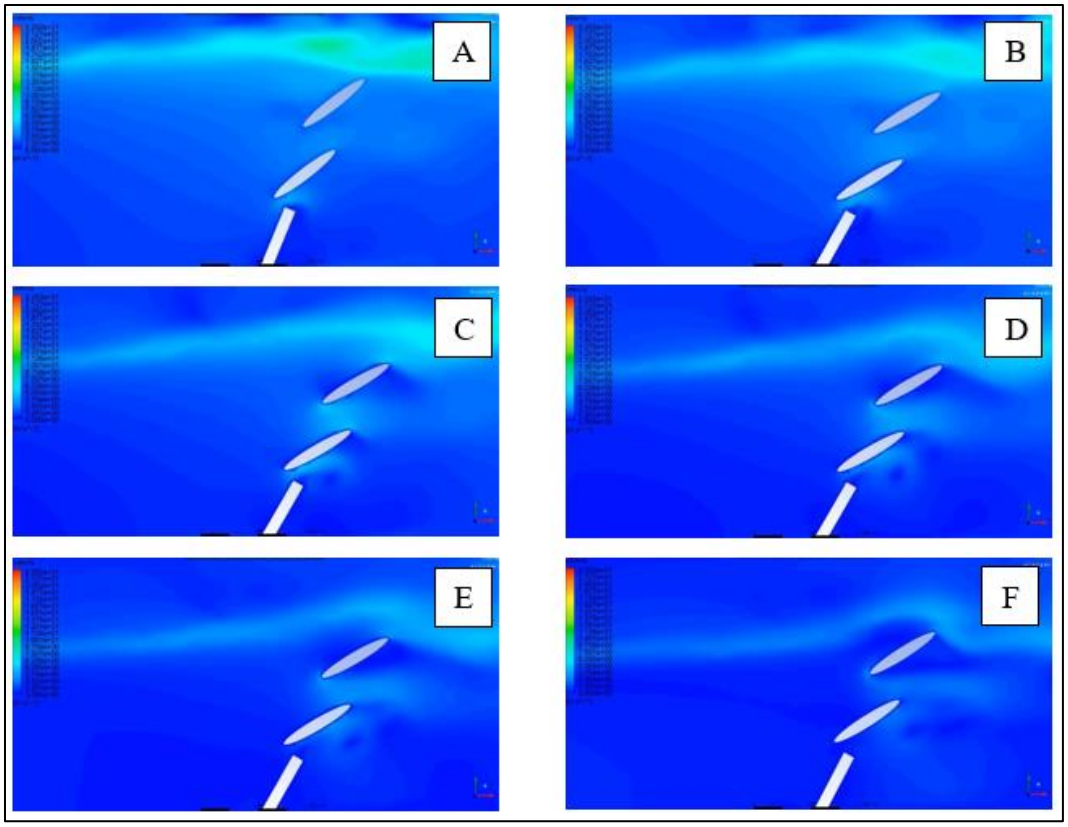

Figure 4-61. Velocity Profile for 60° Configuration in Wave Condition 2

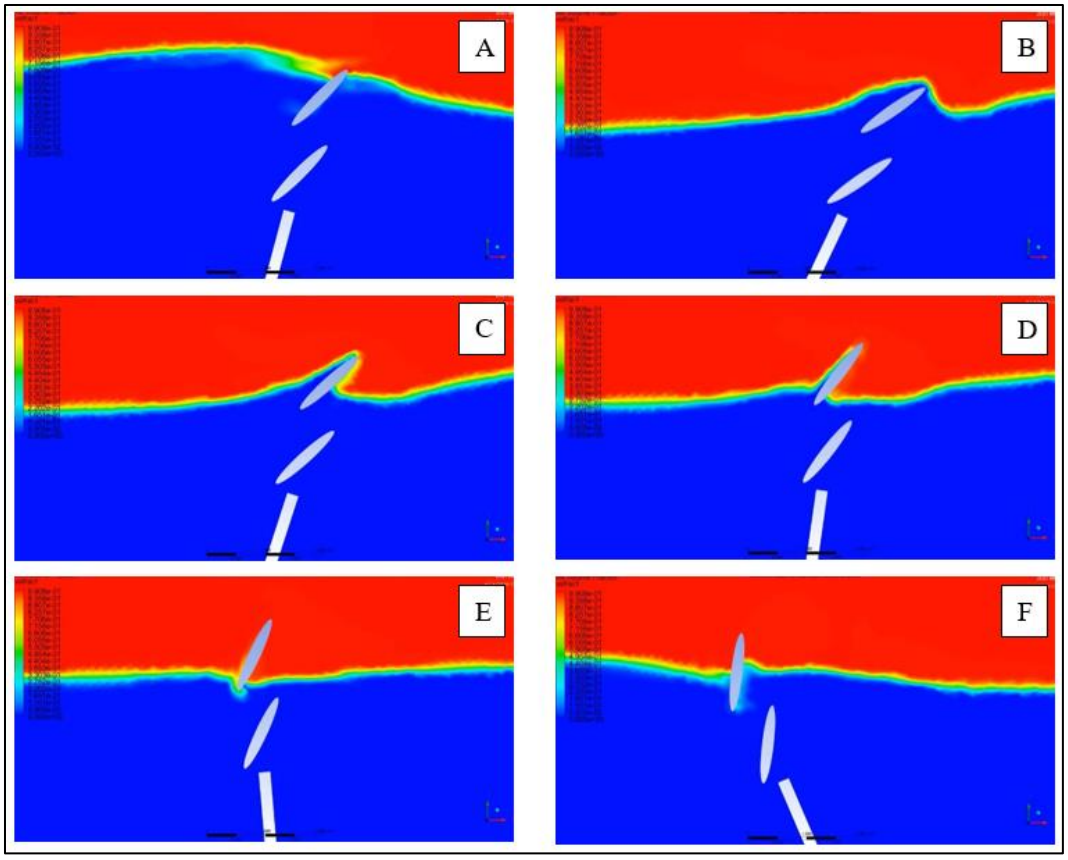

Figure 4-62. Wave Slamming Mitigation for 60° Configuration in Wave Condition 2

4.3.7 45° Configuration

For the 45° configuration in wave condition 1, the OWSC experienced more overtopping than the previous configurations, which resulted in hydraulic jump that acted as another wave impacting the OWSC from the landward side. This extra thrust resulted in radiated waves being generated at a velocity of 2.06 m/s. Wave slamming appeared to be more frequent in this wave state and configuration compared to the 60° configuration. During the OWSC's landward pitching motion, most of the swirling motions were located at both tips of the upper vane, while the seaward pitching motion resulted in turbulence along the entire surface area of the upper vane. The water near the tips lower vane experienced the most swirling during the landward pitch. Similar to the 60° configuration, the OWSC experienced the most pressure underneath the lower vane and in the gap between the upper and lower vane. Unlike the 60° configuration, the 45° configuration experienced a large magnitude of dynamic pressure on the tip of the upper vane and lower vane as it impacted its end stop while pitching landward: a value of 2,763 Pa and

2,585 Pa respectively. During the restorative seaward pitch, the maximum pressure occurred at the lower tip of the upper vane, having a magnitude of 3,345 Pa.

For the 45° configuration in wave condition 2, the OWSC was able to mitigate the wave slamming phenomenon, but it complicated the flow field by introducing many disturbances in the process. This can be seen in frames A – H of Figure 4-63. The hydrodynamic jumps and air pocket formations on both sides of the upper vane created radiated waves that may have dampened the incident wave. The radiated wave had a maximum velocity of 6.3 m/s. The vortices occurred in similar locations as the other wave condition and OWSC configurations—at the tip of the upper vane and on the landward side of the OWSC as it pitched seaward. The water near the tips lower vane experienced the most swirling during the landward pitch as shown in Figure 4-64. The velocity at the tips the device reached a maximum of 9.2 m/s. No wave slamming events were observed in this case, but there were instances where the angle of the vanes caused disturbances in the water that disrupted flow. Although consistently opening the vanes led to a lower torque on the device, it does appear to complicate the flow field. This could lead to issues with power capture since there is not a consistent frequency at which the device oscillates. The pressure spike that occurred on the tip of the upper vane had a magnitude of 10,619 Pa as it impacted the landward end stop. As it impacted, the dynamic pressure was concentrated on the tip of the lower vane, having a magnitude of 10,009 Pa. Aside from these spikes, most of the dynamic pressure fields were due to landward oscillation and were centralized on the upper surfaces of the upper and lower vane, as well as underneath the lower vane. All of which appeared to have similar magnitudes of pressure of approximately 9,525 Pa.

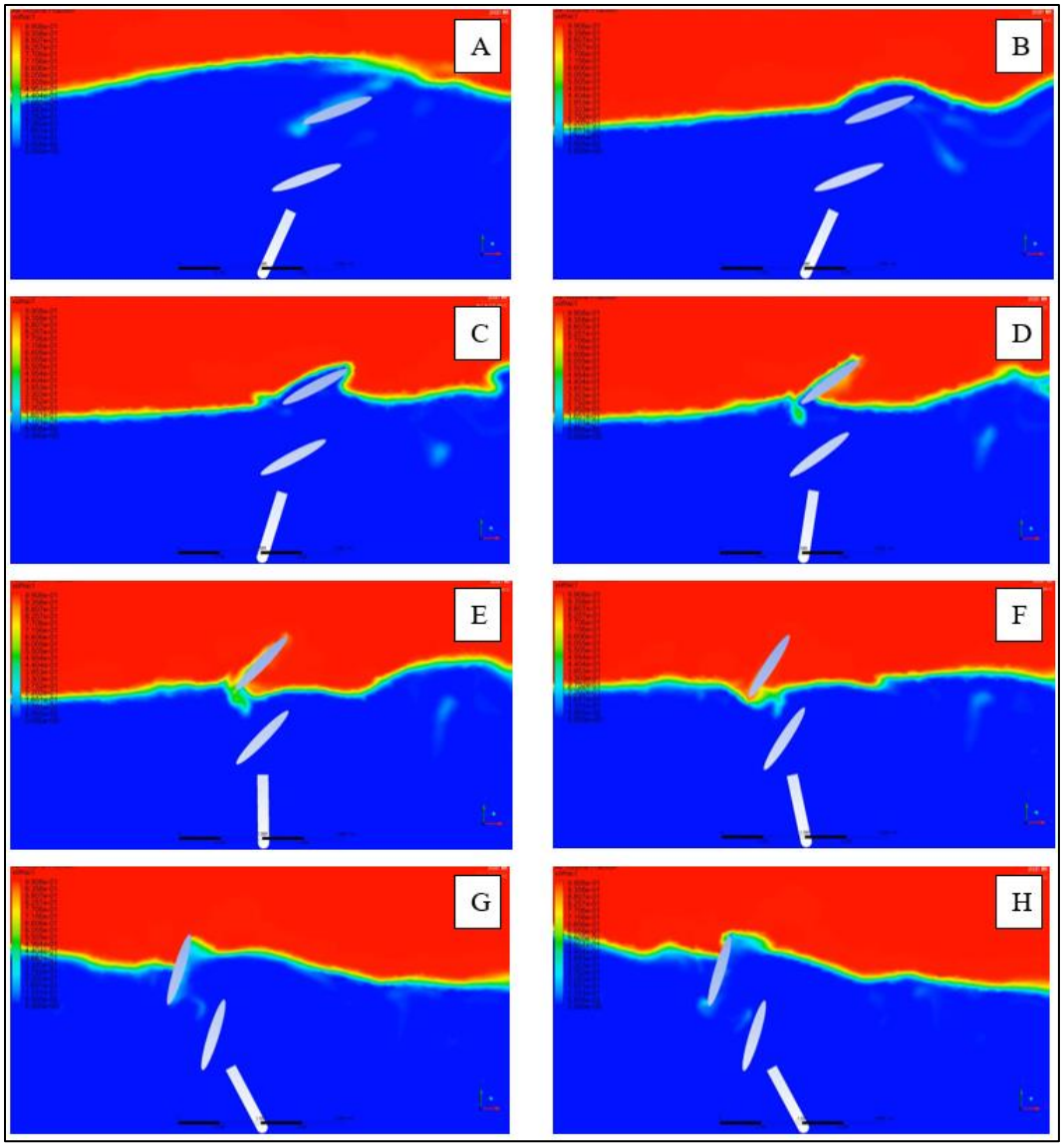

Figure 4-63. Wave Slamming Mitigation and Radiation Wave Formation for 45° Configuration in Wave Condition 2

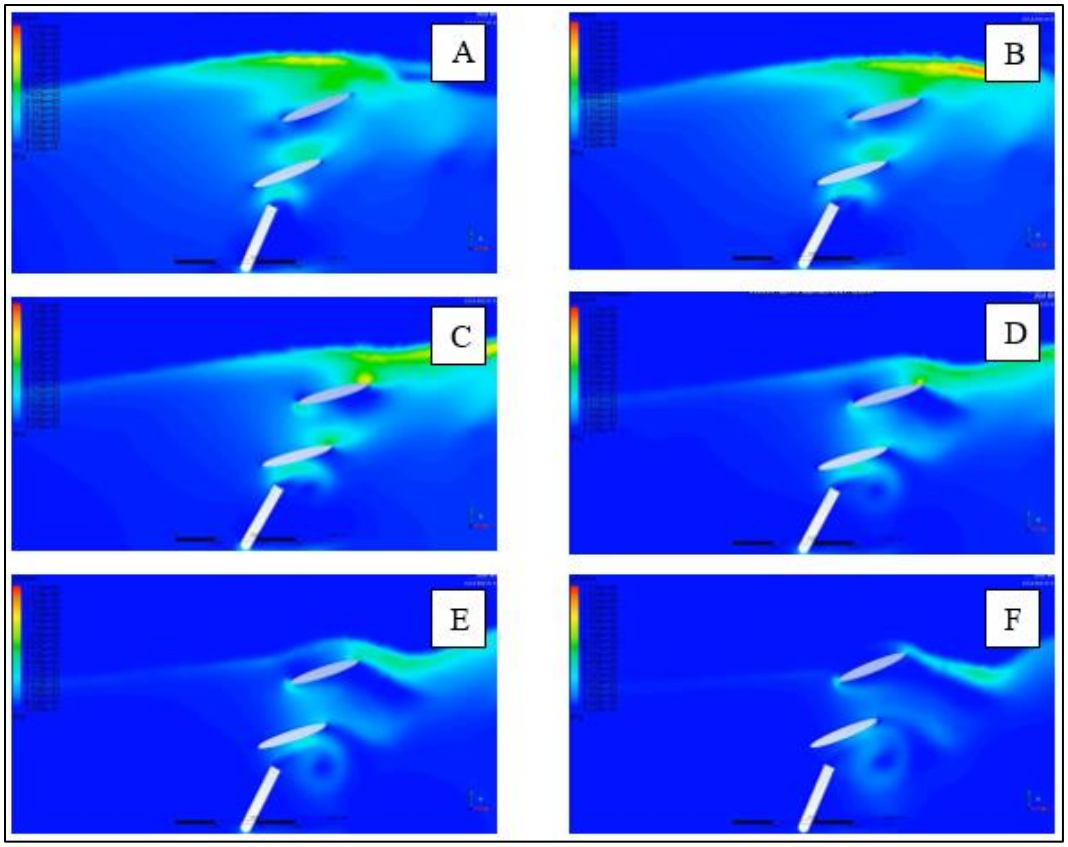

Figure 4-64. Dynamic Pressure Contour for 45° Configuration in Wave Condition 2

4.3.8 30° Configuration

For the 30° configuration in wave condition 1, there existed a small amount of overtopping when the OWSC pitched landward, which resulted in an air pocket forming on the landward side of the upper vane. Similar to the other configurations, this resulted in a hydraulic jump which induced a wave that acted in the negative x-direction on the OWSC. In this case, the wave from the hydraulic jump helped the OWSC reach the seaward end stop until the subsequent wave acted on the device again, which caused it to pitch landward again. The seaward pitching motion resulted in a radiated wave that had a velocity of 3.5 m/s. This did not have much effect on the ensuing wave since the radiated wave quickly diminished. The maximum velocity occurred at the tips of the upper vane, while other large velocity profiles formed across its entire surface area of the upper vane as the OWSC pitched seaward. Most of the vorticity formation occurred on the landward side of the OWSC around the upper vane. Neither wave slamming, nor preliminary signs of wave slamming occurred during this case. During the first incident wave, the upper tip

of the upper vane experienced a dynamic pressure of 3,643 Pa on its landward pitch, and 4,988 Pa on the lower tip of the upper vane during its subsequent seaward pitch.

For the 30° configuration in wave condition 2, depicted in frames A – F in Figure 4-65, the OWSC seemed to shed water very well, but hydraulic jump and radiated waves were still prevalent. The wave that was created by the hydraulic jump impacted the landward face of the OWSC, causing overtopping, which formed a radiated wave with a velocity of 9.25 m/s, shown in Figure 4-66. In this case, the wave from the first hydraulic jump helped the OWSC pitch all the way to its seaward hard stop, thus maximizing motion. When the OWSC impacted its landward end stop, the vanes were almost horizontal. Therefore, the water tended to rest on the surface of the vane longer than normal, which could dampen its consistency of oscillation. The areas that experienced the most dynamic pressure varied depending on which direction the OWSC was pitching. While pitching landward, the largest dynamic pressure occurred on the seaward surface of both vanes. The stagnation point, where velocity is zero, occurred at the tips of both vanes while the OWSC pitched landward and seaward. While oscillating seaward, much of the dynamic pressure occurred on the lower landward side of the OWSC towards the fixed region and lower vane. As the OWSC impacted the end stops, most of the pressure was located at the tips of the lower vane. This may have been due to the OWSC's abrupt stop and the continuation of water flow over this area.

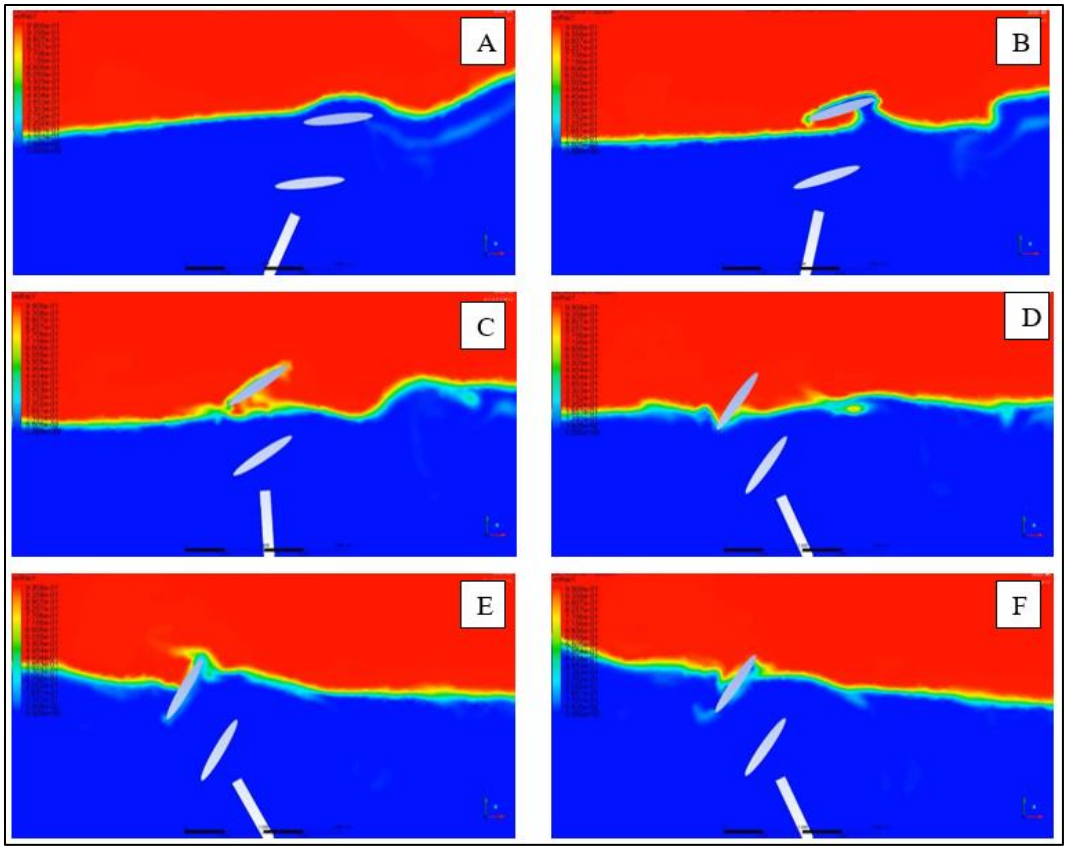

Figure 4-65. Wave Slamming Mitigation and Radiation Wave Formation for 30° Configuration in Wave Condition 2

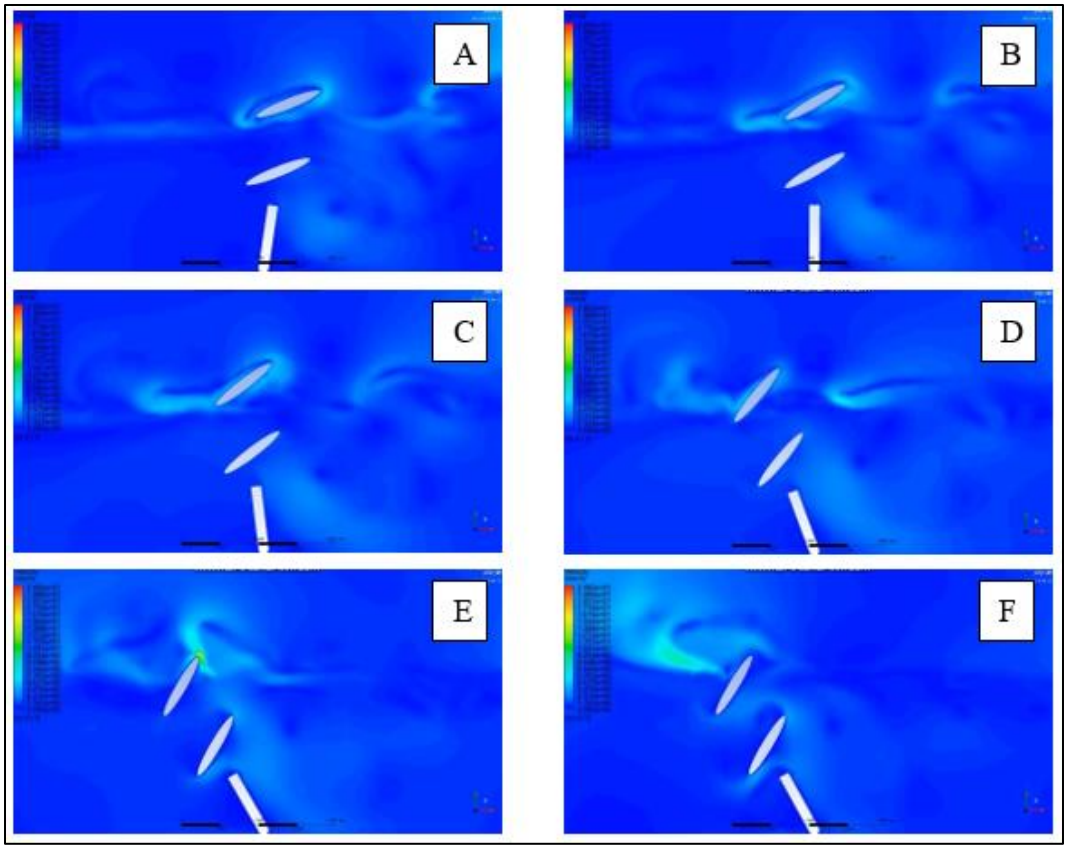

Figure 4-66. Velocity Profile for 30° Configuration in Wave Condition 2

4.3.9 Open Configuration

For the open configuration in wave condition 1, the OWSC never impacted its end stops and no wave slamming occurred. As the force due to the incident wave impacted the OWSC, it slowly pitched landward but stopped soon after due to the rising water level force acting on the bottom face of the upper vane. The open configuration was able to shed water very effectively and pierced through the free surface water level with ease as it oscillated. There existed a small, radiated wave with velocity of 1.83 m/s, but this did not appear to negatively impact on the propagation of the ensuing wave. Most of the turbulence was concentrated on the top surface of the upper vane, and the stagnation point occurred at the sharp radii of the OWSC vanes. Most of the dynamic pressure occurs underneath the lower vane and on the surface of the lower vane, and the contours tend to rotate in the shape of an analemma.

For the open configuration in wave condition 2, depicted in frames A – H in Figure 4-67, the OWSC appeared shed loads better than any other configuration. There was no wave slamming and the radiated wave had velocity of 0.63 m/s. Although there was no wave slamming, the OWSC appeared to easily slice through the water, which caused some disturbances to the surrounding fluid's velocity as shown in Figure 4-68. These disturbances appeared to interrupt the consistency of oscillation, which could negatively impact the device's ability to consistently harvest power. Furthermore, the inconsistent oscillations made it difficult to determine how frequently the OWSC would impact the end stops. This is important since most of the pressure spikes formed when the OWSC impacted its end stops. They were located primarily off the seaward edge of the fixed base, and the landward tips of the upper and lower vanes. There existed some hydrodynamic jump that was similar to the other cases. However, in this case, the radiation wave caused by the hydrodynamic jump did not appear to affect the ensuing wave's speed or height. The water from the ensuing wave appeared to flow naturally over the vanes with little resistance. The pressure contours were mostly concentrated underneath the lower vane and dissipated quickly, possibly due to the profile of the vanes which allowed for water shedding.

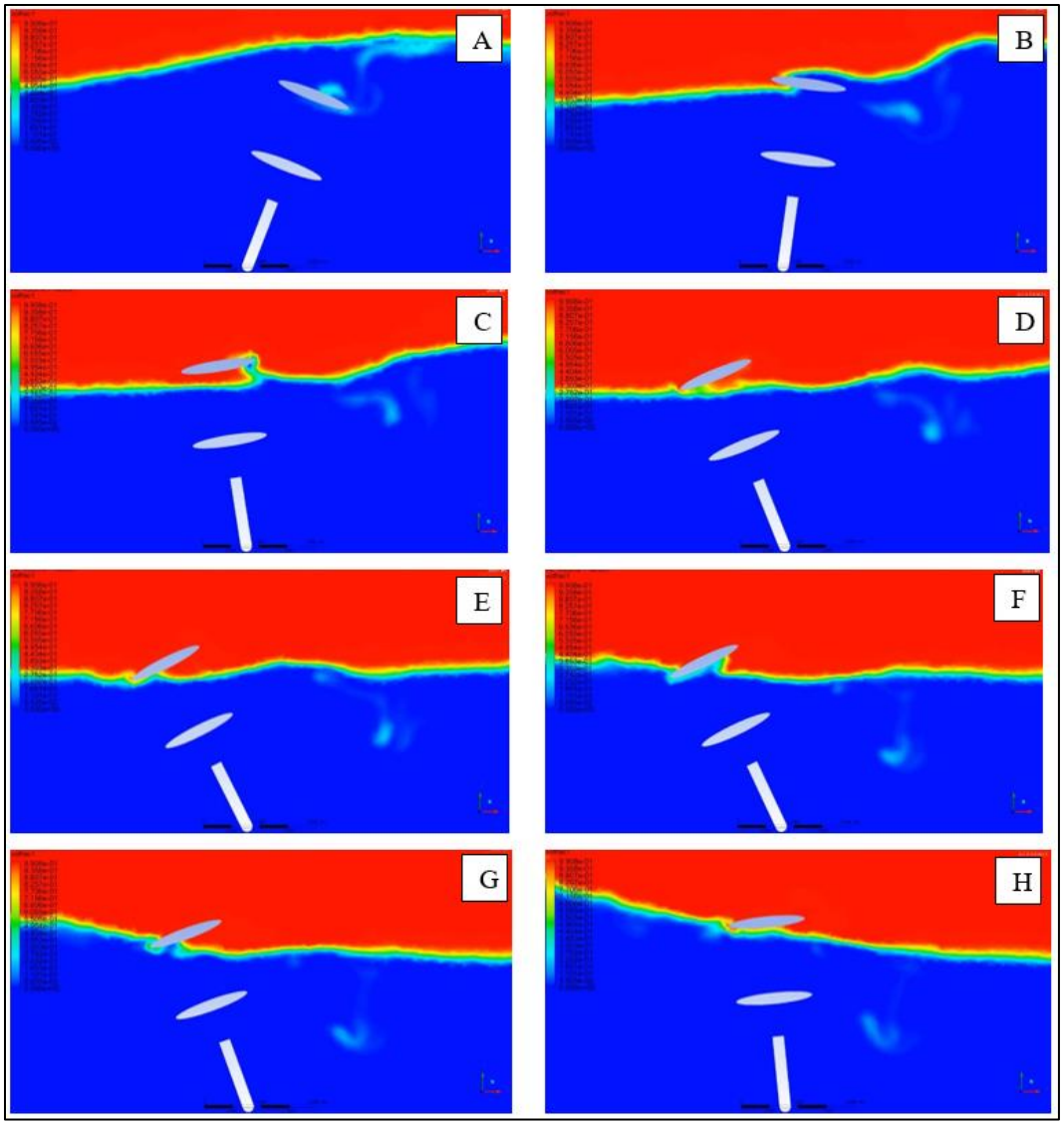

Figure 4-67. Wave Slamming Mitigation and Radiation Wave Formation for Open Configuration in Wave Condition 2

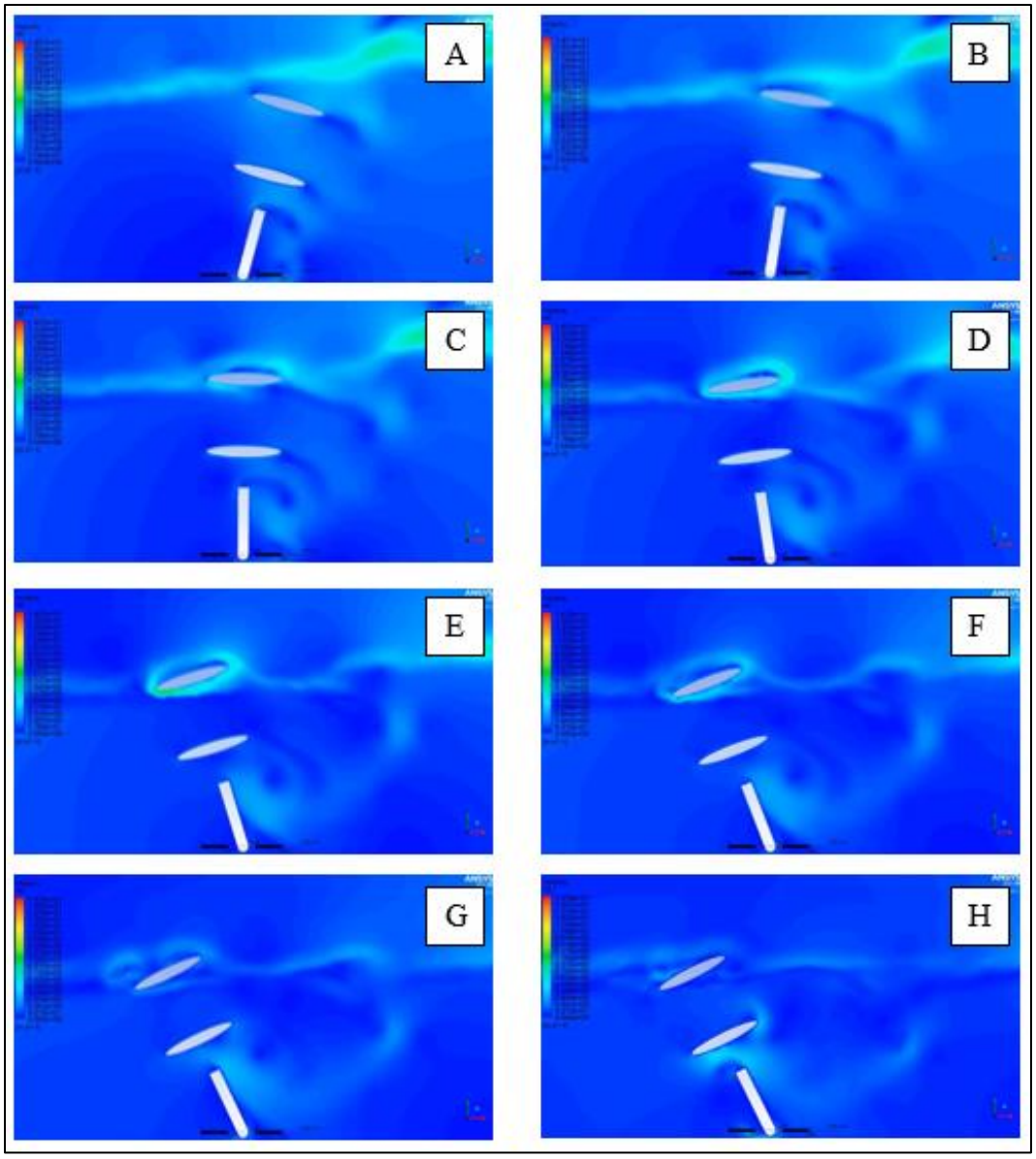

Figure 4-68. Fluid Disturbances Due to Open Configuration

5 Conclusion

The overall purpose of this research was to advance ocean renewable technologies so ocean energy can become utilized as another renewable energy technology. Specifically, this work continues to investigate a nearshore OWSC similar to Nathan Tom et al.'s variable geometry OWSC [9]. Explored in this work was the investigation of the hydrodynamic performance, power generation capabilities, and flow field response of different nearshore OWSC arrangements and configurations in shallow waves under various sea states. This was completed using a combination of frequency-domain analyses, time-domain analyses, and computational fluid dynamics analyses. The configurations included 90° (fully closed), 60°, 45°, 30°, and 0° (fully open). From the fully closed configuration, the vanes were rotated clockwise to 60°, 45°, and 30° until fully open at 0°. The arrangements studied in the frequency-domain analysis included a singular OWSC with 2 adjustable vanes, a 2x2 array and 3x3 array with 2 adjustable vanes, and singular OWSC with 4 adjustable vanes. In the time-domain tool and in CFD, only the single 2-vane OWSC was studied. In all analyses, however, all vane angle configurations were investigated. It was hypothesized that opening the vanes would significantly and consistently reduce the fluid-structure interaction resulting from the surge motion of waves, leading to lower magnitude hydrodynamic coefficients, lower average power production per wave state, and lower potential for wave slamming. The hydrodynamic and power production results indicated that most configurations had consistent and predictable responses, while the closed and 60° vane angle configurations were more sensitive to the vane angle changes. The CFD results indicated that opening the vanes led to a reduction in wave slamming. However, the fluid flow became more unpredictable as the vane angles approached fully open. This resulted in incident waves being dampened by radiated waves, inconsistent OWSC oscillations, and hydraulic jump formation. All of these parameters could lead to challenges with consistent power capture since the OWSC was not oscillating at a consistent frequency and since the fluid flow was less predictable.

5.1 Hydrodynamic Coefficients Conclusions

Regarding the 2-vane OWSC in each vane angle configuration, the results indicated that opening the vanes resulted in less fluid-structure interaction since the magnitude of each coefficient decreased significantly as the vane angles approached 0°. Furthermore, among each configuration,

the radiation damping, and wave excitation values approached zero as the wave frequency increased, and the added mass value approached a constant asymptote, indicating hydrodynamic stability. The results showed that the closed configuration experienced a much higher magnitude of hydrodynamic coefficients for the 2-vane and 4-vane arrangement. An interesting trend was recognized in the 2-vane and 4-vane arrangement. As the vanes were incrementally opened from 60° to 45° to 30° to open, the results also incrementally reduced. However, the change in magnitudes from the closed configuration to the 60° configuration was drastically greater compared to the incremental changes of the other configurations. Regarding the 2x2 and 3x3 array, the results indicated that OWSCs located next to one another had no effect on hydrodynamic coefficients, while OWSCs located in front or behind one another experienced some instability. A potential source of error was that the Aqwa solver is limited to 12,000 diffracting elements, which meant that the mesh quality had to be reduced to fit this criteria.

5.2 Power Production Conclusions

The results from the power matrices indicated that the sea state that would theoretically produce the most power may not always be the sea state that would actually lead to the highest power contribution. The raw maximum power was multiplied by the frequency of sea state occurrence to determine what sea state realistically would lead to the highest contribution of power. To obtain the overall MEAP, all these values were summed to determine how much energy a specific location and specific device would produce annually. Similar to the hydrodynamic coefficient results, there was a drastic change in MAEP between the closed and 60° configuration—42.4%. Whereas the change in MAEP values for the other configurations was not as drastic. When the vanes were incrementally opened from the initial closed position, the fluid-structure interaction decreased since OWSC absorbed less energy. A potential source of error may be due to the fact that WEC-Sim does not account for flow field effects such as turbulence, dynamic pressure, and velocity profile, therefore the velocity of the OWSC may not be accurate once the waves become more energetic.

5.3 Fluid Flow Analysis Conclusions

Two wave conditions were examined in 2D using the VOF method in Ansys Fluent. Wave condition 1 was the calmer condition which did not result in wave slamming for any of the configurations. Wave condition 2 was more energetic and did result in some wave slamming phenomenon. The velocity profile and pressure field were investigated for areas of pressure spikes and turbulence identification. For wave condition 1, most of the turbulence occurred at the tips of the upper vane since it experienced the most interaction with the free surface water level. For wave condition 2, most of the turbulence and pressure spikes occurred as a result of the OWSC impacting the end stops at a high velocity. A concern for the OWSC for both wave conditions was the formation of radiated waves as the OWSC pitched seaward. These radiated waves impacted the ensuing wave before it impacted the OWSC and may have led to dampening of the wave's heigh and velocity. Another interesting observation was the formation of hydraulic jump, which caused a wave to form on the landward side of the OWSC that flows in the negative x-direction. Consistently opening the vanes complicated the flow field and is believed to actually lead to further issues with consistent power capture. That is, if an incident wave housed a certain amount of power, the radiated wave coming from the pitching OWSC may dampen some of that wave, resulting in lower power capture capability. This is a potential source of error.

5.4 Future Work

For the hydrodynamics section and power production section of this work, it is recommended for future studies to investigate an OWSC with a 75° vane angle configuration since there was such a large variability between the closed and 60° configuration. Regarding the arrays, future simulations may include a 1x2 array or 1x3 array. This would result in a finer boundary mesh on each OWSC which could lead to better numerical stability. Finally, for the fluid flow analysis, the 45° and 30° configurations appeared to have similar force, torque, and pressure results. Therefore, it is recommended that future studies include either the 45° configuration or the 30° configuration instead of both. Furthermore, future studies could include analyzing whether or not wave slamming occurs for intermediate wave conditions. Finally, a full fluid structure interaction could be included in the future to understand the stresses, strains, and fatigue life of these devices.

6 References

[1] F. Dias *et al.*, "Analytical and computational modelling for wave energy systems: the example of oscillating wave surge converters," *Acta Mechanica Sinica/Lixue Xuebao*. 2017.

[2] M. Previsic, "Optimal WEC Controls using Causal and MPC Methods."

[3] N. Tom, M. Lawson, Y. Yu, and A. Wright, "Preliminary Analysis of an Oscillating Surge Wave Energy Converter with Controlled Geometry," in *11th European Wave and Tidal Energy Conference*, 2015.

[4] B. Drew, A. R. Plummer, and M. N. Sahinkaya, "A review of wave energy converter technology," *Proceedings of the Institution of Mechanical Engineers, Part A: Journal of Power and Energy*. 2009.

[5] A. A. E. Price, C. J. Dent, and A. R. Wallace, "On the capture width of wave energy converters," *Appl. Ocean Res.*, 2009.

[6] Y. H. Yu, K. Hallett, Y. Li, and C. Hotimsky, "Design and analysis for a floating oscillating surge wave energy converter," *Proc. Int. Conf. Offshore Mech. Arct. Eng. - OMAE*, vol. 9B, no. March, 2014.

[7] N. M. Tom, M. J. Lawson, Y. H. Yu, and A. D. Wright, "Development of a nearshore oscillating surge wave energy converter with variable geometry," *Renew. Energy*, 2016.

[8] G. M. Kelly, N. Tom, Y. H. Yu, R. Thresher, and N. Abbas, "Development of the second-generation oscillating surge wave energy converter with variable," in *Proceedings of the International Offshore and Polar Engineering Conference*, 2017.

[9] Y. H. Yu, K. Hallett, Y. Li, and C. Hotimsky, "Design and analysis for a floating oscillating surge wave energy converter," in *Proceedings of the International Conference on Offshore Mechanics and Arctic Engineering - OMAE*, 2014.

[10] R. G. Coe, V. S. Neary, M. J. Lawson, Y. Yu, and J. Weber, "Extreme Conditions Modeling Workshop Report," 2014.

[11] G. Chang, C. A. Jones, J. D. Roberts, and V. S. Neary, "A comprehensive evaluation of factors affecting the levelized cost of wave energy conversion projects," *Renew. Energy*, 2018.

[12] A. R. Dallman and V. S. Neary, "Characterization of U.S. Wave Energy Converter (WEC) Test Sites: A Catalogue of Met-Ocean Data," *Sandia Natl. Lab.*, 2015.

[13] Y.-H. Yu, D. S. Jenne, R. Thresher, A. Copping, S. Geerlofs, and L. Hanna, "Reference Model 5: Oscillating Surge Wave Energy Converter," *NREL Rep.*, vol. 5, no. January, 2015.

[14] Y. Wei, T. Abadie, A. Henry, and F. Dias, "Wave interaction with an Oscillating Wave Surge Converter. Part II: Slamming," *Ocean Eng.*, 2016.

[15] W. Bach, "Fossil fuel resources and their impacts on environment and climate," *Int. J. Hydrogen Energy*, 1981.

[16] I. R. E. Agency, *Renewable Power Generation Costs in 2018*. 2018.

[17] "Wave Catcher," Aug. 2010.

[18] J. Leijon and C. Boström, "Freshwater production from the motion of ocean waves – A review," *Desalination*, vol. 435, no. June 2017, pp. 161–171, 2018.

[19] Y. H. Yu and D. Jenne, "Analysis of a wave-powered, reverse-osmosis system and its economic availability in the United States," *Proc. Int. Conf. Offshore Mech. Arct. Eng. - OMAE*, vol. 10, no. August, 2017.

[20] A. Muratoglu and M. I. Yuce, "Advances in hydropower production: marine energy conversion," no. November, 2016.

[21] D. S. Jenne, Y.-H. Yu, and V. Neary, "Levelized Cost of Energy Analysis of Marine and Hydrokinetic Reference Models," in *3rd Marine Energy Technology Symposium*, 2015.

[22] M. Folley, T. Whittaker, and M. Osterried, "The Oscillating Wave Surge Converter," in *Proceedings of the International Offshore and Polar Engineering Conference*, 2004.

[23] R. Pelc and R. M. Fujita, "Renewable energy from the ocean," *Mar. Policy*, 2002.

[24] A. Clément *et al.*, “Wave energy in Europe: Current status and perspectives,” *Renewable and Sustainable Energy Reviews*. 2002.
[25] K. Gunn and C. Stock-Williams, “Quantifying the global wave power resource,” *Renew. Energy*, 2012.
[26] L. Kilcher, M. Fogarty, M. Lawson, L. Kilcher, M. Fogarty, and M. Lawson, “Marine Energy in the United States : An Overview of Opportunities Marine,” 2021.
[27] NOAA, “Why does the ocean have waves?,” *Form. Wave*, 2018.
[28] van ’t Hoff, “Hydrodynamic Modelling of the Oscillating Wave Surge Converter,” *Queen’s Univ. Belfast*, 2009.
[29] M. Folley, “The Wave Energy Resource,” 2017.
[30] A. D. D. Craik, “GEORGE GABRIEL STOKES ON WATER WAVE THEORY,” *Annu. Rev. Fluid Mech.*, 2005.
[31] S. M. Elsayed, H. Oumeraci, and N. Goseberg, “Erosion and breaching of coastal barriers in a changing climate: Associated processes and implication for contamination of coastal aquifers,” in *Proceedings of the Coastal Engineering Conference*, 2018.
[32] M. J. Tucker and E. G. Pitt, “Waves in Ocean Engineering,” in *Waves in Ocean Engineering*, 2001.
[33] “Technology white paper on wave energy potential on the U.S. outer continental shelf,” in *Ocean Energy: Technologies and Potential Environmental Effects*, 2012.
[34] L. H. Holthuijsen, *Waves in oceanic and coastal waters*. 2007.
[35] “Wave Energy and Wave Changes with Depth | manoa.hawaii.edu/ExploringOurFluidEarth.” [Online]. Available: https://manoa.hawaii.edu/exploringourfluidearth/physical/waves/wave-energy-and-wave-changes-depth. [Accessed: 18-Mar-2020].
[36] J. Twidell, *Renewable Energy Resources*. 2006.
[37] R. Weiss and H. Bahlburg, “A Note on the Preservation of Offshore Tsunami Deposits,” *J. Sediment. Res.*, 2006.
[38] G. F. Vargas and E. B. C. Schettini, “Application of an alternative mesh morphing method on the numerical modeling of oscillating wave surge converters,” *Rev. Bras. Recur. Hidricos*, 2019.
[39] A. Babarit, “A database of capture width ratio of wave energy converters,” *Renew. Energy*, 2015.
[40] National Renewable Energy Laboratory (NREL), “Renewable Electricity Futures Study,” *U.S. Dep. Energy*, vol. 1, p. 280, 2012.
[41] S. Doyle and G. A. Aggidis, “Development of multi-oscillating water columns as wave energy converters,” *Renew. Sustain. Energy Rev.*, vol. 107, no. January, pp. 75–86, 2019.
[42] M. Windows, M. Corporation, K. Hori, and A. Sakajiri, “Conceptual Design, Feasibility Analysis, Modeling, and Simulation,of the Dynamics and Control, of a Mobile Underwater Turbine System to harvest Marine Hydrokinetic Energy from the Gulf Stream.”
[43] M. Folley, T. W. T. Whittaker, and J. V. Hoff, “The design of small seabed-mounted bottom-hinged wave energy converters,” *Proc. 7th Eur. Wave Tidal Energy Conf.*, 2007.
[44] J. Lucas, M. Livingstone, M. Vuorinen, and J. Cruz, “Development of a wave energy converter (WEC) design tool – application to the WaveRoller WEC including validation of numerical estimates,” *Proc. 4th Int. Conf. Ocean Energy*, 2012.
[45] Eere, “Powering the Blue Economy: Exploring Opportunities for Marine Renewable Energy in Maritime Markets,” 2019.
[46] A. Babarit, J. Hals, M. J. Muliawan, A. Kurniawan, T. Moan, and J. Krokstad, “Numerical benchmarking study of a selection of wave energy converters,” *Renew. Energy*, vol. 41, pp. 44–63, 2012.
[47] Y. Li and Y. H. Yu, “A synthesis of numerical methods for modeling wave energy converter-point absorbers,” *Renewable and Sustainable Energy Reviews*. 2012.
[48] R. A. Fine and F. J. Millero, “Compressibility of water as a function of temperature and pressure,” *J. Chem. Phys.*, 1973.
[49] A. D. D. Craik, “THE ORIGINS OF WATER WAVE THEORY,” *Annu. Rev. Fluid Mech.*, 2004.

[50] H. E. Krogstad, “LINEAR WAVE THEORY Regular waves,” *Sci. Technol.*, 2000.
[51] J. A. Clarke, G. Connor, A. D. Grant, and C. M. Johnstone, “Design and testing of a contra-rotating tidal current turbine,” *Proc. Inst. Mech. Eng. Part A J. Power Energy*, 2007.
[52] S. A. Thorpe and O. M. Phillips, “The Dynamics of the Upper Ocean,” *Math. Gaz.*, 1968.
[53] B. Bosma, “On the design, modeling, and testing of ocean wave energy converters.” 2013.
[54] W. Koo and J. D. Kim, “Simplified formulas of heave added mass coefficients at high frequency for various two-dimensional bodies in a finite water depth,” *Int. J. Nav. Archit. Ocean Eng.*, 2015.
[55] A. H. Techet, “2.016 Hydrodynamics.”
[56] K. Ruehl, C. Michelen, S. Kanner, M. Lawson, and Y. H. Yu, “Preliminary verification and validation of WEC-SIM, an open-source wave energy converter design tool,” in *Proceedings of the International Conference on Offshore Mechanics and Arctic Engineering - OMAE*, 2014.
[57] Y. H. Yu and D. Jenne, “Numerical modeling and dynamic analysis of a wave-powered reverse-osmosis system,” *J. Mar. Sci. Eng.*, 2018.
[58] Y. Wei, A. Rafiee, A. Henry, and F. Dias, “Wave interaction with an oscillating wave surge converter, Part I: Viscous effects,” *Ocean Eng.*, 2015.
[59] A. Babarit, J. Hals, M. J. Muliawan, A. Kurniawan, T. Moan, and J. Krokstad, “Numerical benchmarking study of a selection of wave energy converters,” *Renew. Energy*, 2012.
[60] T. D. Canonsburg, “AQWA User Manual,” *Knowl. Creat. Diffus. Util.*, vol. 15317, no. October, pp. 724–746, 2012.
[61] ANSYS, “Aqwa Theory Manual,” *Ansys*, 2015.
[62] S. X. Du, D. A. Hudson, W. G. Price, and P. Temarel, “The occurrence of irregular frequencies in forward speed ship seakeeping numerical calculations,” *Ocean Eng.*, 2011.
[63] K. Ruehl, C. Michelen, S. Kanner, M. Lawson, and Y. H. Yu, “Preliminary verification and validation of WEC-SIM, an open-source wave energy converter design tool,” in *Proceedings of the International Conference on Offshore Mechanics and Arctic Engineering - OMAE*, 2014.
[64] Y.-H. Yu, M. Lawson, K. Ruehl, and C. Michelen, “Development and Demonstration of the WEC-Sim Wave Energy Converter Simulation Tool,” *2nd Mar. Energy Technol. Symp.*, pp. 1–8, 2014.
[65] K. Ruehl and Y.-H. Yu, “WEC-Sim (Wave Energy Converter SIMulator),” 2014. [Online]. Available: https://wec-sim.github.io/WEC-Sim/man/publications.html.
[66] Z. Yu and J. Falnes, “State-space modelling of a vertical cylinder in heave,” *Appl. Ocean Res.*, 1995.
[67] R. Taghipour, T. Perez, and T. Moan, “Hybrid frequency-time domain models for dynamic response analysis of marine structures,” *Ocean Eng.*, 2008.
[68] J. Sun, “Research on vocal sounding based on spectrum image analysis,” *Eurasip J. Image Video Process.*, 2019.
[69] W. J. Pierson and L. Moskowitz, “A proposed spectral form for fully developed wind seas based on the similarity theory of S. A. Kitaigorodskii,” *J. Geophys. Res.*, 1964.
[70] K. Hasselmann *et al.*, “Measurements of wind-wave growth and swell decay during the joint North Sea wave project (JONSWAP).” 1973.
[71] M. Pawłowski, “Sea spectra revisited,” *Fluid Mech. its Appl.*, 2011.
[72] J. V. Ringwood, G. Bacelli, and F. Fusco, “Energy-maximizing control of wave-energy converters: The development of control system technology to optimize their operation,” *IEEE Control Syst.*, vol. 34, no. 5, pp. 30–55, 2014.
[73] P. Balitsky, N. Quartier, G. V. Fernandez, V. Stratigaki, and P. Troch, “Analyzing the near-field effects and the power production of an array of heaving cylindrical WECS and OSWECs using a coupled hydrodynamic-PTO model,” *Energies*, 2018.
[74] G. Moretti, D. Forehand, R. Vertechy, M. Fontana, and D. Ingram, “Modeling of an oscillating wave surge converter with Dielectric Elastomer power take-off,” in *Proceedings of the International Conference on Offshore Mechanics and Arctic Engineering - OMAE*, 2014.
[75] X. Jiang, S. Day, and D. Clelland, “Hydrodynamic responses and power efficiency analyses of an oscillating wave surge converter under different simulated PTO strategies,” *Ocean Eng.*, 2018.

[76] R. P. F. Gomes, M. F. P. Lopes, J. C. C. Henriques, L. M. C. Gato, and A. F. O. Falcão, "The dynamics and power extraction of bottom-hinged plate wave energy converters in regular and irregular waves," *Ocean Eng.*, 2015.
[77] M. Eslahpazir, R. Krull, and U. Krühne, "Computational fluid dynamics," in *Comprehensive Biotechnology*, 2019.
[78] A. Fluent, "Ansys Fluent Theory Guide," *ANSYS Inc., USA*, 2013.
[79] Douglas, "Fluid Mechanics Fifth Edition," *Pearson*, 2005. .
[80] B. E. Launder and D. B. Spalding, "Lectures in Mathematical Models of Turbulence," *Acad. Press*, 1972.
[81] V. Yakhot and S. A. Orszag, "Renormalization group analysis of turbulence. I. Basic theory," *J. Sci. Comput.*, 1986.
[82] T. H. Shih, W. W. Liou, A. Shabbir, Z. Yang, and J. Zhu, "A new k-ϵ eddy viscosity model for high reynolds number turbulent flows," *Comput. Fluids*, 1995.
[83] D. C. Wilcox, *Turbulence modeling for CFD*. 1993.
[84] F. R. Menter, "Two-equation eddy-viscosity turbulence models for engineering applications," *AIAA J.*, 1994.
[85] F. R. Menter, M. Kuntz, and R. Langtry, "Ten Years of Industrial Experience with the SST Turbulence Model Turbulence heat and mass transfer," *Cfd.Spbstu.Ru*, 2003.
[86] a W. Adamson and a P. Gast, *Physical Chemistry of Surfaces Sixth Edition*. 1997.
[87] D. R. Smith, I. W. Geer, E. W. Mills, J. M. Moran, and R. S. Weinbeck, "The maury project, datastreme ocean, and online ocean studies: Ams initiatives in ocean science education," *Mar. Technol. Soc. J.*, 2005.
[88] N. Tom, M. Lawson, and Y. H. Yu, "Demonstration of the recent additions in modeling capabilities for the WEC-Sim wave energy converter design tool," in *Proceedings of the International Conference on Offshore Mechanics and Arctic Engineering - OMAE*, 2015.
[89] Y. H. Yu, J. Van Rij, R. Coe, and M. Lawson, "Preliminary wave energy converters extreme load analysis," in *Proceedings of the International Conference on Offshore Mechanics and Arctic Engineering - OMAE*, 2015.
[90] Y. Wei, A. Rafiee, B. Elsaesser, and F. Dias, "Numerical simulation of an oscillating wave surge converter," in *Proceedings of the International Conference on Offshore Mechanics and Arctic Engineering - OMAE*, 2013.
[91] K. L. De Koker, G. Crevecoeur, B. Meersman, M. Vantorre, and L. Vandevelde, "A power take-off and control strategy in a test wave energy converter for a moderate wave climate," *Renew. Energy Power Qual. J.*, 2016.
[92] N. M. Tom, "Revisiting theoretical limits for one-degree-of-freedom wave energy converters," in *ASME 2020 14th International Conference on Energy Sustainability, ES 2020*, 2020.
[93] A. Albert, G. Berselli, L. Bruzzone, and P. Fanghella, "Mechanical design and simulation of an onshore four-bar wave energy converter," *Renew. Energy*, 2017.
[94] F. F. Wendt *et al.*, "International Energy Agency Ocean Energy Systems Task 10 Wave Energy Converter Modeling Verification and Validation," in *12th European Wave and Tidal Energy Conferenc, Cork, Ireland*, 2017.
[95] J. D. Isdale and R. Morris, "Physical properties of sea water solutions: density," *Desalination*, 1972.
[96] a Fluent, "ANSYS Fluent 12.0 user's guide," *Ansys Inc*, 2009.
[97] I. M. Hauner, A. Deblais, J. K. Beattie, H. Kellay, and D. Bonn, "The Dynamic Surface Tension of Water," *J. Phys. Chem. Lett.*, 2017.
[98] A. Büchner, T. Knapp, M. Bednarz, P. Sinn, and A. Hildebrandt, "Loads and dynamic response of a floating wave energy converter due to regular waves from CFD simulations," in *Proceedings of the International Conference on Offshore Mechanics and Arctic Engineering - OMAE*, 2016.
[99] "Water Wave Theories." [Online]. Available: https://commons.wikimedia.org/wiki/File:Water_wave_theories.svg.

[100] M. A. Bhinder and J. Murphy, “Evaluation of the viscous drag for a domed cylindrical moored wave energy converter,” *J. Mar. Sci. Eng.*, 2019.
[101] J. N. Newman, B. Sortland, and T. Vinje, “ADDED MASS AND DAMPING OF RECTANGULAR BODIES CLOSE TO THE FREE SURFACE.,” *J. Sh. Res.*, 1984.
[102] J. P. Kofoed and M. Folley, “Determining Mean Annual Energy Production,” in *Numerical Modelling of Wave Energy Converters*, 2016.
[103] S. Ashwindran, A. A. Azizuddin, and A. N. Oumer, “Computational fluid dynamic (CFD) of vertical-axis wind turbine: Mesh and time-step sensitivity study,” *J. Mech. Eng. Sci.*, 2019.
[104] “(2) (PDF) Power Extraction by a Nearshore Oscillating Wave Surge Converter (OWSC).” [Online]. Available: https://www.researchgate.net/publication/327791391_Power_Extraction_by_a_Nearshore_Oscillating_Wave_Surge_Converter_OWSC. [Accessed: 20-Mar-2020].
[105] N. Fatchurrohman and S. T. Chia, “Performance of hybrid nano-micro reinforced mg metal matrix composites brake calliper: Simulation approach,” in *IOP Conference Series: Materials Science and Engineering*, 2017.

Appendix A

6.1 SolidWorks Design

6.1.1 Orientation

It was important that the OWSC was oriented in the proper direction. Since the WEC-Sim and Aqwa coordinate systems were defined with the z-axis being the vertical axis, the x-axis being the direction of wave propagation, and the y-axis defined by the right-hand rule, this orientation remained consistent for the SW model. It should be noted that the origin of the z-axis was at the free surface water level (FSWL) with the positive z-direction being away from the sea floor. The profile of the OWSC was designed in the XZ plane, namely the Top Plane in SW.

6.1.2 Design

It was important that the units being used are from the metric system. This was verified by navigating to *Tools* > *Options* > *Document Properties Tab* > *Units* > *MKS*. The metric system was used consistently throughout SW, Aqwa, and WEC-Sim.

Some of the design considerations that were abided by include sea depth, amount that which the OWSC pierces the surface of the water, and the OWSC width. For this study, these details, along with several others, are described in Table 6-1. The fillet radius of the OWSC is important because sharp edges can create vortices which lead to undesirable hydrodynamic diffraction effects [104].

Table 6-1. OWSC Dimensions

Sea Depth	3.3 m
OWSC height, width, thickness	4 m, 2 m, 0.1 m
Surface Piercing	20% of OWSC height
OWSC Fillet Radius	0.1 m

6.1.3 Coordinates

Aforementioned, it was very important that the origin was centered with respected to the OWSC's thickness and width, and then vertically above the FSWL. This is because Aqwa imports the SW file with the same coordinate system. Since the geometry studied here was piercing the surface of the water by 20% of the OWSC height, or 0.8 m, the global coordinate system was at the line

where the OWSC pierces the surface of the water. That is, at the origin, the coordinates were [0, 0, 0] meters. This can be seen in Figure 6-1. At this point, the center of gravity of the OWSC was located at [0, 0, 1.81132] meters.

6.1.4 Moment of Inertia Properties

The moment of inertia properties were a critical aspect of this study. First a material or density was specified. In this case, the OWSC had a density of 256.25 kg/m^3, or half the density of sea water. SW displayed two values for the moment of inertia. The first one, L_{xx}, L_{yy}, and L_{zz}, was the moments of inertia taken with the center of mass and aligned with the output coordinate system. This was the moment of inertia about the center of mass of the OWSC. The second one, I_{xx}, I_{yy}, and I_{zz}, was the moments of inertia that were taken at the output coordinate system. For this study, L_{xx}, L_{yy}, and L_{zz} were used. These properties were obtained by navigating to *Evaluate > Mass Properties*. Figure 6-2 shows how to navigate to SW Mass Properties, and Table 6-2 outlines the properties given by SW for this specific case.

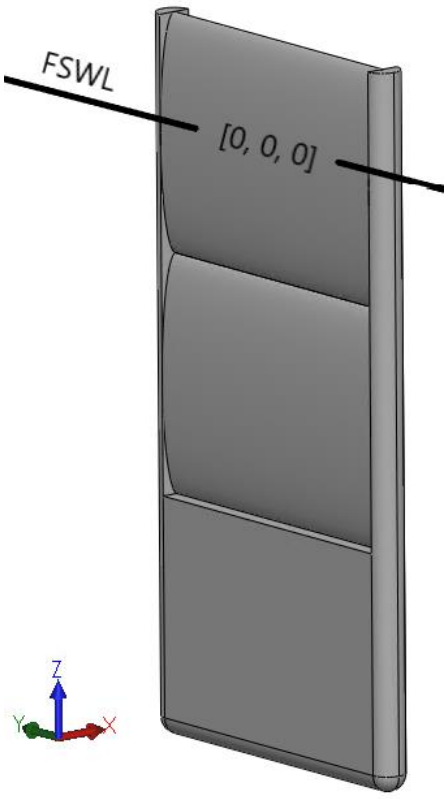

Figure 6-1. OWSC Coordinates

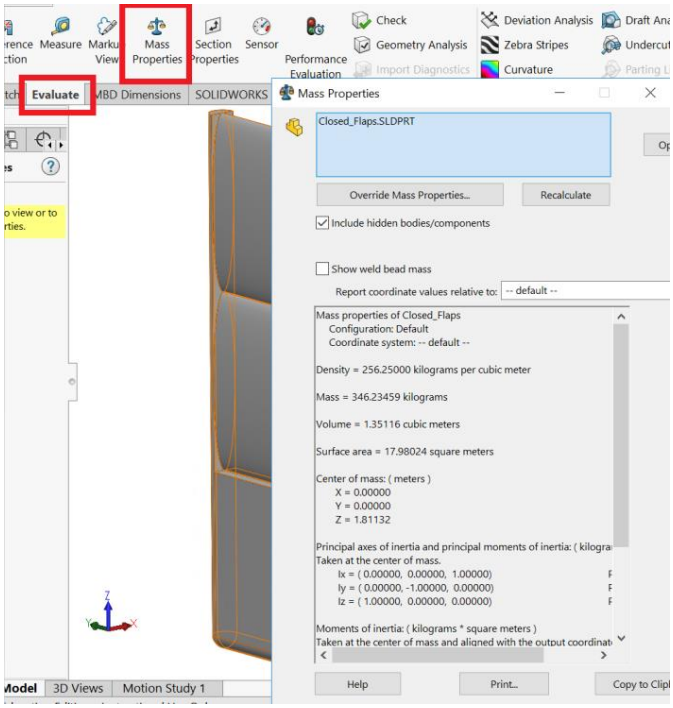

Figure 6-2. Navigating to Mass Properties in SW

Table 6-2. Mass Properties Summary for OWSC

Mass [kg]	346
Density [kg/m^3]	256.25
Locataion of Mass [m]	[0, 0, 1.28688]
Moments of Inertia, L_{xx}, L_{yy}, and L_{zz} [kg/m^2]	1710.7, 1598.4, 114.2

6.1.5 Exporting Files

There were various files saved for the OWSC: an IGES file (.IGS) for Aqwa, a default SolidWorks Part file (.SLDPT), and a stereolithographic file (.STL) to later be used in WEC-Sim.

It should be noted that SW would sometimes export .STL files in units of millimeters (mm) instead of meters (m). This was changed by navigating to *Tools* > *Options* > *Export* > *File Format* > *.STL* > Unit: *Meters.* Also, it is important that the *Do not translate STL output data to positive space* box was checked. This can be seen in Figure 6-3 and Figure 6-4.

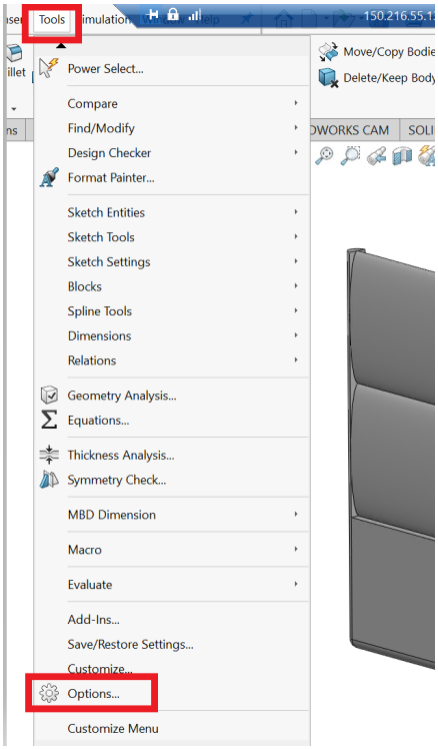

Figure 6-3. STL Export Step 1 of 2

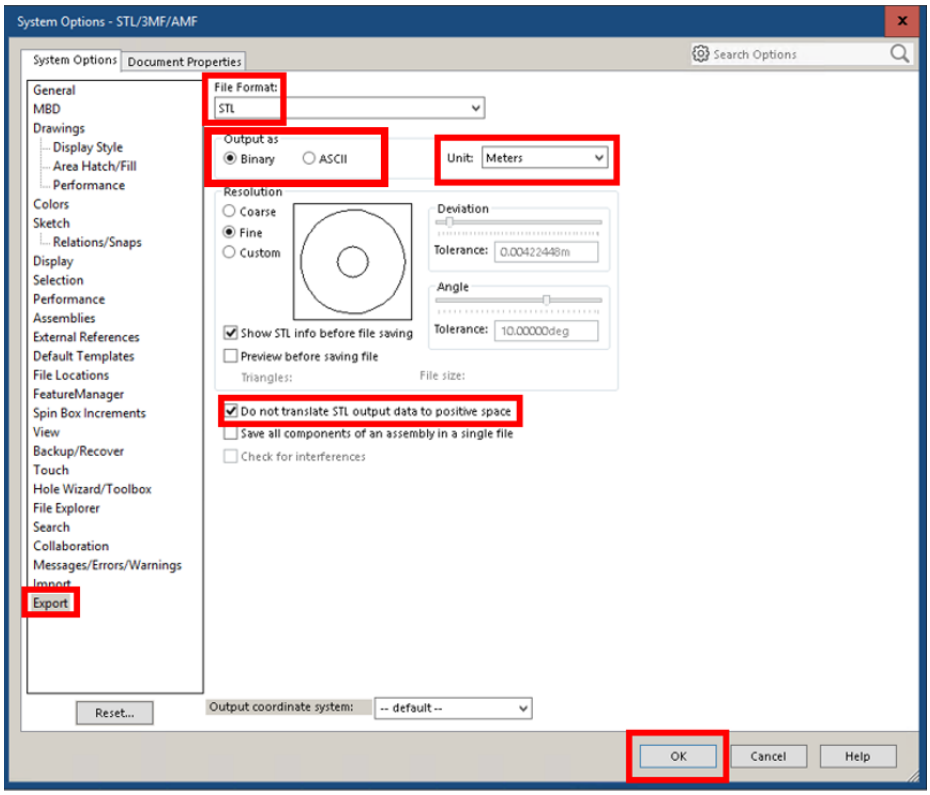

Figure 6-4. STL Export Step 2 of 2

Appendix B

6.2 Hydrodynamic Simulation Setup

The units being used were from the metric system. In the Workbench suite, this was verified by navigating to the toolbar and selecting *Units* > *Metric*. Next, the *Hydrodynamic Diffraction* module was selected and dragged from the *Toolbox* window, into the *Project Schematic* window. A name was given to this module once imported. For this case, the name "*Closed OWSCs*" was used. A new Design Modeler geometry was created, shown in Figure 6-5. Here, the geometry created in SolidWorks was imported in IGS format.

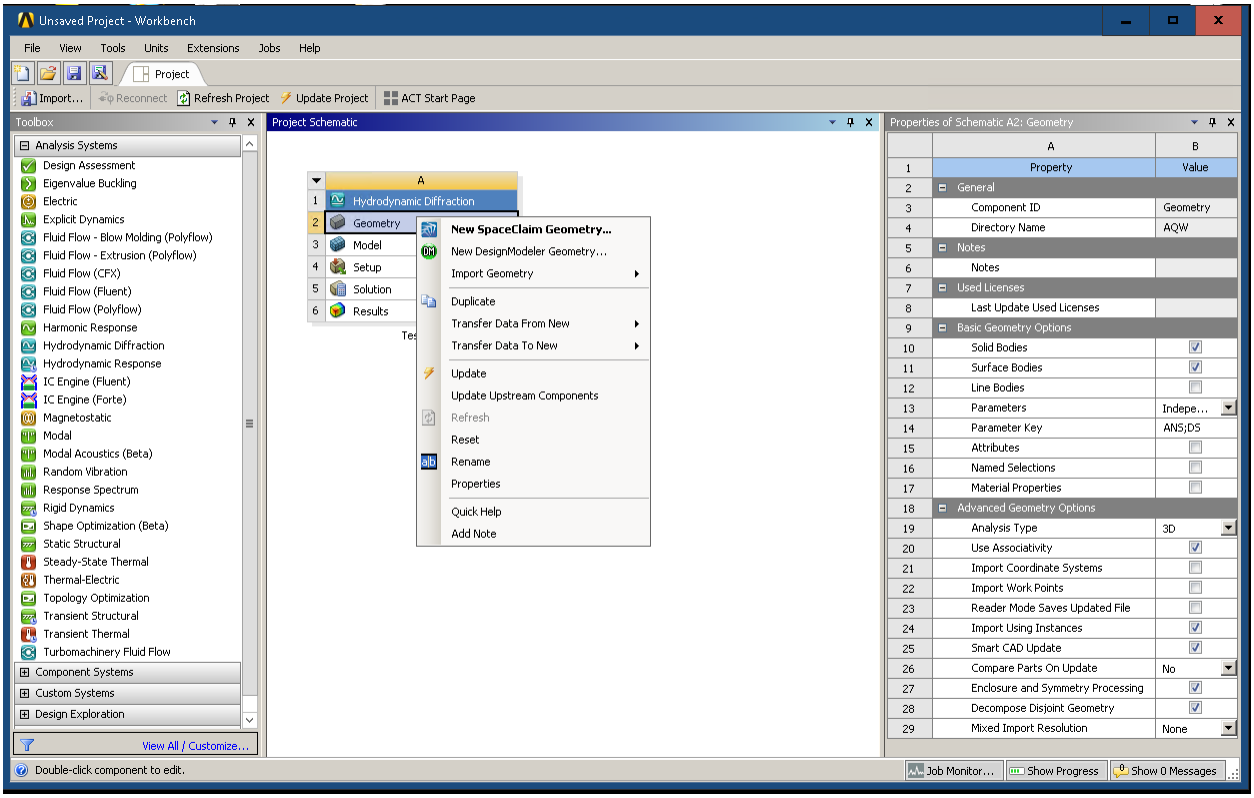

Figure 6-5. Getting Started and Opening *DesignModeler* to Import External SolidWorks Geometry

A geometry file was imported by navigating to the toolbar and selecting *File* > *Import External Geometry File* and the .IGS file that was created in SolidWorks was imported. When the file was imported, it did not show up in the graphics window immediately. The yellow lightning bolt that

says Generate  was used to display the model. Before this, it was necessary to navigate to the *Details View* panel and ensure the *Surface Bodies* option was set to *Yes* and the *Simplify Geometry* option was set to *Yes*. This simplified the geometry so Aqwa could make any necessary repairs. Finally, it was ensured that the *XYPlane* was selected for the *Base Plane*. Once this was done, the *Generate* button was selected. This process is shown in Figure 6-6.

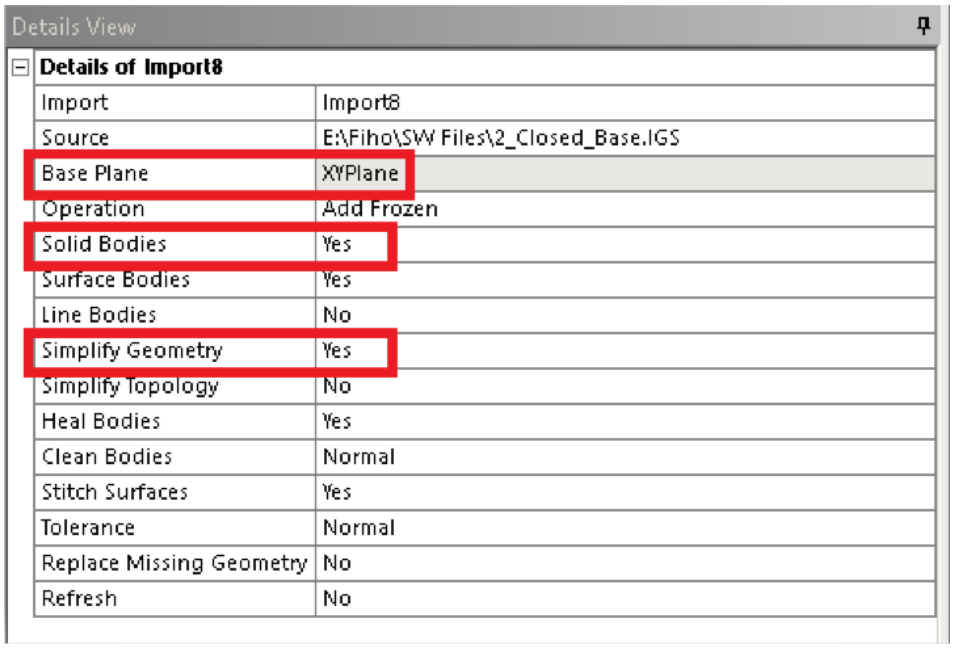

Figure 6-6. Simplifying Geometry in the *Details View* Panel

The thickness of the OWSC was 0. In order to do this, *Create* > *Thin/Surface* was selected from the toolbar. Then in the *Details View* panel, *Selection Type* was changed to *Bodies Only*. Next, the yellow highlighted region that said *Geometry* was selected, and *Not Selected* was clicked. This allowed selection of the OWSC using CTRL + Click. Next, the thickness was changed by navigating to *FD1, Thickness (>=0)* and the value was changed to 0. Finally, the *Generate* was selected to finalize the changes. See Figure 6-7 and Figure 6-8 for this procedure.

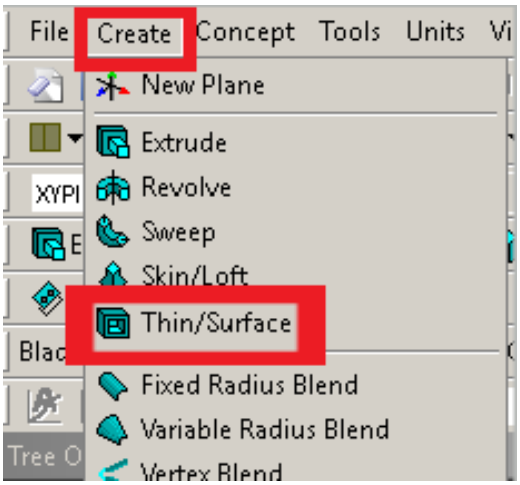

Figure 6-7. Details of the Thin Feature

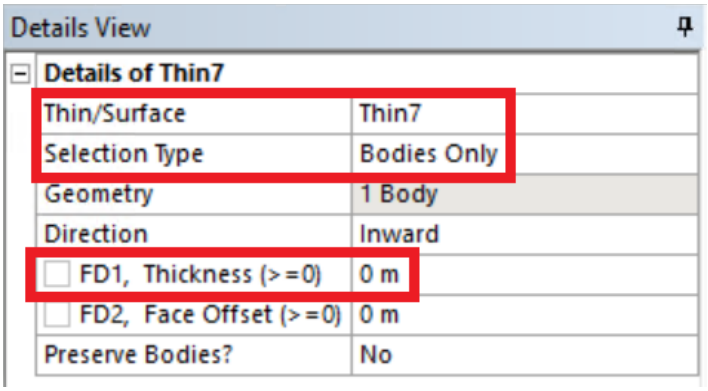

Figure 6-8. Slicing the Geometry at the FSWL

At this point there were be 2 bodies and 2 parts in the *Tree Outline* – One for the portion of the OWSC that pierced the surface of the water and one for portion of the OWSC that was submerged. These sections were renamed and can be seen below in Table 6-3.

Table 6-3. Renaming Surface Parts for Ease of Identification

Default Name	**Renamed**
"Surface1"	"top"
"Surface2"	"bottom"

The final requirement to make sure was satisfied was the formation of parts that were specific for each part. That is, there was 1 unique part for the OWSC. This was accomplished by navigating

to the *Tree Outline* and CRTL + Clicking the newly named surface parts “top” and “bottom”. *Form New Part* was selected, and the new part was renamed “Flap.” At this point in the *Tree Outline* there was 1 part and 2 bodies, shown in Figure 6-9.

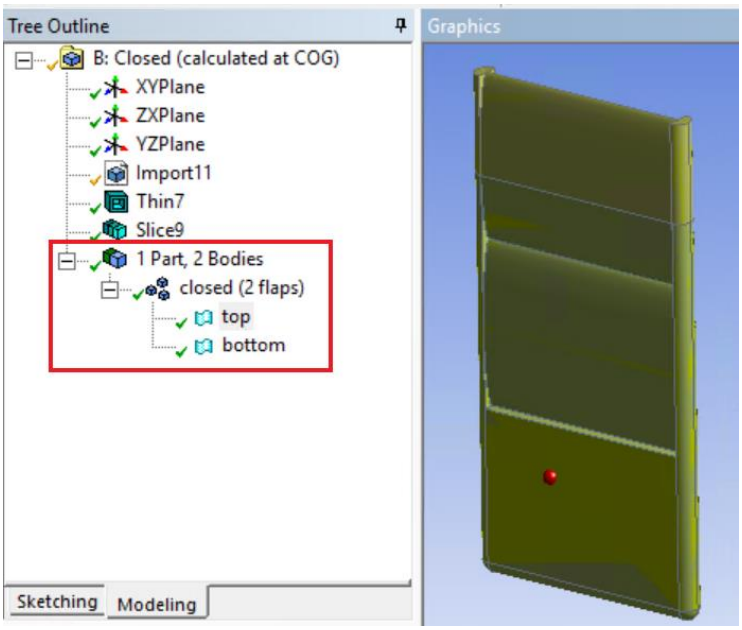

Figure 6-9. 1 Part and 2 Bodies

6.2.1 Defining Physical Parameters

The computational domain parameters that pertain to the water depth, water density, and water size were specified in *Geometry* > *Details* window > *Environment Constants*. For this research, a *Water Depth* of 3.3 m was selected, with a nominal *Water Density* of 1025 kg/m^3. This depth was selected so there were not any nodes that coincide with the sea bed. Had a water depth of 3.25 m been selected, Aqwa would have reported an error that the device was too close to the seabed. The *Water Size* mimicked the size of the ocean. Here, a water size of 50m^2 was selected. This can be seen in Figure 6-10. It should be noted that the *Import Preferences* portion of the *Details* window said that solid bodies were not imported. This was an important verification since Aqwa does not solve for solid bodies, only surface bodies.

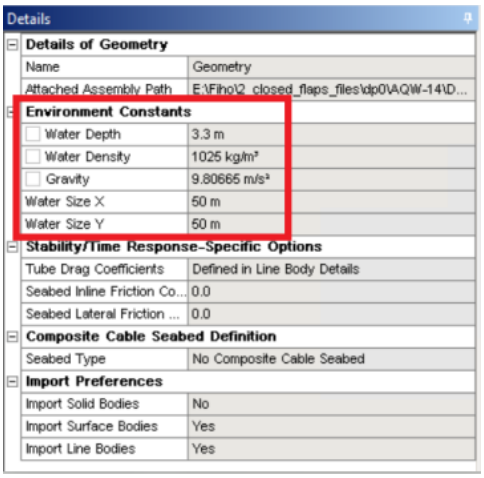

Figure 6-10. Computational Domain Parameters

6.2.2 OWSC Parameter Specification

Since the OWSC was free to move, and therefore, not be suppressed, it was ensured that *Structure Fixity* was set to *Structure is Free to Move*. Table 6-4 shows the device properties that were obtained previously in SolidWorks.

Table 6-4. Mass Properties Obtained from SolidWorks

Mass [kg]	346
Density [kg/m^3]	256.25
Location of Mass [m]	[0, 0, 1.28688]
Moments of Inertia, L_{xx}, L_{yy}, and L_{zz} [kg/m^2]	574.75, 462.47, 114.2

A point mass was added by selecting *Add* > *Point Mass.* A point mass was added at the OWSC's COG. For calculation at the COG, the values for *X Position Y Position* and *Z Position* were changed to *[0, 0, 1.28688]*. For calculation at the hinge, a point mass was added at *[0, 0, -3.1]*. Next, the *Mass* was set to *346* kilograms, and the D*efine Inertia Values* was changed to *Direct Input of Inertia*, allowing specification of the inertia values. It is worth noting that Aqwa presents the inertia values in terms of I_{xx}, I_{yy}, and I_{zz}, whereas the moment of inertia values that were

obtained from SW have terms L_{xx}, L_{yy}, and L_{zz}. In this case, I_{xx} is consistent with L_{xx} and so on. Figure 6-11 shows the point mass parameters for the closed OWSC.

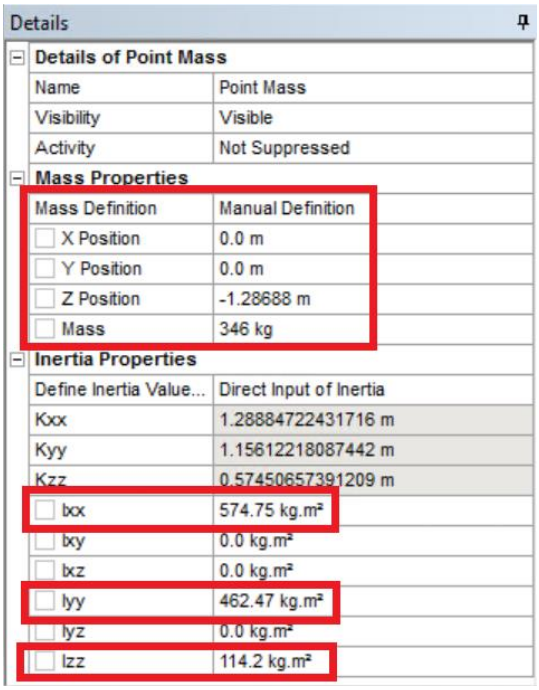

Details	
Details of Point Mass	
Name	Point Mass
Visibility	Visible
Activity	Not Suppressed
Mass Properties	
Mass Definition	Manual Definition
X Position	0.0 m
Y Position	0.0 m
Z Position	-1.28688 m
Mass	346 kg
Inertia Properties	
Define Inertia Value...	Direct Input of Inertia
Kxx	1.28884722431716 m
Kyy	1.15612218087442 m
Kzz	0.57450657391209 m
Ixx	574.75 kg.m²
Ixy	0.0 kg.m²
Ixz	0.0 kg.m²
Iyy	462.47 kg.m²
Iyz	0.0 kg.m²
Izz	114.2 kg.m²

Figure 6-11. Details of Point Mass

6.2.3 Meshing

In the *Mesh* section of Aqwa, the defeaturing tolerance and maximum element size was specified. These two parameters define the density of the mesh as well as the maximum allowable wave frequency that can be analyzed. The exact details of the mesh can be seen in Figure 6-12.

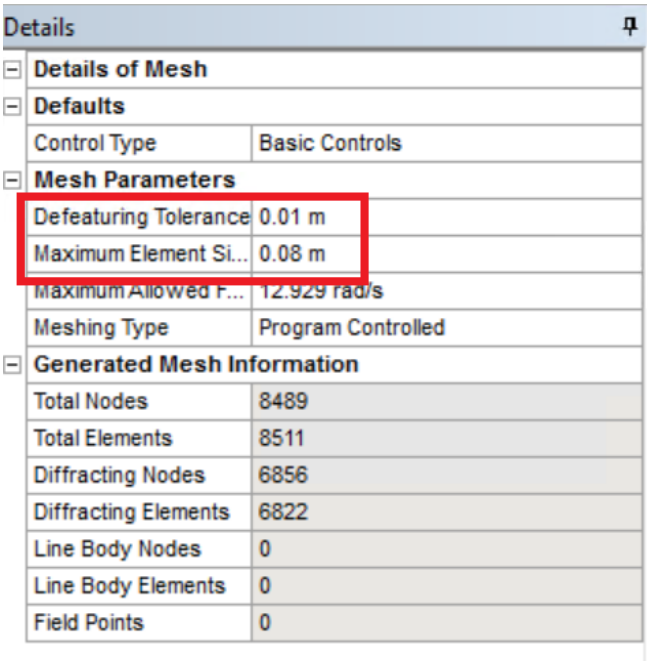

Figure 6-12. Details of Mesh

6.2.4 Simulation Parameter Setup

After the geometry, connection, and meshing parameters had been configured, the simulation setup was initiated, starting with the analysis settings, *Hydrodynamic Diffraction* > *Analysis Settings*. These parameters will control how the analysis will be conducted and which results are reported to the output .AH1 and .LIS files. These two files were used later in WEC-Sim and are very important. Most of the settings here remained default, with the exception of a few. First, *Ignore Modelling Rule Violations* was changed to *Yes*. This avoided minute geometrical errors that do not affect the hydrodynamic coefficient results. Next, *Calculate Full QTF Matrix* was set to *No* since the quadratic transfer function (QTF) is related to the second order exiting forces. In this case, only the first order exiting forces were of interest. Finally, *ASCII Hydrodynamic Database* was set to *Yes.* This provided both the .AH1 and .LIS files needed as inputs for WEC-Sim. It should be noted that many of the options in the *Analysis Settings* are for modeling offshore structures, not particularly nearshore wave energy converters. This process can be seen in Figure 6-13.

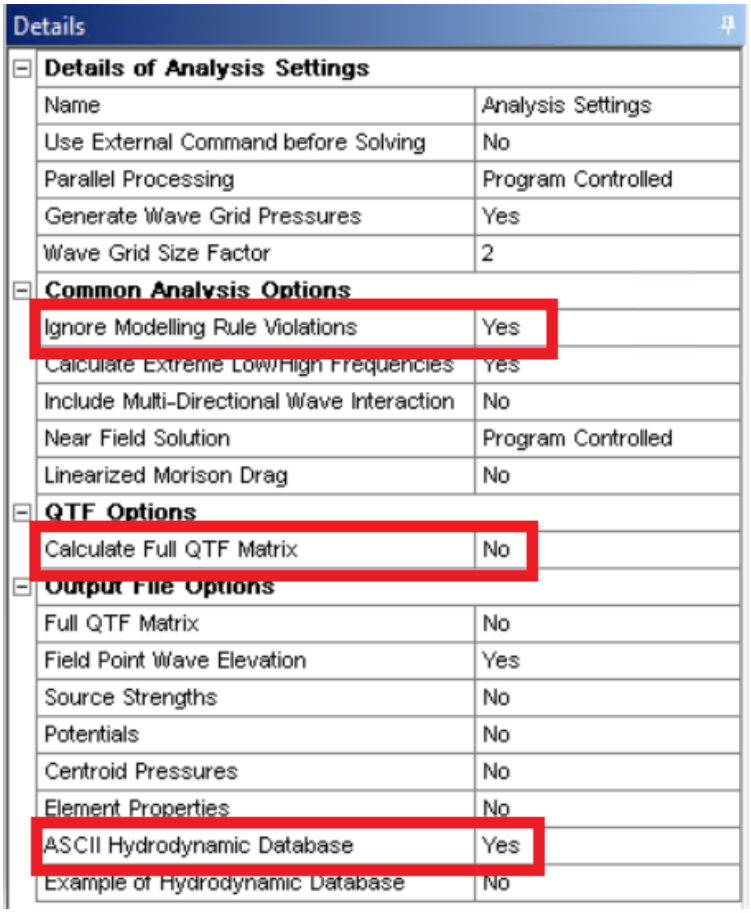

Figure 6-13. Analysis Settings for Aqwa Diffraction

Moving on to the *Structure Selection* branch, the *Interacting Structure Groups* was set to *None*, since only the OWSC flap was simulated, as pictured in Figure 6-14.

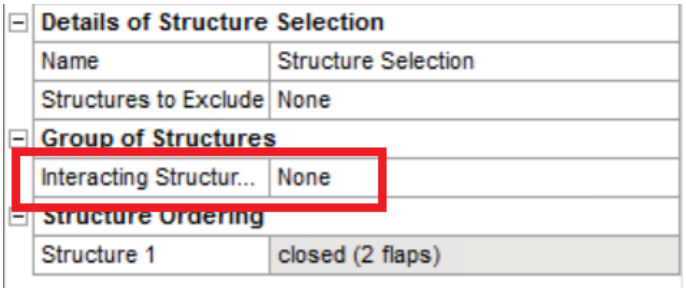

Figure 6-14. Interacting Structure Selection

The *Wave Directions* branch is where the desired wave directions are specified. By default, the wave *Type* will be set to *Range of Directions, No Forward Speed. Wave Range* was set to *-180° to 180°*, the *Interval* was changed to *90°*, and the *Number of Intermediate Directions* was *3*. This

resulted in four directional arrows in the *Graphics* window that showed which wave directions were being analyzed. However, only the 0° wave heading was analyzed, as this was the wave direction that acts perpendicular to the OWSC face. This can be seen in Figure 6-15 and Figure 6-16.

Details

Details of Wave Directions	
Name	Wave Directions
Visibility	Visible
Type	Range of Directions, No Forward Speed
Required Wave Input	
Wave Range	-180° to 180°
Interval	90°
Number of Intermediate Directions	3
Optional Wave Directions A	
Additional Range	None
Optional Wave Directions B	
Additional Range	None
Optional Wave Directions C	
Additional Range	None
Optional Wave Directions D	
Additional Range	None

Figure 6-15. Wave direction Specification

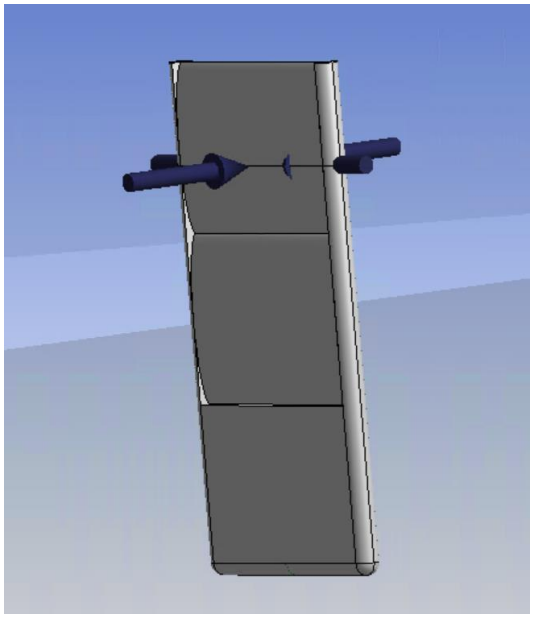

Figure 6-16. Directional Arrows in Aqwa Graphics Window

The *Wave Frequencies* branch allows the user to specify a range of wave frequencies that will be analyzed once the solution is conducted. Aforementioned, the maximum allowable frequencies is determined by the mesh size, so the range was from 0.01 rad/s to 12.929 rad/s. The total number of intermittent frequencies that were evaluated can be determined by navigating to *Wave Frequencies > Total Number of Frequencies*. Aqwa is capable of handling up to 100 wave frequencies. In this case, 80 frequencies were used to capture a sufficient amount of data points, as shown in Figure 6-17. A large number of wave frequency data also helped WEC-Sim generate more accurate results since the radiation IRFs had time to converge.

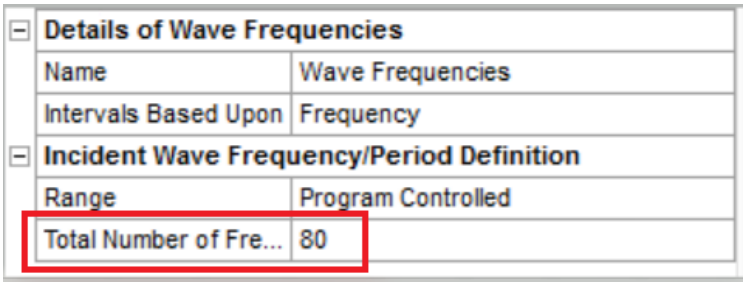

Figure 6-17. Number of Wave Frequencies

Finally, the solution was solved. If desired, it is possible to view specific values by navigating to *Solution > Insert Result > [Select Desired Result]*. For example, to view the results for the Radiation Damping term, navigate to *Solution > Insert Result > Radiation Damping.* Next, the *Structure* would be specified as *closed (2 flaps).* The *Sub Type* and *Component* tabs can be changed to *Global RY.* Here, X, Y, Z refer to the translation in the X, Y, and Z direction, while RX, RY, and RZ refer to the rotation about the X, Y, and Z axis respectively. Since the primary interest is in the rotation about the y-axis, *Global RY* was selected. Radiation Damping, Added Mass, and Diffraction and Froude-Krylov Torque, also referred to as the Wave Excitation Torque, responses can be seen in Figure 6-18, Figure 6-19, and Figure 6-20 below. It should be noted that for the Wave Excitation Torque, the wave direction was specified as 0.

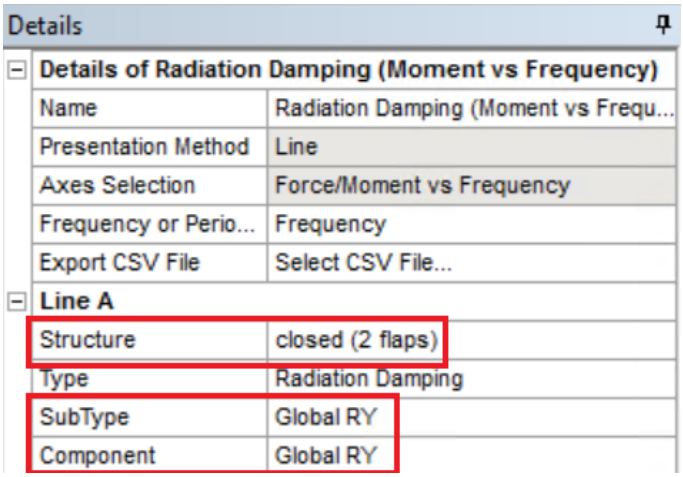

Figure 6-18. Radiation Damping Solution View

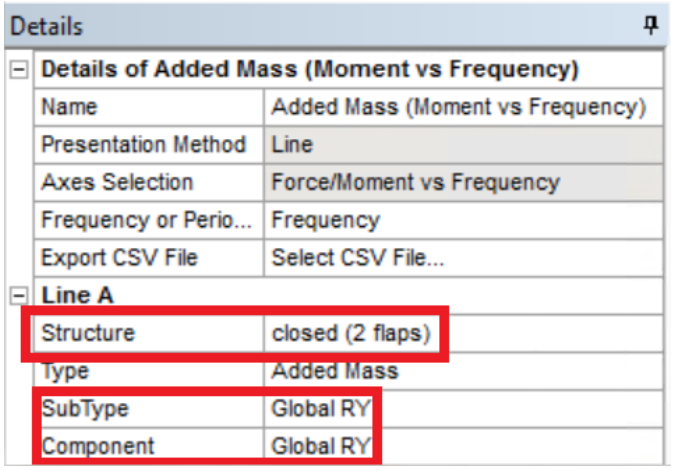

Figure 6-19. Added Mass Solution View

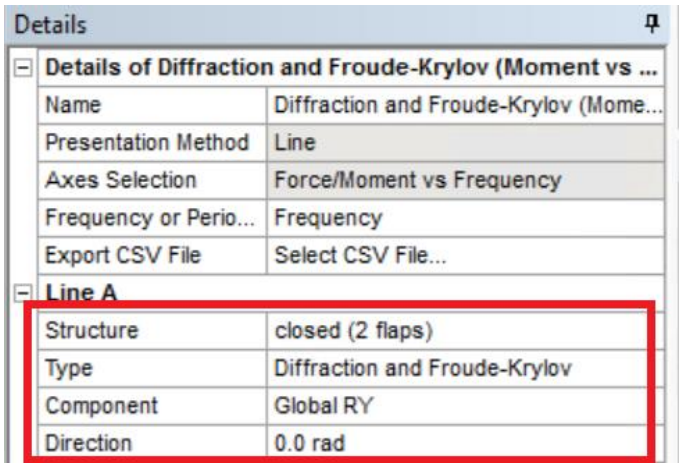

Figure 6-20. Diffraction and Froude-Krylov Torque, also known as Wave Excitation Torque

6.2.5 Accessing the Output Files

On the local machine's desktop, the File Explorer was opened, and the file path was located in which the Ansys Workbench Project was saved. Here, there were two files: The actual .wbpj file, and a folder containing all the project information. In this study, the Ansys Workbench project was named "AQWA SOP test.wbpj." This can be seen in Figure 6-21.

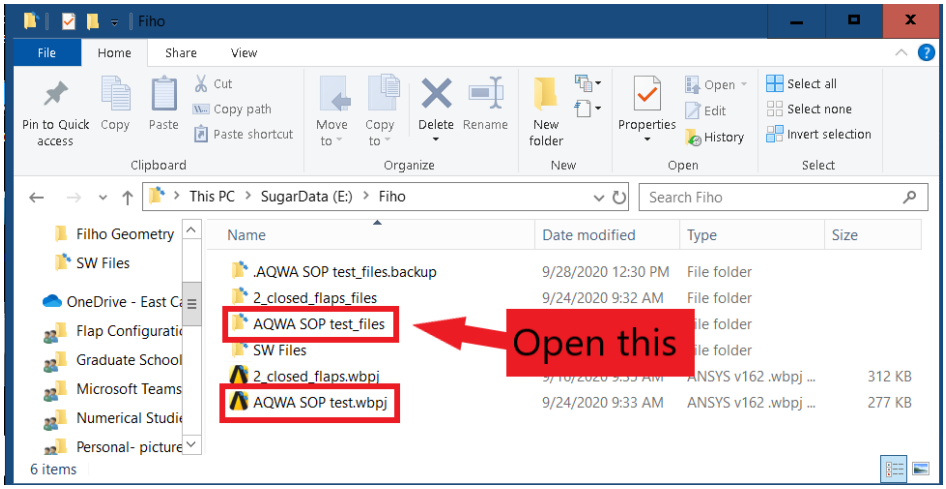

Figure 6-21. Navigating to the Aqwa Output Files

Next, locate the .AH1 and .LIS files to be used in WEC-Sim by following the path *AQWA SOP test_files > dp0 > AQW-14 > AQW > AQ > Analysis*, as seen in Figure 6-22.

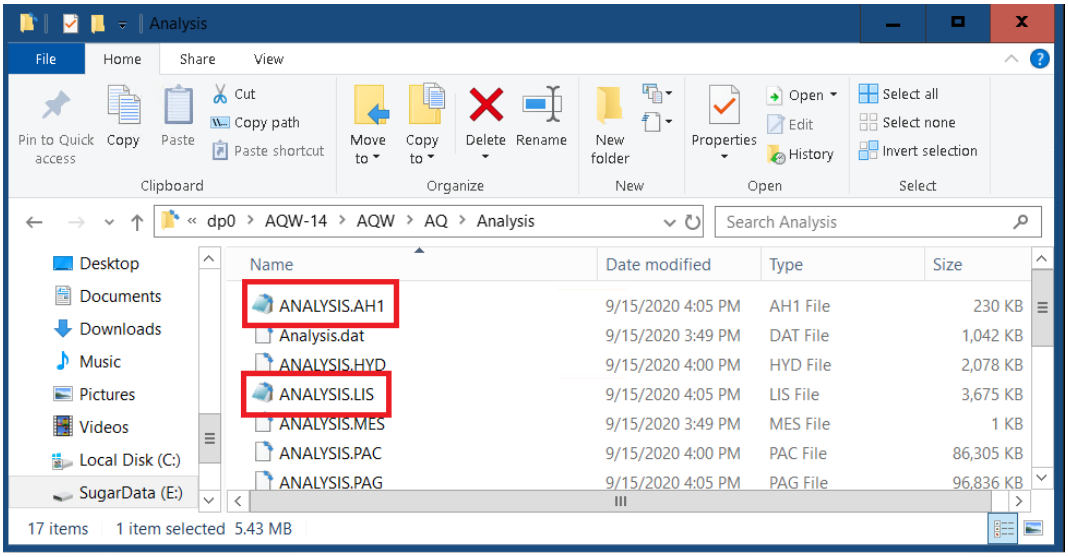

Figure 6-22. The.AH1 and .LIS Files

Appendix C

6.3 Simulation in WEC-Sim

The four main requirements to run a simulation in WEC-Sim are as follows:

- Hydrodynamic coefficients from Aqwa in .h5 format calculated at the COG
- SolidWorks geometry files in .STL format
- Simulink model including a global reference frame, various bodies, PTOs, and constraints
- A WEC-Sim input file code that is populated properly

6.3.1 BEMIO

WEC-Sim requires the hydrodynamic coefficients from Aqwa are calculated at the COG and are given in HDF5 format, or as *.h5* files. This was accomplished using BEMIO. To analyze hydrodynamic data from Aqwa, the *BEMIO.m* MATLAB file was opened, and the two output files obtained from Aqwa, *ANALYSIS.AH1* and *ANALYSIS.LIS,* were copied to the *hydroData* case directory. Within the BEMIO.m script, the *Read_AQWA* command was changed to

hydro = Read_AQWA(hydro, 'ANALYSIS.AH1', 'ANALYSIS.LIS')

The BEMIO.m script was run and the *.h5* file was generated to be used in the WEC-Sim input file.

6.3.2 STL Generation

Next, the STL files were acquired from SolidWorks and inserted to the *geometry* case directory.

6.3.3 Simulink Model

Two rigid bodies were used to model the OWSC base, *body(2),* and the OWSC flap itself, *body(1).* It should be noted that in this case, a base was modeled in SW and used in WEC-Sim solely for visual purposes. It is OK if the user desires to model only the OWSC itself. The base was modeled as a non-diffracting body, so it was not considered in any calculations and therefore

does not affect any of the results. The OWSC base was connected to the global reference frame via a fixed constraint, *constraint(1)*, and its location was specified in the wecSimInputFile.m code. The global reference frame was connected to the *base* side of the constraint while the *follower* side was connected to the OWSC base. A proper *base/follower* connection is required to successfully run a simulation. The OWSC base was then connected to the OWSC flap via a rotational joint, *pto(1)*, that was constrained so that it only pitched about the y-axis. Within this joint, the rotational joint was limited to rotate ± 30°. Damping and stiffness values can be specified to model the rotational joint as a linear PTO. Figure 6-23 depicts the Simulink model that was used for each vane angle configuration.

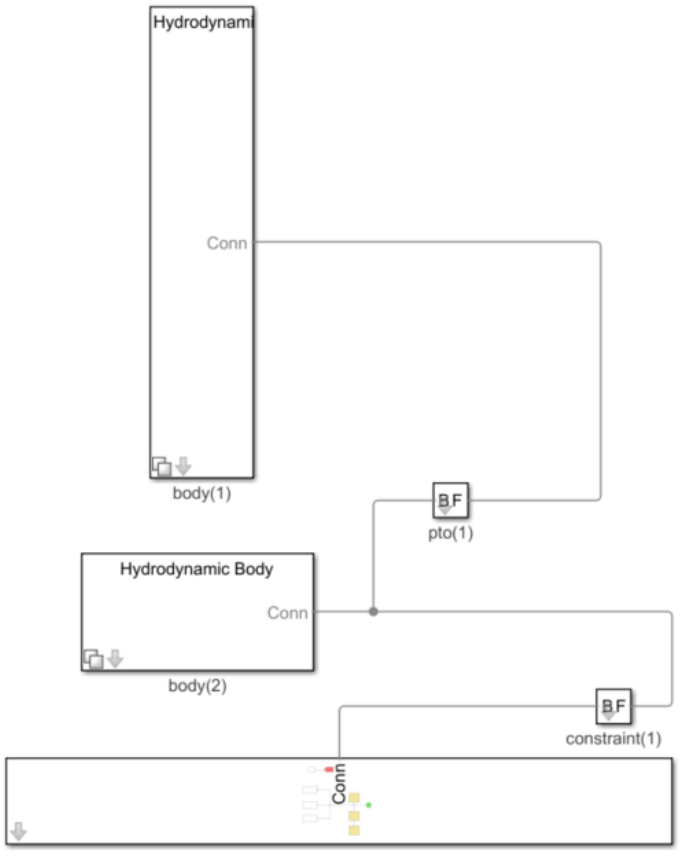

Figure 6-23. Simulink Model for OWSC

6.3.4 Populating the WEC-Sim Input File

In WEC-Sim, the input file stores information as objects in MATLAB such as simulation data, wave information, body data, PTO parameters, and constraint parameters. The name for this file is *wecSimInputFile.m*, and it will be referred to from here on as "the input file."

6.3.4.1 Simulation Data

The code used to populate the *Simulation Data* is shown in Figure 6-24.

```
%% Simulation Data
simu = simulationClass();
simu.simMechanicsFile = 'wecsim.slx'; % Specify Simulink Model File
simu.solver = 'ode4'; %Fixed Time Step
simu.explorer='off'; %SimMechanics Viewer: OFF
simu.startTime = 0;
simu.rampTime = 100;
simu.endTime=400;
simu.dt = 0.01;

simu.mcrCaseFile = 'mcrClosed.mat'; %Contains Wave & PTO Info
```

Figure 6-24. WEC-Sim Input File: Simulation Data Class

6.3.4.2 Wave Information

Figure 6-25 shows the input data for wave information.

```
%% Wave Information
%Irregular Waves using PM Spectrum
waves = waveClass('irregular'); %initializes irregular waves
%waves.H = ;
%waves.T = ;
waves.spectrumType = 'PM';      %Pierson-Moskowitz spectrum
waves.phaseSeed=1;              %1 phase seed used to replicate PM spectrum
                                %for each case
```

Figure 6-25. WEC-Sim Input File: Wave Information Class

6.3.4.3 *Body Data*

Figure 6-26 shows the body data code used in the input file.

```
%% Body Data
% Flap
body(1) = bodyClass('hydroData/smaller_mass/ANALYSIS.h5');
body(1).geometryFile = 'geometry/CG_2_Closed_Flaps.STL';
body(1).mass = 346.23459; %kg
body(1).momOfInertia = [574.75 462.468 114.20137];

% Base
body(2) = bodyClass('');
body(2).nhBody = 1;
body(2).name = 'Base';
body(2).geometryFile = 'geometry/CG_2_Closed_Base.STL';
body(2).mass = 999;
body(2).momOfInertia = [1 1 1];
body(2).cg = [0 0 -3.25];
body(2).dispVol = 0;
```

Figure 6-26. WEC-Sim Input File: Body Data Class

6.3.4.4 *PTO and Constraint Parameters*

The code used in the input file for PTO and constraint parameters can be seen in Figure 6-27.

```
%% PTO and Constraint Parameters
% Fixed Constraint
constraint(1)= constraintClass('Constraint1');
constraint(1).loc = [0 0 -3.25];

% Rotational PTO
pto(1) = ptoClass('PTO1');   % Initialize ptoClass
%pto(1).k = ;
%pto(1).c = ;
pto(1).loc = [0 0 -3.1];     % PTO Location [m]
```

Figure 6-27. WEC-Sim Input File: PTO and Constraint Parameters Class

6.3.5 Multiple Condition Runs (MCR)

An example of the first seven wave states used in the MCR table can be seen in Table 6-5.

Table 6-5. Wave Conditions and Optimum Damping Values used in MCR

Wave Height, H_s	Wave Period, T_e	Optimum Damping, B_{opt}
0.25	2.5	118435.3
0.25	3.5	73403.79
0.75	3.5	73403.79
0.25	4.5	51446.98
0.75	4.5	51446.98
1.25	4.5	51446.98
0.25	5.5	37980.07

Appendix D

6.4 CFD Geometry

When analyzing the flow around a structure in CFD, a computational domain (CD) is that includes a cavity of the structure of interest. This will be discussed further below. In Figure 6-28, created in SolidWorks, there are three surfaces (from left to right):

- Outer Domain Surface
- Inner Domain Surface
- OWSC Surface

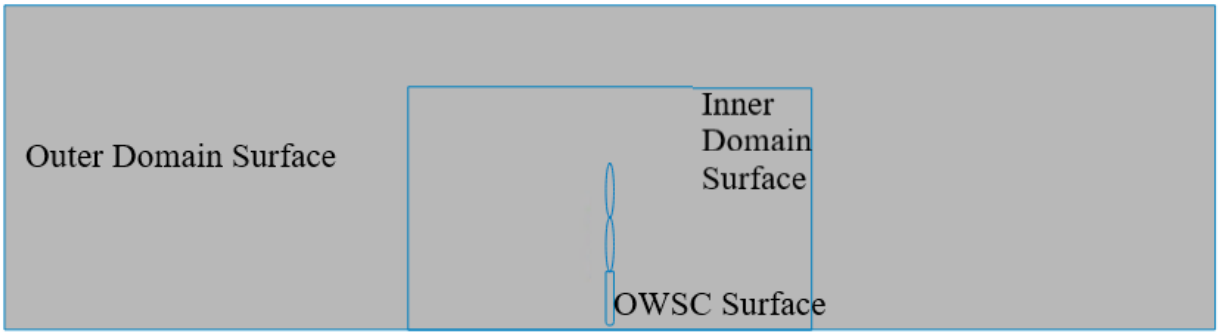

Figure 6-28. Computational Domain for Fluent

This geometry was then exported as an .IGS file and imported to DesignModeler. Two Boolean operations were used: one to subtract the OWSC from the inner domain surface without preserving tool bodies, while the other subtracted the inner domain surface from the outer domain surface while preserving tool bodies. The last step in DesignModeler was to create named surfaces. This was done by left-clicking the line segments of interest, right-clicking and selecting *Named Selection*. A named selection must be created for the OWSC so it can be modeled as a rigid, rotating body in Fluent. This was done by activating the line selection icon and selecting each line on the OWSC and creating a named surface. This can be seen in Figure 6-29. Finally, the inner domain and outer domain surface bodies were renamed to *INNER* and *OUTER* respectively, as shown in Figure 6-30.

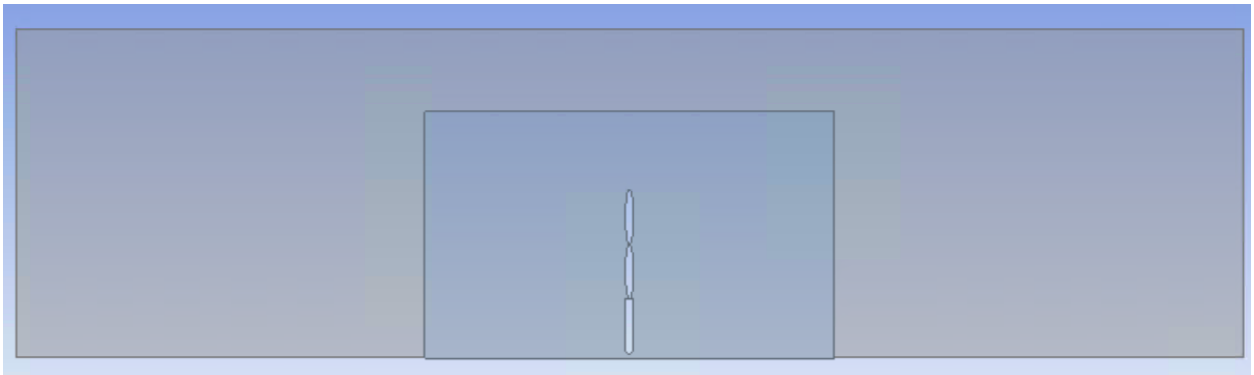

Figure 6-29. Creating a Named Selection for the OWSC Surface

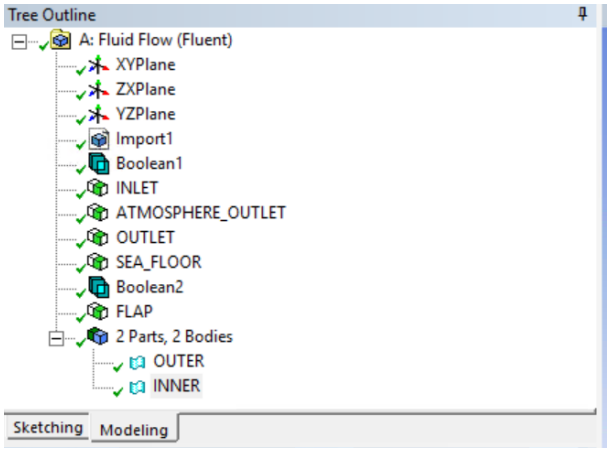

Figure 6-30. Tree Outline Indicating Surface Names

6.4.1 Mesh Setup

Next, the *Mesh* icon was selected in the *Outline Tree* and the physics and solver preferences were set to *CFD* and *Fluent* respectively. The element size was set to 0.1 meters, and was refined later. The mesh metric was set to *Skewness* initially, and the smoothing parameter was set to *High*. In order to ensure the quality of the mesh was sufficient for dynamic meshing, the mesh metric was analyzed for both *Skewness* and *Orthogonal Quality*. Here, the target skewness was lower than 0.7 and the target orthogonal quality was larger than 0.6. One mesh sizing function and one mesh refinement parameter were used to control the mesh distribution. Mesh sizing's were inserted by right-clicking *Mesh* > *Insert* > *Sizing*. For the mesh sizing, the scoping method was changed to *Named Selection* and the named selection was changed to *FLAP*. The element size was changed to 0.075 and *Curvature* and *Proximity* were captured since there are sharp curvatures along the

vanes. Finally, triangular mesh method was applied to the inner domain surface, shown in Figure 6-31, while the outer domain surface remained quadrilateral.

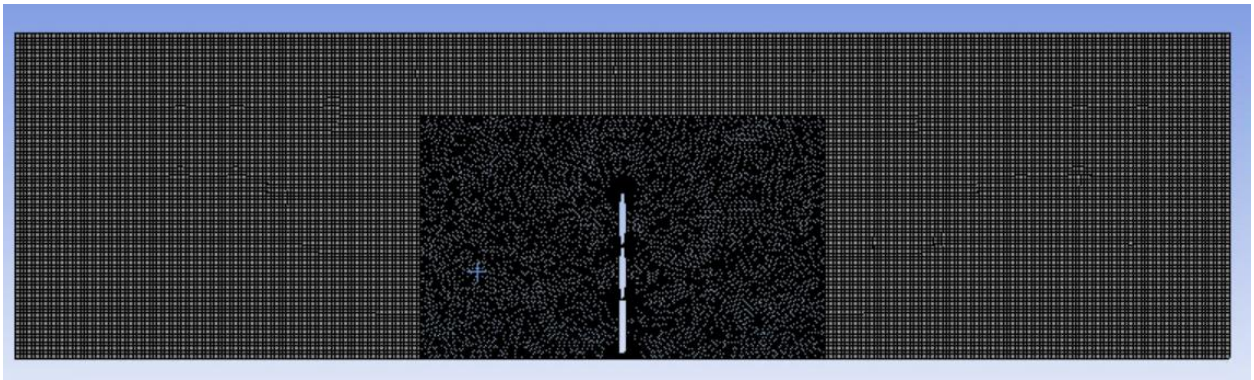

Figure 6-31. Applying Triangular Mesh Method to Inner Domain Surface

6.4.2 Fluent Setup

A pressure-based solver was used with transient time activated, and *Gravity* was activated in the y-direction using *-9.81* m/s^2. The model used here was the *multiphase* flow model, and the sub-model was the *volume of fluid* model. Figure 6-32 shows the VOF model selected with the *Open Channel Flow* and *Open Channel Wave BC* VOF Sub-Models activated. Furthermore, *Implicit Body Force* was activated.

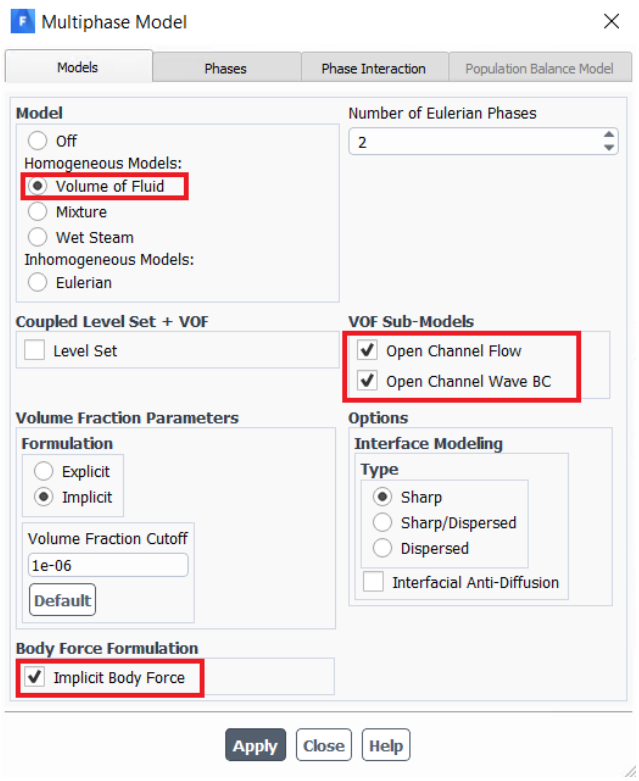

Figure 6-32. Multiphase Model Setup

Under the *Phases* tab, the characteristics of the two phases, air and sea water, were defined. The primary phase, air, had a density of 1.225 kg/m^3 and a dynamic viscosity of 1.7894e-5 kg/ms. These values are default in the Fluent database. The density and dynamic viscosity of seawater, the secondary phase, were changed to 1,025 kg/m^3 and 0.0014 kg/ms respectively. These changes can be seen in Figure 6-33.

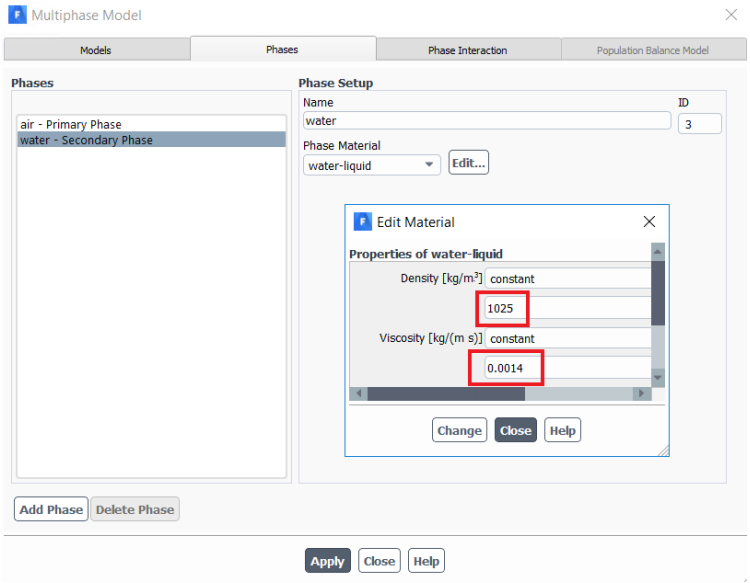

Figure 6-33. Defining the Two Phases being used in the VOF Model

Under the *Phase Interaction* tab, the surface tension was set to a constant value of 0.0728 N/m. This can be seen in Figure 6-34.

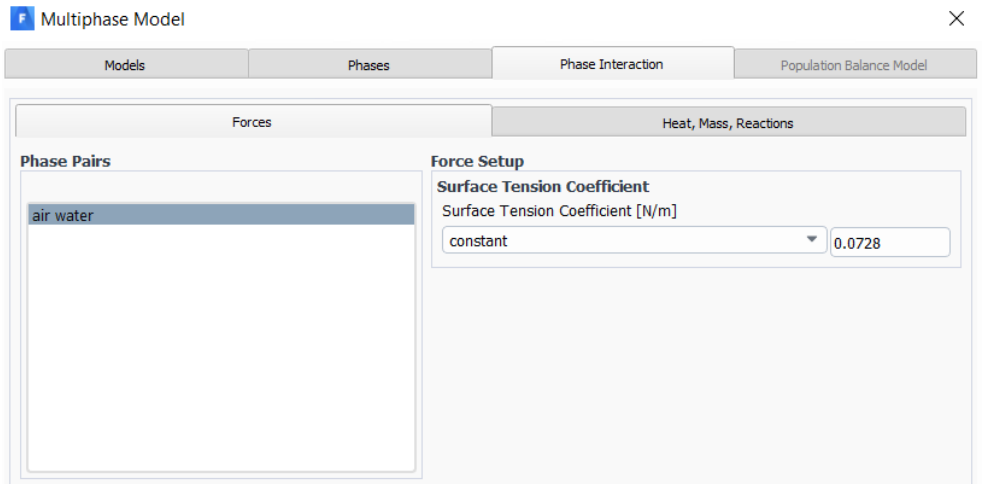

Figure 6-34. Defining Surface Tension Coefficient Between Air and Water

The *Realizable k-ε* with *scalable wall functions* turbulence model was used to close the RANS equations. In the *Boundary Conditions* tab, the *Inlet* was set to *Velocity-Inlet* and the *Open Channel Wave BC* checkbox was selected. Default values were used in the *Momentum* tab since air flow was not modeled—only waves. Under the *Multiphase* tab, the secondary phase of water was

enabled. *Shallow/Intermediate Waves* were used. The *Free Surface Level* was at a y-coordinate of 3.1 m, and the *Bottom Level* was -0.2016 m. These values were obtained in SolidWorks using the *Measure* feature under the *Evaluate* tab. One wave was used using the *Third Order Stokes* wave theory. Aforementioned, the most commonly occurring wave condition at the reference site, whose depth was 3.3 m, was a wave height of 0.75 m and a wave period of 5.5 s. The corresponding wavelength to this wave condition is 30 m. The inlet boundary condition can be seen in Figure 6-35.

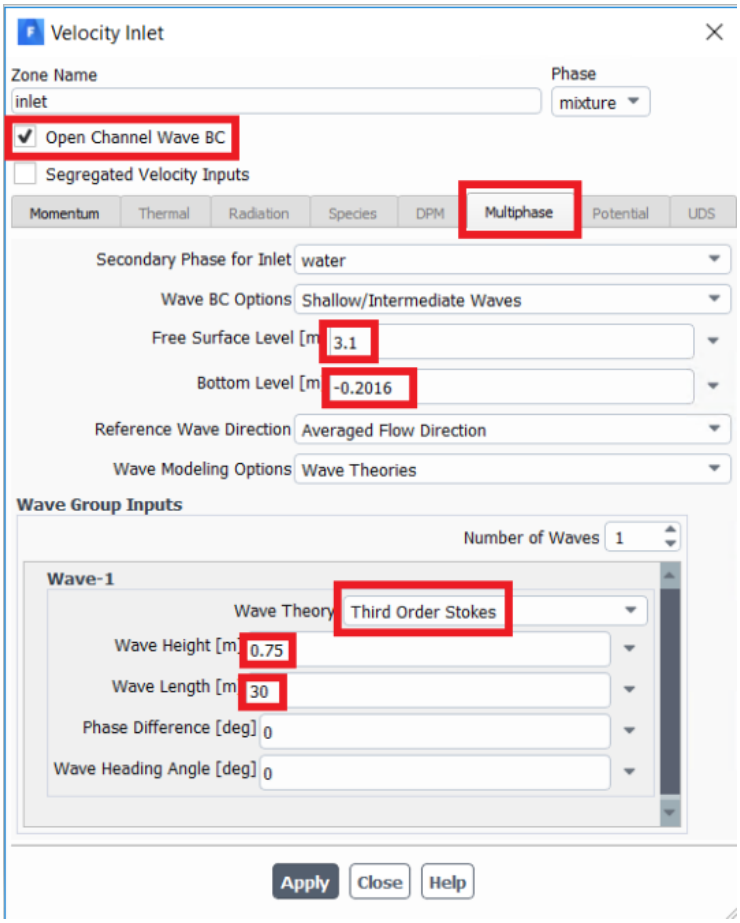

Figure 6-35. Inlet Boundary Conditions for Wave Setup

Since there were two outlets in the domain, the atmosphere, and the outlet domain, both were modeled as pressure outlets. In the *Multiphase* tab, the *Open Channel* box was selected, and the *Free Surface Level* and *Bottom Level* parameters were defined. These were the same values used for the inlet boundary conditions. Finally, the *Operating Conditions* box was selected, and the

Reference Pressure Location was set to 7.7984 m. This was the y-coordinate obtained from SolidWorks where the top of the computational domain was. This can be seen in Figure 6-36.

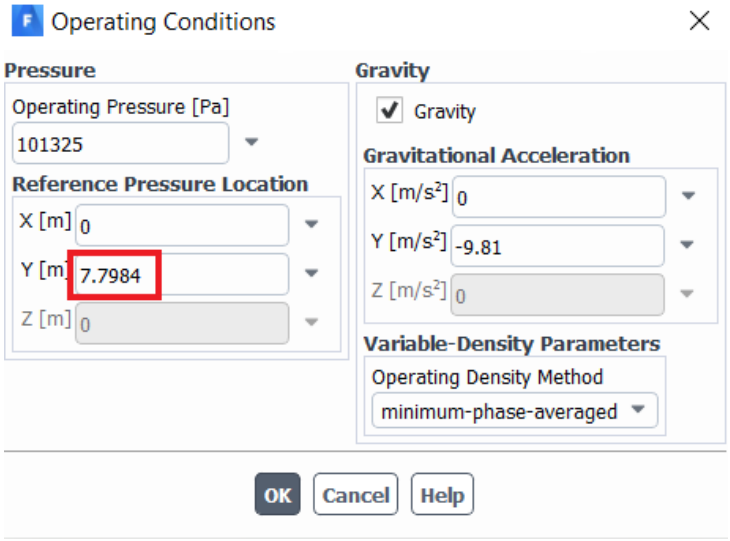

Figure 6-36. Defining Operating Conditions

After navigating to *Cell Zone Conditions*, *Outer* was selected from list of available zones. Under the *Multiphase* tab, *Numerical Beach* was selected, and *Compute From Inlet Boundary* was changed from *none* to *Inlet*. The process for defining the numerical beach can be seen in Figure 6-37.

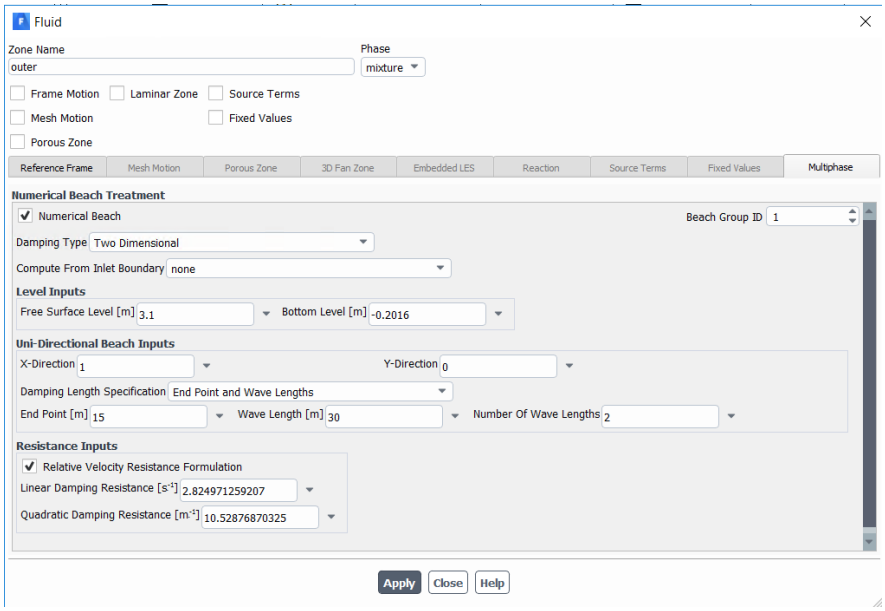

Figure 6-37. Defining Cell Zone Conditions for Numerical Beach Implementation

Once dynamic mesh was activated, *Smoothing* and *Remeshing* mesh methods were applied. The *Spring/Laplace/Boundary Layer* method was applied for this scenario where the deforming elements occurred at *Tri in Mixed Zones*, shown in Figure 6-38.

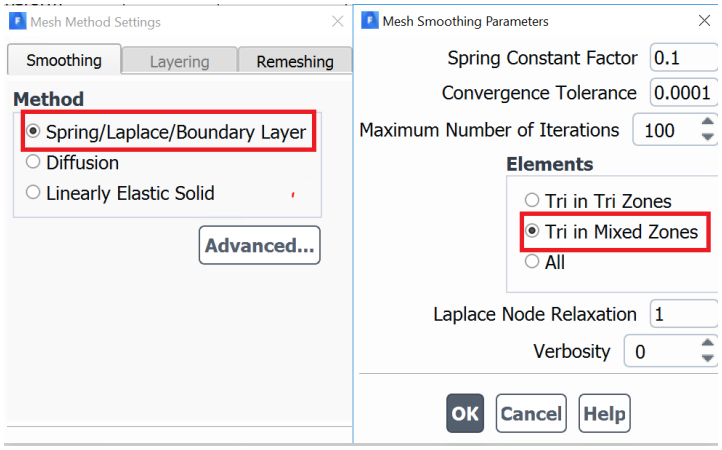

Figure 6-38. Dynamic Mesh—Smoothing Settings

Unified Remeshing was used with the length scale parameters being similar to the values in *Mesh Scale Info*. If desired, the exact values in *Mesh Scale Info* can be copied and pasted into the respective *Parameter* boxes. These *Remeshing* parameters can be seen in Figure 6-39.

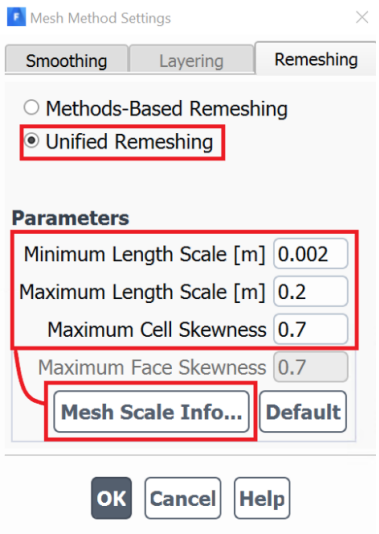

Figure 6-39. Dynamic Mesh—Remeshing Settings

Within the *Options* section, *Six DOF* and *Implicit Update* were selected. Since the OWSC is a simple 1-DOF system, it was modeled by selecting *Settings* > *Create/Edit.* The OWSC was named "flap" for simplicity and it was modeled as a *One DOF Rotation* system. Its mass, center of rotation coordinates, and inertia values were obtained from SolidWorks' *Mass Properties* option. The same spring constant used in WEC-Sim for this specific wave state was used for *Constant* to mimic the PTO forces, and the OWSC was constrained to rotate ±30°. After defining these values, *Write Motion History* was enabled to track the motion of the OWSC throughout the simulation. Under the *Implicit Update* tab, *Residual Criteria* was changed to 0.001, and all other default values were left unchanged. The setup used here for *Six DOF* and *Implicit Update* can be seen in Figure 6-40 and Figure 6-41 respectively.

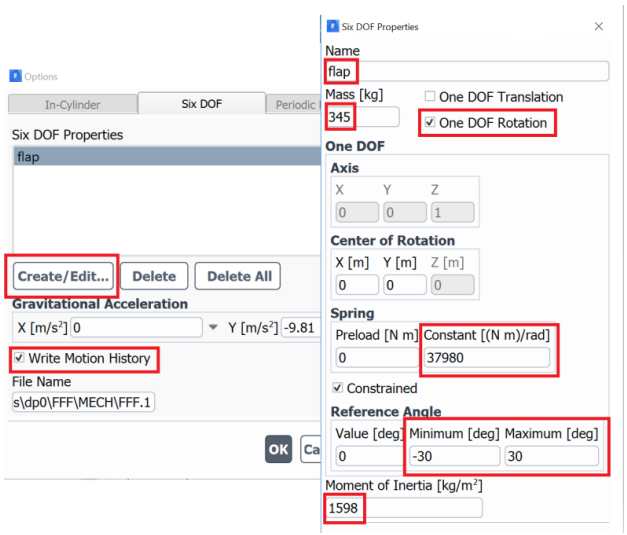

Figure 6-40. Six DOF Solver Settings

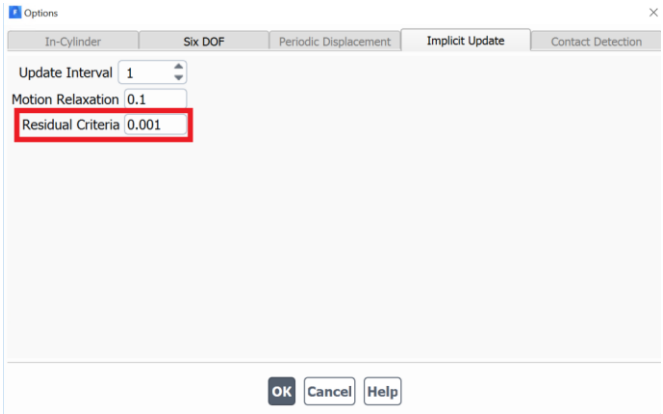

Figure 6-41. Implicit Update Solver Settings

Under the *Dynamic Mesh Zones* box, *Create/Edit* was selected to prescribe the *Six DOF Properties* to the OWSC and to define the inner domain as a deforming body. *Zone Names* was changed to *flap* and its *Type* to *Rigid Body* was changed to indicate that the selected region had motion, but no deformation. Under the *Motion Attributes* tab, the *flap* UDF was assigned to *Six DOF UDF/ Properties*, and *Six DOF* was ensured to be *On*. Finally, the *Center of Gravity Location* was changed to the center of gravity found in SolidWorks, in this case *[0, 1.81132] m.* This process can be seen in Figure 6-42.

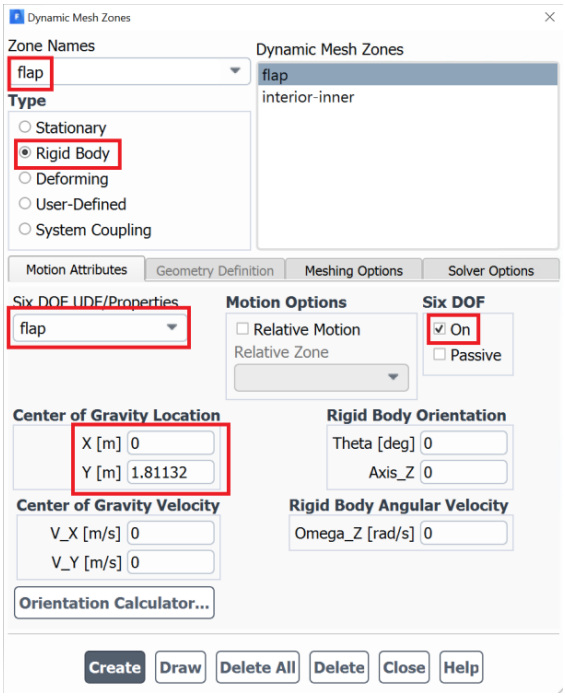

Figure 6-42. Dynamic Mesh Zone Setup for OWSC

Next, the inner domain was modeled as a deforming body so the triangular mesh could deform as the OWSC oscillated. This was done by changing *Zone Name* to *interior_inner* and changing *Type* to *Deforming.* It was ensured that *Remeshing*, *Smoothing*, *Global Settings*, and *Spring Method* were selected, and then the mesh motion was created . This is shown in Figure 6-43.

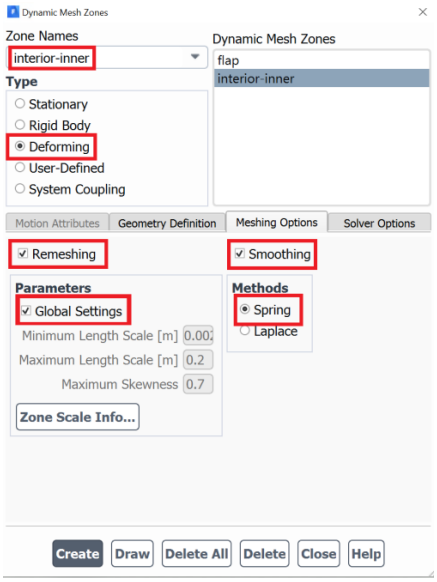

Figure 6-43. Dynamic Mesh Zone Setup for Deforming Mesh

The *PISO* scheme was selected and *Pressure Discretization* was selected to be *PRESTO!* The remaining discretization techniques and under-relaxation factors were optimized using the *VOF Solution Stability Controls* option. These parameters are shown in Figure 6-44.

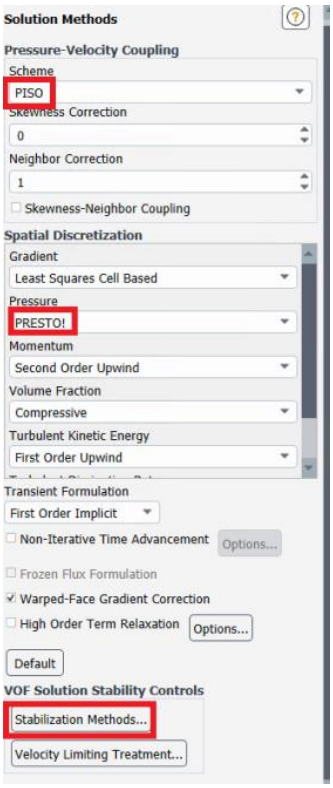

Figure 6-44. Solution Methods Parameters in Fluent

Next, the simulation was initialized using *Hybrid Initialization* that was computed from the *Inlet* boundary. The *Open Channel Initialization Method* was set to *Flat.* The initialization methods can be seen in Figure 6-45.

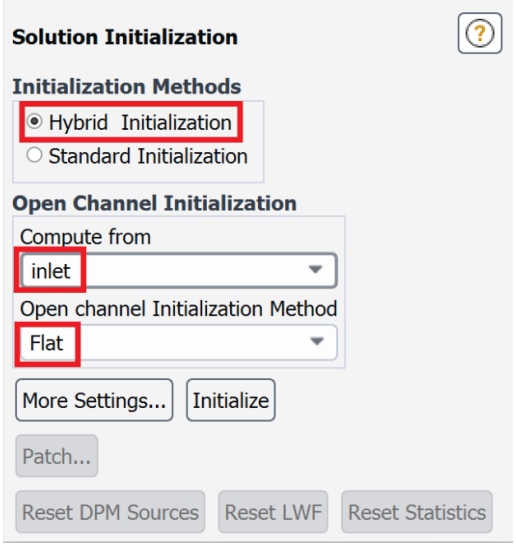

Figure 6-45. Initialization Methods used in Fluent

To create export files, navigate to *Report Definitions*, right click, and select *New*. In this simulation, the important pieces of information included total pressure on the OWSC, x- and y-forces that act on the OWSC, as well as the torque on the OWSC due to waves. Figure 6-46 shows an example defining the x-direction force report that acts on the OWSC.

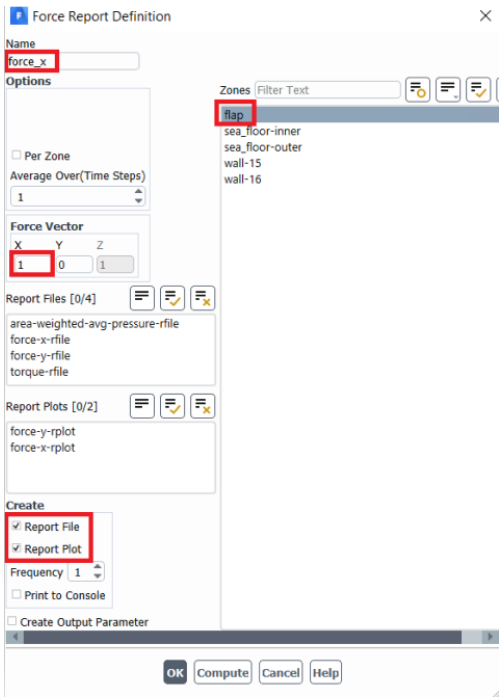

Figure 6-46. Defining a Report File to be used in Post-Processing

In order to save data files to be later analyzed in *CFD Post*, a *Solution Data Export* was created. It was ensured that the *File Type* was *CDAT for CFD-Post* and that all 95 data quantities were selected. This process can be seen in Figure 6-47.

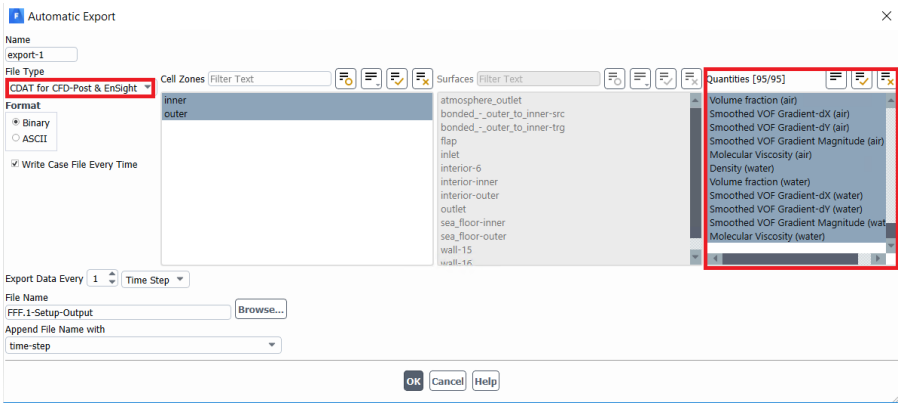

Figure 6-47. Solution Data Export for CFD-Post

The final step was to define the time advancement parameters in *Run Calculation. 2500* time-steps were used with a time step size of *0.01* seconds, and *75* iterations per times step were selected. These were chosen to ensure each iteration converged to 1.0e-3, and the total simulation was at least 25 seconds for adequate data capture. Once this is complete, the solution was commenced by selecting *Calculate*. This process can be seen in Figure 6-48.

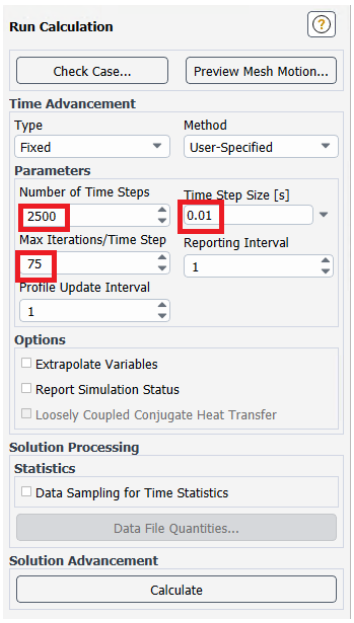

Figure 6-48. Time Advancement Parameters in Fluent